

AD-A243 403

## DOCUMENTATION PAGE



IC

ITE

1991

## 2b. DECLASSIFICATION/DOWNGRADING SCHEDULE

## 4. PERFORMING ORGANIZATION REPORT NUMBER(S)

VPI-E-91-20

## 1b. RESTRICTIVE MARKINGS

3. DISTRIBUTION/AVAILABILITY OF REPORT  
Approved for public release, distribution unlimited

## 5. MONITORING ORGANIZATION REPORT NUMBER(S)

## 6a. NAME OF PERFORMING ORGANIZATION

ESM Department

6b. OFFICE SYMBOL  
(If applicable)7a. NAME OF MONITORING ORGANIZATION  
Office of Naval Research  
Fluid Dynamics Program

## 6c. ADDRESS (City, State, and ZIP Code)

Virginia Polytechnic Institute and State Univ.  
Blacksburg, VA 24061

## 7b. ADDRESS (City, State, and ZIP Code)

800 N. Quincy St.  
Arlington, VA 222178a. NAME OF FUNDING/SPONSORING  
ORGANIZATION Defense Advanced  
Research Projects Agency8b. OFFICE SYMBOL  
(If applicable)

## 9. PROCUREMENT INSTRUMENT IDENTIFICATION NUMBER

N00014-89-J-1275, N00014-90-J-1909

## 8c. ADDRESS (City, State, and ZIP Code)

Submarine Technology Program  
1400 Wilson Blv.  
Arlington, VA 22209

## 10. SOURCE OF FUNDING NUMBERS

PROGRAM  
ELEMENT NO.PROJECT  
NO.TASK  
NO.WORK UNIT  
ACCESSION NO.

## 11. TITLE (Include Security Classification)

OBSERVATION AND MEASUREMENTS OF FLOW STRUCTURES IN THE STAGNATION REGION OF A  
WING-BODY JUNCTION

## 12. PERSONAL AUTHOR(S)

S. Kim, D. A. Walker, and R. L. Simpson

## 13a. TYPE OF REPORT

Technical

## 13b. TIME COVERED

FROM 12/1/88 TO 8/31/91

## 14. DATE OF REPORT (Year, Month, Day)

1991 September 1

## 15. PAGE COUNT

280

## 16. SUPPLEMENTARY NOTATION

## 17. COSATI CODES

FIELD	GROUP	SUB-GROUP
13	10	01
14	02	

## 18. SUBJECT TERMS (Continue on reverse if necessary and identify by block number)

Boundary Layer  
Three Dimensional Separation  
Turbulence

## 19. ABSTRACT (Continue on reverse if necessary and identify by block number)

The behavior of a junction vortex formed around an obstacle in a boundary layer flow was studied experimentally in a water tunnel for two low speed cases. A wing consisting of a 3 : 2 elliptical nose and an NACA 0020 tail was used to simulate the junction vortex.

A visual study using a hydrogen bubble technique was extensively conducted to investigate the flow structures in the stagnation region of the wing. It was observed that a multiple vortex system exists in this region and shows an acyclic flow pattern.

LDV measurements were performed in the plane of symmetry upstream of the wing. The general behavior of the flow agrees with an earlier wind tunnel test of Devenport and Simpson which was conducted at higher speed. A low frequency, bistable flow structure was observed as in the wind tunnel measurements. The switching between two flow modes (a backflow mode and a zero flow mode) was analyzed using LDV signals in the zone of a bimodal structure. A dimensionless frequency group ( $St_T$ ) was found to represent the average frequency of successive switches from a given mode to the other.

## 20. DISTRIBUTION/AVAILABILITY OF ABSTRACT

☒ UNCLASSIFIED/UNLIMITED ☐ SAME AS RPT ☐ DTIC USERS

## 21. ABSTRACT SECURITY CLASSIFICATION

NONE

## 22a. NAME OF RESPONSIBLE INDIVIDUAL

## 22b. TELEPHONE (Include Area Code)

## 22c. OFFICE SYMBOL

The visual evidence of acyclic flow pattern was consistent with the LDV measurements, and revealed that aperiodic stretching of the junction vortex appears responsible for the bimodal (double-peaked) structure in the velocity histograms.

An attempt to measure the three-dimensional instantaneous velocity field in this region was made. A unique PIDV (particle image displacement velocimetry) technique was developed using a multiple wire hydrogen bubble method and a high speed video system. A stereo vision approach was implemented to capture two orthogonal views simultaneously for the three-dimensional motion analysis.



Accession For	
NTIS GRA&I	<input checked="" type="checkbox"/>
DTIC TAB	<input type="checkbox"/>
Unannounced	<input type="checkbox"/>
Justification	
By	
Distribution/	
Availability Codes	
Dist	Avail and/or Special
A-1	

91-17140



91 12 5 022

## TABLE OF CONTENTS

<b>Abstract</b>	<b>ii</b>
<b>Acknowledgements</b>	<b>iv</b>
<b>Table of Contents</b>	<b>v</b>
<b>List of Tables</b>	<b>ix</b>
<b>List of Figures</b>	<b>x</b>
<b>List of Symbols</b>	<b>xvi</b>
<b>1. Introduction</b>	<b>1</b>
<b>2. Background</b>	<b>6</b>
2.1 Investigations of a Junction Flow . . . . .	6
2.2 Hydrogen Bubble Technique . . . . .	12
2.3 Image Processing Technique Application . . . . .	14
<b>3. Experimental Setup and Apparatus</b>	<b>17</b>
3.1 Water Tunnel . . . . .	17
3.2 Model . . . . .	18
3.2.1 Wing . . . . .	18
3.2.2 False Floor . . . . .	19
3.2.3 Side Walls . . . . .	19
3.2.4 Contraction Section . . . . .	20
<b>4. Experimental Techniques</b>	<b>21</b>
4.1 Hydrogen Bubble Technique	21

4.1.1 General Description . . . . .	21
4.1.2 Probe and Circuit Design . . . . .	23
4.1.3 Lighting . . . . .	24
4.2 Laser Doppler Velocimetry . . . . .	25
4.2.1 General Description of LDV . . . . .	25
4.2.2 LDV Setup . . . . .	26
4.2.3 LDV Data Acquisition . . . . .	28
<b>5. Image Data Processing . . . . .</b>	<b>30</b>
5.1 Image Capturing System . . . . .	30
5.1.1 High Speed Video System . . . . .	30
5.1.2 Cameras and Setup . . . . .	30
5.1.3 Image Data Formats . . . . .	32
5.2 Mathematical Background . . . . .	33
5.2.1 Coordinate System . . . . .	33
5.2.2 Mathematical Model . . . . .	34
5.2.3 Camera Calibration . . . . .	35
5.2.4 Stereo Vision . . . . .	36
5.3 Preprocessing . . . . .	37
5.3.1 Background Subtraction . . . . .	38
5.3.2 Local Averaging Technique . . . . .	39
5.3.3 Histogram Equalization Technique . . . . .	40
5.3.4 Thresholding Technique . . . . .	41
5.4 Motion Analysis . . . . .	43
5.4.1 Introduction . . . . .	43



5.4.2 Centroid Search Routine . . . . .	44
5.4.3 Correspondence Algorithm . . . . .	46
5.4.4 Matching Algorithm . . . . .	48
5.4.5 Split-Merging Detection Algorithm . . . . .	49
5.4.6 Instantaneous Velocity Field . . . . .	50
<b>6. Experimental Results</b>	<b>51</b>
6.1 Introduction . . . . .	51
6.2 Test Conditions . . . . .	52
6.3 Flow Visualization Results . . . . .	52
6.4 Results of LDV Measurements . . . . .	53
6.4.1 Characteristics of Approach Boundary Layer . . . . .	54
6.4.2 Mean Flow Data . . . . .	55
6.4.3 Some Turbulence Data . . . . .	56
6.4.4 Switching Frequency Analysis (SFA) . . . . .	57
6.5 Results of PIDV . . . . .	62
<b>7. Discussions of the Results</b>	<b>63</b>
7.1 Description of the Junction Flow . . . . .	63
7.2 Estimation of Friction Velocity ( $u_\tau$ ) . . . . .	70
7.3 Mean Velocity Profiles . . . . .	71
7.4 Low Frequency Unsteadiness . . . . .	72
7.5 Discussion of Higher Order Turbulence Results . . . . .	74
7.6 Dimensional Analysis on $\overline{f}_{sw}$ . . . . .	75
7.7 Vortex Stretching . . . . .	78
7.8 3-D PIDV Results . . . . .	80

<b>8. Conclusions</b>	<b>82</b>
<b>Bibliography</b>	<b>84</b>
<b>Tables</b>	<b>94</b>
<b>Figures</b>	<b>105</b>
<b>Appendices</b>	<b>254</b>
Appendix A: Uncertainty Analysis . . . . .	255
Appendix B: Q-R Algorithm . . . . .	257
Appendix C: $m_i$ 's Coefficients . . . . .	258
<b>Vita</b>	<b>261</b>

## LIST OF TABLES

Table 1.	Test conditions at $X/T = -2.15$ . . . . .	95
Table 2.	Uncertainty of the measured variables . . . . .	96
Table 3.	Camera calibration coefficients . . . . .	97
Table 4.	Camera characteristics . . . . .	98
Table 5.	Test log for LDV measurements . . . . .	99
Table 6.	Mean properties of junction vortex structure on different $Re_\theta$	100
Table 7.	File list related to LDV data reduction . . . . .	101
Table 8.	File list related to the PIDV motion analysis . . . . .	102
Table 9.	Some statistical results from flow visualization . . . . .	103
Table 10.	Comparison of dimensionless frequency groups obtained by other studies . . . . .	104

## LIST OF FIGURES

<b>Figure 1.</b>	Streamline patterns in the plane of symmetry of small obstacle separated flow showing (a) six vortex system and (b) four vortex system . . . . .	<b>106</b>
<b>Figure 2.</b>	The water tunnel facility . . . . .	<b>107</b>
<b>Figure 3.</b>	Hot film measurements for the turbulence level(% of $U_{ref}$ ) in the test section with a wing-body junction model mounted . .	<b>108</b>
<b>Figure 4.(a).</b>	General description of flow model . . . . .	<b>110</b>
<b>Figure 4.(b).</b>	Schematic diagram of the test model setup . . . . .	<b>111</b>
<b>Figure 4.(c).</b>	Assembled wing-body junction model in the test section .	<b>112</b>
<b>Figure 5.</b>	Side wall location with a boundary layer displacement thickness correction . . . . .	<b>113</b>
<b>Figure 6.</b>	Schematic diagram for the hydrogen bubble generation sequence in the upstream view . . . . .	<b>114</b>
<b>Figure 7.</b>	Examples of the flow visualization using hydrogen bubble method: (a) a time-line technique (b) a continuous sheet method (c) a combined time-streak marker method (d) an inverted time-line method . . . . .	<b>115</b>
<b>Figure 8.</b>	Hydrogen bubble probe . . . . .	<b>117</b>
<b>Figure 9.(a).</b>	Schematic diagram of hydrogen bubble generator circuit . .	<b>118</b>
<b>Figure 9.(b).</b>	Hydrogen bubble generator circuit . . . . .	<b>119</b>
<b>Figure 10.</b>	Lighting setup . . . . .	<b>120</b>

<b>Figure 11.(a).</b>	<b>Schematic diagram of LDV setup . . . . .</b>	<b>121</b>
<b>Figure 11.(b).</b>	<b>LDV setup . . . . .</b>	<b>122</b>
<b>Figure 12.</b>	<b>Fringe spacing measurement device . . . . .</b>	<b>123</b>
<b>Figure 13.</b>	<b>Fringe spacing measurement across the probe volume . . .</b>	<b>124</b>
<b>Figure 14.</b>	<b>Coordinate system . . . . .</b>	<b>125</b>
<b>Figure 15.</b>	<b>Mirror arrangement for the upstream and bottom views in one imager plane . . . . .</b>	<b>126</b>
<b>Figure 16.(a).</b>	<b>Image capturing system setup for Kodak Ektapro 1000 motion an- alyzer . . . . .</b>	<b>127</b>
<b>Figure 16.(b).</b>	<b>Ektapro 1000 motion analyzer system . . . . .</b>	<b>128</b>
<b>Figure 17.(a).</b>	<b>Mathematical model relating 3-D object points to image points 129</b>	
<b>Figure 17.(b).</b>	<b>Generalized pinhole camera model . . . . .</b>	<b>129</b>
<b>Figure 18.</b>	<b>Stereo vision . . . . .</b>	<b>130</b>
<b>Figure 19.</b>	<b>Effect of the background subtraction . . . . .</b>	<b>131</b>
<b>Figure 20.</b>	<b>Windows for local averaging technique . . . . .</b>	<b>132</b>
<b>Figure 21.</b>	<b>Algorithm for histogram equalization technique . . . . .</b>	<b>133</b>
<b>Figure 22.</b>	<b>Examples of bilevel images . . . . .</b>	<b>134</b>
<b>Figure 23.</b>	<b>Identification of the bubble elements for centroid search . .</b>	<b>135</b>
<b>Figure 24.</b>	<b>Bubble overlapping problem . . . . .</b>	<b>136</b>
<b>Figure 25.</b>	<b>Algorithm for the detection of the split-merging bubbles .</b>	<b>137</b>
<b>Figure 26.</b>	<b>Sequence of the flow upstream of the nose of a wing-body junction : an inverted hydrogen bubble time-line (flow is from left to right) 138</b>	

<b>Figure 27.</b>	Sequence of the continuous bubble sheet pictures showing the strong interaction of the two vortices near the wall . . . . .	149
<b>Figure 28.</b>	Some examples of the flow structures near the nose region of the wing-body junction : a conventional time-line technique .	154
<b>Figure 29.</b>	Measuring locations for LDV tests . . . . .	160
<b>Figure 30.</b>	Law of the wall plots of three different data set measured at $X/T = -2.15$ : $Re_\theta = 330$ and $1100$ — present data ; $Re_\theta = 6700$ — hot-wire measurement by Devenport and Simpson . . . . .	161
<b>Figure 31.</b>	Turbulent normal stress distribution across the boundary layer at $X/T = -2.15$ for $Re_\theta = 330, Re_\theta = 1100$ (LDV measurements) and $Re_\theta = 6700$ (Hot-wire measurements by Devenport and Simpson)	162
<b>Figure 32.</b>	Estimation of the local friction coefficient at $X/T = -2.15$ using the “cross plot of log region” procedure for $Re_\theta = 1100$ . .	163
<b>Figure 33.</b>	Law of the wall plot at $X/T = -2.15$ for $Re_\theta = 1100$ : $u_\tau$ is calculated using the “cross plot of log region” procedure assuming $\frac{dP}{dx} = 0$ . . . . .	164
<b>Figure 34.</b>	Law of the wall plot at $X/T = -2.15$ for $Re_\theta = 1100$ : $u_\tau$ is calculated using the “wall profile plot” assuming $\frac{dP}{dx} = 0$ . .	165
<b>Figure 35.</b>	Estimation of local friction coefficient at $X/T = -2.15$ using the “cross plot of log region” procedure for $Re_\theta = 330$ . . . .	166
<b>Figure 36.</b>	Law of the wall plot at $X/T = -2.15$ for $Re_\theta = 330$ : $u_\tau$ is calculated using the “cross plot of log region” procedure assuming $\frac{dP}{dx} = 0$ . . . . .	167

<b>Figure 37.</b>	Law of the wall plot at $X/T = -2.15$ for $Re_\theta = 330$ : $u_\tau$ is calculated using the "wall profile plot" assuming $\frac{dP}{dx} = 0$ . . . . .	168
<b>Figure 38.</b>	Mean velocity profiles using LDV measurements for $Re_\theta = 1100$ at all measuring locations . . . . .	169
<b>Figure 39.</b>	Mean velocity profiles using LDV measurements for $Re_\theta = 330$ at all measuring locations . . . . .	170
<b>Figure 40.</b>	Mean boundary layer profiles constructed using only axial component velocity for (a) $Re_\theta = 330$ , and (b) $Re_\theta = 1100$ . . . . .	171
<b>Figure 41.</b>	Mean velocity profile comparison for three Reynolds numbers at each measurement location ( $Re_\theta = 330$ and $Re_\theta = 1100$ — present data : $Re_\theta = 6700$ — Devenport and Simpson) . . . . .	173
<b>Figure 42.</b>	U-component turbulent fluctuations for three Reynolds numbers at each measurement location ( $Re_\theta = 330$ and $Re_\theta = 1100$ — present data : $Re_\theta = 6700$ — Devenport and Simpson) . . . . .	177
<b>Figure 43.</b>	Contour plot for the $\overline{u'^2}$ upstream of the nose of the wing-body junction for $Re_\theta = 330$ and $Re_\theta = 1100$ . . . . .	181
<b>Figure 44.</b>	Velocity histograms across the boundary layer (a) for $Re_\theta = 1100$ at $X/T = -0.10$ , (b) for $Re_\theta = 1100$ at $X/T = -0.125$ , (c) for $Re_\theta = 1100$ at $X/T = -0.150$ , (d) for $Re_\theta = 1100$ at $X/T = -0.175$ , (e) for $Re_\theta = 1100$ at $X/T = -0.20$ , (f) for $Re_\theta = 330$ at $X/T = -0.10$ , (g) for $Re_\theta = 330$ at $X/T = -0.125$ , (h) for $Re_\theta = 330$ at $X/T = -0.150$ , (i) for $Re_\theta = 330$ at $X/T = -0.175$ , (j) for $Re_\theta = 330$ at $X/T = -0.20$ . . . . .	183
<b>Figure 45.</b>	Flatness factor plots across the boundary layer for $Re_\theta = 1100$	193

<b>Figure 46.</b>	Skewness factor plots across the boundary layer for $Re_\theta = 1100$	197
<b>Figure 47.</b>	Flatness factor plots across the boundary layer for $Re_\theta = 330$	201
<b>Figure 48.</b>	Skewness factor plots across the boundary layer for $Re_\theta = 330$	205
<b>Figure 49.</b>	Some results obtained from a single threshold switching frequency analysis (SFA) with $\delta T_{min}$ . . . . .	209
<b>Figure 50.</b>	FIR low pass filter design (a) for $N = 15$ , $f_c = 0.3f_{sample}$ , (b) for $N = 21$ , $f_c = 0.3f_{sample}$ , (c) for $N = 15$ , $f_c = 0.35f_{sample}$ , (d) for $N = 21$ , $f_c = 0.35f_{sample}$ . . . . .	211
<b>Figure 51.</b>	Comparison of all the filters designed to detect the mode switching in time series of LDV signal (a) original signal, (b) filtered signal $N = 15$ , $f_c = 0.30f_{sample}$ (c) filtered signal $N = 15$ , $f_c = 0.35f_{sample}$ (d) filtered signal $N = 15$ , $f_c = 0.30f_{sample}$ (e) filtered signal $N = 15$ , $f_c = 0.25f_{sample}$ (f) filtered signal $N = 21$ , $f_c = 0.35f_{sample}$ (g) filtered signal $N = 21$ , $f_c = 0.30f_{sample}$ (h) filtered signal $N = 21$ , $f_c = 0.25f_{sample}$ . . . . .	215
<b>Figure 52.</b>	A schematic diagram showing the parameters used in three threshold level SFA . . . . .	217
<b>Figure 53.</b>	Typical example of triggered LDV signals using three threshold values . . . . .	218
<b>Figure 54.</b>	Probability density function of the normalized switching frequency ( $\bar{f}_{sw}/(f_{sw})_{avg}$ ) across the bimodal zone at (a) $X/T = -0.10$ for $Re_\theta = 1100$ : $N = 21$ , $f_c = 0.35f_{sample}$ , (b) $X/T = -0.125$ for	



	$Re_\theta = 1100$ : $N = 21$ , $f_c = 0.35f_{sample}$ , (c) $X/T = -0.15$ for	
	$Re_\theta = 1100$ : $N = 21$ , $f_c = 0.35f_{sample}$ . . . . .	219
<b>Figure 55.</b>	Variations of the average switching time ( $\overline{T}_{sw}$ ) in the bimodal zone for each flow condition . . . . .	222
<b>Figure 56.</b>	Variations of the average switching frequency ( $\overline{f}_{sw}$ ) in the bimodal zone for each flow condition . . . . .	223
<b>Figure 57.</b>	Fraction of a backflow mode ( $\gamma_b$ ) and in the bimodal zone for each flow condition . . . . .	224
<b>Figure 58.</b>	Contour plots of the estimated fraction of backflow mode ( $\gamma_b$ ) for $Re_\theta = 330$ and $Re_\theta = 1100$ . . . . .	225
<b>Figure 59.</b>	Sequence of bilevel images obtained by local averaging technique and thresholding . . . . .	227
<b>Figure 60.</b>	Sequence of three-dimensional velocity vector field in the nose region of the wing-body junction (measured by PIDV) . . .	233
<b>Figure 61.</b>	Three-Dimensional instantaneous velocity component measured by the 3-D PIDV : following individual bubble elements . . .	240
<b>Figure 62.</b>	Descriptive model for the sequence of flow events in the nose region of a wing-body junction . . . . .	250
<b>Figure 63.</b>	Typical LDV signal in the backflow region . . . . .	252
<b>Figure 64.</b>	Variations of Strouhal numbers ( $St_T$ ) in the bimodal zone for each flow condition . . . . .	253

## LIST OF SYMBOLS

$a$	length of the major axis of the elliptical nose of the wing
$a_{ijk}$	camera calibration coefficients
$C_f$	local skin friction coefficient
$D$	diameter of a cylinder
$D_r$	diameter of the rotating disk
$d_f$	fringe spacing
$\delta T_{min}$	minimum allowed switching time
$f$	camera parameter
$f_D$	Doppler frequency
$f_s$	shifted frequency
$\bar{f}_{sw}$	average frequency of successive switches of the flow back to the previous mode
$f(x_i, y_i)$	image function representing the gray level at each image point
$g(x_i, y_i)$	image function after local averaging
$G$	gray level
$h(x_i, y_i)$	image function after histogram equalization
$h_1, h_3$	heights of the local maxima in velocity histograms of LDV signals
$H$	shape factor of the approach boundary layer
$H(G)$	histogram of image gray level values
$m_i$	coefficients in the correspondence constraint equation

$N_i$	number of pixels in $i$ -th bubble element
$Re_\theta$	Reynolds number based on momentum thickness ( $\theta$ ) ( $= \frac{U_{ref} \theta}{\nu}$ )
$St_T$	Strouhal number based on model thickness ( $= \frac{\bar{f}_{sw} T}{U_{ref}}$ )
$t_f$	sampling interval between two successive frames
$T$	maximum thickness of the wing model
$T_k$	transformation matrix from the object point to the $k$ -th image plane point
$\bar{T}_{sw}$	average switching time
$(U, V, W)$	flow velocity in Cartesian coordinate system
$\bar{U}$	mean axial velocity
$U_e$	external velocity of the boundary layer
$U_{fs}$	axial velocity shift due to the shifted frequency ( $f_s$ )
$U_{ref}$	reference velocity measured at $X/T = -5.312$
$U_\infty$	free-stream velocity
$U_w$	velocity at the edge of the rotating disk
$(u', v', w')$	fluctuating velocity in Cartesian coordinate system
$u'_s$	small-scale fluctuations
$u'_l$	large-scale fluctuations
$\overline{u'^2}$	axial turbulent stress
$u_\tau$	friction velocity
$u^+$	nondimensional velocity used for law of the wall plot ( $= \frac{U}{u_\tau}$ )
$\hat{u}_j$	instantaneous velocity vector in the $j$ -th frame
$v_{t1}, v_{t2}, v_{t3}$	threshold values to trigger the switching between two flow modes
$(X, Y, Z)$	global coordinate system in Cartesian coordinate

- $(x_i, y_i)_k$  image plane coordinate system in  $k$ -th image plane
- $(\overline{x}_{c_i}, \overline{y}_{c_i})$  centroid location of the  $i$ -th bubble element in image plane coordinate
- $x_s$  the distance from the obstacle center to the separation line upstream of the obstacle in the plane of symmetry)
- $x_v$  the distance from the obstacle center to the vortex core
- $\hat{X}_{ik}$  image point in the  $k$ -th image plane in homogeneous coordinate system
- $\hat{X}_o$  object point in homogeneous coordinate system
- $y^+$  nondimensional height used for law of the wall plot  $(= \frac{y u_\tau}{\nu})$

### Greek Symbols

- $\delta_{99.5}$  approach boundary layer thickness measured at the location where  $\frac{u}{U_e} = 0.995$
- $\delta^*$  displacement thickness of the boundary layer  $(= \int_0^{\delta_{99.5}} (1 - \frac{u}{U_e}) dy)$
- $\theta$  momentum thickness of the boundary layer  $(= \int_0^{\delta_{99.5}} \frac{u}{U_e} (1 - \frac{u}{U_e}) dy)$
- $\lambda$  wave length of the laser beam
- $\kappa$  half angle between the two incident beams
- $\gamma_b$  fraction of a backflow mode in a bimodal zone
- $\gamma_z$  fraction of a zero flow mode in a bimodal zone
- $\mu$  dynamic viscosity of fluid
- $\nu$  kinematic viscosity of fluid
- $\rho$  fluid density

- $\omega_r$  angular velocity of the rotating disk used to measure fringe spacing
- $\vec{\Omega}$  vorticity vector
- $\Omega_s$  streamwise component of vorticity

## 1. INTRODUCTION

When a two-dimensional boundary layer encounters an obstacle protruding from the floor, the flow experiences the change of the pressure field near the obstacle. The blockage effect due to the obstacle causes the approaching mean boundary layer, initially with only spanwise vorticity, to be deflected to also have a longitudinal component of vorticity (secondary flow of Prandtl's first kind). Upstream of the obstacle, the flow separates from the floor due to the adverse pressure gradient. The flow entrained down along the edge of the obstacle is recirculated into the separated flow region. The separation with the secondary flow forms a very complicated, three-dimensional vortical structure in this region. This vortical structure trails downstream along each side of the obstacle. A main feature of this vortex system is its persistence downstream (Sedney and Kitchens, 1975). The vortex system is a form of "horseshoe" vortex.

The formation of the horseshoe vortex system is an inviscid process, not produced directly by viscosity or turbulent stresses. It is formed around any type of junction whether the flow is laminar or turbulent (Baker, 1978; 1979). Yet, in a turbulent boundary layer, the turbulent Reynolds stresses also create the cross-stream gradients in the flow, leading to the secondary flow (Prandtl's second kind). Thus, the flow behavior becomes more complicated with the time-dependent nature of a turbulent flow.

The junction vortex flow can be found in many practical examples, such as the wing-fuselage and wing-pylon junctions of aircraft, the appendage-hull junction

of ships, and blade-shroud junction of turbomachinery. This flow structure has undesirable effects on the flow characteristics in many cases; degraded aerodynamic performance, increase in heat transfer in this region, noise, and interference with devices that follow the wing.

Drag increases in the region of the separated flow due to the increased shear stresses caused by the high momentum fluid entrained from the outer part of the boundary layer flow or from the potential flow down along the edge of the obstacle. The flow around a bridge pier in a river is an example that shows the increase of the surface shear stresses. This causes accelerated erosion of the pier base as the sand upstream of the pier is dug out and flows downstream. Non-uniformity of the flow in the wake region (Hawthorne, 1954) interferes with the operation of the control devices mounted downstream. In the junction between the sail appendage and the hull of a submarine, this vortex results in noise due to the time-dependent nature of the vortical flow trailing downstream.

Attempts have been made to reduce these undesirable effects caused by the junction vortex. Leading edge strakes, and fairings or fillets have been used to improve the aerodynamic performance (Bertelrud, 1988; Devenport *et al.*, 1989). However, to achieve optimum performance, it is necessary to understand the physics of the flow structure of the junction vortex.

A number of researchers have studied this flow using numerical and experimental methods. Numerical simulation of the formation of the junction flow is not difficult to achieve (Rubel, 1978) since the generation of this secondary flow is an inviscid process. However, downstream of separation, a mathematical model becomes complicated because of a lack of the knowledge of the mechanism which

causes the junction vortex phenomenon. Recently, computational methods for the laminar horseshoe vortex flow were developed (Kaul, Kwak, and Wagner, 1985; Briley and McDonald, 1985). Comparison with the experimental data in the separated zone was made using the oil flow visualization studies and wall pressure measurements. More recently, the laminar flow fields around the juncture formed by a cylinder/flat plate were simulated using the full three-dimensional unsteady Navier-Stokes equations (Visbal, 1991). Most of experimental work includes flow visualization, hot-wire anemometer, and LDV measurements.

Flow visualization techniques have contributed to improving the physical understanding of complicated flow phenomena (Kline, 1978), and have been an essential element in current experimental fluid mechanics research. Especially in turbulence research, flow visualization has been used as an experimental tool to investigate flow structures by observing complex physical phenomena and identifying them as combinations of simple ones.

In most of the studies made on a junction flow, a surface oil flow technique has been used to visualize the mean flow characteristics on the surface around an obstacle (Bělík, 1973; Sedney and Kitchens, 1975; Baker, 1980; Rood, 1984; Moore and Forlini, 1984; Abid and Schmitt, 1986; Eckerle and Langston, 1986; Devenport and Simpson, 1986, 1987, 1988, 1990; Ölçmen, 1990; and many others). It has been observed that there is a system of vortices (Sedney and Kitchens, 1975; Baker, 1979, 1980, *etc.*). The flow field with multiple vortex systems was constructed using topology and some flow field information was obtained using a smoke wire visualization and local flow field measurements (see Figure 1). However, this technique is



confined to the visualization of the surface region, and cannot provide the characteristics of the instantaneous flow field. In order to understand the flow structure in this region, a method is required that can visualize three-dimensional instantaneous motion in the flow.

Many researchers have studied the horseshoe vortex system formed around a junction using various measurement techniques: hot-wire anemometers (Shabaka and Bradshaw, 1981; McMahon *et al.*, 1982; Mehta, 1984; Kubendran, McMahon, and Hubbartt, 1984; Eckerle and Langston, 1986; Devenport and Simpson, 1986, 1990; Greco, 1990), pressure measurements (Baker, 1979, 1980; Moore and Forlini, 1984; Eckerle and Langston, 1986; Devenport and Simpson, 1986), and LDV measurements (Tree, 1986; Abid and Schmitt, 1986; Devenport and Simpson, 1987, 1990). These methods were point measurements requiring repetitive measurements to obtain the mean flow characteristics. Point by point measurements are necessary to map the entire mean flow field.

Techniques to make measurements of the instantaneous velocity field have been developed with the aid of recent advances in electronic and optical technology. Using a photographic method with image processing, the velocity field can be mapped by tracing the particles present in the photographic images. PIDV (Particle Image Displacement Velocimetry) is the method that has been used widely to obtain the velocity field.

In this research, various experimental techniques were used to make the global and detailed investigations of the flow structure formed around the junction. The junction flow was produced using a flat plate and a wing mounted on it. The wing was composed of a 3 : 2 elliptical nose an NACA 0020 airfoil tail connected at

its maximum thickness. The tests were conducted in a water tunnel at low speeds. First, hot-film measurements were made to calibrate the flow field near the entrance of the test section of the water tunnel. LDV measurements were performed to obtain the averaged velocity in the plane of symmetry upstream of the wing. The results were compared with the wind tunnel data (Devenport and Simpson, 1987) measured on a half-size wing of the same geometry at different speed. The LDV signals obtained in the strong vortex region were analyzed to understand the low frequency fluctuations of the flow. Emphasis was placed on developing the flow visualization using a hydrogen bubble technique and the application of the PIDV technique using image processing techniques to extract the three-dimensional instantaneous velocity field upstream of the wing. An attempt to describe the flow field in the junction region were made using the observations obtained from the flow visualization.

The objectives of the current research are as follows:

- (a) to visualize the flow field using a hydrogen bubble wire technique to confirm the previous observation of the multiple vortex system (Sedney and Kitchens, 1975; Baker, 1979, 1980, *etc.*),
- (b) to determine the connection between the multiple vortices, backflow, and vortex stretching using the flow visualization and the local LDV measurements,
- (c) to check the dependency of the junction vortex behavior on the Reynolds number,
- (d) to analyze the low frequency fluctuations in LDV signals to obtain the physical understanding of the bimodal structure found by Devenport and Simpson (1987, 1988a, 1988b, 1990),
- (e) and to develop the PIDV technique to obtain the 3-D instantaneous velocity vector field.

## 2. BACKGROUND

### 2.1 Investigations of a Junction Flow

Previous investigations of a junction flow can be divided into two main categories. One is the study of a cylinder-end wall junction flow and the other is the study of the idealized wing-body junction flow. Both experimental models use a simplified geometry to reduce the complexity of the flow; a flat plate for the development of the oncoming boundary layer, and an obstacle (cylinder or wing model) mounted normal to it for deflecting the boundary layer. The study can be again categorized according to the flow state of a laminar boundary layer or a turbulent boundary layer.

#### Study of a cylinder-end wall junction

Bělík (1973) conducted experimental studies of the secondary flow about a circular cylinder mounted normal to a flat plate to simulate a flow formed in blade cascades bounded by two parallel flat walls. He used surface oil visualization and static pressure measurements on the flat wall in the separation region to determine the position and size of the vortex core. He obtained  $r/R \approx 1.43$ , where  $R$  is the radius of the circular cylinder and  $r$  is the radial distance from the center of the obstacle to the core of the vortex. This was in good agreement with the estimates of location from his visualized flow pattern. His results show that the separation region can be characterized by a single similarity number (the vortex Fourier number ( $Fo_v = 0.5 \frac{\nu}{U_\infty \delta}$ ) or the Reynolds number based on cylinder diameter  $D$ ).

Sedney and Kitchens (1975) performed investigations of the structure of three-dimensional separated flows in obstacle, boundary layer interactions. Their study was conducted in a turbulent, supersonic boundary layer flows ( $M = 1.5, 2.5, 3.5, 4.0, \text{ and } 4.5$ ) over protuberances. They used small obstacles, which had  $k < \delta$  where  $k$  is the obstacle height and  $\delta$  is the 99 % boundary layer thickness. They found that the cylinder height affects the strength and characteristics of the vortex when  $k < \delta$ .

Baker (1979) investigated the horseshoe vortex formed around the base of a cylinder of diameter  $D$  by a separating laminar boundary layer. He made a dimensional analysis on  $x_v$  (the distance from the obstacle center to the center of vortex core),  $x_s$  (the distance from the obstacle center to the separation line upstream of the obstacle in the plane of symmetry), and  $f$  (the frequency of oscillations of the horseshoe vortex system), and the corresponding dimensionless group can be expressed as follows:

$$\frac{x_v}{D}, \quad \frac{x_s}{D}, \quad \frac{fD}{U} = f\left(\frac{UD}{\nu}, \frac{D}{\delta^*}\right) \quad (2.1)$$

where  $\frac{fD}{U}$  is the Strouhal number.

Using a smoke-wire visualization technique, he observed three different types of vortex systems, which were ; i) steady horseshoe vortex systems with 2, 4 or 6 vortices, the number of vortices increasing as  $UD/\nu$  increases, ii) horseshoe vortex systems which exhibit a regular oscillatory motion, and iii) horseshoe vortex systems which exhibit an irregular unsteady behavior. Spectral analyses of the hot-wire signals

were implemented to investigate the oscillating behavior of the horseshoe vortex system. He made explanations that at certain values of  $UD/\nu$  and  $U/\delta^*$  the horseshoe vortex itself becomes unstable for some reason, and begins to oscillate in one of two 'natural' modes, the higher frequency mode becoming more dominant as the Reynolds number increases. He found that  $St_D = 0.26$  for low frequency oscillation, and  $St_D = 0.40$  for high frequency oscillation ( $St_D$  increased up to 0.60 at higher  $UD/\nu$ )

For the turbulent horseshoe vortex, Baker (1980) made experimental investigations of the model of the same geometry. He observed, by the surface oil-flow visualization, that only the vortex system consisting of four vortices (see Figure 1(b)) exists for the test conditions used ( $4000 < UD/\nu < 90000$ ,  $4 < D/\delta^* < 30$ ).

Eckerle and Langston (1986) made measurements of a turbulent horseshoe vortex formed around a cylinder. They made detailed surface flow visualization and static pressure measurements, and extensive mean velocity and pressure measurements in and around the flow field of the vortex system. They observed only a single horseshoe vortex in their visualization.

The study by Greco (1990) showed the flow behavior near a cylinder-end wall junction using hydrogen bubble flow visualization and hot-film anemometry in a low-speed, free-surface water channel. Five distinct laminar flow regimes were investigated, and he documented that, in a periodic flow regime, the periodicity of the generation of the junction vortex was found to be a function of free-stream velocity, cylinder diameter, fluid viscosity, and streamwise location. He observed that above a critical Reynolds number, the vortex system breaks down to become a large-scale turbulent horseshoe vortex.

### Idealized wing-body junction

Schwind (1962) made a study on an incompressible laminar boundary layer separation at the junction of a wall and a  $60^\circ$  included-angle wedge. He used smoke-wire visualization and observed five flow regimes according to the flow characteristics; three steady flow regimes at low speeds, and two periodic flow regimes at higher flow velocities.

Shabaka and Bradshaw (1981) made extensive cross-wire measurements of turbulent quantities in an idealized wing-body junction. The wing consisted of a semi-elliptical leading edge followed by a slab of constant thickness. Their measurements were confined to the region of nearly constant pressure downstream of the leading edge. The results showed that the vortex decayed only slowly with distance downstream, and its diameter remained roughly equal to the thickness of the boundary layer on the body. They found that the attenuation of the skew-induced secondary flow by the Reynolds stresses was very slow.

McMahon, Hubbart, and Kubendran (1982) measured three mean velocity components and six turbulent stresses in a juncture flow formed by a constant thickness body having an elliptical leading edge (which was mounted perpendicular to a large flat plate). Two single hot wire sensors were used at two different streamwise stations. They found that the strength of the secondary flow vortex in the juncture increases as the leading edge of a body of constant thickness is made more blunt, and that this stronger vortex has an effective core which is closer to the surface of the body than that of a weaker vortex caused by a leading edge of a smaller fineness ratio.

Mehta (1984) studied the effects of the wing nose shape on the flow in a wing-body junction. He used the same model as Shabaka and Bradshaw (1981) except that he had three nose shapes. Using miniature cross-wire probes, the secondary flow was measured while the streamwise velocities were measured using standard pitot tubes. It was found that the nature of the horseshoe vortex is strongly dependent on the wing nose shape. The size and the strength of the vortex increase with nose bluntness.

Moore and Forlini (1984) investigated the horseshoe vortex formed around a Rankine half-body. The body was located in a duct bounded by two plane endwalls and two side walls shaped like potential-flow streamlines. They made surface oil-flow visualization and static pressure measurements on the endwall and on the surface of the body on the planes downstream of the leading edge. A five-hole pressure probe was traversed to measure the secondary flow in their measurements.

Abid and Schmitt (1986) used a directionally sensitive, three-component laser Doppler velocimeter to make the mean velocities and turbulent Reynolds measurements with oil flow visualization and static pressure measurements at the wall. The horseshoe vortex system was generated by the obstacle mounted perpendicular to a flat plate. The leading edge of the obstacle was a semi-circular cylinder and its downstream part had a streamlined shape intended to avoid additional flow separation and to keep the flow as steady as possible. They presented LDV measurement data in the separated region.

Kubendran, McMahon, and Hubbartt (1986) made measurements of mean velocity components and turbulent stresses in the entire flow field surrounding the leading edge of a wing/fuselage-type juncture. A constant thickness body with a

1.5 : 1 leading edge was mounted normal to a flat plate. They found that both the strength and the location of the horseshoe separation vortex can be controlled by modifying the leading edge shape of the wing.

Dickinson (1986a, 1986b) presented LDV measurements for the geometrically similar model as the one used in this research. He reported that the larger cross-flow velocities resulted with increased bluntness of the nose shape. He used oil film and oil dot flow visualization techniques (1988) to find surface separation and attachment lines and streamline patterns.

Devenport and Simpson (1986, 1987, 1988a, 1988b, 1990) have contributed to the understanding of the time-dependent behavior of the turbulent wing-body junction flow through their experiments. Using a single hot-wire probe and a three component laser doppler anemometer, they made measurements of the mean velocity and turbulent stresses in the region surrounding the wing. Instantaneous spanwise distributions of the skin friction were obtained using an array of surface hot-wire sensors. Surface pressure measurements and oil flow visualization were conducted on the flat wall surrounding the wing. They found bimodal velocity histograms in the junction region, related to low frequency fluctuations in the flow.

Devenport *et al.* (1989) made mean pressure and hot-wire measurements to show the effects of a simple fillet on the flow of a turbulent boundary layer past an idealized wing-body junction.



## 2.2 Hydrogen Bubble Technique

Hydrogen bubbles are used as tracer particles to visualize the flow. The hydrogen bubble method is based on the electrolysis of water. Although the ions depend upon the electrolyte involved, in this case, the reaction is the decomposition of water ( $2H_2O \rightarrow 2H_2 + O_2$ ). When two electrodes with a potential difference are immersed in water, hydrogen is generated at the cathode and oxygen at the anode. If the cathode is a thin wire, very fine hydrogen bubbles are formed — the bubbles released from the wire are one-half the wire diameter. A wire may be used as either an anode or a cathode, but since the hydrogen bubbles are produced at twice the rate, they are used as flow tracers in this technique.

The hydrogen bubble technique was first described in 1953 by Kolins. Using a copper wire across a Lucite tube, he visualized the parabolic distribution of the velocity in a laminar pipe flow. A fundamental improvement in this method was discovered by Geller (1955) when he investigated the boundary layer on a water tunnel wall. He began to use a thin platinum wire of diameter of  $0.025\text{mm}$  as a cathode in his study. This technique was further developed by Clutter and Smith (1961).

In the 1960s, this technique began to prevail in investigating the turbulent flows because of its ease and flexibility in application. Schraub *et al.* (1965) applied the hydrogen bubble technique to the study of time-dependent low speed water flows. They presented detailed descriptions of various applications of this technique. In particular, a time-line and a combined time-streak marker method provided quantitative information on the time-dependent velocity and trajectories of the fluid elements.

Asanuma and Takeda (1965) and Mattingly (1966) extended the use of this technique to higher velocities (up to 7m/s and 5m/s, respectively) using a higher cathode potential and increased electrolyte additive concentration.

Criminale and Nowell (1965) showed that this technique could be extended to the measurements in liquid-water mixtures. They succeeded in using this method in a glycerine-water mixture up to 40 % (by weight) of glycerine. Roos and Willmarth (1969) reported some results obtained through use of the hydrogen bubble technique in high concentration glycerine mixtures in their study of low Reynolds number unsteady wake flows. In particular, they provided the justification for using hydrogen bubbles as tracer particles by showing that the relative motion between the bubble and the surrounding fluid is negligible.

Thompson reviewed this technique in his paper (1972): His discussion included the number of bubbles produced at the cathode, the variation of cathode current with electrode potential, variation of water path resistance with electrolyte concentration, effect of anode size and electrode spacing on water path resistance, and the effect of water temperature on water path resistance.

Kim *et al.* (1968, 1971) and Grass (1971) used this technique to study the turbulent boundary layer near smooth and rough walls, respectively. McAllister and Carr (1978) investigated the dynamic stall over an oscillating airfoil using this technique. In the latter study, a wire cathode was stretched across the test section and oriented normal to the direction of the flow.

Smith and Paxson (1983) at Lehigh University developed the computer-augmented hydrogen bubble-wire flow visualization system. Using digitally interfaced dual-view video sequences of a bubble time-line, the three dimensional motion of the time-line was recreated, and the Lagrangian velocity was obtained.

Applications of this technique has greatly increased since its introduction due to increasing need to understand global flow patterns and improvements in electronic and optical instrumentation. In a turbulent flow, the hydrogen bubble method has played an important role as an experimental tool for identifying new flow structures.

### **2.3 Image Processing Technique Applications**

Flow visualization resulting from the interaction between light and matter has been useful to design experiments and for proper interpretation of the conventional measurements. Recently, rapid advances in scientific technology have enabled flow visualization to be used as a direct measurement tool for the flow characteristics through the application of digital image processing techniques.

Our motivation for using digital image processing was the current emphasis on detecting and classifying large-scale structures in flows. Employing digital picture processing techniques, the information of the entire flow field frozen in the flow visualization pictures can be measured, while conventional measurement techniques such as hot-wire anemometry and LDV measurements only allow single point measurements.

One application of digital image processing to flow visualization is particle image velocimetry (PIV) or particle image displacement velocimetry (PIDV). According to the classification of digital image processing and flow visualization techniques by Hesselink (1988), this belongs to the group that obtains the images by scattering. Two other distinct approaches that have been widely applied using scattering are laser speckle velocimetry (LSV), and laser induced fluorescence (LIF).

This group uses light sheet generated by a laser beam to scatter light from the seeding particles in the flow. Since PIDV uses a low density of seeding particles, the measurements are possible only at those locations where particles happen to be during exposure. Difficulties that arise in the application of PIDV are that particles are indistinguishable from each other unless special care is taken and particles moving out of the illumination thickness of the light sheet may not be distinguished from the particles staying inside. The major disadvantage of PIDV is that this technique can be applied only to the measurements in one plane so that it is not easy to use the PIDV in regions where one is interested in three-dimensional flow.

A number of researchers have used the flow visualization pictures to obtain the quantitative information of the entire flow field. Grass (1971) used hydrogen bubble flow tracers and medium high-speed motion photography to obtain an instantaneous visual and quantitative description of the flow field. Using instantaneous longitudinal and vertical velocity profiles, he computed the distributions of the instantaneous Reynolds stress contribution. Imaichi and Ohmi (1983) developed a system for evaluating some of the physical variables of fluid flows through flow visualization and image processing techniques. Their measurements were within reasonable accuracy for two-dimensional vortical flow examples.

Utami and Ueno (1984) developed a tracer method to visualize the three-dimensional flow structure of a turbulent open channel flow. They designed a movable lighting system in which horizontal cross-sections of the flow could be illuminated instantaneously in a sequence by shifting the lighting plane using a stepping motor. A Lagrangian description of the flow field was used in the presentation of their results.

Lu and Smith (1985) employed automated image processing of hydrogen bubble flow visualization pictures to establish local, instantaneous velocity profile information. They used the time-of-flight technique to construct the local velocity profiles from the hydrogen bubble images, and attempted to correlate prototype turbulent burst detection techniques with corresponding visualization data.

Adamczyk and Rimai (1988a) used two-dimensional particle tracking velocimetry (PTV) to determine the fluid velocity in a transparent test section simulating an engine throttle body assembly. They further developed automated three-dimensional PTV using two cameras in their following study (Adamczyk and Rimai, 1988b).

Racca and Dewey (1988) developed a technique to automatically analyze the three-dimensional motion of tracers in a fluid flow. They designed the split field mirror system in order to obtain simultaneous orthogonal views in a single high speed cine camera. Eulerian information was derived from the pooled velocity data points by interpolation on a regular spatial grid.

Ensemble-averaging and correlation techniques were developed by Kerstens and Rockwell (1988) when they studied macroscale features of unsteady flows. They used hydrogen bubble time-line images for tracking and averaging.

Liu, Landreth, Adrian, and Hanratty (1991), improved the PIDV technique by developing high resolution particle image velocimetry to obtain the turbulent velocity field for fully developed flow. They made comparison of their PIDV results with those of direct numerical simulation and LDV measurements, and showed good agreement.

### 3. EXPERIMENTAL SETUP AND APPARATUS

#### 3.1 Water Tunnel

The water tunnel of the Aerospace and Ocean Engineering Department at Virginia Polytechnic Institute and State University is a horizontal closed-loop type with test section size of  $0.61m \times 0.61m \times 2.44m$ . The water tunnel is made up of circular cross sections of 0.46m O.D. PVC pipe except the rectangular honeycomb-screen section and test section. The flow is driven by an Ingersoll-Rand 0.46m I.D. axial pump (Model No. B0104DLF2UD) connected through a timing belt to a 3 phase, 10 hp induction motor, which is controlled by a Toshiba TOSVERT-130 H/H1 low acoustic-noise transistorized inverter.

Three honeycomb and eight screen sections are located upstream of the test section to isolate the test section from the pump and improve the uniformity of the flow (see Hsu (1989) for detailed description). The test section is made of 1.27cm thick glass to provide a visual access to the working area. Figure 2 shows the general layout of the water tunnel.

The flow in the test section was surveyed for two speed cases using hot film measurements at three stations with the wing-body junction model installed. The flow velocities surveyed were 21cm/sec and 49cm/sec, respectively. The turbulence level of the low speed case at the entrance of the test section ranged from 0.4% to 1.6% in the plane of symmetry. For the high speed case, the turbulence level of 0.8% - 1.3% was obtained at the same location. It was observed that as the

wing is approached the turbulence level becomes higher in the lower center which is closest to the wall among the measuring stations. The explanation of the increasing turbulence level as the flow approached the wing may be made as due to several possible reasons, which may be the effect of the axial pump not reduced even through the honeycomb section or impurities in the screens. However, it is believed that this does not influence the experimental results and conclusions obtained in this study. The measuring locations and the turbulence level at each location are as shown in Figure 3.

### 3.2 Model

The wing-body junction model consists of a wing, a false floor, and two side walls, all made of plexiglas for the purpose of flow visualization. The assembled wing-body junction model mounted in the test section is as in Figure 4.

#### 3.2.1 Wing

The wing has a 61cm chord, a 58.4cm height, and a 14.35cm thickness. The cross section of the wing is composed of a 3 : 2 elliptical nose and an NACA 0020 airfoil section, which are connected at the maximum thickness location. Plexiglas was used to build the wing model to provide a view looking upstream at the flow in the nose region of wing-body junction. The view was accessed from the bottom through the wing, where a 45° inclined plane mirror was installed to face upstream. The wing was reinforced using five inner aluminum ribs coated with marine epoxy.

A thermal forming technique was employed to obtain the leading edge shape of the plexiglas wing. A plywood form was so built that the thickness of the plexiglas

(3.175mm) was taken into account for the outermost contour to have the desired shape. The form and a square of 3.175mm thick plexiglas placed over it were heated to 310°F in an oven until the softened plexiglas reached the proper shape. After the plexiglas obtained approximately correct contour, minor manual adjustment was required to trim the desired shape. Natural cooling in the oven was necessary until a room temperature was reached. When cooled, the plexiglas was deformed along the outer edge. Therefore, the pieces were made oversized so that they could be trimmed after cooling.

### *3.2.2 False Floor*

A false floor consisted of a horizontal flat plate designed to mount the wing and join two side walls. It was constructed to maintain visual access from the bottom of the test section. This floor started after the contraction section. The total length of the false floor from the entrance to the leading edge of the wing was approximately 1.19m.

### *3.2.3 Side Walls*

To compensate for the blockage effect due to the large size of the wing model, two flexible side walls were mounted vertically on the false floor. The outer contour of the side walls was shaped to match the streamlines calculated by an inviscid source panel method with a boundary layer displacement thickness correction. To determine the final contour of the side walls, the displacement thickness was calculated using a turbulent flat plate boundary layer originated from the end of the contraction section. This values of displacement thickness were added to the Y locations of streamline obtained by the potential flow calculation. The location of the side walls with and without a displacement correction is compared in Figure 5.



#### ***3.2.4 Contraction section***

A 1.6:1 contraction section was built to prevent the flow separation which otherwise would occur at the leading edge of the test section floor and two side walls. The section was located immediately downstream of the last screen and connected at the leading edge of the false floor.

## 4. EXPERIMENTAL TECHNIQUES

### 4.1 Hydrogen Bubble Technique

#### 4.1.1 General Description

A 0.025mm tungsten wire was employed as the cathode immersed in the test section of the water tunnel. The anode was a piece of aluminum foil and floated aft of the wing model to avoid disturbance of the flow. We used a low speed ( $U = 9.07\text{cm/s}$  producing  $Re_\theta = 330$ ) to prevent cavitation-induced air bubbles which interfere with the small hydrogen bubbles. Hydrogen bubbles produced at the wire were swept off by the flow and followed downstream. The predominant force on the hydrogen bubbles was the drag due to the local water motion. Generally, the buoyancy force on the bubbles is greatly reduced by decreasing the wire diameter, and was almost negligible at the wire diameter of 0.025mm (Schraub *et al.* 1965). In this situation, the hydrogen bubbles can be considered to follow the local flow motion. It is noted that the velocity defect due to the wire should be taken into account before the bubbles reach the local flow speed. According to Schraub *et al.* (1965), The bubble velocity reaches the free-stream velocity in less than 70 wire diameter, which corresponds to 1.75mm in this study. A small amount of additive (0.15 gr of  $\text{Na}_2\text{SO}_4$  per a liter of water as suggested by Schraub *et al.* (1965)) was used to enhance the contrast with the increased production of hydrogen bubbles.

In this study, we developed three techniques as we applied the hydrogen bubble flow visualization. First of all, a time-line technique was used to visualize the flow

structure near the nose region of the wing model. The time-line patterns were obtained by producing the potential difference between the wire and the anode in square-wave pulses. The frequency of the time-lines was adjustable through the function generator connected to the hydrogen bubble generator circuit. The hydrogen bubble probe for the time-line patterns had a vertical wire of 7.62cm height and a support to hold the wire in a vertical position in the symmetry plane. The details of the probe are described in the next section.

A continuous sheet technique is analogous to the smoke-wire technique used in the wind tunnel flow visualization. The continuous sheet of hydrogen bubbles is generated by supplying the circuit with a constant voltage difference. The time-line and a continuous sheet technique can be combined to generate inverted time-lines using series of inverted pulses. This technique had an advantage that the individual time-lines could be seen while the flow field was still observable with hydrogen bubbles just like the smoke-wire technique.

A combined time-streak marker technique was developed to get quantitative data from flow visualization by picture processing. Here, the bubble generating wire was insulated with fine enamel at regular intervals so that approximately square areas of bubbles were produced when pulsed by the generator circuit as used in the time-line technique. A brush with a very fine tip and a pattern template were used to mask the wire.

A multiple wire hydrogen bubble technique was developed to visualize the three-dimensional flow structure by generating bubble patterns by the sequenced pulsing to the wires. Since the probe was located near the wing and flow speed at each wire was different, the sequence of pulsing to each wire was chosen to avoid

bubbles overlapping in the image plane. This may take place though the bubbles are independent in three-dimensional space. The details of the probe and circuit design are described in the next section. The sequenced multiple wire hydrogen bubble technique used the combined time-streak marker method. Figure 6 shows an example of the sequence of hydrogen bubble generation in the upstream view with the corresponding side view. Examples of each application are presented in Figure 7.

#### *4.1.2 Probe and Circuit Design*

We used a D-shaped probe with width of  $22.86\text{cm}$  and height of  $17.78\text{cm}$ . The probe was reinforced with cross bars and it was connected to the hydrogen bubble generator circuit outside the test section. The probe designs for each application are illustrated in Figure 8.

Each cross-section of the probe had a streamlined shape to minimize flow interference when placed in the flow. A Kevlar holder was built to form a tight rectangular loop along the edges of the D-shaped probe. Four glass posts of length of  $2.54\text{cm}$  and diameter of  $3.18\text{mm}$  were installed at two lower ends and  $8.89\text{cm}$  above the probe leg. These were used to make a stiff electrically isolated holder.

Two probes were designed for each application. A single  $0.025\text{mm}$  tungsten wire was mounted vertically in the center of the probe as shown in Figure 8(b). Time-line patterns, continuous sheet and inverted time-lines of hydrogen bubbles used the single wire probe.

Five  $0.025\text{mm}$  tungsten wires were mounted on a Kevlar holder with a  $1.27\text{cm}$  spacing and connected to the top of the probe. All but  $8.89\text{cm}$  of wires from the

bottom were masked with enamel in order not to generate the hydrogen bubbles outside the region of interest. This probe is as shown in Figure 8(c) and was used for the sequenced multiple wire technique.

A bubble generator circuit was designed and built to generate the pulses at an adjustable time constant interval. These were then distributed to each wire in sequence. The interval between pulses and the order of bubble generating wires were adjustable. Mercury relays were used to reduce the bouncing effect of the switch. A schematic diagram of the generator circuit is as shown in Figure 9.

#### *4.1.3 Lighting*

Lighting is crucial in the hydrogen bubble technique. The lighting setup is described in Figure 10.

For still photography, we used two flash lights located at opposite side of the test section to the camera to produce forward-scattered light from the hydrogen bubbles. Two synchronized flashes were used to eliminate the shade created by the probe. The location of the flashes was restricted by the external configuration of the test section, such as the threaded rods located vertically at every foot outside the test section. We used ASA 400 film at a setting of 1/125sec and an f number of 16 for still pictures.

We needed more light for the high speed video camera than for still photography. For a side view, a 600W quartz halogen lamp was located outside the test section at an angle inclined to the test section and configured to yield forward scatter on the hydrogen bubbles. A second lamp was needed to eliminate shading by the probe. For a bottom view, three thousand-watt focusable halogen lamps were

used for the illumination of the hydrogen bubbles from the top of the test section (see Figure 10). Yet, this was not enough to get high quality images since water absorbed most of the light energy on the way to the bubble region.

Approximately  $60^\circ$  inclined to the line normal to the test section wall produced an effective scattering on hydrogen bubbles.

## **4.2 Laser Doppler Velocimetry**

A dual beam, forward-scattered, frequency-shifted LDV (see Figure 11) was used to measure the axial component velocities and the turbulent quantities in the plane of symmetry upstream of the nose of the wing-body junction.

### **4.2.1 General Description of LDV**

Frequency shifted laser velocimetry was first introduced by Yeh and Cummins (1964). They added an artificial frequency difference between the two incident laser beams to generate a set of moving fringe at the intersection of the beams. Since the fringes are moving in one direction, even a stationary particle will produce a Doppler frequency at the shifted frequency. Consequently, a negative velocity of maximum value corresponding to less than the shift frequency can be measured.

When a particle passes through the intersection volume of two beams, a pedestal is generated along with the Doppler frequency. A pedestal is related to the amount of time taken for a particle to pass through the probe volume and is removed using a high-pass filter. The Doppler frequency produced by the interference pattern has a direct linear relationship with the particle velocity as follows,

$$U = \frac{f_D \lambda}{2 \sin \kappa} \quad (4.1)$$

$$= f_D d_f.$$

where  $U$  = flow velocity,

$f_D$  = Doppler frequency,

$\lambda$  = wave length of laser beam,

$\kappa$  = half angle between two incident beams,

and  $d_f$  = fringe spacing.

With a frequency shift, Equation (4.1) is modified as follows,

$$U + U_{f_s} = \frac{(f_D + f_s) \lambda}{2 \sin \kappa} \quad (4.2)$$

$$= (f_D + f_s) d_f$$

where  $f_s$  is the shifted frequency.

Using Equation (4.2), the flow velocity can be calculated with the known fringe spacing and shifted frequency.

#### 4.2.2 LDV Setup

The LDV consisted of an INNOVA 70 argon-ion laser operated at  $514.5 \mu m$ . As shown in Figure 11, the beam from this laser was reflected using several mirrors to be directed to the test section. A beam splitter was used to form two incident beams. After passing through two Bragg cells, two approximately 40 Mhz shifted first order beams were generated. One of the beams was shifted about 100 Khz from the other in order to measure the velocity in the separated flow region. The amount of frequency shift was decided to cover the negative velocity range for all

the test conditions. A lens of focal length of 38.1cm was mounted on the optical bench to obtain an intersection volume in the test section of the water tunnel. The intensity of the fringe pattern produced by the interference of the incident beams was checked at the wall furthest from the test section using a microscope objective located at the intersection volume.

Fringe spacing  $d_f$  can be calculated with the known wavelength ( $\lambda$ ) of the laser beam and the half angle ( $\kappa$ ) between two beams. However, a direct measurement was made using a rotating disk with constant angular velocity with its edge at the probe volume as shown in Figure 12 (for detailed descriptions see Furey and Walker, 1990). With the known disk diameter ( $D_r$ ) and angular velocity ( $\omega_r$ ), the velocity at the edge of the disk was calculated. A 0.025mm wire attached vertically at the edge of the disk disturbed the fringe pattern in the probe volume for every revolution to yield the Doppler frequency. With the known edge velocity and Doppler frequency, the fringe spacing,  $d_f$ , was calculated as follows,

$$\begin{aligned} U_w &= \frac{D_r}{2} \times \omega_r, \\ d_f &= \frac{U_w}{f_D} \\ &= \frac{D_r \omega_r}{2f_D}. \end{aligned} \tag{4.3}$$

where  $U_w$  = velocity at the edge of the rotating disk

and  $\omega_r$  = angular velocity of the disk

The fringe spacing was measured across and outside the probe volume to check a fringe divergence, the effect of which was not significant inside the probe volume as shown in Figure 13. In this figure, fringe spacing measurements outside the probe



volume were included and marked by a dotted line. Fringe spacing measured inside the probe volume was approximately  $5.38 \mu\text{m}$  with uncertainty of less than 0.8 %. The uncertainty of each measurement of the fringe spacing was accurate up to 0.1 % according to the uncertainty analysis method described in Appendix A. The size of the effective probe volume was calculated to be  $200\mu\text{m} \times 4350\mu\text{m}$  using the method proposed in Durst, Melling, and Whitelaw (1981). Approximately 37 fringes were estimated to exist inside the probe volume.

Seeding particles were not necessary because of many particles present in a water flow.

The receiving optics of the same focal length as the incident lens was so arranged that the scattered beam was directed to the photodetector. The focused beam was detected by a UDT PIN3D photodiode in a hybrid cascode circuit (Walker, 1984) through a  $300 \mu\text{m}$  pinhole.

Details of the current LDV setup are described in Hsu (1989).

#### *4.2.3 LDV Data Acquisition*

The signals detected by the photo-detector were processed by TSI counter-type processor (Model 1990C) with input conditioner, timer, and analog output module. Amplitude limit control was used to detect particles producing big pedestals and reject the measurement made on these particles. The low limit filter was used to remove the low frequency component of the LDV signal caused by the Gaussian envelope of the LDV burst signal (the pedestal part of the LDV signal). The high limit filter was used to eliminate high frequency noise from the signal to aid in processing. A timer was used to measure the width of the gate signal (the period

corresponding to a fixed number of cycles in a burst) by counting the number of cycles of a 4-phase, 250 Mhz clock and obtain  $\pm 1ns$  accuracy through phase information. Analog frequency output was generated by the D/A conversion in the counter processor and sent to the IBM PC/AT compatible through an RTI-850 16 bit A/D board. By the above procedure time-averaged signals were obtained at each measuring location.

## 5. IMAGE DATA PROCESSING

### 5.1 Image Capturing System

#### 5.1.1 High Speed Video System

Since the physical phenomenon visualized by the sequenced multiple-wire hydrogen bubble wire technique was a complex three-dimensional turbulent flow, a high speed video system was required to freeze the instantaneous motion of the hydrogen bubbles in a sequence of instantaneous images. A Kodak Ektapro 1000 Motion Analyzer was used to record the images on digital cassettes. The system consisted of a main video processor, two high intensity cameras, various lenses and accessories. It had a full screen framing rate of up to 1000 fps (frame per second). The frame rate used in this research to capture both of the views was 250 fps. The resolution of image in a full screen format was  $240 \times 192$  (pixels)

#### 5.1.2 Cameras and Setup

Three orthogonal views were captured by two cameras located at the side and the bottom of the test section. The side view consists of the image containing the probe, hydrogen bubbles and the wing with the flow direction from left to right. The bottom and upstream views appear on the same image using mirror arrangements. The bottom view is produced by looking at the flow field from the bottom, and shows up in the left side of the image with flow direction from right to left. The upstream view is generated by the camera located at the bottom of the test section

looking at the flow field upstream of the wing through the mirror installed inside the wing.

### Side View

Figure 10(a) shows two flood lights located at the opposite side of the test section to the camera. Masking with flat black plastic electric tape was made on the wall of the test section to allow the light to be directed toward the flow region of interest. On the camera side of the wall of the test section, masking other than the rectangular region of  $8.9\text{cm} \times 10.16\text{cm}$  was used to prevent the scattered or reflected light from various sources from entering the camera viewing angle.

The side view camera was focused on the plane of symmetry and located far apart from the test section to avoid the effect of image distortion. The field of view was of the size of  $7.1\text{cm} \times 8.13\text{cm}$ .

### Upstream and Bottom View

In order to obtain three orthogonal views with two cameras, the upstream and bottom views were arranged to appear on the same image plane while one camera captured the side view in one image plane. Figure 15 shows the mirror arrangement producing double images. Three plane mirrors were installed inside the mirror box to capture the image from the flow field. The approximate size of  $7.62\text{cm} \times 12.7\text{cm}$  was used for mirror 1 and 2. These were inclined at  $45^\circ$  to reflect the bottom view image to the mirror 3 of the size of  $7.62\text{cm} \times 25.4\text{cm}$ . The upstream view was received by the same camera through two consecutive reflections made by the  $45^\circ$  slanted mirror inside the wing and the mirror 3 in the mirror box. The mirror box was located just below the test section to capture two images simultaneously. The

average optical distances for both of the views were designed to be approximately equal. The field of view of the upstream view was approximately  $7.62\text{cm} \times 7.62$ , and that of the bottom view was  $7.62\text{cm} \times 8.9\text{cm}$ .

### Camera Setup

Two cameras were employed for a stereo vision analysis. Ektapro 1000 system was operated in a full screen format where a full screen was devoted to the digital image from each imager. The camera for the bottom view was set to the high intensity mode, in which the sensitivity of the camera was increased though the resolution of the image was reduced. Each view was recorded on cassettes in an alternate manner.

After recording the flow visualization events on cassettes, the digitized images for each view were transferred to IBM PC/AT through an IEEE-488 interface and, finally, stored on optical disks. A GPIB-AT IEEE-488 interface made by the National Instruments was employed. The data transfer program was developed using the C language for fast transfer. Figure 16 shows the image capturing system.

#### *5.1.3 Image Data Formats*

The captured images were recorded on the video cassettes in a digital format. Each pixel in an image has 8 bits corresponding to 256 gray levels.

Two formats were used for the data transfer. The compressed data format is the one where one bit expresses one pixel of information (2 gray levels). The file size for an image was 5,736 bytes. The other one is using one byte per pixel (full gray scale image:  $2^8$  gray levels) and the file size was 45,888 bytes per an image. The compressed format saved storage without losing much image information by

thresholding after preprocessing the original image. This will be discussed in later part of this chapter. But the data transfer time for a compressed format image took longer than that for full gray scale image since the preprocessing was performed on the digital image during the data transfer.

## 5.2 Mathematical Background

### 5.2.1 Coordinate System

As shown in Figure 14, the right-handed coordinate system  $(X, Y, Z)$  and  $(U, V, W)$  with the origin at the leading edge of the wing was used as a global coordinate system. When processing the hydrogen bubble images, the image plane coordinate system  $(y_i, z_i)_k$  was adopted to describe the individual pixels in the  $k$ -th image plane. The origin of the image plane coordinate was the lower left corner for each image plane.

Another coordinate system employed in processing the images was a homogeneous coordinate system. The idea of homogeneous coordinates is a technique commonly used in the development of computer graphics (Riesenfeld, 1981). The homogeneous coordinates for the object points  $(x_o, y_o, z_o)^T$  in a global coordinate system are represented by a  $4 \times 1$  vector  $(kx_o, ky_o, kz_o, k)$ , where  $k$  is a nonzero and arbitrary constant. Therefore, there is no unique representation of a physical point in this coordinate system. An image point is represented in homogeneous coordinates by augmenting the  $2 \times 1$  physical vector dimension by one (scale factor) and multiplying the physical image point coordinates by this nonzero factor.

### 5.2.2 Mathematical Model

The object of this section is to develop a mathematical model that relates the 3-D object point locations measured with respect to a global coordinate system to the image point locations measured with respect to the image plane coordinate system. This is described briefly in Figure 17(a).

#### p-p (perspective-projective) transform

Consider the pinhole camera model (see Figure 17(b)). The relation between object points and image points can be derived using the constraint that the image point, the center of projection and the object point should lie on the same 3-D line segment.

$$k(x_i - x_c) = (x_c - x_o) \quad (5.1)$$

Expanding the above,

$$k \left\{ \begin{pmatrix} 0 \\ y_i \\ z_i \end{pmatrix} - \begin{pmatrix} f \\ 0 \\ 0 \end{pmatrix} \right\} = \begin{pmatrix} f \\ 0 \\ 0 \end{pmatrix} - \begin{pmatrix} x_o \\ y_o \\ z_o \end{pmatrix} \quad (5.2)$$

which yields,

$$\begin{aligned} y_i &= -\frac{y_o}{k} = \frac{fy_o}{(f - x_o)} \\ z_i &= -\frac{z_o}{k} = \frac{fz_o}{(f - x_o)} \end{aligned} \quad (5.3)$$

The above relations are nonlinear in both of the object points and camera parameter ( $f$  : focal length).

Using homogeneous coordinate system, the nonlinear relation can be written as

$$\hat{\underline{x}}_i = P \hat{\underline{x}}_o \quad (5.4)$$

$$\text{where } \hat{\underline{x}}_i = \begin{pmatrix} wy_i \\ wz_i \\ w \end{pmatrix}, \hat{\underline{x}}_o = \begin{pmatrix} x_o \\ y_o \\ z_o \\ 1 \end{pmatrix} \text{ and } P = \begin{pmatrix} 0 & f & 0 & 0 \\ 0 & 0 & f & 0 \\ -1 & 0 & 0 & f \end{pmatrix}$$

Note that the representation of  $P$  is not unique.

If the global coordinate system is offset and rotated from the image plane coordinate, the relation becomes

$$\hat{\underline{x}}_{ik} = P R^{i-g} \hat{\underline{x}}_o = T_k \hat{\underline{x}}_o \quad (5.5)$$

where  $R^{i-g}$  is the transformation matrix which is related with rotations and translations, and the index  $k$  represents the expression in the  $k$ -th image plane. Here, the final form of the transformation matrix  $T_k$  can be expressed as follows,

$$T_k = \begin{pmatrix} a_{11} & a_{12} & a_{13} & a_{14} \\ a_{21} & a_{22} & a_{23} & a_{24} \\ a_{31} & a_{32} & a_{33} & a_{34} \end{pmatrix}_k \quad (5.6)$$

### 5.2.3 Camera Calibration

The transformation matrix  $T_k$  in Equation (5.5) is not unique and consists of 12 entities. Each entity is a function of 7 parameters (3 rotational angles, 3 translations, and  $f$ ) that determine the sensor system geometry. With careful measurements of the sensor system geometry, each entity of the matrix  $T_k$  can be determined using



the expressions derived in Hall (1972). More practically, this transformation matrix can be obtained using the camera calibration procedure.

A rectangular grid box with grid points known in the physical coordinate system was located in the flow region of interest and used to calibrate the two cameras. To find all of the eleven parameters ( with setting  $a_{14} = 1.0$  for uniqueness), at least six points, which were non-coplanar, were needed to close the equations.

Least squares estimation (Q-R Algorithm) was adopted to calculate matrix elements out of more than twelve equations for each view. Q-R algorithm is described in Appendix B.

Imager calibration coefficients thus obtained are provided in Table 2 for each imager. Each cell of the table represents  $a_{ij}$  in Equation (5.6).

#### *5.2.4 Stereo Vision*

With the mathematical model described herein, the transformation from a global location to image point locations is always possible if the transformation matrix  $T_k$  is known. However, the inverse transformation is not unique and only tells a line along which the object points corresponding to the image point should lie. This implies that more than one calibrated camera are needed to determine the object point location in 3-D space. Using two cameras, the intersection of two lines resulting from each inverse transformation tells the global coordinate of the object point. Here, the correspondence between image points in each image plane is assumed. The correspondence problem is usually the most difficult task in handling with a stereo vision application and will be discussed separately in the later section. Figure 18 shows an example of a stereo vision application and the constraint between image points.

Since Equation (5.5) represents two equations in a physical coordinate for each imager, there are four equations and 3 unknowns ( $x_o, y_o, z_o$ ) using a stereo vision. Regrouping Equation (5.5) gives the following form.

$$A\hat{X}_o = \hat{F} \quad (5.7)$$

$$\text{where } A = \begin{pmatrix} a_{111} - a_{131}x_{i1} & a_{112} - a_{132}x_{i1} & a_{113} - a_{133}x_{i1} \\ a_{121} - a_{131}y_{i1} & a_{122} - a_{132}y_{i1} & a_{123} - a_{133}y_{i1} \\ a_{211} - a_{231}x_{i2} & a_{212} - a_{232}x_{i2} & a_{213} - a_{233}x_{i2} \\ a_{221} - a_{231}y_{i2} & a_{222} - a_{232}y_{i2} & a_{223} - a_{233}y_{i2} \end{pmatrix},$$

$$\hat{X}_o = \begin{pmatrix} x_o \\ y_o \\ z_o \end{pmatrix}, \quad \text{and} \quad \hat{F} = \begin{pmatrix} a_{134}x_{i1} - a_{114} \\ a_{134}y_{i1} - a_{124} \\ a_{234}x_{i2} - a_{214} \\ a_{234}y_{i2} - a_{224} \end{pmatrix}$$

Least squares estimation needed to be employed to obtain the object point location ( $x_o, y_o, z_o$ ) in Equation (5.7).

### 5.3 Preprocessing

In order to solve for Equation (5.7), the image point locations,  $(x_i, y_i)_k$ , which correspond to the object points in the global coordinate, should be determined first in each image plane. In the present study, the image points to be traced were the centroid locations of the square shaped area consisting of small bubbles generated from the hydrogen bubble wires. These centroid locations cannot be obtained directly from the image data recorded in the cassettes since the image data consist of just intensity levels (values of gray scale),  $f(x_i, y_i)$ , at every pixel in the image plane. Here,  $f(x_i, y_i)$  is the image function which represents a specific image. Thus, what should be done next is to transform the intensity level information into the specific locations in the image plane. This can be achieved by first changing 256 gray levels into bilevel image which is black and white.

In the present study, the preprocessing consists of three parts: i) the background subtraction, ii) the local averaging technique, iii) the histogram equalization technique, and iv) the thresholding technique

### 5.3.1 Background Subtraction

The typical image function,  $f_o(x_i, y_i)$ , can be seen in Figure 19(a). It shows the intensity distribution of the scene with a wing, a false wall, hydrogen bubbles, and light reflection from various sources, etc. This figure illustrates that it is difficult to find the reasonable threshold value that enables the original image to be transformed into the bilevel image. A dynamic thresholding technique may be applied here to determine the locally varying threshold values according to the local intensity values. However, since the distribution of the hydrogen bubbles is not uniform for the successive images the dynamic thresholding needs to be applied to every frame. In practice, it takes extra amount of time in processing the image with a dynamic thresholding technique.

Instead, the subtraction of the nonuniform background from the original image leaves only the hydrogen bubbles in the field of view. Ideally, the intensity levels in the image will vary only due to the presence of the hydrogen bubbles. In practice, the intensity levels also included other noise and the increased intensity at the wire due to the generation of the hydrogen bubbles.

The background subtraction can be written as follows:

$$f_h(x_i, y_i) = f_o(x_i, y_i) - f_b(x_i, y_i) \quad (5.8)$$

where  $f_h(x_i, y_i)$  is the image function consisting of the hydrogen bubbles only,  $f_o(x_i, y_i)$  is the original image function taken from the video system, and  $f_b(x_i, y_i)$  is the image function for the background scene.

In this study, background images were captured before and after the run for every test with water flow, and used to help process the data. Figure 19 shows the effect of the background subtraction. In the original image as shown in Figure 19(a), the intensity representing the hydrogen bubbles seemed buried in other higher level of intensity mainly due to the background. However, the local peaks of intensity showing the existence of the hydrogen bubbles appear after background subtraction as shown in Figure 19(c).

### 5.3.2 Local Averaging Technique

The image function,  $f_h(x_i, y_i)$ , obtained after subtracting the background subtraction, still contained noise imposed on the intensity levels, which needed to be eliminated. One source that arises from an electronic sensor appears as "snow", which is random and uncorrelated. Since this type of noise shows extreme change in intensity between the adjacent pixels, a local averaging technique was used to remove it.

In this technique, the intensity value that shows the extreme difference is replaced by a local average calculated using neighboring pixels. This nonlinear operation can be described by

$$g(x_i, y_i) = \begin{cases} \bar{f}_h(x_i, y_i) & \text{if } |f_h(x_i, y_i) - \bar{f}_h(x_i, y_i)| > T \\ f_h(x_i, y_i) & \text{otherwise,} \end{cases} \quad (5.9)$$

where  $T$  is a threshold value dependent on the noise variance.

The present study used 8 neighboring pixels for the local averaging. Figure 20 describes the windows used for calculating the local average in the vicinity of a pixel. The center point in the  $3 \times 3$  window was excluded to eliminate extreme values in the averaging. If too many pixels are subject to local averaging, the image is further smoothed out with the adverse effect of smearing the image.

### *5.3.3 Histogram Equalization Technique*

For the image function,  $g(x_i, y_i)$ , the intensity levels of the image very near the leading edge of the wing are low when compared to those at other pixel locations. The intensity of the reflected light from the wing has almost the same level as those of the hydrogen bubbles. We lose contrast in this region, and therefore, need enhance the image by further processing.

As an contrast enhancing technique, a histogram equalization technique was adopted since a uniform distribution of gray levels makes equal use of all the quantization levels and enhances low-contrast information. The algorithm for this technique is presented in Figure 21, and will be described as follows.

If  $P$  is the total number of pixels in an image, and  $N$  is the number of available gray levels, one must have  $P/N$  pixels at each gray level for a perfectly flat histogram. Therefore, for the intensity level ( $G$ ) with the number of occurrences  $k$  times greater than the average level, that particular level should be redistributed to  $k$  different levels, i.e.  $(G_1, G_k)$ .

There are several possible ways to redistribute the pixel intensity (Pavlidis, 1982). But, in the present study, an empirical distribution function was computed by adding the relative frequency values and used for reassigning a new intensity

level at low contrast region. The distribution curve illustrates that the low contrast region may be enhanced by stretching the low intensity range so that these values can be reassigned to higher levels of intensity according to the distribution curve.

The steps presented below are the procedure used for the histogram equalization:

- (a) Compute the histogram ( $H(G)$ ) of the image gray level values,
- (b) Obtain a distribution curve by accumulating the histogram values,
- (c) Use this distribution curve for the gray level transformation

$$h(x_i, y_i) = D(f_h(x_i, y_i)) \quad (5.10)$$

where  $D$  is the operator performing the redistribution of the intensity level.

#### 5.3.4 Thresholding Technique

The final step to obtain a bilevel image employs a thresholding technique. In this technique, the intensity value at each pixel is compared to a given threshold value, and the pixel is assigned to one of two categories depending on whether the threshold value is exceeded or not.

The threshold value, in general, is selected from the intensity histogram. For example, if the histogram has two peaks, each representing the bright area and the dark area in the image, a reasonable choice will be a point between the two peaks. However, the histogram of the intensity does not always show two peaks, and the intensity level for each image can vary due to the limitations of the Ektapro 1000 System. Therefore, we could not obtain a uniform value for the threshold for the image used in data reduction.

Instead, the threshold level was established automatically in the data reduction program for the image, based on a table for the percentage of "ON" pixels for a specific scene. In order to do this, the image sequences were recognized using the location of the hydrogen bubbles in the flow field. This was possible because the five wires generate hydrogen bubbles at different times and locations.

This technique can be briefly described by

$$h_b(x_i, y_i) = \begin{cases} 1 & \text{if } h(x_i, y_i) > T_h \\ 0 & \text{otherwise,} \end{cases} \quad (5.11)$$

where  $h_b(x_i, y_i)$  is the image function of bilevel intensity, and  $T_h$  is a selected threshold value. Figure 22 shows examples of bilevel images after thresholding analysis.

## 5.4 Motion Analysis

### 5.4.1 Introduction

The bilevel images constructed after preprocessing are made up of the pixels with two gray levels ("ON" and "OFF" pixels). Hydrogen bubbles are represented by the "ON" pixels. Figure 22 illustrates the bilevel image.

The three-dimensional analysis of the motion of the flow used in this study determines the three-dimensional instantaneous velocity field. To do this, the gray level information in the images should be transformed into the information of bubble location. The displacement of a particular bubble region for successive frames is used to calculate the corresponding instantaneous velocity.

This can be obtained by applying the following algorithms successively.

#### 1) Centroid search routine

In this routine, a bubble element numbering is done by tracing "ON" pixels in the  $j$ -th frame. For the  $i$ -th bubble element, the location of the centroid is determined.

#### 2) Correspondence Algorithm

This algorithm determines the correspondence of the image points between the image planes. The same bubble element number is assigned to the corresponding bubble elements.

#### 3) Matching algorithm

In this routine, matched pairs of the same bubble elements between two successive frames (the  $j$ -th and  $(j+1)$ -th frames) are determined. Two criteria are applied to determine the matched pairs.



#### 4) Split-merging algorithm

In this algorithm, an attempt is made to retrieve the bubble elements lost due to the merging of them in the image plane.

Using the above algorithms, the corresponding  $i$ -th element in both image planes is found and the element in the  $j$ -th frame which is matched to the  $i$ -th bubble element in the  $(j+1)$ -th frame is determined. Thus, the physical location of the  $i$ -th bubble element can be calculated using Equation (5.7) with the constraints on the correspondence between the bubbles. The difference in the centroid locations of the  $i$ -th element between the  $j$ -th and  $(j+1)$ -th frames can be used to calculate the displacement vectors of the individual bubble elements between frames.

##### 5.4.2 Centroid Search Routine

As shown in Figure 22, we needed some criteria to determine the bubble elements and numbering. The procedure to search the centroid location of all the bubble elements is as follows.

The groups of the "ON" pixels were searched, row by row, starting from the origin in the image plane to the last pixel. Once the first "ON" pixel was found, the neighboring pixels were checked if there were other "ON" pixels, and this was applied to all the neighboring pixels until there were no more "ON" pixels. The noise was still imposed on the bilevel image with all the preprocessing techniques described in the previous section and the bubble elements with smaller numbers of pixels appeared irregularly from frame to frame. Therefore, the groups with very small numbers of the "ON" pixels were not considered to be bubble elements. This caused some bubble elements to be lost during the centroid search, but resulted

in less error in the computer processing than the inconsistent appearance of some images from frame to frame. After the first bubble element was found, the routine went to the previous row where the first "ON" pixel was found, and restarted to search the next "ON" pixel in the same row. This routine was applied to the end of the row to search all the bubble elements that had a pixel or pixels belonging to the same row. The bubble elements found in sequence were assigned unique numbers in an increasing order.

In searching the bubble elements, the "ON" pixels belonging to a bubble element may be well closed and do not show any confusion with any other bubble elements. However, this did not happen always. Sometimes, two bubble elements merged to one, while one element split into two or more bubble elements due to strong vortex motion or the diffusion of the hydrogen bubbles. In addition, the bubble elements at different locations in the physical coordinate could appear in the same location in the image plane. Therefore, the criteria on the connectivity of the pixels to form a bubble element should not be rigid to take the above cases into account. Figure 23 shows the example of the bubble element identification. Here, the pixels connected diagonally to another group of pixels were treated as separate bubble elements as shown in Figure 23(b). In this figure, it is illustrated that some isolated "ON" pixels connected diagonally to a group of "ON" pixels are treated as not belonging to that group.

From the next row to the last, the algorithm checked if the "ON" pixels belonged to the previous bubble elements and, if so, were excluded. The same routine was applied to all the rows in each image plane until all the bubble elements could be identified.

For each bubble element found in this routine, the centroid location could be calculated using the pixel locations in the image plane as follows,

$$\begin{aligned}\bar{x}_{ci} &= \frac{\sum_{k=0}^{N_i} x_k}{N_i} \\ \bar{y}_{ci} &= \frac{\sum_{k=0}^{N_i} y_k}{N_i}\end{aligned}\tag{5.12}$$

where  $N_i$  is the number of pixels of the  $i$ -th bubble element

#### 5.4.2 Correspondence Algorithm

After the centroid locations of the bubble elements existing in the image plane were found, it remained to determine the coordinates of the centroid locations. To obtain the locations of the bubble elements in the three-dimensional space, the correspondence of the bubble elements between the image planes should be recognized. This is the most difficult problem in processing the stereo vision images.

As expressed in Equation (5.7), knowing the corresponding points in each image plane, the object point in the global coordinate system could be determined by applying least squares analysis to these equations. However, not all the locations are required to estimate  $\hat{X}_o$ . The object point  $\hat{X}_o$  is determined using three out of four equations, assuming that the three equations were linearly independent.

In a homogeneous coordinate system, Equation (5.7) becomes

$$C\hat{X}_o = 0\tag{5.13}$$

$$\text{where } C = \begin{pmatrix} a_{131}x_{i1} - a_{111} & a_{132}x_{i1} - a_{112} & a_{133}x_{i1} - a_{113} & a_{134}x_{i1} - a_{114} \\ a_{131}y_{i1} - a_{121} & a_{132}y_{i1} - a_{122} & a_{133}y_{i1} - a_{123} & a_{134}y_{i1} - a_{124} \\ a_{231}x_{i2} - a_{211} & a_{232}x_{i2} - a_{212} & a_{233}x_{i2} - a_{213} & a_{234}x_{i2} - a_{214} \\ a_{231}y_{i2} - a_{221} & a_{232}y_{i2} - a_{222} & a_{233}y_{i2} - a_{223} & a_{234}y_{i2} - a_{224} \end{pmatrix}$$

Equation (5.13) requires that every row (or column) of  $C^T$  is orthogonal to  $\hat{X}_o$ . The algebraic significance of Equation (5.13) is that the column must not span  $R^4$ , which indicates that the determinant of matrix  $C$  should be zero. Therefore,

$$\det |C| = 0 \quad (5.14)$$

which yields the following equation.

$$\begin{aligned} m_1 x_{i1} x_{i2} + m_2 y_{i1} y_{i2} + m_3 x_{i1} y_{i2} + m_4 x_{i2} y_{i1} \\ + m_5 x_{i1} + m_6 x_{i2} + m_7 y_{i1} + m_8 y_{i2} + m_9 = 0. \end{aligned} \quad (5.15)$$

The coefficients  $m_i$ 's given in Equation (5.15) are functions of the  $a_{ij}$  sensor calibration parameters and derived in Appendix C. The geometric significance of Equation (5.15) is that, given a point in one image plane *e.g.*,  $(x_{i1}, y_{i1})$ , the set of corresponding image points,  $(x_{i2}, y_{i2})$ , in the second image plane is constrained to lie along a line formed by Equation (5.15). The constraint on the correspondence problem is illustrated in Figure 18 and Figure 24.

The constraints given in Equation (5.15) cannot solve the correspondence problem uniquely because any points near that line are the possible candidates for the corresponding point. In our study, the sequence of the generation of bubble from the wires was used for another constraint to determine the image point in one image plane corresponding to the point in other image plane.

At the instant of pulsing to the wire, the bubble elements were generated simultaneously at some band of Z coordinate in the image plane representing a

upstream view and there were five bands corresponding to each wire. The bubble elements found during the centroid search routine described in the previous section would be given their unique numbers from the bottom to the top in the side view image plane. The corresponding bubble elements were easily found in the upstream view image plane because the bubble elements should be located at the first  $Z$  band and the bubble elements which satisfied Equation (5.15) should lie near the line which is almost normal to that band of constant  $Z$  line. This means that the corresponding bubble elements should be located near the intersection of a corresponding line and a band of constant  $Z$ . After all the corresponding bubble elements were found in the  $j$ -th frame, the corresponding bubble elements were always given the same number. From  $(j+1)$ -th frame on, this bubble number was used to trace the corresponding bubble elements.

Since we know the sequence of bubble generation, the next expected  $Z$  band in the upstream view image plane can be searched for the correspondence at the bubble generation from the next wire, and the numbers that followed the previous numbering would be distributed to the newly found bubble elements until the whole cycle was completed.

#### *5.4.3 Matching Algorithm*

We applied the matching algorithm to the successive frames ( $j$ -th and  $(j+1)$ -th frames) for the same image plane to find the same bubble elements as time proceeded. The criteria on the matched bubble elements were using the area of the individual bubble elements in the  $(j+1)$ -th frame, which were expected to be at some pixel distance from the centroid location in the  $j$ -th frame.

The distance between the matched bubble elements in the  $j$ -th and  $(j+1)$ -th was restricted by the estimated maximum flow velocity. Thus, only the bubble elements, the centroid locations of which were within certain range of the distance from the previous centroid location, were investigated to search the matched bubble element.

The maximum expected pixel distance was approximately 3 pixels, which was obtained by considering the screen resolution, the field of view in the absolute scale, and the maximum expected flow speed. The calculation of the pixel distance is presented in Table 4.

#### *5.4.4. Split-Merging Detection Algorithm*

All the bubble elements, which at first were independent of each other, could merge together as the bubbles approached the wing. Especially, the bubble elements in the strong vortex region were easily stretched and mixed with the others, and, in the long run, became not discernible with the others. Once the bubble elements entered the strong vortex region, it was difficult to retrieve those bubble elements as separate ones. In addition, though the bubble elements were not actually merged, it could happen that several bubble elements in 3-D space appeared to be just one bubble element in 2-D image plane.

Therefore, efforts were made to extract more information in the region very near the wing by retrieving the bubbles lost due to merging and other reasons. In particular, as illustrated in Figure 24, for the bubble elements that took apart in one image plane, but appeared merged in other image plane, we could retrieve the lost information of the centroid though it was subject to have some uncertainties.

The algorithm for the detection of the split-merging of the bubble elements is provided as a flowchart in Figure 25.

#### 5.4.5 Instantaneous Velocity Field

After a cycle of the motion analysis algorithms described above is completed, a set of bubble element locations in the global coordinate is acquired. As the process goes on, the trajectories of each bubble element in the global coordinate are obtained as a solution set.

The velocity vector in the  $(j+1)$ -th frame,  $\hat{v}_{j+1}$ , can be written as follows,

$$\hat{v}_{j+1} = \frac{(\hat{x}_{oj+1} - \hat{x}_{oj})}{t_f} \quad (5.16)$$

where  $t_f$  is the sampling interval between  $j$ -th and  $(j+1)$ -th frames.

#### Uncertainty Consideration

As provided in Table 4, the maximum expected pixel distance in the axial direction for the given test condition was 3 pixels between successive frames. This indicates that the uncertainty in the axial velocity is at least 16.7% since the centroid locations of each bubble element are always subject to the error of half pixel distance.

One way to reduce such a large uncertainty in velocity calculation is to use several successive frames and compute the averaged velocity of certain bubble element in these frames, and then use this average value for the velocity in certain frame. Using five frames to obtain the averaged velocity, the uncertainty was reduced to 7.5%.

## 6. EXPERIMENTAL RESULTS

### 6.1 Introduction

This chapter presents the experimental results of the hydrogen bubble visualization, LDV measurements, and three-dimensional PIDV (Particle Image Displacement Velocimetry) using a high speed video system. Experimental results are provided using a right-handed coordinate system for physical plane data, and an image coordinate system for image plane data as described in Figure 14. The uncertainties of the experimental results were estimated by the method discussed in Appendix A, and are tabulated in Table 2.

The first part of this chapter consists of a general description of the junction flow using hydrogen bubble flow visualization. Several sequences of hydrogen bubble pictures are presented for illustration.

LDV measurements are provided to show the general mean flow characteristics in the plane of symmetry upstream of the wing. These are compared with the wind tunnel data of Devenport and Simpson (1987).

Next, the three-dimensional instantaneous velocity vector field in the junction region is presented, which was obtained by the 3-D PIDV method.



## 6.2 Test Conditions

The requirements for the test conditions for the present study were that the potential flow be steady and uniform, and the approach boundary layer should be turbulent.

For flow visualization using the hydrogen bubble technique, the flow speed was restricted due to the production of cavitation-induced air bubbles, which, at higher speed, interfered with the hydrogen bubbles. For best flow visualization results, the flow speed was approximately  $9.1\text{cm/sec}$  at  $X/T = -5.33$ , which corresponded to  $Re_\theta = 330$  at  $X/T = -2.15$ . Here,  $T$  is the maximum thickness of the wing and  $Re_\theta$  is the Reynolds number based on the momentum thickness of the oncoming boundary layer. However, since at this flow speed the boundary layer was barely turbulent, a higher speed was also used with LDV measurements for comparison. For the higher speed,  $Re_\theta = 1100$  was obtained at  $X/T = -2.15$ . Test conditions are listed in Table 1.

## 6.3 Flow Visualization Results

Flow visualization using a hydrogen bubble wire technique was used in the nose region of the wing-body junction. Tests were conducted at low water speed ( $Re_\theta = 330$ ), and flow visualization results were taped using a standard VHS camcorder. Photographs presented in this section were obtained via a Nikon 2020 35mm camera either directly from the flow or from a TV screen displaying a frozen frame of a recorded VHS tape on a Panasonic Model AG1960 super VHS VCR. An FDL (Fluorescent to Daylight) filter was used for the TV photographs for improved color balance.

Figure 26 shows a sequence in which inverted time-lines generated every second were used as flow tracers. The location of the hydrogen bubble wire was at 6.35cm upstream of the leading edge of the wing ( $X/T = -0.443$ ). It should be noted that the wire was not exactly vertical to the floor (about  $6^\circ$  inclined toward the wing), but still in the plane of symmetry. The dark area near the wing is in the shadow of the wing. The field of view (from the wire to the leading edge of the wing) is about 6.35cm  $\times$  7.20cm. The disturbed flow near the top of the view was caused by the interference of the wire junction of the probe with the flow.

Figure 27 shows a sequence of pictures which captured the flow near the saddle point formed between two vortices. The location of the wire was at 5.50cm upstream of the leading edge of the wing. The field of view is about 5.50cm  $\times$  7.20cm. Near the top, the wire had a foreign material such as dust or small bubbles, so that no bubbles were generated on that spot.

Figure 28 shows the time-line patterns of the various flow structures found in this region. The wire was at 7.62cm upstream of the leading edge of the wing ( $X/T = -0.531$ ). The field of view is 7.62cm  $\times$  7.94cm.

#### 6.4 Results of LDV Measurements

LDV measurements were made in the plane of symmetry upstream of the wing. Figure 29 shows the measurement locations.

#### 6.4.1 Characteristics of Approaching Boundary Layer

The characteristics of the approaching boundary layer were investigated at  $X/T = -2.15$  using LDV measurements (Figure 11 shows the setup), and the mean flow data at this location were used as parameters for comparison with the wind tunnel data of Devenport and Simpson (1987). The boundary layer characteristics at this location are tabulated in Table 1.

The momentum-thickness Reynolds numbers ( $Re_\theta$ ) measured at this location were 330 and 1100, respectively, under the nominal test conditions. These correspond to the boundary layer thicknesses ( $\delta_{99.5}$ ) of 40.6mm ( $\delta_{99.5}/T = 0.283$ ) for the  $Re_\theta = 330$  case, and 27.3mm ( $\delta_{99.5}/T = 0.190$ ) for the  $Re_\theta = 1100$  case. The mean velocities measured at  $X/T = -5.312$  were used as reference velocities ( $U_{ref}$ ), and  $U_{ref}$  of 9.07cm/s and 44.75cm/s were obtained, respectively.

Figure 30 shows the comparison of the law of the wall plots measured at  $X/T = -2.15$  for each test condition including Devenport's wind tunnel data. Three data sets coalesced fairly well in the logarithmic region. The Reynolds number effect shows up in the outer region of this plot where the highest Reynolds number case deviates up from the slope of the logarithmic region. The present data do not have enough data points in this region, but have the trend showing the Reynolds number effect.

Figure 31 shows the distribution of the axial turbulent stresses across the boundary layer for both of the test conditions. It should be noted that the turbulence level in the external flow was high as shown in the hot-film measurement data in Figure 3.

Figures 32 – 37 show the procedures of obtaining the local skin friction coefficients ( $C_f$ ) at  $X/T = -2.15$ . For the high Reynolds number case, the local skin friction coefficients of 0.0053 and 0.0078 were obtained using the “cross-plot of log region” method and the “wall-profile” method, respectively. Law of the wall plots were made for both of the test conditions.

#### 6.4.2 Mean Flow Data

The mean velocity profiles at all the measurement locations are plotted in Figure 38 and Figure 39 for each test condition. The mean flow profile at  $X/T = -0.86$  was still very similar to that of the two-dimensional turbulent boundary layer. As the flow approached the wing, the effect of the primary junction vortex appeared in the outer part of the boundary layer for both of  $Re_\theta = 330$  and  $Re_\theta = 1100$  cases. The flow in the outer layer was observed to be accelerated faster than the external flow due to the action of the strong junction vortex. This happened at all the measuring points from  $X/T = -0.67$  to the point nearest to the leading edge of the wing for  $Re_\theta = 1100$ , and from  $X/T = -0.40$  on for  $Re_\theta = 330$ . This indicates that the influence of the junction vortex reaches far upstream at higher speed.

The backflow reached a maximum of  $-0.41U_{ref}$  at  $X/T = -0.125$  and  $Y/T = 0.0078$  for the  $Re_\theta = 330$  case and of  $-0.48U_{ref}$  at  $X/T = -0.075$  and  $Y/T = 0.0032$  for the  $Re_\theta = 1100$  case. Comparing with Devenport's wind tunnel data of  $-0.49U_{ref}$  at  $X/T = -0.153$  and  $Y/T = 0.0047$ , the present data shows that the maximum backflow scaled with  $U_{ref}$  did not change much at higher  $Re_\theta$ .

Figure 40 shows the boundary layer profiles at all the measuring points in the plane of symmetry upstream of the wing. This plot was constructed using only U-component velocities. The region surrounded by a solid line indicates the bimodal zone found.

In Figure 41, three data sets with different  $Re_\theta$  were plotted together to take the effect of the Reynolds number into account. In these plots, Y-location was scaled with the approach boundary layer thickness  $\delta$ , while X-locations of measurement were scaled with  $T$ .

#### 6.4.3 Some Turbulence Data

The  $\overline{u'^2}$  variations across the boundary layer were obtained at all the measurement locations and plotted with Devenport's wind tunnel data as shown in Figure 42. These data show how the flow fluctuations near the junction vary as the wing is approached. At all the measuring points, the characteristics of the flow deviated from the typical turbulent stress distribution in the boundary layer due to the presence of the wing.

Here, the U-component fluctuations ( $\overline{u'^2}/U_{ref}^2$ ) increased as the flow approached the wing. The magnitude of fluctuations reached a maximum approximately at  $X/T = -0.125$ , or  $-0.150$ , and then reduced to very small value in the vicinity of the wing. In these plots, the  $\overline{u'^2}$  variations show similar behavior across the boundary layers for all the test cases. In particular, in the case of  $Re_\theta = 1100$  and Devenport's data, where both of them were comparatively high Reynolds number cases, the local maximum in  $\overline{u'^2}/U_{ref}^2$  at high Y location was observed first, and then another peak in  $\overline{u'^2}/U_{ref}^2$  at low Y location followed as the wing was approached. Figure 43(a) and Figure 43(b) show the contour plots of  $\overline{u'^2}$  for  $Re_\theta = 330$  and  $Re_\theta = 1100$ , respectively.

The velocity histograms across the boundary layer at each measuring station where vortex motion was considered to be approximately centered, are presented in

Figure 44. The tic marks in these plots show zero velocity points in the histogram. Here, one can see the bimodal (double-peaked) velocity histograms in some  $X/T$  and  $Y/T$  range. Note that these bimodal velocity histograms appeared in both of the test cases.

#### Higher-order turbulent results

The skewness factor ( $S_u$ ) and flatness factor ( $F_u$ ) for  $u$  were calculated from the velocity histograms  $P(U)$  at all the measurement locations.

The skewness factors ( $S_u$ ) and flatness factors ( $F_u$ ) are given by

$$\begin{aligned} S_u &= \frac{\overline{u^3}}{\overline{u^2}^{\frac{3}{2}}} \\ F_u &= \frac{\overline{u^4}}{\overline{u^2}^2} \end{aligned} \quad (6.1)$$

where the third and fourth moments can be obtained by setting  $n = 3$  and  $4$  from the following expression,

$$\overline{u^n} = \int_{-\infty}^{+\infty} (U - \bar{U})^n P(U) dU$$

The results are presented in Figure 45 - Figure 48 for each test condition.

#### *6.4.4 Switching Frequency Analysis (SFA)*

As pointed out by Devenport and Simpson (1987, 1990), the flow in this region appears to have two distinct modes: a backflow mode and a zero flow mode. In the backflow mode, the flow in the separation region reaches far upstream forming a large vortical structure, while the fluid in the zero flow mode flows downstream reducing the extent of the separated region.

For the LDV data which had bimodal velocity histograms, the average frequency of switching ( $\bar{f}_{sw}$ ) from one mode of flow to another was calculated to study the relations among the experimental parameters, especially between the switching frequency and the flow structure.

#### A Single Threshold Level SFA with $\delta T_{min}$

This analysis method employed a single threshold between two peaks in the velocity histogram and a minimum switching time ( $\delta T_{min}$ ) as parameters to determine the switching of flow mode. In this technique, flow mode was considered to be switched when time series of LDV signals encountered a threshold level and lasted more than  $\delta T_{min}$  in one flow mode.

Figure 49 illustrates some results obtained by this analysis method. Eleven threshold levels were selected between two peaks and  $\delta T_{min}$  also varied from 0.075 sec. to 0.20 sec. As seen in these plots, the average switching time ( $\bar{T}_{sw}$ ) depends on the two selected parameters. However, it is notable that  $\bar{T}_{sw}$  did not change much with a selected threshold level when two flow modes existed almost at the same rate.

#### Three Threshold Level SFA with Digital Filtering

In this method, the time series of velocity data were filtered digitally to remove the high frequency turbulent fluctuations which were considered not to be associated with the change of the flow mode. Four different kinds of FIR (Finite Impulse Response) filters were designed according to N (number of filter taps) and 3dB points, and compared to each other. The characteristics of each digital filter are

presented in Figure 50. Figure 51 illustrates how each filter works on LDV signals in the bimodal region.

After passing through the digital filter, the velocity histogram was obtained and smoothed further to calculate the extremal locations in the histogram without the influence of the local variation of the shape of the histogram. This was confirmed at every data point by the visual inspection through the program developed to produce an interactive graphics during computation. Two local maximum locations ( $v_{max_1}$  and  $v_{max_2}$ ) and one local minimum location ( $v_{min}$ ) were obtained in a velocity histogram which had a bimodal shape.

Three threshold levels between minimum and maximum velocity were selected to trigger the switching between the modes. Since the shape parameters of a bimodal histogram, such as the heights of two peaks and the widths between the local extremes, are dependable factors, the threshold levels were selected to include the effect of those parameters as below. 1

$$\begin{aligned} v_{t_1} &= C_1 \times \frac{h_1}{(h_1 + h_3)} \times (v_{min} - v_{max_1}) \\ v_{t_2} &= v_{min} \\ v_{t_3} &= C_3 \times \frac{h_3}{(h_1 + h_3)} \times (v_{max_2} - v_{min}) \end{aligned} \tag{6.2}$$

where  $h_1$  and  $h_3$  are the heights of each peak in the velocity histograms. Figure 52 is the schematic drawing describing the parameters employed in Equation (6.2). The constants  $C_1$  and  $C_3$  in Equation (6.2) were selected to give better visual results on the values of  $v_{t_1}$  and  $v_{t_3}$ , and the values of 0.5 for each constant worked well after a series of numerical experiments. The typical example of the triggered LDV signals using three threshold values is given in Figure 53.



Figure 54 shows the variations of the probability density function of the switching frequency at several  $X/T$  locations. As pointed out by Devenport and Simpson (1990), the probability density function of the switching frequency resembled the log-normal distribution at the measuring points showing a bimodal velocity histogram.

Figure 55 shows the variation of the average switching time ( $\bar{T}_{sw}$ ) in the bimodal zone. The average switching time is defined as the average period for the flow to switch back to the previous flow mode. For  $Re_\theta = 330$  case, the average switching times ( $\bar{T}_{sw}$ ) at  $X/T = -0.150$  and  $X/T = -0.175$  were 4.72 and 4.43 seconds, respectively, which were shorter than those at other locations. This implies that switching from one mode to another occurred more often in this region. As the wing was approached, the mode change took place slowly ( $\bar{T}_{sw} \approx 9(sec.)$ ) especially at low Y locations.

For the  $Re_\theta = 1100$  case, the switching occurred more frequently at low Y location for  $X/T = -0.125$ , and at high Y location for  $X/T = -0.150$ .

Figure 56 shows the variations of the average switching frequency ( $\bar{f}_{sw}$ ) in the bimodal zone for each flow condition. The switching frequency is defined as the average of the inverse of the period for the flow to switch back to the previous mode. For the  $Re_\theta = 330$  case, the values of the switching frequency were widely spread across the bimodal zone ranging from 0.20 Hz to 0.80 Hz. The switching occurred in a wide Y range at X location of  $X/T = -0.150$ .

For the  $Re_\theta = 1100$  case, the switching frequency varied from 0.85 Hz to 1.72 Hz. The variations of  $\bar{f}_{sw}$  across the bimodal zone at each X location explain the intensity of the switching activity as follows. At  $X/T = -0.175$ , which was

the most upstream location showing a bimodal histogram, only one location was observed to be bimodal, and had the lower switching frequency than the other points at different  $X$  locations. The variations at  $X/T = -0.15$  show that the switching appeared to occur more often at higher  $Y$  location and became slower at lower  $Y$  location. On the other hand, this trend became reversed at  $X/T = -0.125$  where the most intense large-scale fluctuations appeared. The averaged switching frequency at  $X/T = -0.125$  was estimated as approximately 1.23 Hz. As the wing was approached to  $X/T = -0.10$ , the switching activity became intense, and the values of the switching frequency at each  $Y$  location were approximately 0.89 Hz.

Figure 57 illustrates the results showing the fraction of the backflow mode ( $\gamma_b$ ) during each point measurement. For  $Re_\theta = 330$  case, the back flow mode was prevailing for most of the time near the wing ( $X/T = -0.10$  and  $X/T = -0.125$ ). However, at  $X/T = -0.15$ , the chances were almost equal for each flow mode to take place across all the  $Y$  locations. For the flow far upstream, the zero mode flow began to last longer especially near the wall. The same trend was found for  $Re_\theta = 1100$ . However, the location where each mode took place at approximately equal rate was at  $X/T = -0.125$  near the wall, which means that the frequent switching occurs near the wing for the high Reynolds number case. Figure 58 shows the contour plots of the backflow mode ( $\gamma_b$ ) in the bimodal zone. The dotted lines were constructed based on the assumption that  $\gamma_b$  does not vary much with height apart from the wall (Devenport and Simpson, 1990a).

The switching frequency analysis was performed on an IBM PC/AT compatible for every data point having the bimodal velocity histograms. The listing of the programs developed for the switching frequency analysis is tabulated in Table 7, and a diskette containing those files is attached on the back. can be expressed

## 6.5 Results of PIDV

The three-dimensional instantaneous velocity vector field was obtained in the region near the leading edge of the wing from the high speed video images.

Figure 59 shows a sequence of the bilevel images that are preprocessed with the techniques including the background subtraction, the 8-point local averaging and the thresholding. The images in the left-hand side of this figure represent side views, and the ones in the right-handed side are combined images for the bottom and upstream views. The combined images were produced by the mirror arrangement described in Figure 15.

Figure 60 shows the graphical reconstruction of the three-dimensional instantaneous velocity vector field in the nose region of the wing. The three-dimensional reconstruction of the velocity field was obtained by the perspective transformation from the three-dimensional points in the physical plane into the points in a two-dimensional plane. In addition, animation movie was made by shooting frame by frame using Super 8mm moviecorder. The animation movie shows the instantaneous velocity field information and the trajectory of the individual bubble elements.

The color coding was used to represent the variations in Z-coordinate. Since the number of color that can be used at once in the VGA mode of the maximum resolution ( $640 \times 480$ ) is restricted to sixteen, the color coding looks coarse.

Figure 61 shows the three instantaneous velocity components of the individual hydrogen bubble elements. This was obtained by the 3-D PIDV following the individual bubble elements. The top figure represents the time trajectory of the bubble element, and the bottom one contains three components of the velocity at the corresponding location. Here, the hydrogen bubble elements generated from the first wire are plotted.

## 7. DISCUSSIONS OF THE RESULTS

### 7.1 Description of the Junction Flow

Flow visualization using the hydrogen bubble technique revealed details of the time-dependent flow structures in the stagnation region of the wing, which was not possible by the surface oil flow visualization technique or single point LDV measurements that have been used in most of the previous studies.

In Figure 26, at the instant of the generation of the inverted time-line, three distinct regions marked by " $v_1$ ", " $v_2$ ", and " $v_3$ " were observed near the wall. Each region was approximately centered at  $X/T$  of -0.4, -0.25 and -0.09, respectively. In the outer layer, some disturbance as seen at location " $s_1$ " approached the wing. In region " $v_3$ ", a primary junction vortex was observed while a weak vortex with the same rotation direction was present in region " $v_2$ ". Occasionally, a vortex-like movement was observed between " $v_2$ " and " $v_3$ ", which will be explained later in this section. Near the bubble generating wire, the flow seemed to lift up in region " $v_1$ ". The cores of individual vortices are indicated by " $C_1$ " and " $C_2$ ".

In Figure 26(b), the inverted time-line had a disturbed region as seen at location " $d$ ". In Figure 26(b) - (h), the fluids in region " $v_1$ ", which were lifted up, were observed to leap-frog over the larger vortex structure. Here, the fluid marked by " $d$ " experienced a rotational motion and merged into the primary junction vortex from the outer layer. In Figure 26(b) - (f), the two vortex structures " $C_1$ " and " $C_2$ " were apparent although some disturbances from upstream rolled up over

these structures. In Figure 26(g), large-scale vortex-like motions indicated by " $s_2$ " and " $s_3$ " were built upstream due to the lifted-up fluids and leap-frogged over two junction vortices,  $C_1$  and  $C_2$ . During leap-frogging of the small vortices, the vortex marked by " $C_2$ " lost its strength, finally merging into the primary junction vortex " $C_1$ ", as shown in Figure 26(g) - (l).

In Figure 26(i) - (l), the flow very near the wall was divided into two regions, " $v_1$ " and " $v_3$ ". Region " $v_1$ " contained low momentum fluids. In Figure 26(i), some backflow existed in region " $v_1$ ". In Figure 26(j) - (l), the primary vortex moved downstream. Later, another inverted time-line was generated in Figure 26(l). A fluid region in the outer layer, which was clearly discernible from others, is marked by " $d_2$ " in Figure 26(m) - (u). This sequence of photographs showed that a vortical structure existed in the outer layer, which did not merge into the primary junction vortex upstream of the wing. However, the height of " $d_2$ " above the wall reduced as the structure approached the wing, which implies that it might be affected by the primary junction vortex. In Figure 26(v), it was not possible to trace " $d_2$ " since it wrapped around the wing.

In Figure 26(m) - (t), the lift-up of the flow was again observed and marked by " $l$ ". The disturbances created in the outer part of the approaching boundary layer as seen at location " $s_4$ " in Figure 26(o) - (r) together with the lifted-up flow " $l$ " from the wall layer were observed to merge into the primary junction vortex. Here, the leap-frogging of fluid regions over the larger vortical structure again appeared.

From Figure 26(m) on, the region marked by " $v_2$ " appeared, but there was no distinct vortex structure in this region. Instead, a concentration of fluids with very

low momentum seemed to exist around the region " $v_2$ ", where some of the fluids merged into " $v_3$ " and some followed the local direction of the lifted-up fluid flow.

The three distinct regions, " $v_1$ ", " $v_2$ ", and " $v_3$ ", observed from the flow sequence observed in Figure 26, correspond to the lift-up region, the secondary vortex region, and primary vortex region, respectively. The existence of these regions is consistent with the LDV measurements as in Figure 43, in which there exist three regions with higher turbulent stresses.

The sequence of the photographs (Figure 26) further shows that the secondary vortex region merges into the primary vortex. The primary vortex, when it gained strength to some extent, moves downstream while the high momentum fluid enter this region from upstream just like the "sweep-inrush" phase in a turbulent boundary layer. This leads to the stretching of the primary vortex.

Flow near the saddle point formed between the primary and the secondary vortex was captured in a sequence of photographs in Figure 27. In this sequence, fluid region ("T") followed the secondary vortex motion marked by "S" and moved down to the near wall region. Later, some of that fluid changed the flow direction to follow the primary vortex motion ("P"). This shows that the interaction between two active vortices created a tertiary vortex between them (see Figure 27(j)). This may explain the observation of the multiple vortex system existing in this region by the previous researchers.

In Figure 28, the leap-frogging of the smaller-scale structures over a large structure was again observed. In particular, Figure 28(a) - (b) illustrate that smaller-scale eddies, as seen at locations " $a_1$ ", " $a_2$ ", " $b_1$ ", " $b_2$ ", and " $b_3$ ", rolled up around a primary junction structure marked by region "M" to merge into a larger structure.

In Figure 28(c), there was a region marked by "J" where the distance between the time-lines was longer than the others. This indicates that the strong activity of the junction vortex induced the flow acceleration in this region. The approximate location of the core of the primary junction vortex is marked by "C".

Figure 28(d) shows an instant when an axial component of vortex filaments existed at location "L" and started to rise due to the presence of the junction vortex. This was again observed in Figure 28(e) and Figure 28(f). The region marked by "S<sub>1</sub>" in Figure 28(e) shows that the flow in the outer region was accelerated toward the junction vortex.

In Figure 28(c) - (g), the vortex core as seen at location "C" was observed to change its location upstream of the wing with its strength varying occasionally. The strength of the junction vortex may be estimated by the intensity of the white area in the picture formed by the agglomeration of the hydrogen bubbles. The region consisting of low momentum fluids was observed upstream of the junction vortex although this was hardly discernible in the photographs. In most of the pictures, the low momentum fluid region existed between the wire location and the primary junction vortex.

Figure 28(h) shows an instant when the time-lines proceeded to the leading edge of the wing without much interference, which may indicate the junction vortex was stretched around the nose of the wing as seen at the region "S<sub>t</sub>". Indeed, the flow near the wall was accelerated, and the vortex core indicated by the white area was not observed due to the effect of the stretching. It should be notable that the instability observed along the leading edge is possibly a result of the amplified

unsteadiness in the vicinity of the stagnation point due to the high free-stream turbulence level.

Figure 28(i) again shows a axial component of vortex filaments formed upstream of the junction vortex which was observed in region "R".

The location marked by " $S_2$ " in Figure 28(j) shows a large structure in the outer layer. The time-lines surrounding this structure indicate that the convective speed of the large structure in the outer layer is slower than the velocity of the external flow. However, the faster speed near the wall region indicates that the vortex was being stretched.

Figure 28(k) shows that the multiple vortex-like disturbances around a large vortical structure near the junction contributed to the formation of the primary vortex structure. The location marked by " $k_1$ " shows the engulfment from the outer energetic flow into the region of low momentum fluid flow to make a stronger vortical structure.

As observed from flow visualization, a repetitive flow behavior was found in this region, and may be considered to be made up of several characteristic events. Yet, on some occasions, some of the events could not be observed. Those events observed from flow visualization can be summarized as follows:

- i ) Primary and secondary vortices are formed upstream of the wing.
- ii ) The backflow leads to the lift-up of the fluid in the region of low momentum flow. The backflow is produced in the mean sense by the formation of the secondary vortex upstream of the primary vortex. This lift-up of fluid generates the disturbances in the flow.



- iii ) Multiple vortices exist in the form of disturbances or small structures, upstream of the primary junction vortex. In some instances, the axial vortex filaments are observed.
- iv ) Smaller-scale structures leap-frog over a primary junction vortex to form a stronger vortical structure. The secondary vortex also merges into the primary vortex.
- v ) When the primary junction vortex gains sufficient strength, it seems to stretch at a faster rate around the nose of the wing, and this was observed repetitively.
- vi ) Very unstable flow follows after faster stretching while flow is stable during the stretching due to the activity of the primary junction vortex.
- vii ) After a while, the backflow reaches far upstream to make a large, but weak junction vortex structure. Here, the primary and secondary vortex are formed again.

The above sequence of events is described in Figure 62. The percentage at the end of each comment represents the time proportion of that event in the average period of the acyclic flow.

This acyclic process helps explain the existence of the two flow modes suggested by Devenport and Simpson (1987). When the secondary vortex exists, the backflow reaches far upstream, which appears on the average as the backflow mode. The zero flow mode can be explained as the merging of the secondary vortex into the primary one, and the stretching of the primary vortex accompanying the entrainment of the high momentum fluid into this region. The acyclic behavior of the junction flow seems to be driven by the repetitive increase in the rate of stretching of the vortex system.

### Some statistics on the flow visualization results

Some statistical information was extracted from the flow visualization by inspecting the specific points in the flow region or specific events in the flow. Repetitive measurements were possible by watching the recorded tapes as much as needed. Ten minutes of the flow visualization results was used to get quantitative data as shown in Table 9.

The switching frequency of two flow modes was studied apart from the wall at  $X/T = -0.15$  by counting time for each switching to occur. The switching was decided by visual inspection. The fraction of a backflow mode ( $\gamma_b$ ) at the same location was obtained statistically by counting the total duration time in the backflow mode. From ten minutes of the flow visualization videos, the average switching frequency ( $\bar{f}_{sw}$ ) was approximately 0.18(Hz), and  $\gamma_b$  was approximately 0.78. Comparing to the results from SFA in Figure 57, the time fraction of the backflow mode ( $\gamma_b$ ) is considered to be overestimated. The corresponding Strouhal number ( $St_T = \bar{f}_{sw}T/U_{ref}$ ) was approximately 0.28.

The average lapse time between the formation of successive structures was estimated to be around  $1.26 \pm 0.39(sec)$ . This number represents the average period of the acyclic flow structure. The average time proportion for a primary vortex to last before the separation vortex forms was about 20% of the total period, which is about  $0.25 \pm 0.08(sec)$ . The average time for the leap-frogging process to occur was approximately  $0.55 \pm 0.16(sec)$ , which corresponds to 44% of the total period.

## 7.2 Estimation of friction velocity ( $u_\tau$ )

The friction velocity ( $u_\tau$ ) was estimated and compared by two methods : the "cross plot of log-region" procedure used by Runstadler *et al.* (1963) and the "wall-profile method" by Schraub and Kline (1965). The procedures and results of the two methods are described in Figure 32 - Figure 37. It should be noted that since the procedure by the "cross plot of log-region" assumes the universal law of the wall, the resulting  $u_\tau$  depends on which part of data is forced to fit. The current study adopted the universal logarithmic relation given by Clauser (1954) :

$$u^+ = 2.44 \ln y^+ + 4.9 \quad (7.1)$$

Therefore, this method becomes unreliable if there are regions near the wall where the law of the wall is not universal.

The wall-profile method assumes the existence of a linear region where  $u^+ = y^+$  holds. Thus, this method to estimate a value of wall shear can be applied if there are enough data points in the viscous sublayer region for fitting.

Figure 32 shows the repetitive procedure to obtain the local skin friction coefficient for the high Reynolds number case by forcing the data points in the logarithmic region to the adopted straight line. The local skin friction coefficient of 0.0053 was obtained by this method. With the friction velocity calculated using this estimated skin friction coefficient, the law of the wall plot was made in Figure 33. Some deviation of the data points from the relation ( $u^+ = y^+$ ) was observed.

However, the "wall profile" method used in Figure 34 suggested that another value of local skin friction coefficient ( $C_f = 0.0078$ ) works well in the viscous sublayer region, and the universal relation in the logarithmic region might have the different coefficients ( $u^+ = 2.44 \ln y^+ + 1.9$ ).

Figure 35 – 37 shows the same procedure for the low Reynolds number case. The local skin friction coefficients of 0.0070 and 0.0077 were obtained, respectively. In this case, the logarithmic relation did not deviate much from the Clauser coefficients, but some differences were again observed. In either test condition, some deviations in the viscous sublayer occurred when the “cross plot of the log-region” procedure was used. On the other hand, the “wall profile” method created deviations in the log region.

In general, the resulting wall shear estimated using each method does not coincide very well as pointed out by Schraub *et al.* Table 1 presents a summary of the estimated friction velocities. Differences up to 18% existed between  $u_\tau$ 's determined by the two methods. The uncertainty of determining the friction velocity for each method separately is estimated to be  $\pm 7\%$  as shown in Table 2.

### 7.3 Mean Velocity Profiles

The mean location of the core of the primary junction vortex was estimated from the mean velocity profile plot by locating the intersection between the maximum gradient of the mean velocity and the zero mean velocity. The approximate locations were at  $X/T = -0.125$  and  $Y/T = 0.032$  for  $Re_\theta = 1100$ , and  $X/T = -0.150$  and  $Y/T = 0.04$  for  $Re_\theta = 330$ . Comparison with Devenport's data ( $X/T = -0.20$  and  $Y/T = 0.05$ ) indicates that the locations of the vortex cores did not show good correlation when scaled with  $T$ , but the physical  $X$ -location approached the leading edge of the wing and the physical  $Y$ -location was getting lowered with the increasing  $Re_\theta$ . This implies that the mean location data for the vortex cores may

be correlated when different nondimensionalizing parameters are used for scaling. For instance, the use of  $\delta$  gives  $X/\delta = -0.530$  and  $Y/\delta = 0.141$  for  $Re_\theta = 330$ , and  $X/\delta = -0.442$  and  $Y/\delta = 0.113$  for  $Re_\theta = 1100$ . Devenport's data can be scaled to  $X/\delta = -0.4$  and  $Y/\delta = 0.10$  ( $Re_\theta = 6700$ ). These nondimensional mean locations of the vortex cores for each case show some Reynolds number dependency that the vortex is getting closer to the junction with the increasing Reynolds number.

It is considered that the Reynolds number did not change the mean flow behavior qualitatively. However, some of the plots in Figure 38 and Figure 39 show that there existed very similar profiles among three momentum thickness Reynolds number cases. As with the case of the mean vortex core location, the use of  $\delta$  as a scaling parameter gives a correlation.

#### 7.4 Low Frequency Unsteadiness

Figure 63 shows the typical LDV signals observed in the region where the backflow was found to be very dominant. As pointed out by Devenport and Simpson (1988a, 1990), it seemed like there existed two modes of flow (a backflow mode and a zero flow mode), and these two modes of flow were switching back and forth in the vicinity of the vortex core. In addition, the evidence of flow visualization reveals that the flow in this region has an "acyclic" behavior. The vortex system was observed to move around the nose region of the wing with low frequency fluctuations.

In this viewpoint, the flow velocity may be considered to consist of three parts, which are a mean velocity term, a large-scale fluctuation term, and a small-scale fluctuation term. The mean velocity term and small-scale fluctuations are regarded as the Reynolds decomposition terms. On the other hand, the third term, *i.e.*, the

large-scale fluctuation term, is superimposed on this turbulent flow at low frequency due to the presence of the wing-body junction. Three component decomposition of the flow velocity can be written as follows:

$$U = \bar{U} + u'_s + u'_l. \quad (7.2)$$

These large-scale fluctuations ( $u'_l$ ) are considered to be responsible for the large-scale time-dependent junction flow activities such as the bimodal flow structure found by Devenport and Simpson (1986, 1987, 1988a, 1988b, 1990).

The general tendency in  $\overline{u'^2}$  plots reveals that the turbulent activity is more intense at high Y locations in the upstream flow than at low Y location, and, as the flow moves downstream, the intense turbulent region moves down near the wall. This trend was also found in the switching frequency analysis discussed in the previous chapter. The switching between the two flow modes occurred more often at high Y location upstream and at low Y near the wing.

It should be noted that the similar behavior of  $\overline{u'^2}$  variations in three different Reynolds number cases indicates the possibility of the existence of other scaling parameters. Here, the boundary layer thickness ( $\delta$ ) seems to give better scaling between the three cases.

Figure 43 shows the contour plots of  $\overline{u'^2}$  for  $Re_\theta = 330$  and  $Re_\theta = 1100$ , respectively. In Figure 43(a), the most intense turbulent region was found very near the wall approximately at  $X/T = -0.175$  and another distinct region was observed approximately at  $X/T = -0.3$ . Upstream of the main junction vortex structure, which can be identified by the intense turbulent region, the region of fluid consisting of low turbulent intensity was observed. This region is considered as the

one corresponding to region " $v_2$ " of the low momentum fluids, which was discussed in the previous section. For the high  $Re_\theta$  case as shown in Figure 43(b), the vortex structure which contained a large amount of turbulent energy was confined near the leading edge of the wing ( $X/T = -0.125$ ). Here, the small region of the low turbulence intensity was again found upstream of the primary structure.

The results obtained from the analysis of the switching frequency in the bimodal region (Figure 56) show that the switching frequency ranges from 0.2Hz to 0.8Hz for  $Re_\theta = 330$ , and from 0.85Hz to 1.72Hz for  $Re_\theta = 1100$ . Schwind (1962) observed two types of unsteady oscillation according to the flow velocity when he studied a flow around a  $60^\circ$  included-angle wedge. For the flows of regime 4 type (Schwind's definition), a frequency of oscillation of 0.8Hz was measured, and a frequency of 1.4Hz for the flows of regime 5 type. The switching frequency analyzed in this study and the frequency of oscillation measured by Schwind represent different characteristics of flow. Yet, it could seem likely that the low speed case ( $Re_\theta = 330$ ) may be considered as Schwind's regime 4 or 5, and the higher speed case ( $Re_\theta = 1100$ ) as Schwind's regime 5 or above.

## 7.5 Discussion of higher order turbulence results

The skewness and flatness factors for the U-component velocity fluctuations were obtained at all the measurement locations from the present LDV data. Figure 45 shows the flatness factor distributions for the  $Re_\theta = 1100$  case. At  $X/T = -0.86$ , the velocity distribution is still close to that of the Gaussian ( $F_u = 3$ ) in most of the outer layer. As the wing is approached but still before separation, the

flatness factors become deviated from the value of the Gaussian distribution near the wall and in the outer part of the shear layer, while most of measurement point in the shear layer has the velocity distribution still similar to the normal distribution. In the vortical flow region, the flatness factors are far from being the normal distribution.

Figure 46 shows the skewness factor distribution plots. As pointed out by Simpson, Chew, and Shivaprasad (1981), downstream of separation the skewness factor for  $u$  becomes negative values near the wall, while large positive skewness factors are found upstream of separation. This is largely due to the reduced large-amplitude fluctuations in the backflow region. The skewness factors show the tendency to change signs at the location of maximum Reynolds stresses or large fluctuations. The intense exchange of momentum in this region reduces the very large or very small fluctuations of  $u$  component velocity. In the outer part of the shear layer, the skewness factor is negative for almost all the measurement points.

For the  $Re_\theta = 330$  case as shown in Figure 47 and Figure 48, the trend of both factors shows similar behavior across the shear layer at all the measurement points.

## 7.6 Dimensional Analysis on $\bar{f}_{sw}$

A dimensional analysis on the switching frequency was made to obtain the dimensionless parameters associated with the low frequency fluctuations. The average switching frequency,  $\bar{f}_{sw}$ , can be expressed as the following functional form with the other related parameters for a given cylindrical wing shape:

$$\bar{f}_{sw} = g(U_{ref}, T, a, X, Y, \delta, \theta, H, \rho, \mu) \quad (7.3)$$



where  $\bar{f}_{sw}$  is the average switching frequency,  $U_{ref}$  is the reference velocity measured at  $X/T = -5.312$ ,  $T$  is the maximum thickness of the wing,  $a$  is the length of the major axis of the elliptical nose,  $X$  and  $Y$  are the locations upstream of the wing,  $\delta$  is the thickness of the approach boundary layer at  $X/T = -2.15$ ,  $\theta$  is the momentum thickness at the same location,  $H$  is the shape factor, and  $\mu$  and  $\rho$  are the fluid viscosity and density, respectively.

The dimensional analysis on Equation (7.3) gives

$$St_T = g(Re_T, \frac{\theta}{T}, \frac{\delta}{T}, \frac{X}{T}, \frac{Y}{T}, \frac{a}{T}, H) \quad (7.4)$$

$$\text{where } St_T = \frac{\bar{f}_{sw} T}{U_{ref}} \quad \text{and} \quad Re_T = \frac{\rho U_{ref} T}{\mu}.$$

Here,  $St_T$  is the Strouhal number associated with the low frequency fluctuations, and  $Re_T$  is the Reynolds number based on the maximum thickness of the wing. Since only one shape of the model was investigated in this study, the dependence on the slenderness ratio can not be checked and this dimensionless parameter was left out from the functional form. The shape factor,  $H$ , did not show much variation as seen in Table 1, and was assumed not to affect the dependent dimensionless variables. Thus, the remaining terms can be written as

$$St_T = g(Re_T, \frac{X}{T}, \frac{Y}{T}, \frac{\delta}{T})$$

or

$$(7.5)$$

$$St_T = g(Re_T, \frac{X}{T}, \frac{Y}{T}, \frac{\theta}{T})$$

This means that the switching frequency is represented by the Strouhal number ( $St_T$ ), and this Strouhal number is a function of the Reynolds number based on  $T$ , the measurement location upstream of the wing ( $X/T, Y/T$ ), and the characteristics of the approach boundary layer ( $\delta/T$  or  $\theta/T$ ).

Figure 64 shows the variations of the Strouhal numbers at various locations upstream of the wing for each flow condition. For the approximate location of the vortex core ( $X/T = -0.125$ ) the Strouhal number showed near constant value of 0.34 for  $Re_\theta = 330$ , and 0.40 for  $Re_\theta = 1100$ . For the  $Re_\theta = 330$  case, the Strouhal number agreed fairly well with the result obtained from flow visualization ( $St_T = 0.28$  from Table 9). For the  $Re_\theta = 1100$  case, the Strouhal numbers across the whole bimodal zone did not vary much, while the Strouhal numbers showed very much variation at all the locations for  $Re_\theta = 330$ .

These indicate that at the specific Reynolds number the Strouhal number based on the maximum thickness of the wing may be a fairly constant with  $Y$  position near the mean location of vortex core. These results are in good agreement with the spectral analyses made on the hot wire signals measured by Baker (1979). His measurements were made at the height of 1mm from the wind tunnel wall and at  $X/D = -0.82$  which were outside of the primary vortex region but still in the separated region. His results showed that  $St_D = 0.26$  at low speed ( $D/\delta^* = 33.8$ ), and  $St_D = 0.40$  at high speed ( $D/\delta^* = 34.2$ ). He found that the high frequency oscillation  $St_D$  increases as  $UD/\nu$  increases ( $St_D$  increasing up to about 0.6 at higher  $UD/\nu$ ). Devenport and Simpson (1990a) obtained switching frequencies at  $X/T = -0.20$  by constructing the histograms and considering bimodal histograms

as formed by two added Gaussian histograms. At  $U_{ref} = 27m/s$ , they got the average frequency of 38 Hz and the most common frequency of 91 Hz, which correspond to the Strouhal number of 0.1 and 0.24, respectively. Ölcmen *et al.* (1991) made another switching frequency analysis of the pressure fluctuation data obtained near the vortex core in the wind tunnel at  $U_{ref} = 32.5m/s$ . In his measurements, the half-size model of the same geometry was used and the different reduction method was applied to obtain the switching frequency. He obtained the switching frequency of 68 (Hz), which corresponds to the Strouhal number of 0.15.

Several dimensionless frequency groups were tried using different parameters for scaling between several data sets : i)  $U_{ref}/T$ , ii)  $U_{ref}/\delta$ , and iii)  $(\partial U/\partial s)_{nose}$ . As will be described in the next section, the value in iii) represents the rate of vortex stretching and was obtained by an inviscid panel method (Fleming, 1991). Comparison of the results obtained for several sets of data are provided in Table 10. Among those groups,  $\delta$  gives least variation of the results between data sets.

## 7.7 Vortex Stretching

Combined with the descriptive model for the acyclic process observed from flow visualization, the switching frequency between two flow modes discussed in the previous section has a direct relation with the vortex stretching. As discussed in the section 7.1, the vortex stretching occurs almost every cycle, and this creates the inrush of high momentum fluid into the separated flow region (zero flow mode), while the secondary vortex contributed to forming the backflow mode.

Therefore, the switching frequency is approximately equal to the frequency of the acyclic process observed in the junction region. This implies that the Strouhal

number adopted in the current study is directly related to the rate of the vortex stretching.

The vorticity transport equation can be written as follows:

$$\frac{D\vec{\Omega}}{Dt} = \vec{\Omega} \cdot \nabla \vec{V} + \nu \nabla^2 \vec{\Omega}, \quad (7.6)$$

which shows that the rate of change of vorticity is equal to the rate of deformation of the vortex lines (vortex stretching) plus viscous diffusion of the vortex.

Here, the vortex stretching term can be rewritten as

$$\vec{\Omega} \cdot \nabla \vec{V} = \Omega_s \frac{\partial V}{\partial s} \vec{n}_s, \quad (7.7)$$

where  $\vec{n}_s$  is a unit vector in streamwise direction. For the same geometry,

$$\frac{\partial V}{\partial s} \sim \frac{U_\infty}{T}, \quad (7.8)$$

which indicates that the rate of the vortex stretching depends largely on the flow velocity (boundary layer characteristics).

Therefore, the Strouhal number based on model thickness can be related to the vortex stretching as follows:

$$St_T = \frac{fT}{U} = \frac{f}{\left(\frac{U}{T}\right)} \sim \frac{f}{\left(\frac{\partial V}{\partial s}\right)_{v.s.}}. \quad (7.9)$$

This implies that for a constant Strouhal number, the switching frequency is linearly varying with the rate of the vortex stretching. It is noted that, for the same amount of vortex strength, the rate of vortex stretching was much higher in the wind tunnel

measurements ( $Re_\theta = 4450$ ) than in the water tunnel measurements. They are compared as follows:

$$\frac{(\frac{\partial V}{\partial s})_{air}}{(\frac{\partial V}{\partial s})_{water}} \sim 120 \quad \text{for } Re_\theta = 1100$$

$$\frac{(\frac{\partial V}{\partial s})_{air}}{(\frac{\partial V}{\partial s})_{water}} \sim 595 \quad \text{for } Re_\theta = 330$$

Considering this large difference in the stretching rate of vorticity between air and water, the results obtained from the switching frequency analysis in the previous section show good correlation between two test cases ( $St_T = 0.40$  for  $Re_\theta = 1100$  in water and  $St_T = 0.15$  for  $Re_\theta = 4450$  in air by Ölçmen *et al.*).

### 7.8 3-D PIDV Results

The sequence of the bilevel images as shown in Figure 59 illustrates lots of practical difficulties in implementing the motion analysis. First of all, the gray levels of the background image were not uniform from frame to frame. This fluctuation of gray levels could not be removed because it was caused by the limitations of the high speed video system employed. Therefore, the subtraction of the same background level from all the frames may cause the problem of losing information. However, since the processing speed is greatly improved by employing a uniform background subtraction, some routines were added to retrieve the lost information. In order to compensate for the gray level fluctuations, several frames (previous 10 frames) were considered to determine the matching between the bubble elements. Thus, even though we lose some bubble elements at some instant, they may be retrieved after several frames.

Secondly, the bubble overlapping (see Figure 24) was the most troublesome problem in processing the image data. Due to the overlapping of the bubble elements, the information of at least one element was lost and the uncertainty in determining the centroid locations was increased by the factor of two. To improve this problem, the split-merging detection algorithm (see Figure 25) was developed. In the sequence of instantaneous velocity vector field as shown in Figure 60, some of the bubble elements were retrieved using this algorithm.

As seen in Figure 60, most of the bubble elements were lost near the wing and in the vortex region due to the fast diffusion of the hydrogen bubbles. This is the inherent problem which cannot be avoided when the hydrogen bubbles are used as tracer particles.

Figure 61 shows the trajectories of the individual bubble elements and the corresponding three-dimensional instantaneous velocity components. It is notable that axial acceleration exists at  $t = 0.35(\text{sec.})$  for all the bubble elements, which may be explained as the flow event when the vortex is stretched. Among the three velocity components, Z-component fluctuation is dominant at low frequency.

As shown in Figure 60 and Figure 61, the five-wire hydrogen bubble technique presented a new method to obtain three-dimensional velocity components. However, due to the limitation of the bubble patch size, the results were always subject to the sizable uncertainties. Another important factors that affected the results were fast diffusion of hydrogen bubbles in a vortical flow and distortion of the bubble patches. In order to reduce those effects in a highly distorted flow, it is recommended to use another tracking particles, which are small in size and not distorted in a shear layer region.

## 8. CONCLUSIONS

Experimental investigations of the flow structures in the nose region of a wing-body junction were made in the water tunnel at low speeds.

Several flow visualization techniques were developed using the hydrogen bubble method. An inverted time-line pattern allows the easier tracking of the inverted time-lines while the whole flow field is visualized by a sheet of hydrogen bubbles. A sequenced multiple-wire hydrogen bubble technique was developed and used to visualize the three-dimensional flow field.

LDV measurements were performed in the plane of symmetry upstream of the wing. The boundary layer characteristics obtained at  $X/T = -2.15$  were studied. The mean location of the core of the primary vortex is more confined to the junction with the increasing Reynolds number. Scaling the Y coordinates with the approach boundary layer thickness gives better correlation between the test cases of different Reynolds number than scaling with model thickness.

A visual study reveals that there exists an acyclic flow behavior in this region, which is closely related to the stretching of the horseshoe vortex system. Three component decomposition of the flow velocity was attempted to explain the large-scale, low-frequency fluctuations present in this region.

The bimodal velocity histograms found in the wind tunnel experiments by Devenport and Simpson (1987, 1988a, 1988b, 1990) were also obtained in this study. The idea of switching between two flow modes was implemented to calculate the

frequency of switching in a dimensionless form. The Strouhal number at the approximate core of the primary vortex represents the frequency of switching, and was obtained as follows;

$$St_T = 0.34 \quad \text{for } Re_\theta = 330$$

$$St_T = 0.40 \quad \text{for } Re_\theta = 1100.$$

The Strouhal number obtained from flow visualization results ( $St_T = 0.28$ ) showed good agreement with the results from LDV data.

The particle image displacement velocimetry (PIDV) using a multiple wire hydrogen bubble technique was developed to obtain the three-dimensional instantaneous velocity field in the junction region. New algorithms to implement image processing technique and motion analysis were successfully developed. However, the application of the present PIDV technique to the hydrogen bubble images was improper especially in a highly distorted flow region due to the fast diffusion of hydrogen bubbles. Therefore, the use of another tracking media such as solid particles is recommended in a shear flow application of the present PIDV technique.



## BIBLIOGRAPHY

- Abid, R., and Schmitt, R., "Experimental Study of a Turbulent Horseshoe Vortex Using a Three-Component Laser Velocimetry," AIAA-86-1069, 1986
- Acarlar, M. S., and Smith, C. R., "A Study of Hairpin Vortices in a Laminar Boundary Layer. Part 1. Hairpin Vortices Generated by a Hemisphere Protuberance," *J. Fluid Mech.*, Vol. 175, pp.1-41, 1987a
- Acarlar, M. S., and Smith, C. R., "A Study of Hairpin Vortices in a Laminar Boundary Layer. Part 2. Hairpin Vortices Generated by Fluid Injection," *J. Fluid Mech.*, Vol. 175, pp.43-83, 1987b
- Adamczyk, A. A., and Rimai, L., "2-Dimensional particle tracking velocimetry (PTV): Technique and image processing algorithms," *Experiments in Fluids*, Vol. 6, pp.373-380, 1988a
- Adamczyk, A. A., and Rimai, L., "Reconstruction of a 3-dimensional flow field from orthogonal views of seed track video images," *Experiments in Fluids*, Vol. 6, pp.380-386, 1988b
- Asanuma, T., and Takeda, S., "A Study of Flow Visualization by the Hydrogen Bubble Method," *Bull. of JSME*, Vol. 8, pp.599-608, 1965
- Baker, C. J., "The Laminar Horseshoe Vortex," *J. Fluid Mech.*, Vol. 95, part 2, pp.347-367, 1979
- Baker, C. J., "The Turbulent Horseshoe Vortex," *Journal of Wind Engineering and Industrial Aerodynamics*, Vol. 6, pp.9-23, 1980
- Bělik, L., "The Secondary Flow about Circular Cylinders Mounted Normal to a Flat Plate," *Aeronautical Quarterly*, Vol. 24, pp.47-54, 1973
- Bertelrud, A., Szodruch, J., and Olsson, J., "Flow Properties Associated with Wing-Body Junctions in Wind Tunnel and Flight," ICAS-88-4.3.3
- Blackwelder, R. F., and Haritonidis, J. H., "Scaling of the Bursting Frequency in Turbulent Boundary Layers," *J. Fluid Mech.*, Vol. 132, pp.87-103, 1983
- Blackwelder, R. F., and Eckelmann, H., "Streamwise Vortices Associated with Bursting Phenomenon," *J. Fluid Mech.*, Vol. 94, part 3, pp.577-594, 1979
- Bradshaw, P., "Turbulent Secondary Flows," *Ann. Rev. Fluid Mech.*, Vol. 19, pp.53-74, 1987

- Bradshaw, P. and Cutler, A. D., "Three-Dimensional Flows with Embedded Longitudinal Vortices," *Perspectives in Turbulent Studies*, Ed. Meier H. U. and Bradshaw P., pp.382-413, Springer-Verlag, Heidelberg, 1987
- Briley, W. R., and McDonald, H., "Solution of the Three-Dimensional Navier-Stokes Equations For a Steady Laminar Horseshoe Vortex Flow," AIAA-85-1520, 1985
- Burley, R. and Grigg, P. J., "A Solid State Pulser for the Hydrogen Bubble (Flow Visualization) Technique," *J. of Physics, E: Sci. Instr.*, Vol. 3, pp.1018-1020, 1970
- Cantwell, B. J., "Organized Motion in Turbulent Flow," *Ann. Rev. of Fluid Mechanics*, Vol. 13, pp.457-515, 1981
- Clutter, D. W., and Smith, A. M. O., "Flow Visualization by Electrolysis of Water," *Aerospace Engineering*, Vol. 20, pp.24-27, 74-76, 1961
- Corino, E. R., and Brodkey, R. S., "A Visual Investigation of the Wall Region in Turbulent Flow," *J. Fluid Mech.*, Vol. 37, part 1, pp.1-30, 1969
- Criminale, W. O., and Nowell, R. W., "An Extended Use of the Hydrogen Bubble Flow Visualization Method," *AIAA J.*, Vol. 3, p.1203, 1965
- Devenport, W. J., Dewitz, M. B., Agawal, N. K. Simpson, R. L., and Podder, K., "Effect of a Fillet on the Flow past a Wing-Body Junction," AIAA 89-
- Devenport, W. J., and Simpson, R. L., "Some Time-Dependent Features of Turbulent Appendage-Body Junction Flows," *16th Symposium on Naval Hydrodynamics*, July 14-18, 1986, Berkeley, CA.
- Devenport, W. J., and Simpson, R. L., "Turbulent Structure Near the Nose of Wing-Body Junction," AIAA-87-1310, *AIAA 19th Fluid Dynamics, Plasma Dynamics and Laser Conference*, Honolulu, Hawaii, June 8-10, 1987
- Devenport, W. J., and Simpson, R. L., "Time-Dependent Structure in Wing-Body Junction Flows," *Turbulent Shear Flows 6*, Springer-Verlag, 1988
- Devenport, W. J., and Simpson, R. L., "The Turbulent Structure Near an Appendage-Body Junction," *17th Symposium on Naval Hydrodynamics*, The Hague, The Netherlands, Aug. 29 - Sept. 2, 1988

- Devenport, W. J., and Simpson, R. L., "Time-Dependent and Time-Averaged Turbulence Structure Near the Nose of a Wing-Body Junction," *J. Fluid Mech.*, Vol. 210, pp 23-55, 1990a
- Devenport, W. J., and Simpson, R. L., "An Experimental Investigation of the flow past an Idealized Wing-Body Junction," *Report VPI-AOE-172*, July, 1990b
- Dickinson, S. C., *An Experimental Investigation of Appendage-Flat Plate Junction Flow Volume 1 : Description*, DTNSRDC-86/051, December, 1986a
- Dickinson, S. C., *An Experimental Investigation of Appendage-Flat Plate Junction Flow Volume 2 : Elliptical Nose Appendage Data Base*, DTNSRDC-86/052, December, 1986b
- Dickinson, S. C., "Time-Dependent Flow Visualization in the Separated Region of an Appendage-Flat Plate Junction," *Exp. in Fluids*, Vol. 6, 1988
- Durst, F., Melling, A., and Whitelaw, J. H., *Principles and Practice of Laser-Doppler Anemometry*, Academic Press, 1982
- Eckerle, W. A., and Langston, L. S., "Measurements of a Turbulent Horseshoe Vortex Formed around a Cylinder," NASA Contractor Report 3986, June, 1986
- Falco, R. E., "Coherent Motions in the Outer Region of Turbulent Boundary Layers," *Phys. Fluids*, Vol. 20, No. 10, pp.S124-S132, 1977
- Fielder, H. E., "Coherent Structures in Turbulent Flows," *Prog. Aerospace Sci.*, Vol. 25, pp.231-269, 1988
- Fleming, J. L., *An Experimental Study of a Turbulent Wing-Body Junction and Wake Flow*, M.S. thesis, Virginia Polytechnic Institute and State University, 1991
- Foley, J. D., and van Dam A., *Fundamentals of Interactive Computer Graphics*, Addison-Wesley Publishing Company, 1984
- Furey, D. A., and Walker, D. A., "LDV measurements in a NAVY CPS fan," VPI-E-90-15, 1990
- Gad-el-Hak, M., "Visualization Techniques for Unsteady Flows: An Overview," *Journal of Fluids Engineering*, Vol. 110, pp.231-243, September, 1988
- Geller, E. W., "An Electrochemical Method of Visualizing the Boundary Layer," *J. Aeronaut. Sci.*, Vol. 22, No. 12, pp.869-870, 1955

- Goldstein, R. J., *Fluid Mechanics Measurements*, Hemisphere Publishing Corp., 1983
- Grass, A. J., "Structural Features of Turbulent Flow over a Smooth and Rough Boundaries," *J. Fluid Mech.*, Vol. 50, part 2, pp.233-255, 1971
- Greco, J. J., *The Flow Structure in the Vicinity of a Cylinder-Flat Plate Junction : Flow Regimes, Periodicity, and Vortex Interactions*, M.S. thesis, Mech. Engrg., Lehigh University, 1990
- Gursul, I. and Rockwell, D., "Vortex Street Impinging on an Elliptical Leading Edge," *J. Fluid Mech.*, Vol. 211, pp.211-242, 1990
- Hall, E. L., *Computer Image Processing and Recognition*, Computer Science and Applied Mathematics, Academic Press, 1979
- Hancock, P. E., and Bradshaw, P., "The Effects of Free-Stream Turbulence on Turbulent Boundary Layers," *Journal of Fluids Engineering*, Vol. 105, pp.284-289, 1983
- Hasan, M. D., Casarella, M. J., and Rood, E. P., "An Experimental Study of the Flow and Wall-Pressure Field around a Wing-Body Junction," *Shear Flow-Structure Interaction Phenomena*, (ed. A. Akay & M. Reischman), ASME NCA-1, pp.89-95, 1985
- Hesselink, L., "Digital Image Processing in Flow Visualization," *Ann. Rev. Fluid Mech.*, Vol. 20, pp.421-485, 1988
- Hinze, J. O., *Turbulence*, 2<sup>nd</sup> ed., McGraw-Hill Series in Mechanical Engineering, 1975
- Hsu, C.-H., *Laser Doppler Anemometry Measurements of a Confined Turbulent Water Jet with a Uniform Background Flow*, PhD Dissertation, Virginia Polytechnic Institute and State University, 1989
- Imaichi, K., and Ohmi, K., "Numerical processing of flow-visualization pictures — measurements of two dimensional vortex flow," *J. Fluid Mech.*, Vol. 129, pp.283-311, 1983
- Kaul, U. K., Kwak, D., and Wagner, C., "A Computatic of Study of Saddle Point Separation and a Horseshoe Vortex System," AIAA-85-0182, 1985

- Kasagi, N., Hirata, M. and Nishino, K., "Streamwise Pseudo-Vortical Structures and Associated Vorticity in the Near-Wall Region of a Wall-Bounded Turbulent Shear Flow," *Experiments in Fluids*, Vol. 4, pp 19-318, 1986
- Kerstens, P. J. and Rockwell, D., "Ensemble-Averaging and Correlation Techniques for Flow Visualization Images", *Experiments in Fluids*, Vol. 6, pp.409-419, 1988
- Kim, H. T., Kline, S. J. and Reynolds, W. C., "An Experimental Study of Turbulent Production Near a Smooth Wall in a Turbulent Boundary Layer," *Report MD-20*, Thermosciences Division, Dept. of Mech. Engr., Stanford University, Jan., 1968
- Kline, S. J., and McClintock, F. A., "Describing Uncertainties in Single-Sample Experiments," *Mechanical Engineering*, Vol. 75, No. 1, pp.3-8, January, 1953
- Kollin, A., "Demonstration of Parabolic Velocity Distribution in Laminar Flow," *Amer. J. Physics*, Vol. 21, pp.619-620, 1953
- Kubendran, L. R., McMahon, H. M., and Hubbartt, J. E., "Turbulent Flow Around a Wing/Fuselage-Type Juncture," *AIAA J.* Vol. 24, No. 9, pp.1447-1452, 1986
- Liu, Z.-C., Landreth, C. C., Adrian, R. J., and Hanratty, T. J., "High Resolution Measurement of Turbulent Structure in a Channel with Particle Image Velocimetry," *Experiments in Fluids*, Vol. 10, pp.301-312, 1991
- Lu, L. J., and Smith, C. R., "Image Processing of Hydrogen Bubble Flow Visualization for Determination of Turbulent Statistics and Bursting Characteristics," *Experiments in Fluids*, Vol. 3, pp.349-356, 1985
- Lusseyran, D. and Rockwell D., "Estimation of Velocity Eigenfunction and Vorticity Distributions From the Time-line Visualization Technique," *Experiments in Fluids*, Vol. 6, pp.228-236, 1988
- Mattingly, G. E., *The Hydrogen Bubble Flow-Visualization Technique*, David Taylor Model Basin Rep. 2146 (AD 630 468), 1966
- McAllister, K. W., and Carr, L. W., *Water Tunnel Experiments on an Oscillating Airfoil at  $R=21,000$* , NASA TM 78446, 1978
- McMahon H., Hubbartt, J., and Kubendran L., *Mean Velocities and Reynolds Stresses in a Juncture Flow*, NASA CR 3605, 1982

- Meier, H. U., and Kreplin, H. P., "Influence of Free-Stream Turbulence on Boundary Layer Development," *AIAA Journal*, Vol. 18, No. 1, pp.11-15, January, 1980
- Merzkirch, W., *Flow Visualization*, Academic Press, 1974
- Mehta, R. D., "Effect of Wing Nose Shape on the Flow in a Wing/Body Junction," *Aeronautical J.* Vol. 88, pp.456-460, 1984
- Moore, J., and Forlini, T. J., "A Horseshoe Vortex in a Duct," *Trans. ASME J. ; J. Engng. Gas Turbines and Power*, Vol. 106, pp.668-676, 1984
- Nishino, K., Kasagi, N. and Hirata, M., "Three-Dimensional Particle Tracking Velocimetry Based on Automated Digital Image Processing," *Journal of Fluids Engineering*, Vol. 111, pp.384-391, 1989
- Offen, G. R. and Kline, S. J., "Experiments on the Velocity Characteristics of 'Bursts' and on the Interactions between the Inner and Outer Regions of a Turbulent Boundary Layer," *Report MD-91*, Thermosciences Division, Dept. of Mech. Engr., Stanford University, 1973
- Ölçmen, S. M., "An Experimental Study of a Three-Dimensional Pressure-Driven Turbulent Boundary Layer," PhD Dissertation, Virginia Polytechnic Institute and State University, 1990
- Oldfield, M. L. G., *Experimental Techniques in Unsteady Flows*, Lecture Notes for the VKI Lectures on Unsteady Aerodynamics, April, 1988
- Pavlidis, T., *Algorithms for Graphics and Image Processing*, Computer Science Press, 1982
- Peake, D. J., Rainbird, W. J., and Atraghji, E., "Three-Dimensional Flow Separations on Aircraft and Missiles," *AIAA Journal*, Vol. 10, No. 5, pp.567-580, May, 1972
- Perry, A. E. and Hornung, H., "Some Aspects of Three-Dimensional Separation, Part II: Vortex Skeletons," *Z. Flugwiss. Weltraumforschung*, Vol. 8, No. 3, pp.155-160, 1984
- Prahlad, T. S., "Mean Velocity Profiles in Three-Dimensional Incompressible Turbulent Boundary Layers," *AIAA J.*, Vol. 11, No. 3, pp.3589-365, 1973
- Riesenfeld, R., "Homogeneous Coordinates and Projective Planes in Computer Graphics," *IEEE Computer Graphics and Applications*, Vol. 1, pp.50-55, 1981

- Roos, F. W., and Willmarth, W. W., "Hydrogen Bubble Flow Visualization at Low Reynolds Numbers," *AIAA J.*, Vol. 7, pp.1635-1637, 1969
- Rotta, J. C., "A Theoretical Treatment of the Free Stream Turbulence Effects on the Turbulent Boundary Layer," *Viscous and Interacting Flow Field Effects; Proceedings of the 5th US/FRG Data Exchange Agreement Meeting*, AFFDL-TR-80-3088, pp.118-140, June, 1980
- Rubel, A., "Computational Techniques for the Calculation of Inviscid Rotational Jet Impingement," *AIAA-78-1212*, 1978
- Runstadler, P. W., Kline, S. J., and Reynolds, W. C., "An Experimental Investigation of the Flow Structure of the Turbulent Boundary Layer," *REPORT MD-8*, Thermodynamic Division, Dept. of Mech. Engr., Stanford University, June, 1963
- Schalkoff, R. J., *Digital Image Processing and Computer Vision*, John Wiley & Sons, Inc., 1989
- Schetz, J. A., *Foundations of Boundary Layer Theory for Momentum, Heat and Mass Transfer*, Prentice-Hall, Inc., 1984
- Schlichting, H., *Boundary Layer Theory*, 7th ed., McGraw-Hill Book Company, 1979
- Schraub, F. A., Kline, S. J., Henry, J., Runstadler, P. W. Jr., and Littell, A., "Use of Hydrogen Bubbles for Quantitative Determination of Time-Dependent Velocity Fields in Low-Speed Water Flows," *Journal of Basic Engineering*, Vol. 87, pp.429-444, 1965
- Schraub, F. A. and Kline, S. J., "A Study of the Structure of the Turbulent Boundary Layer with and without Longitudinal Pressure Gradients," *Report MD-12*, Thermodynamic Division, Dept. of Mech. Engr., Stanford University, March, 1965
- Schwind, R. G., "The Three-Dimensional Boundary Layer near a Strut," *Report No. 67*, Gas Turbine Lab., M.I.T., 1962
- Sedney, R., and Kitchens, C. W. Jr., "The Structure of Three-Dimensional Separated Flows in Obstacle, Boundary Layer Interactions," *AGARD-CP-168 on Flow Separation*, 1975
- Shabaka, I. M. M. A., and Bradshaw, P., "Turbulent Flow Measurements in an Idealized Wing/Body Junction," *AIAA J.* Vol. 19, pp.131-132, 1981



- Shiloh, H., Shivaprasad, B. G., and Simpson, R. L., "The Structure of a Separating Turbulent Boundary Layer. Part 3. Transverse Velocity Measurements," *Journal of Fluid Mechanics*, Vol. 113, pp.75-90, 1981
- Simpson, R. L., Chew, Y. T., and Shivaprasad, B. G., "The Structure of a Separating Turbulent Boundary Layer. Part 1. Mean Flow and Reynolds Stresses," *Journal of Fluid Mechanics*, Vol. 113, pp.23-51, 1981
- Simpson, R. L., Chew, Y. T., and Shivaprasad, B. G., "The Structure of a Separating Turbulent Boundary Layer. Part 2. Higher Order Turbulence Results," *Journal of Fluid Mechanics*, Vol. 113, pp.53-73, 1981
- Simpson, R. L., Ghodbane, M. G., and McGrath, B. E., "Surface Pressure Fluctuations in a Separating Turbulent Boundary Layer," *Journal of Fluid Mechanics*, Vol. 177, pp.167-186, 1987
- Smith, C. R., and Metzler, S. P., "The Characteristics of Low-Speed Streaks in the Near-Wall Region of a Turbulent Boundary Layer," *J. Fluid Mech.*, Vol. 129, pp.27-54, 1983
- Smith, C. R., and Schwartz, S. P., "Observation of Streamwise Rotation in the Near-Wall Region of a Turbulent Boundary Layer," *Phys. Fluids*, Vol. 26, No. 3, pp.641-652, 1983
- Smith, C. R. and Paxson, R. D., "A Technique for Evaluation of Three-Dimensional Behavior in Turbulent Boundary Layers using Computer Augmented Hydrogen Bubble-Wire Flow Visualization," *Experiments in Fluids*, Vol. 1, pp.43-49, 1983
- Smith, J. H. B., "Vortex Flows in Aerodynamics," *Annual Review of Fluid Mechanics*, Vol. 18, pp.221-242, 1986
- Smith, F. T., "Steady and Unsteady Boundary-Layer Separation," *Annual Review of Fluid Mechanics*, Vol. 18, pp.197-220, 1986
- Smol'yakov, A. V., and Tkachenko, V. M., *The Measurement of Turbulent Fluctuations*, Springer-Verlag, New York, 1983
- Taylor, J. R., *An Introduction to Error Analysis*, University Science Books, 1982
- Thompson, D. H., "A Survey of Water Tunnel Flow Visualization Techniques," *ARL/A. 335*, 1972

- Thompson, D. H., "Flow Visualization Using the Hydrogen Bubble Technique," *ARL/A. 338*,
- Townsend, A. A., *The Structure of Turbulent Shear Flow*, 2<sup>nd</sup> ed., Cambridge University Press, Cambridge, 1976
- Utami, T., and Ueno, T., "Visualization and Picture Processing of Turbulent Flow," *Experiments in Fluids*, Vol. 2, pp.25-32, 1984
- Van Dommelen, L. L. and Shen, S. F., "The Genesis of Separation," *Numerical and Physical Aspects of Aerodynamic Flows*, Ed. Cebeci, T., pp.293-367, Springer-Verlag, 1982
- Van Dyke, M., *An Album of Fluid Motion*, The Parabolic Press, 1982
- Visbal, M. R., "Structure of Laminar Junction Flows," *AIAA Journal*, Vol. 29, No. 8, pp.1273-1282, Aug., 1991
- Vollmers, H., "Integration of Streamlines from Measured Static Pressure Fields on a Surface," *Viscous and Interacting Flow Field Effects; Proceedings of the 6th US/FRG Data Exchange Agreement Meeting*, DFVLR IB 222-81/CP1, pp.259-270, 1981
- Wang, K. C., "On the Current Controversy about Unsteady Separation," *Numerical and Physical Aspects of Aerodynamic Flows*, Ed. Cebeci, T., pp.279-291, Springer-Verlag, 1982
- Werlé, H., "Hydrodynamic Flow Visualization," *Annual Review of Fluid Mechanics*, Vol. 5, pp.361-382, 1973
- White, F. M., *Viscous Fluid Flow*, McGraw-Hill Book Company, 1974
- Willmarth, W. W. and Bogar, T. J., "Survey and New Measurements of Turbulent Structure Near the Wall," *Phys. Fluids*, Vol. 20, No. 10, pp.S9-S21, 1977
- Willmarth, W. W. and Lu, S. S., "Structure of the Reynolds Stress Near the Wall," *J. Fluid Mech.*, Vol. 55, part 1, pp.65-92, 1972
- Willmarth, W. W. and Tu, B. J., "Structure of Turbulence of the Boundary Layer Near the Wall," *Phys. Fluids*, Vol. Suppl. 10, p.3134, 1967
- Wu, J.-Z., Gu, J.-W., and Wu, J.-M., "Steady Three-Dimensional Fluid Particle-Separation from Arbitrary Smooth Surface and Formation of Free Vortex Layers," *Z. Flugwiss. Weltraumforschung*, Vol. 12, pp.89-98, 1988

## TABLES

Table 1. Test conditions at  $X/T = -2.15$

Boundary layer characteristics		
case	high speed	low speed
$U_{ref}^*(cm/s)$	44.75	9.07
$\delta (cm)$	2.73	4.06
$\theta (cm)$	0.254	0.381
$H$	1.306	1.430
$C_f^\dagger$	0.0053	0.007
$u_r^\dagger (cm/s)$	2.155	0.495
$C_f^\ddagger$	0.0078	0.0077
$u_r^\ddagger (cm/s)$	2.615	0.518
$Re_\theta$	1100	330

\* (measured at  $X/T = -5.312$ )

† (estimated by the "cross plot of log-region" procedure)

‡ (estimated by the "wall profile" method)

**Table 2. Uncertainties of measured data**

Uncertainties	
Velocity (LDV)	$U \pm 3\%$
Velocity fluctuations	$u'^2 \pm 4\%$
Fringe spacing	$d_f \pm 0.8\%$
Probe volume location	$Y \pm 2.5 \times 10^{-2} mm$
Friction velocity	$u_\tau \pm 7\%$
Hydrogen bubble probe location	$X \pm 1mm$
Velocity (PIDV)	$U \pm 7.5\%$

**Table 3. Camera calibration coefficients**

Imager I (Side view)			
68.5751	0.6138	-5.6227	230.1952
-0.0181	68.7164	-0.0913	14.2271
0.0010	0.0009	-0.0334	1.0

Imager II (Bottom view)			
-0.7128	38.5617	0.4224	112.9080
-0.1299	-0.0217	37.9156	93.6505
-0.0143	0.0005	0.0022	1.0

**Table 4. Camera characteristics**

Imager resolution	240 × 192 (lines)
Field of view	8.13( <i>cm</i> ) × 7.11( <i>cm</i> )
Estimated maximum axial velocity	12.7( <i>cm/s.</i> )
Frame rate	1/125( <i>sec.</i> )
1 pixel distance in axial direction	0.034( <i>cm</i> )
Estimated movement of centroid location between successive frames	0.102( <i>cm</i> )
Estimated pixel distance of centroid location between successive frames	3 (pixels)

Table 5. Test log for LDV measurements

Profile #	$Re_\theta$	$X/T$	$f_s^\dagger$	$X_T^\ddagger$	Remarks
14	330	-0.86	49870.0	76290	
15	1100	-0.86	49870.0	76290	
16	330	-0.67	49870.0	76290	
17	330	-0.46	49870.0	76290	
18	330	-0.40	49870.0	76290	
19	330	-0.35	49870.0	76290	
20	330	-0.30	49870.0	76290	
21	330	-0.25	49870.0	76290	
22	330	-0.20	49870.0	76290	
23	330	-0.15	49845.2	76290	
24	330	-0.10	49826.9	76290	
25	330	-0.05	49866.1	76290	
26	330	-0.025	49870.0	76290	
27	1100	-0.025	53063.7	76290	
28	1100	-0.05	52853.2	76290	
29	1100	-0.10	51497.4	76290	*
30	1100	-0.15	101269.7	38150	
31	1100	-0.20	199973.1	38150	
32	1100	-0.25	101160.3	38150	
33	1100	-0.30	101183.6	38150	
34	1100	-0.35	101079.4	38150	
35	1100	-0.40	101068.8	38150	
36	1100	-0.46	101176.1	38150	
37	1100	-0.67	101073.9	38150	
38	1100	-0.125	200808.4	38150	
39	1100	-0.075	201008.1	38150	
40	1100	-0.175	101249.8	38150	
41	330	-0.175	99781.7	152600	
42	330	-0.125	99799.6	152600	

$^\dagger$  (Estimated shifted frequency)

$^\ddagger$  (Transfer function)

\* (Transfer function changed to 38150)



Table 6. Mean properties of junction vortex structure on different  $Re_\theta$

Junction Vortex Structure			
$Re_\theta$	330	1100	6700
$\delta/T$	0.283	0.190	0.5
$U_{max}^*$	$-0.41U_{ref}$	$-0.48U_{ref}$	$-0.49U_{ref}$
$(X/T, Y/T)^\dagger$	(-0.125, 0.0078)	(-0.075, 0.0032)	(-0.153, 0.0047)
$(X/T, Y/T)^\ddagger$	(-0.15, 0.04)	(-0.125, 0.032)	(-0.20, 0.05)
$X/T_{range}^\clubsuit$	-0.175... -0.10	-0.20... -0.075	
$Y/T_{range}^\clubsuit$	0.0... 0.0533	0.0... 0.0634	

\* (backflow)

† ( $U_{max}$  location)

‡ (vortex core location)

♣ (bimodal flow range)

Table 7. File list related to LDV measurements

File Name	File Size*	Remarks
ldvkim.c	2,822	main program for LDV data reduction
ldvavg.c	518	routine for mean values
ldvfnam.c	1,134	filename determination
ldvinit.c	204	initialization
ldvinput.c	820	input file
non_dim.c	204	
ldvpdf.c	1,127	routine for probability density function
swfa.c	7,231	main program for switching frequency analysis
swffln.c	344	file name determination routine
fourl.c	966	data smoothing routine <sup>†</sup>
f_mem.c	327	free dynamically allocated memory
get_mem.c	2,001	allocate memory dynamically
hstgrm.c	3,040	find a velocity histogram
swfinit.c	521	initialize the arrays
swfinput.c	1,535	input file
nrutil.c	3,706	†
realft.c	1,006	†
smooft.c	739	†
smooth.c	592	histogram smoothing routine
sh_hst.c	2,986	display program of output histogram
switch.c	11,466	analysis program for switching frequency

\* (in bytes)

† (from *Numerical Recipes in C*)

**Table 8. File list related to PIDV motion analysis**

File Name	File Size*	Remarks
imageflo.c	22,625	main program
centroid.c	3,346	centroid search program
chkerfrm.c	692	program to check error frame LUT
corresp.c	4,453	correspondence checking routine
corresp0.c	11,631	
corresp1.c	923	
corresp2.c	3,383	
datin3d.c	2,019	input file
distan1.c	684	distance between bubbles in an image plane
distan2.c	684	distance between bubbles in an image plane
enhanim.c	2,519	image enhancement algorithm
filename.c	643	a routine generating file name
group.c	539	a routine to check grouping of bubbles
grp.avg.c	949	a routine to solve for the average X or Y location in the same group
g_trans.c	2,043	transformation from 2-D to 3-D
lubksb.c	373	back substitution routine <sup>†</sup>
ludcmp.c	1,114	LU-decomposition routine <sup>†</sup>
match.c	5,813	matching algorithm
m1_coef.c	3,803	a routine for a corresponding line
m2_coef.c	3,803	
nrutil.c	3,497	†
reinit.c	2,109	initializing arrays in the program
renum.c	7,127	bubble element numbering routine
thdval.c	485	a routine for threshold value
thrshold.c	1,322	
vel_inst.c	1,733	a routine for instantaneous velocity
vel_avg.c	1,853	a routine to retrieve the lost bubble information
vthrd.c	838	a routine for varying threshold value

\* (in bytes)

: † (from *Numerical Recipes in C*)

Table 9. Some statistics from flow visualization results.  
 $U_{ref} = 9.07 \text{ cm/s}$ , ( $Re_\theta = 330$ )

Fraction of a backflow mode ( $\gamma_b$ ) <sup>†</sup>	$0.78 \pm 0.23$
Strouhal number ( $St_T$ ) <sup>†</sup>	$0.28 \pm 0.07$
Average lapse time between the formation of the same events	$4.26 \pm 0.39(\text{sec})$
Average duration time of a primary vortex before the separation vortex forms	$0.85 \pm 0.08(\text{sec})$
Average total time for "leap-frogging" process to occur	$1.87 \pm 0.16(\text{sec})$

<sup>†</sup>(estimated at  $X/T = -0.125$ )

**Table 10. Comparison of dimensionless frequency groups obtained by other studies**

	present study		Devenport and Simpson (1990a)	Ölçmen <i>et al.</i> (1991)	Hasan Casarella Rood (1985)
$Re_\theta$	330	1,100	6,700	4,450	6,560
$\delta/T$	0.283	0.190	0.502	0.261	0.5
$St_{v.s.} = \frac{f}{(\frac{\delta}{T})_{v.s.}}$	0.068	0.08	0.02 (0.048)*	0.03	0.0032 – 0.032
$St_T = \frac{fT}{U_{ref}}$	0.34	0.40	0.10 (0.24)*	0.15	0.016 – 0.16
$St_\delta = \frac{f\delta}{U_{ref}}$	0.096	0.076	0.05 (0.12)*	0.039	0.008 – 0.08

\* (most probable value)

## FIGURES

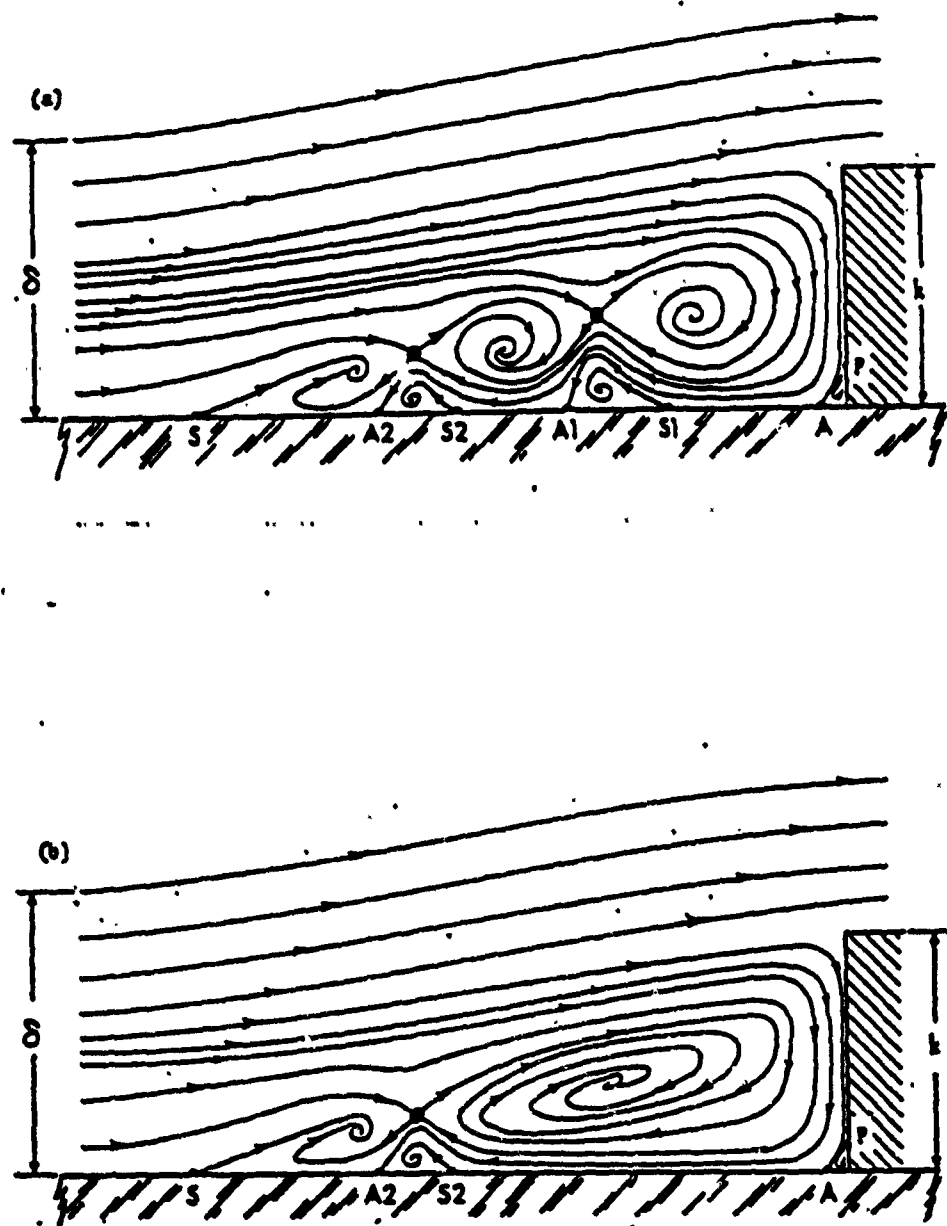


**Figure 1.** Streamline patterns in the plane of symmetry of small obstacle separated flow showing (a) six vortex system and (b) four vortex system. S, separation line ; A, attachment line ; k, height of the obstacle;  $\delta$ , oncoming boundary layer thickness (from Sedney and Kitchens (1975))

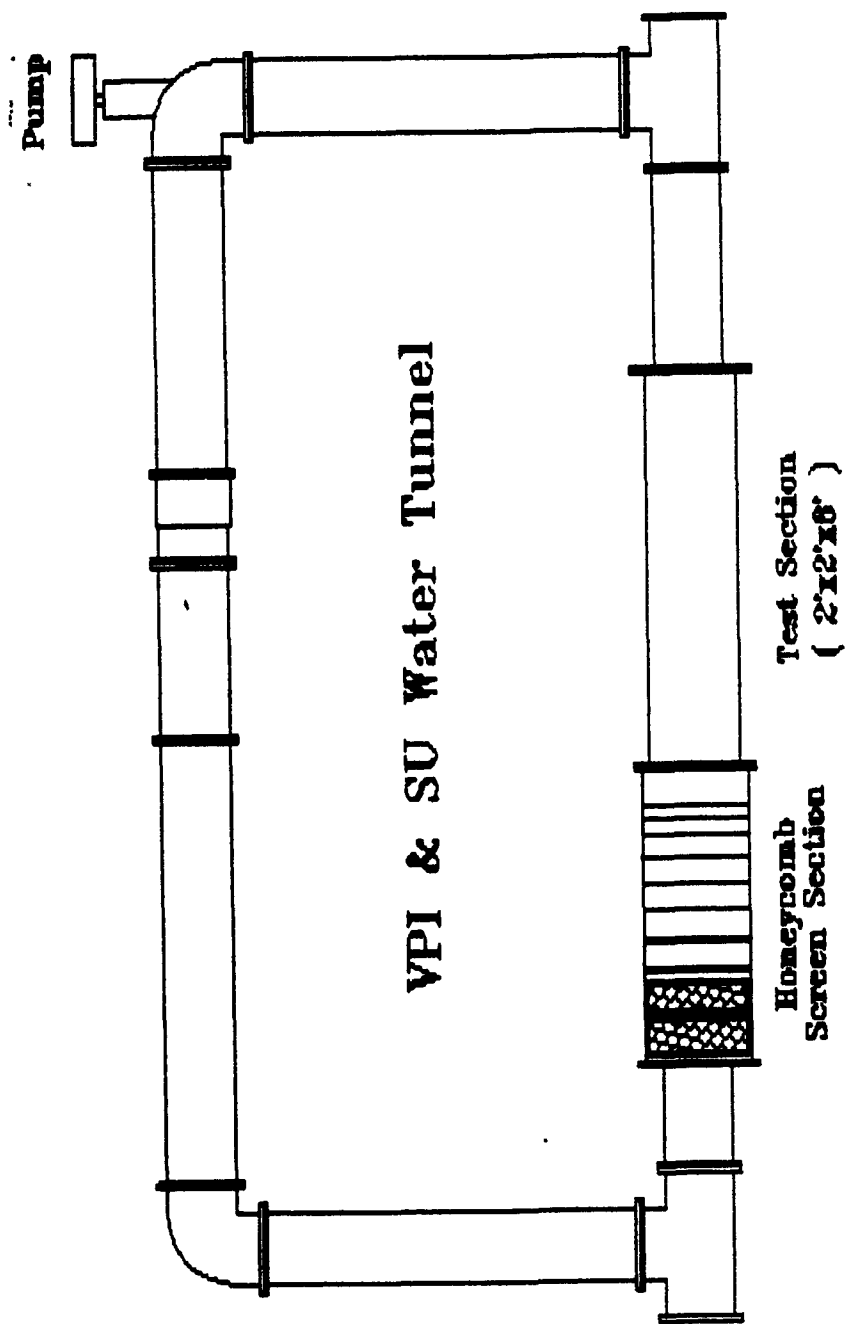
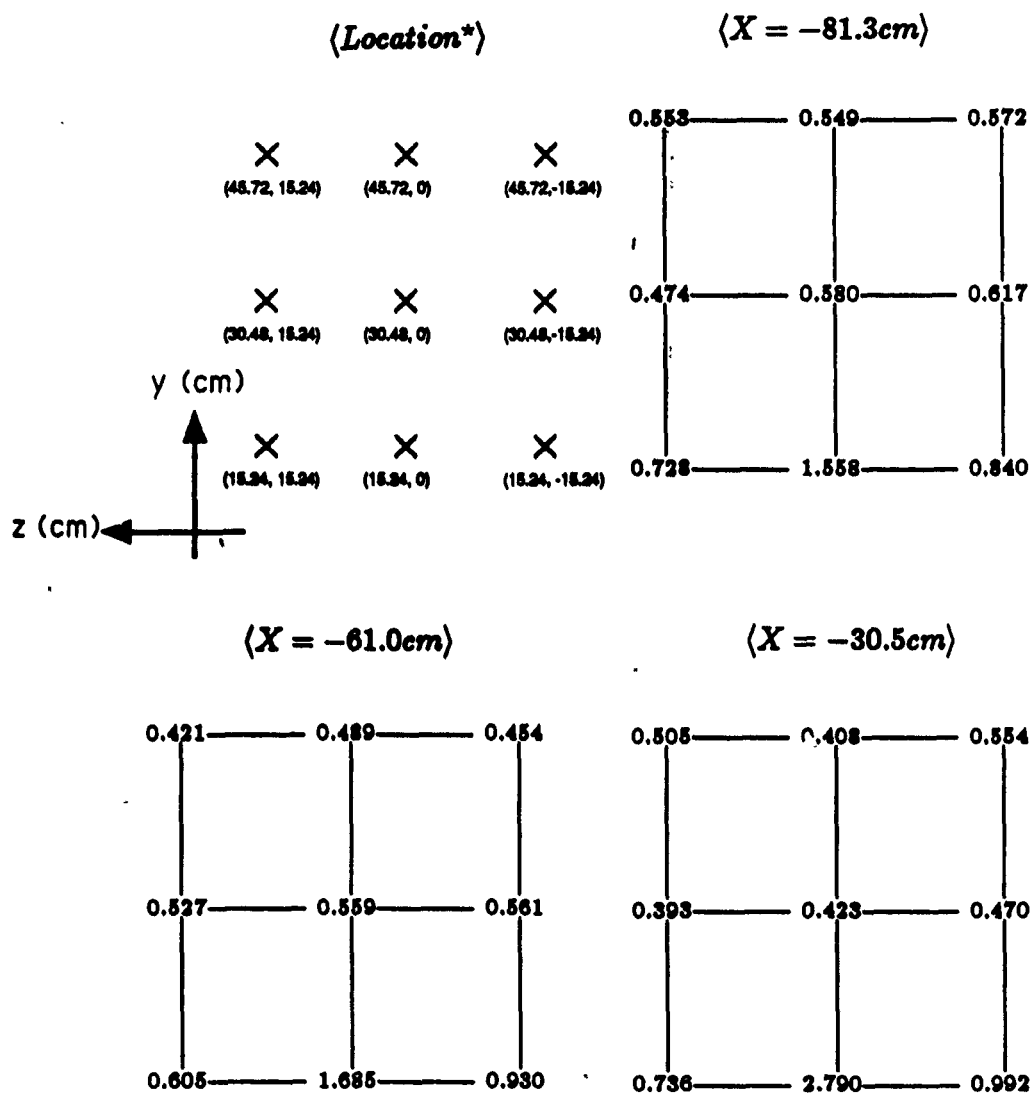
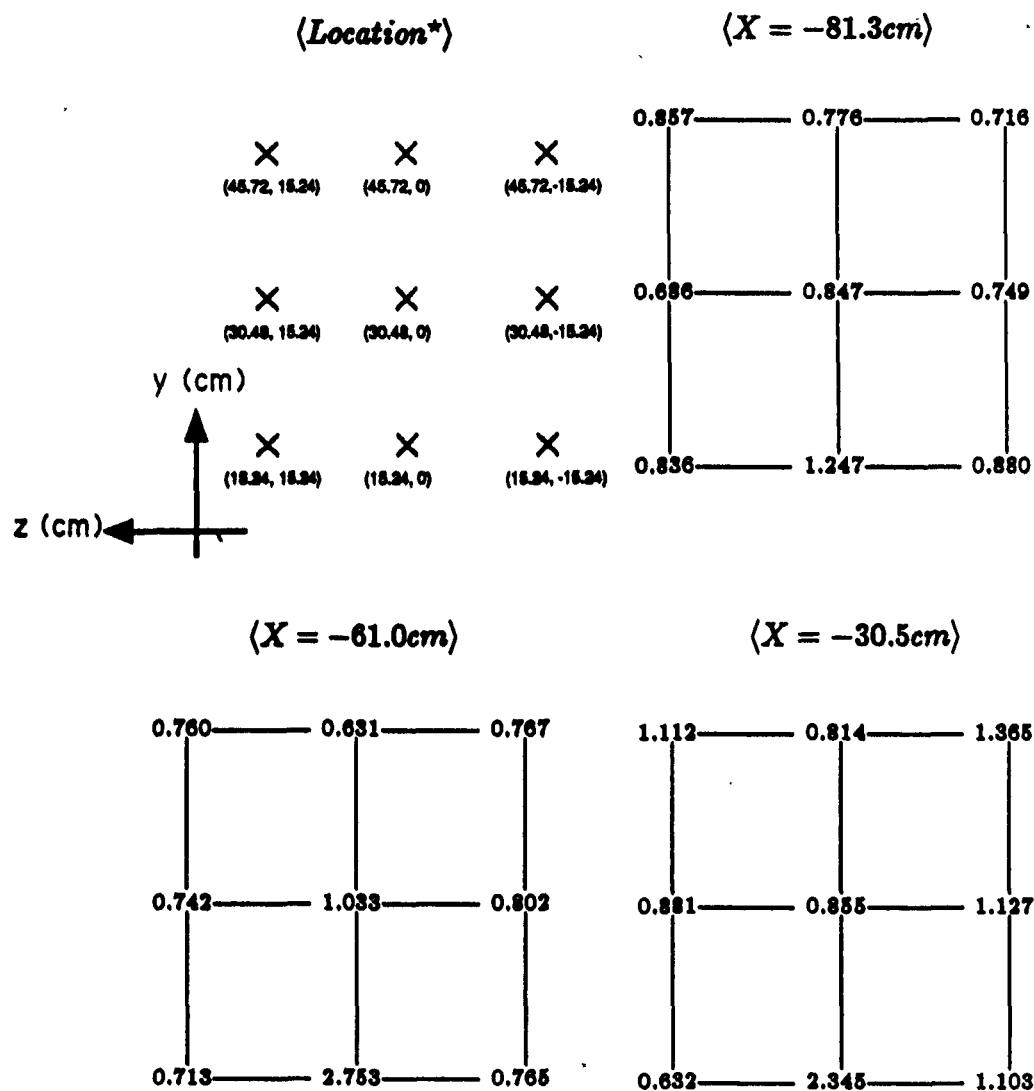


Figure 2. The water tunnel facility





**Figure 3(a).** Hot film measurements for the turbulence level(% of  $U_{ref}$ ) in the test section with a wing-body junction model mounted for low speed case : \* (looking upstream).  $(X, Y, Z)$  coordinate uses a right-handed system with origin at the corner between leading edge of the wing and false wall.



**Figure 3(b).** Concluded — high speed case

# *Plexiglas water tunnel model*

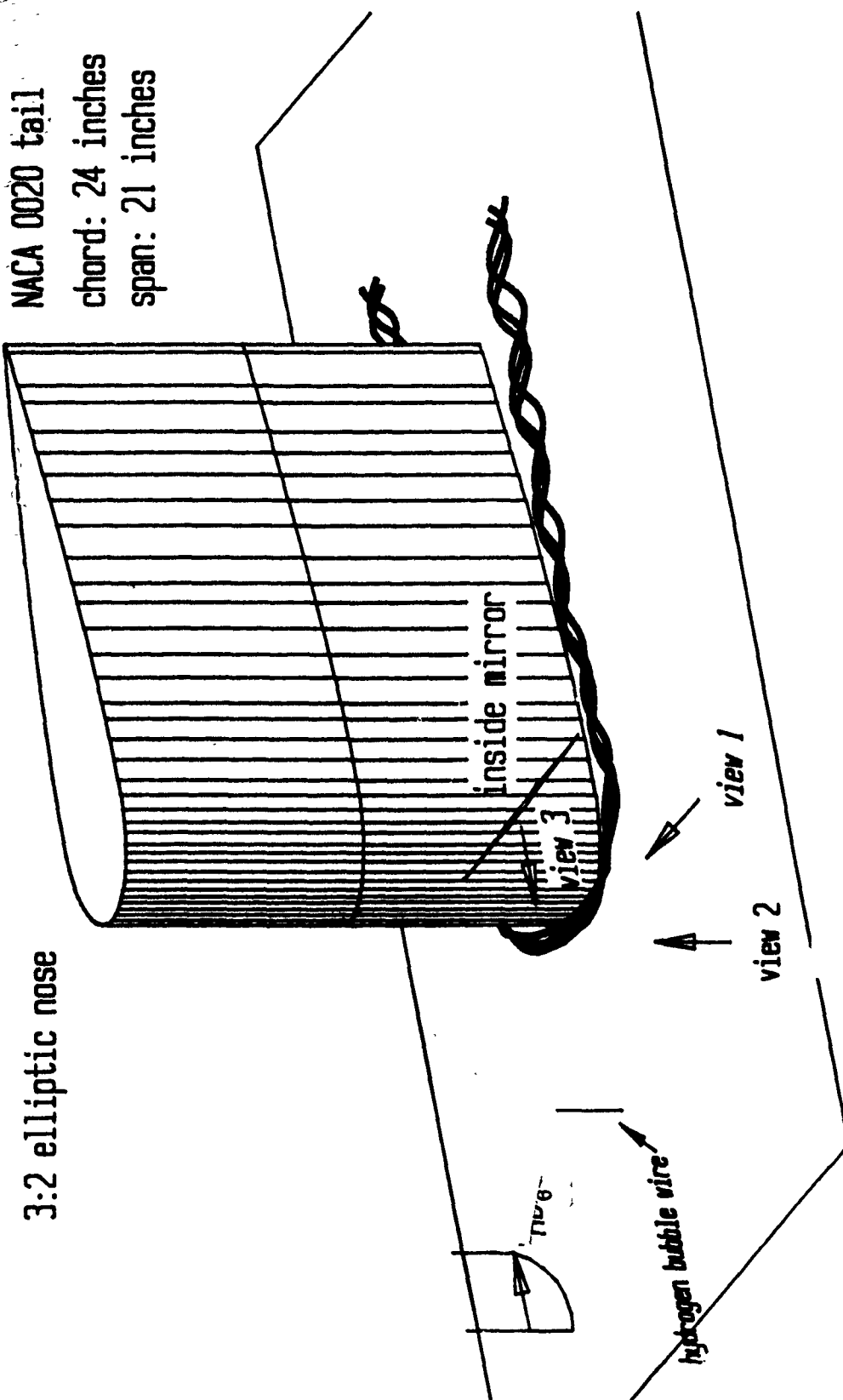


**Figure 4.(a).** General description of flow model

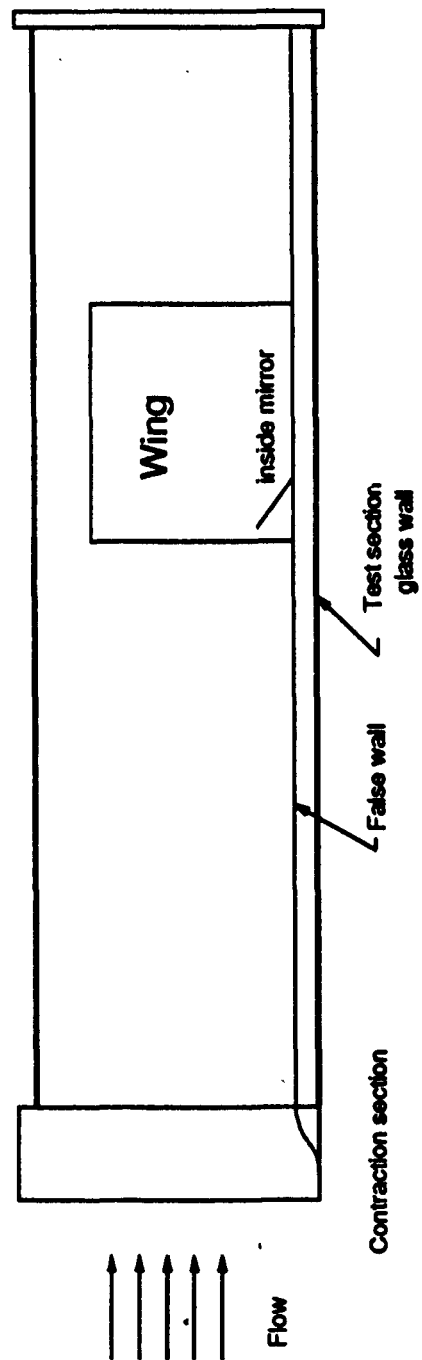


Figure 4.(b).Schematic diagram of the test model setup

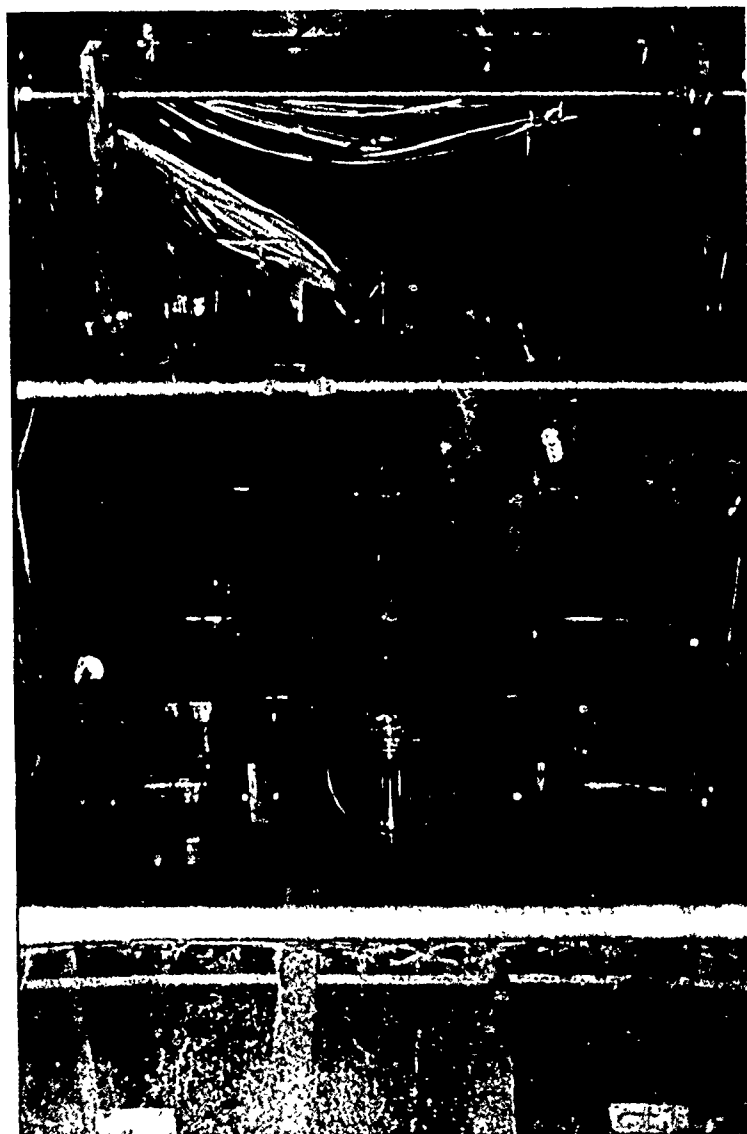


Figure 4(c). Assembled wing-body junction model in the test section

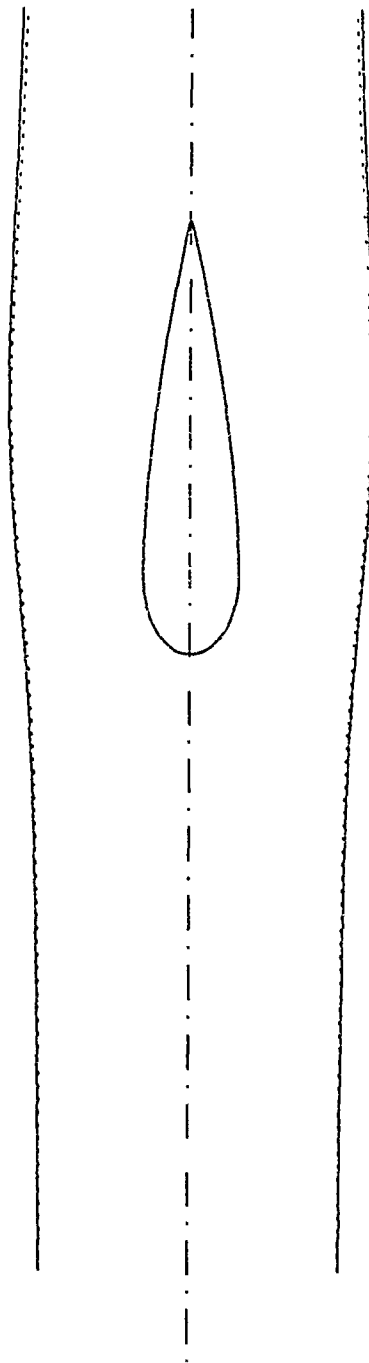


Figure 5. Side wall location with boundary layer displacement thickness correction

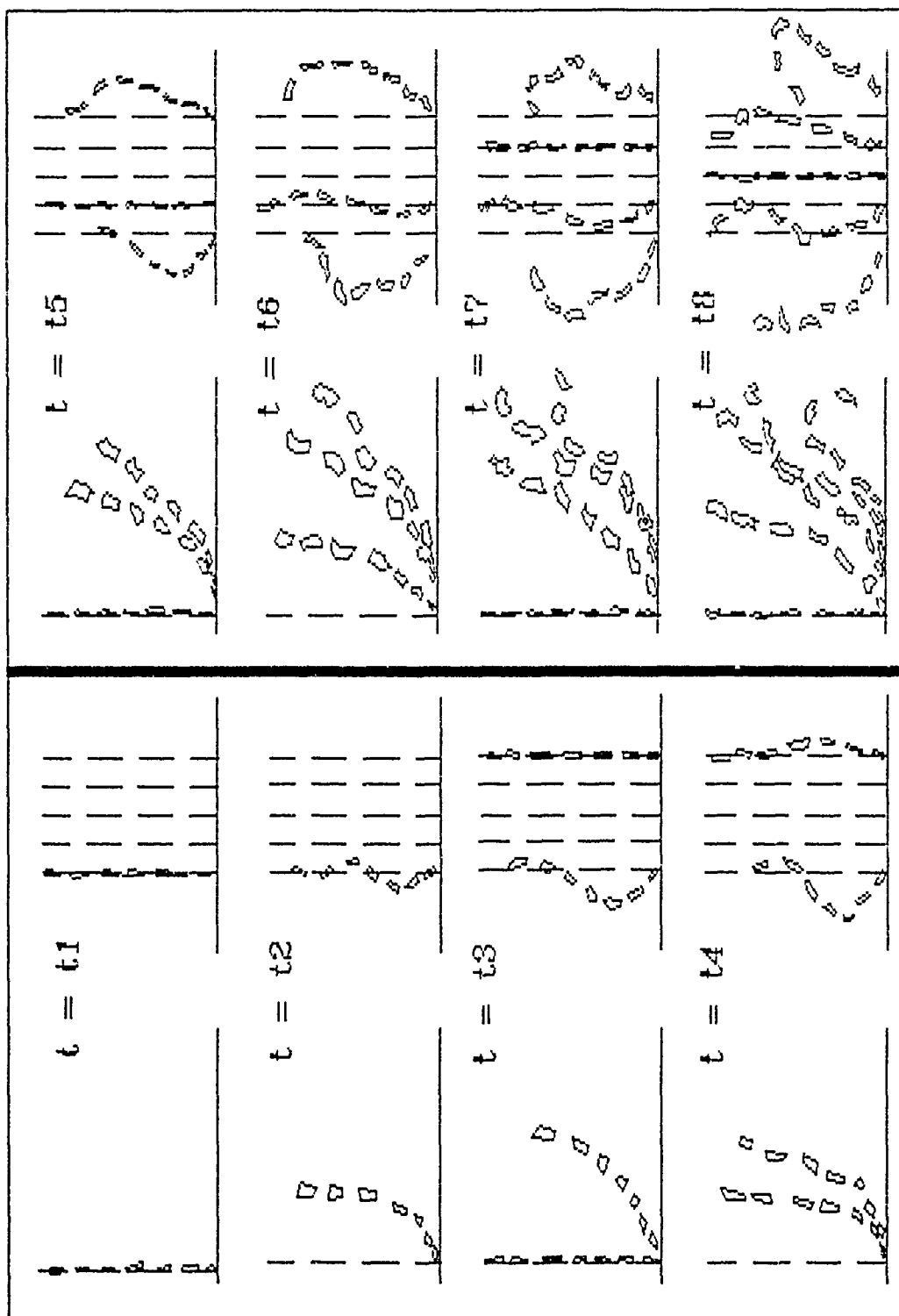
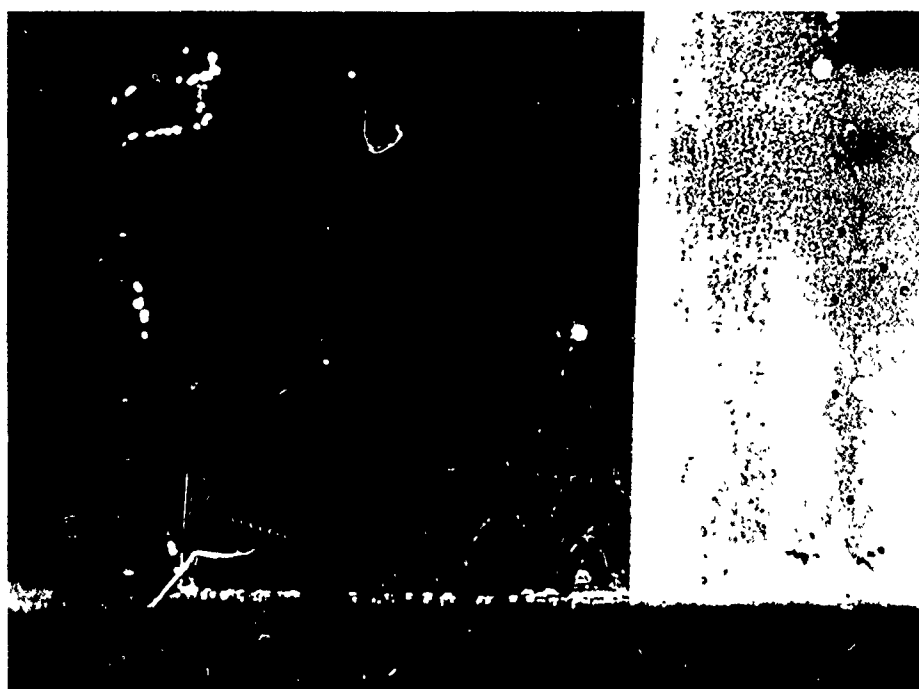


Figure 6. Schematic diagram for the hydrogen bubble generation sequence in the upstream view



(a) Conventional time-line method



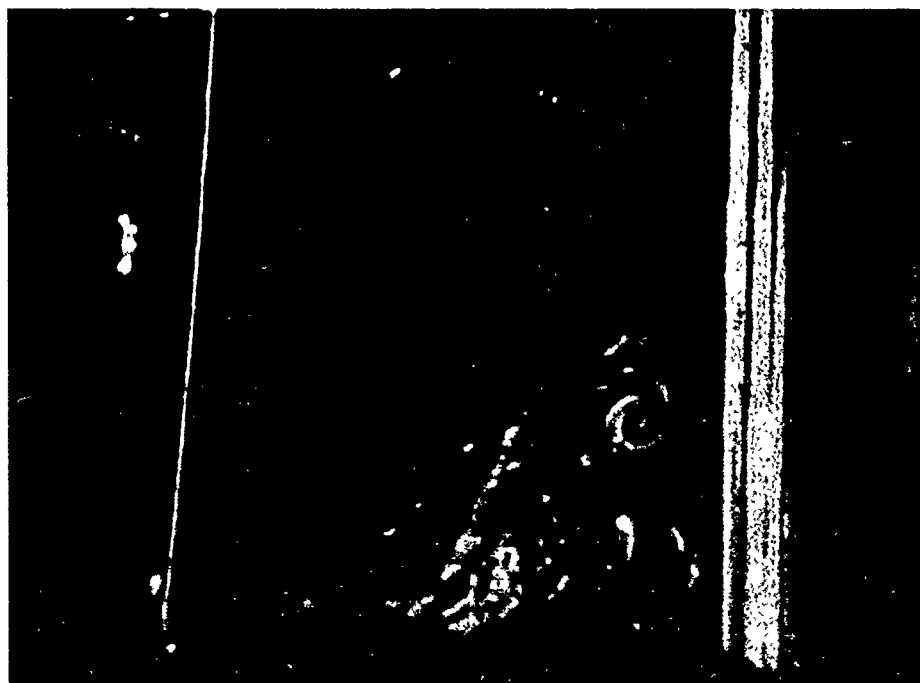
(b) Continuous sheet method

**Figure 7.** Examples of hydrogen bubble techniques





(c) Combined time-streak marker



(d) Inverted time-line method

Figure 7. Concluded

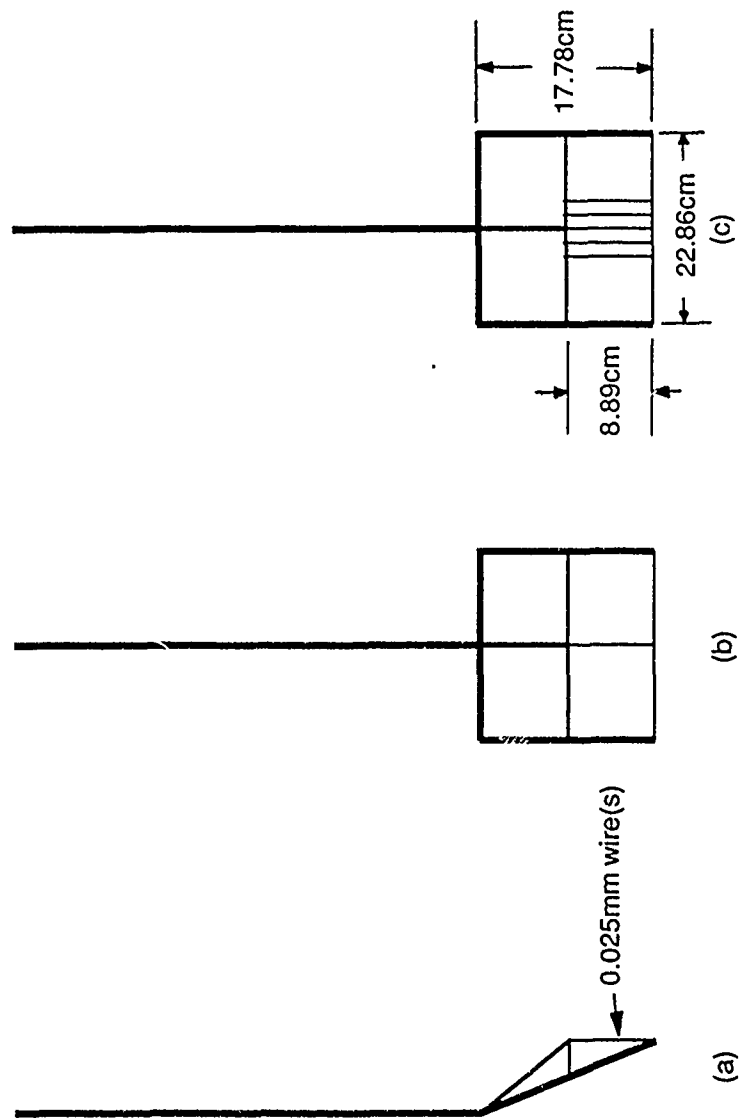


Figure 8. Hydrogen bubble probe

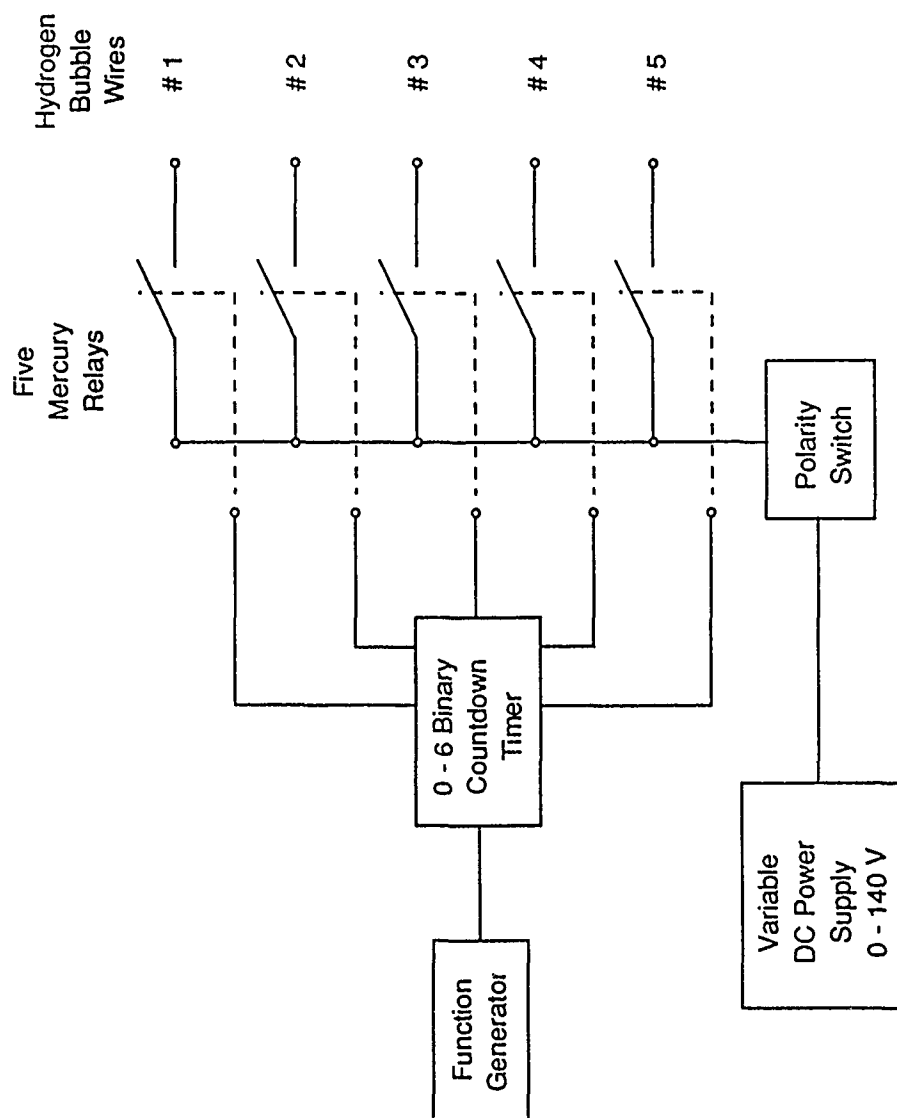


Figure 9.(a). Schematic diagram of hydrogen bubble generator circuit

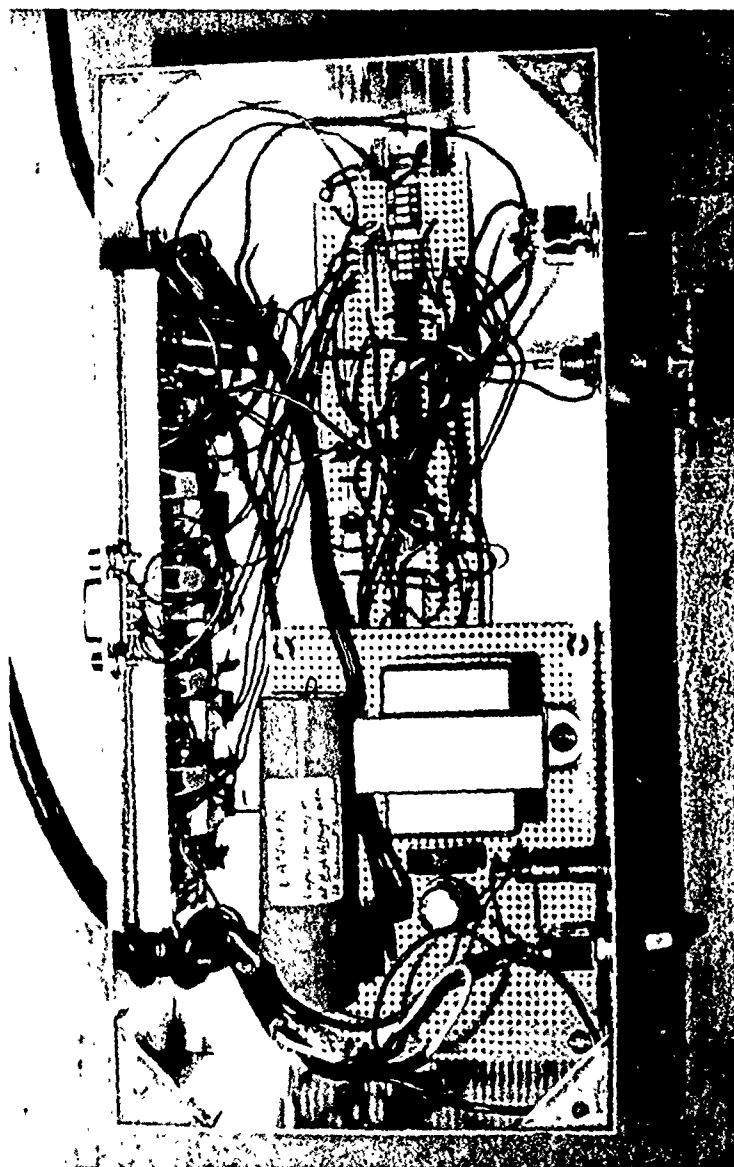


Figure 9.(b). Hydrogen bubble generator circuit

**THIS  
PAGE  
IS  
MISSING  
IN  
ORIGINAL  
DOCUMENT**

## LDV Optics and Data Acquisition System

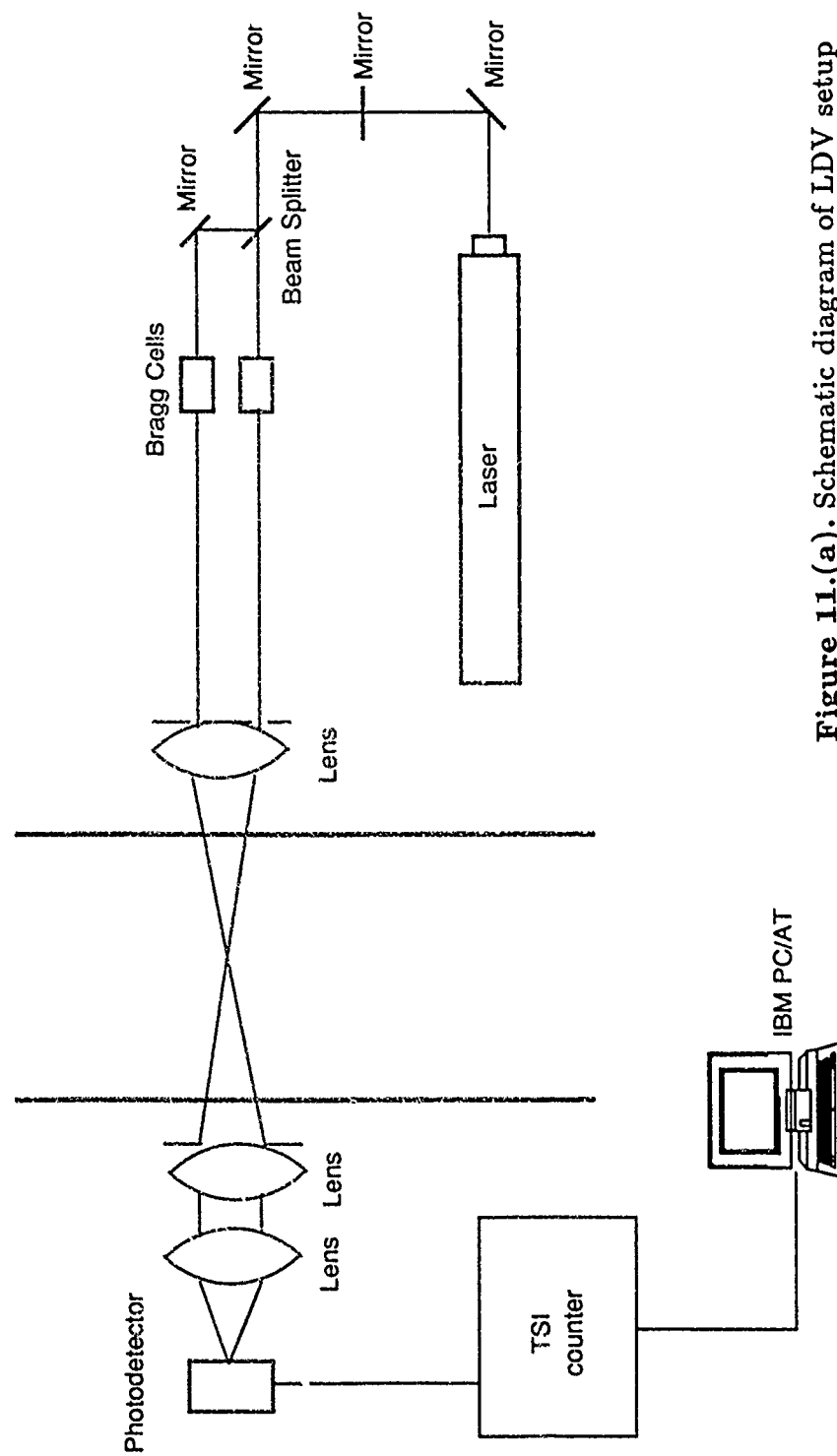


Figure 11.(a). Schematic diagram of LDV setup

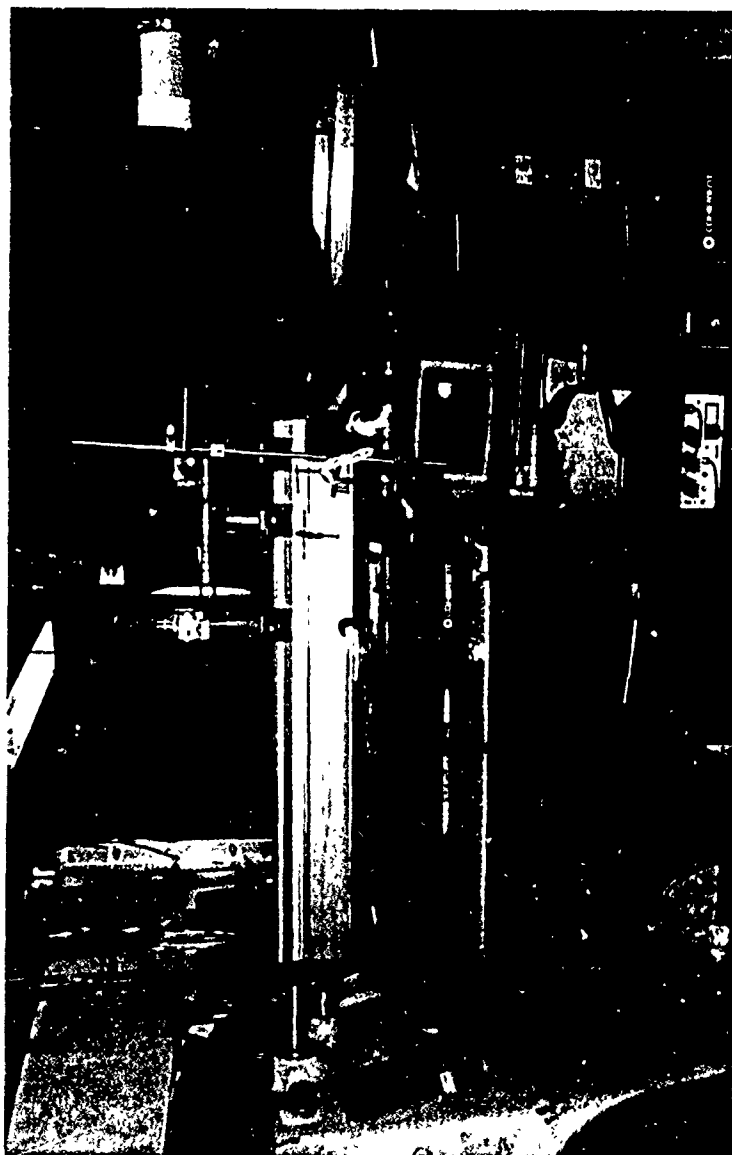


Figure 11.(b). LDV setup

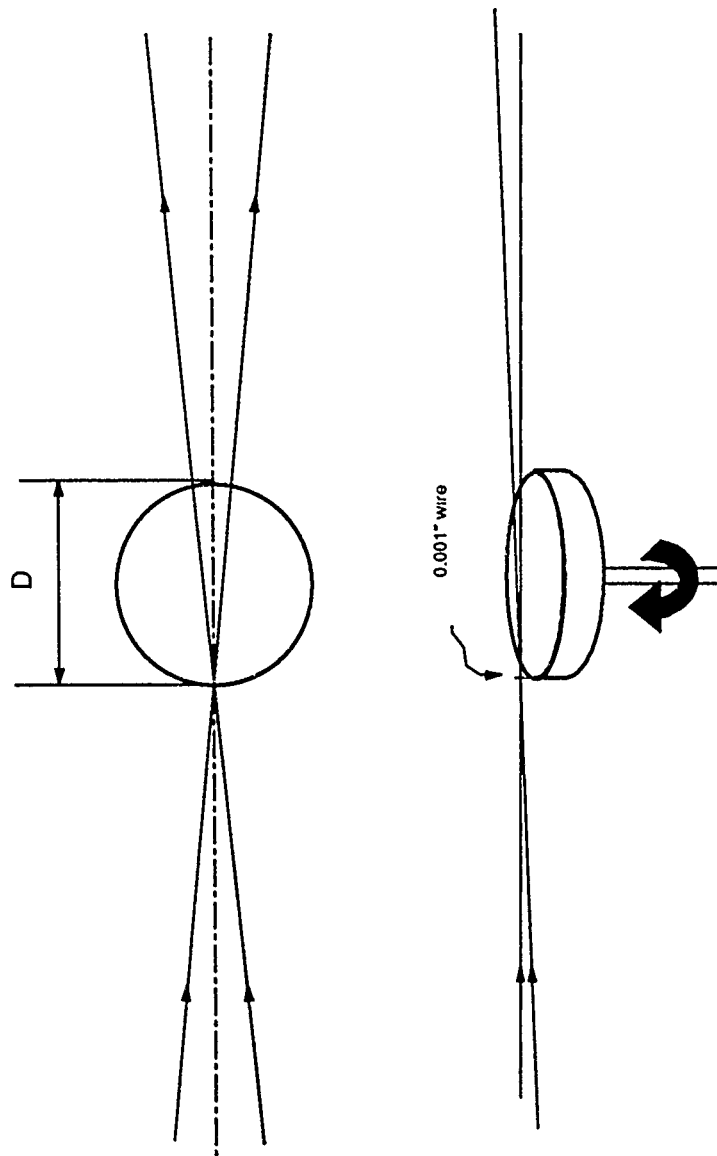


Figure 12. Fringe spacing measurement device



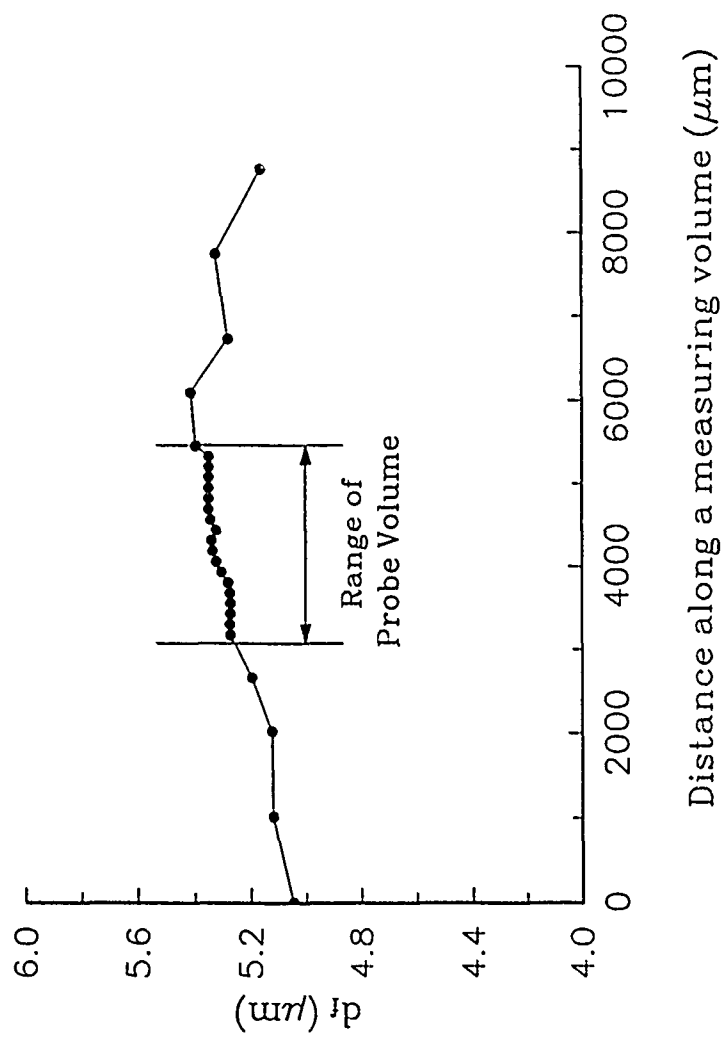
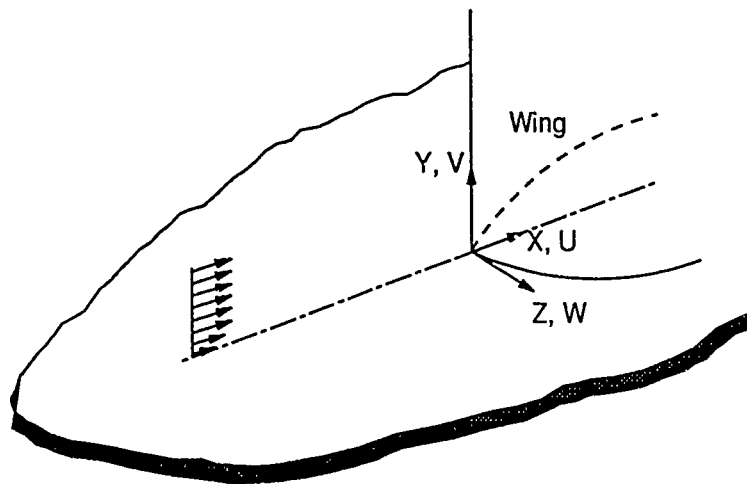
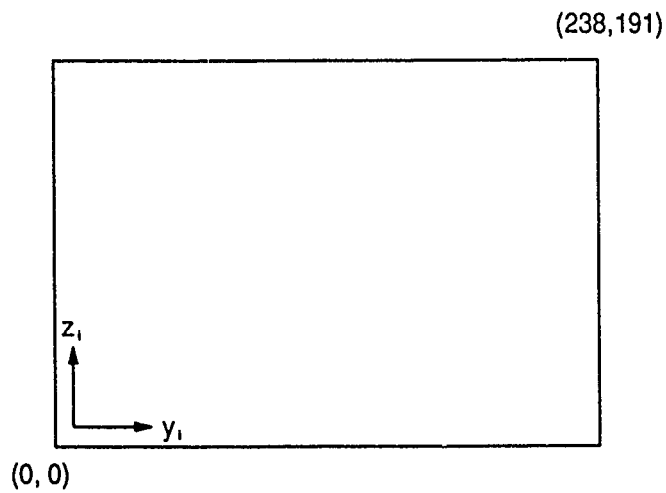


Figure 13. Fringe spacing measurement across the probe volume

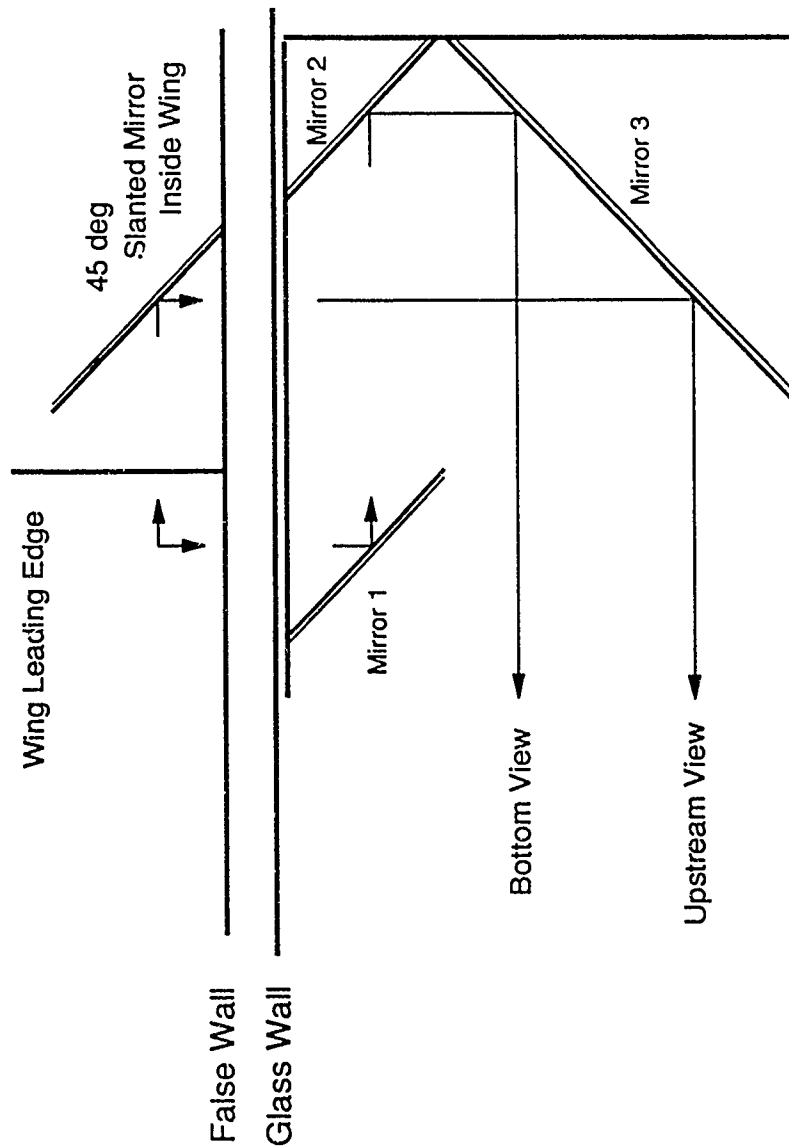


(a) Global coordinate system



(b) Image plane coordinate system

**Figure 14.** Coordinate system



< Mirror Box >

Figure 15. Mirror arrangement for the upstream and bottom views in one imager plane

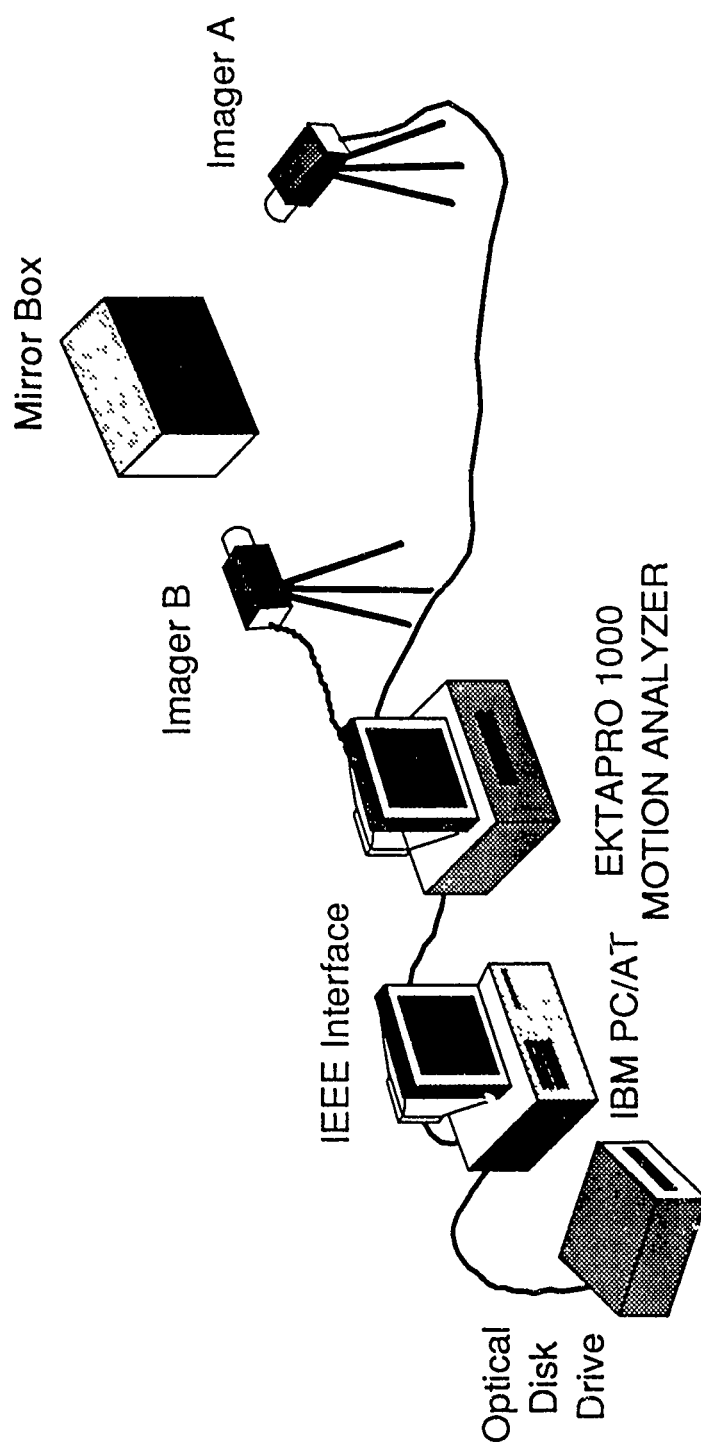


Figure 16.(a). Image capturing system setup for Kodak Ektapro 1000 motion analyzer

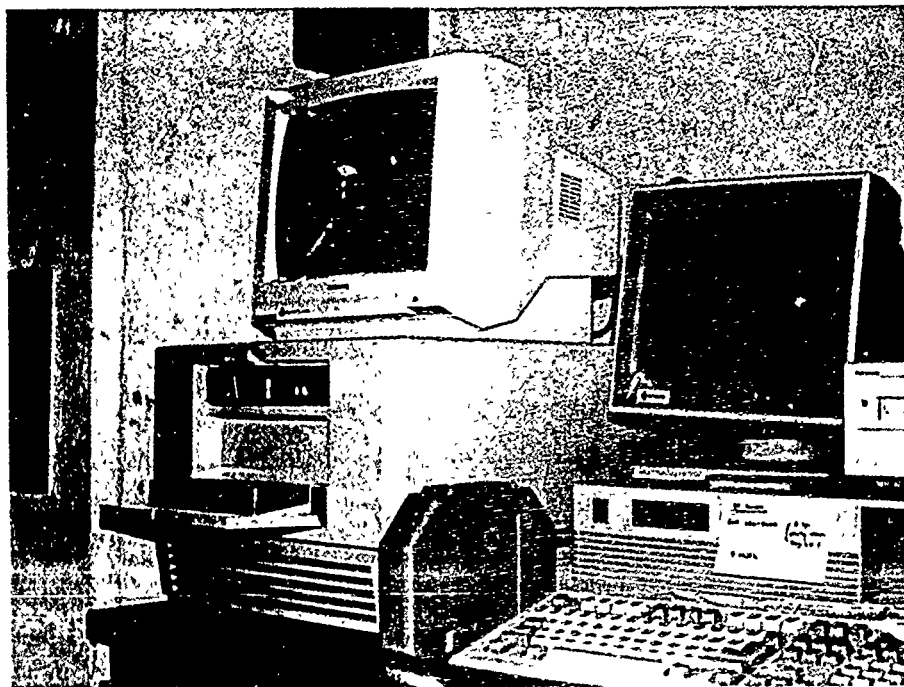


Figure 16.(b). Ektapro 1000 motion analyzer system

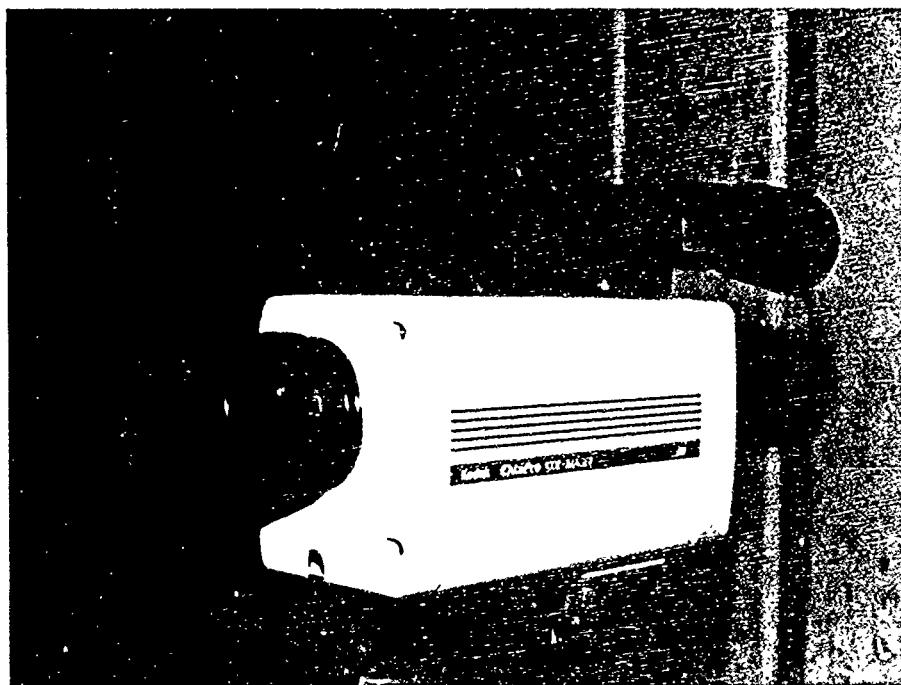


Figure 16.(c). High intensity camera

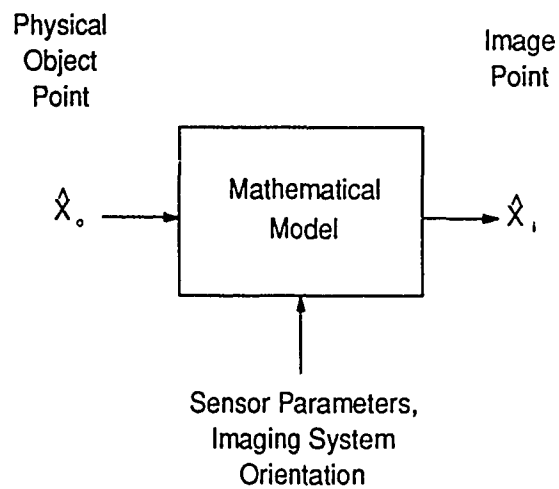


Figure 17.(a). Mathematical model relating 3-D object points to image points

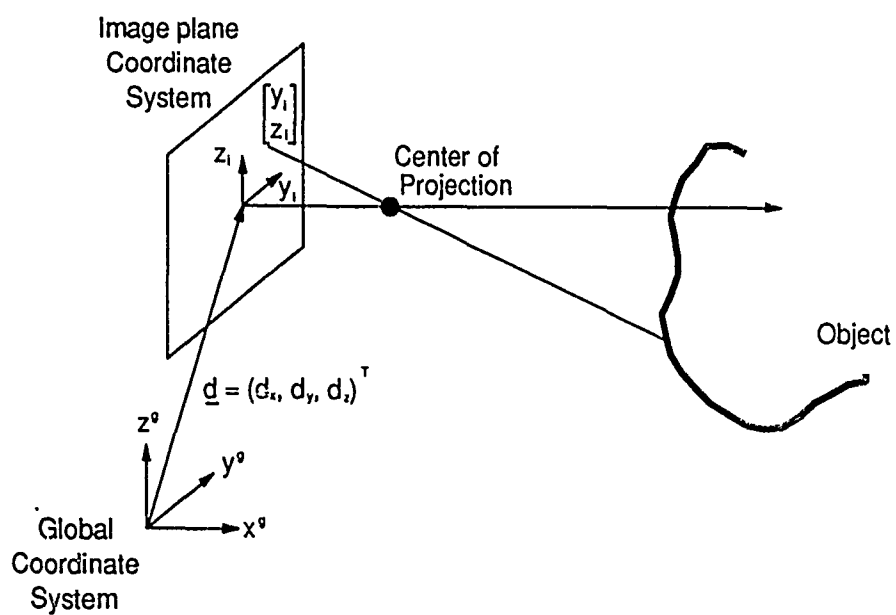


Figure 17.(b). Generalized pinhole camera model

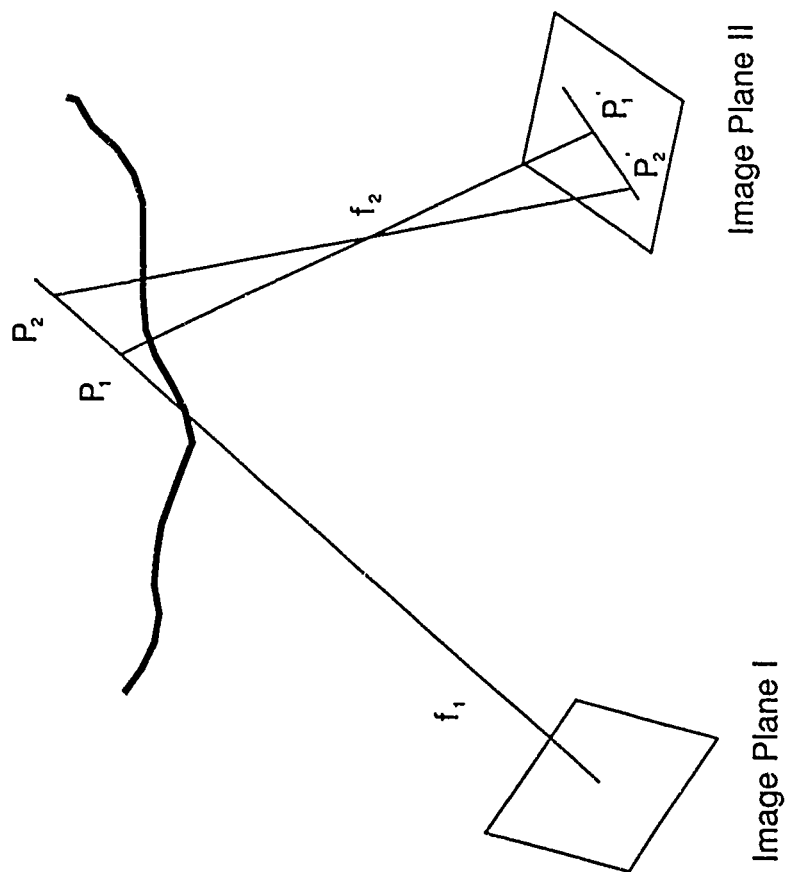
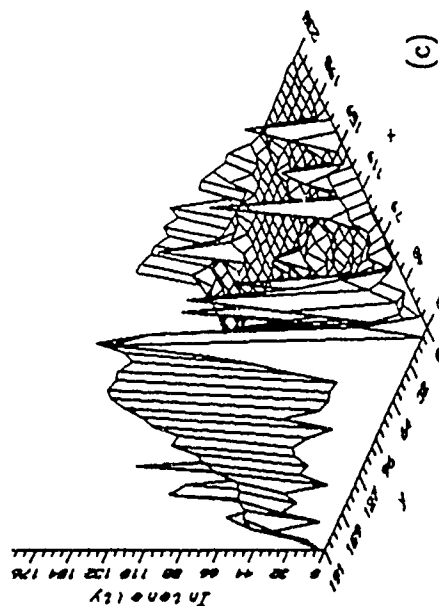
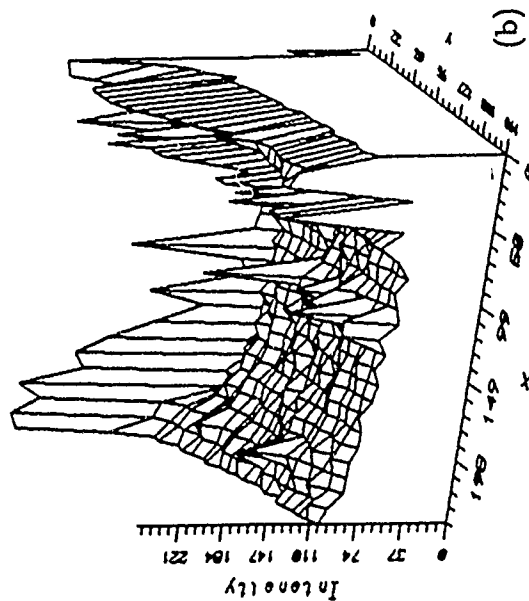
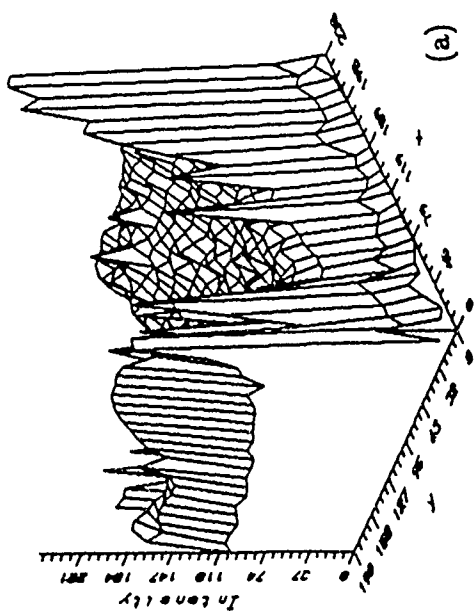


Figure 18. Stereo vision



- (a) Original image function
- (b) Rotated image function
- (c) Background subtraction

Figure 19. Effect of the background subtraction



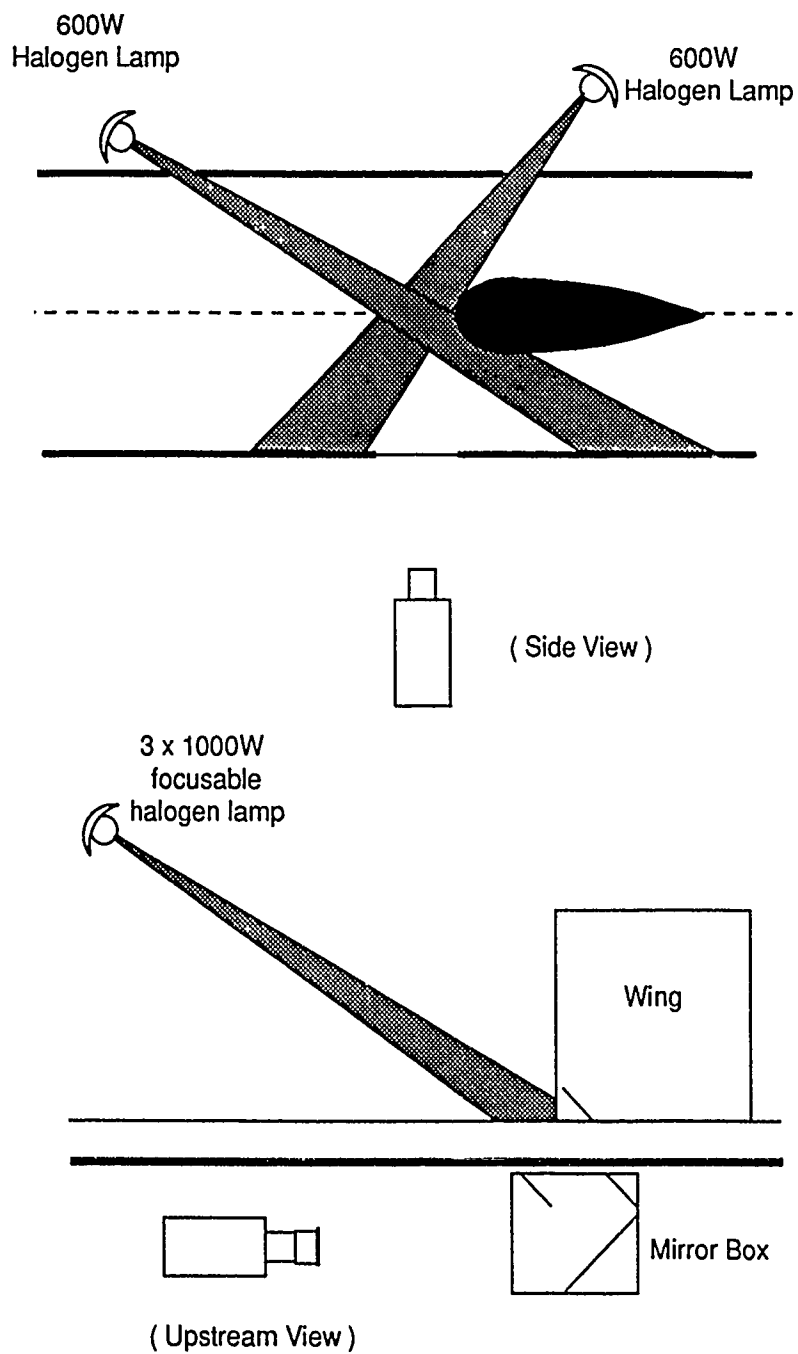
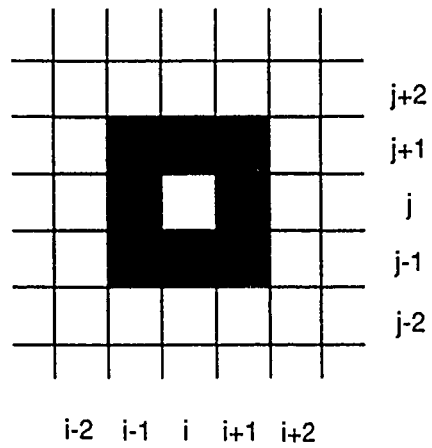
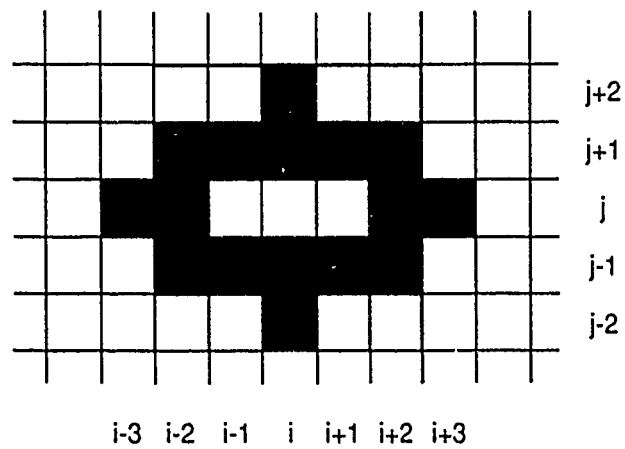


Figure 10. Lighting setup

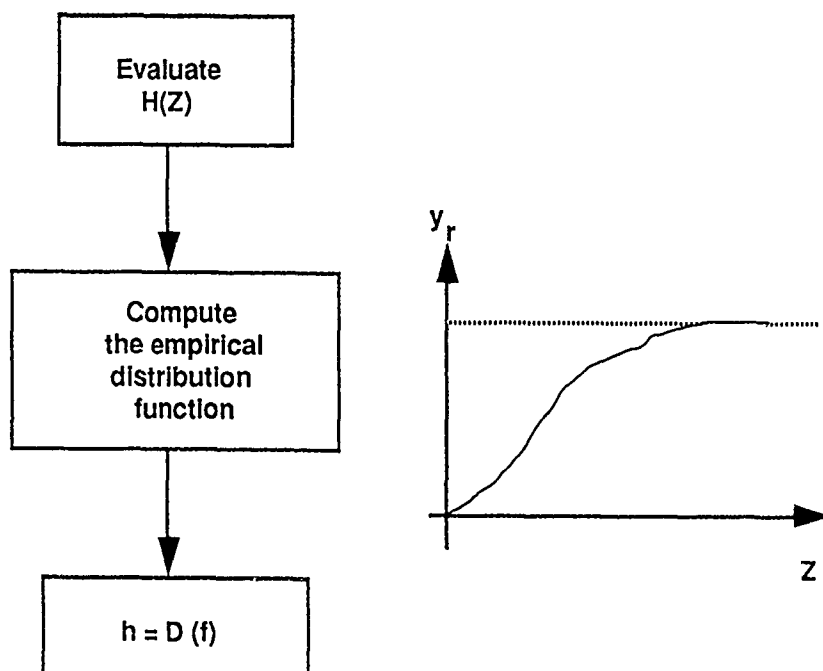


(a) 8 point window



(b) 16 point window

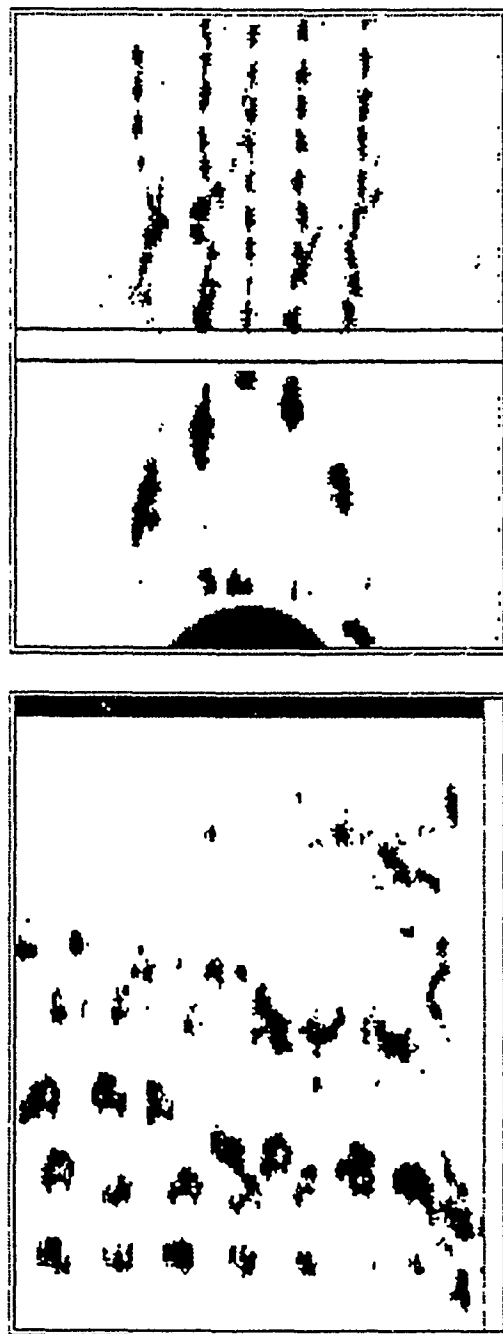
Figure 20. Windows for local averaging technique



$$\text{where } D = \text{Int} \left( R \frac{(y - y_{\min})}{(y_{\max} - y_{\min})} + 0.5 \right)$$

$R$  is the range of the gray level  
 $y$  is the relative frequency  
 $D$  is the scaling operator.

Figure 21. Algorithm for histogram equalization technique



< BottomView >

< SideView >

Figure 22. Examples of bilevel images

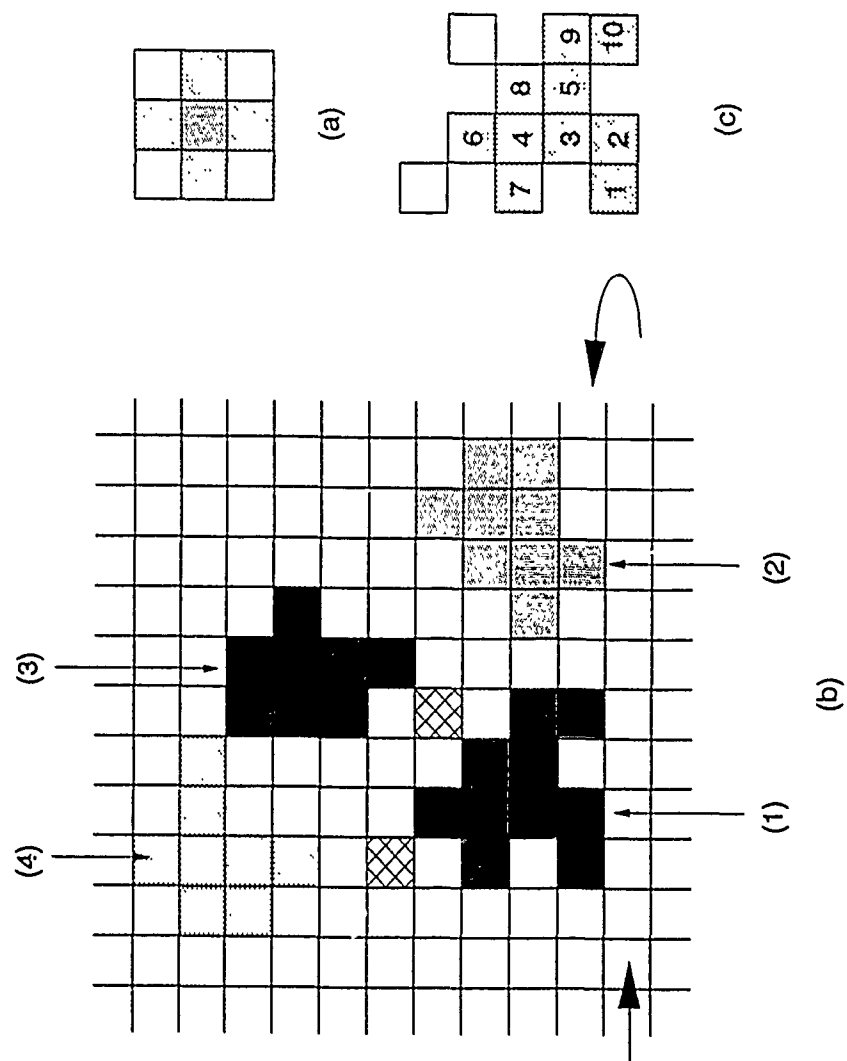


Figure 23. Identification of the bubble elements for centroid search

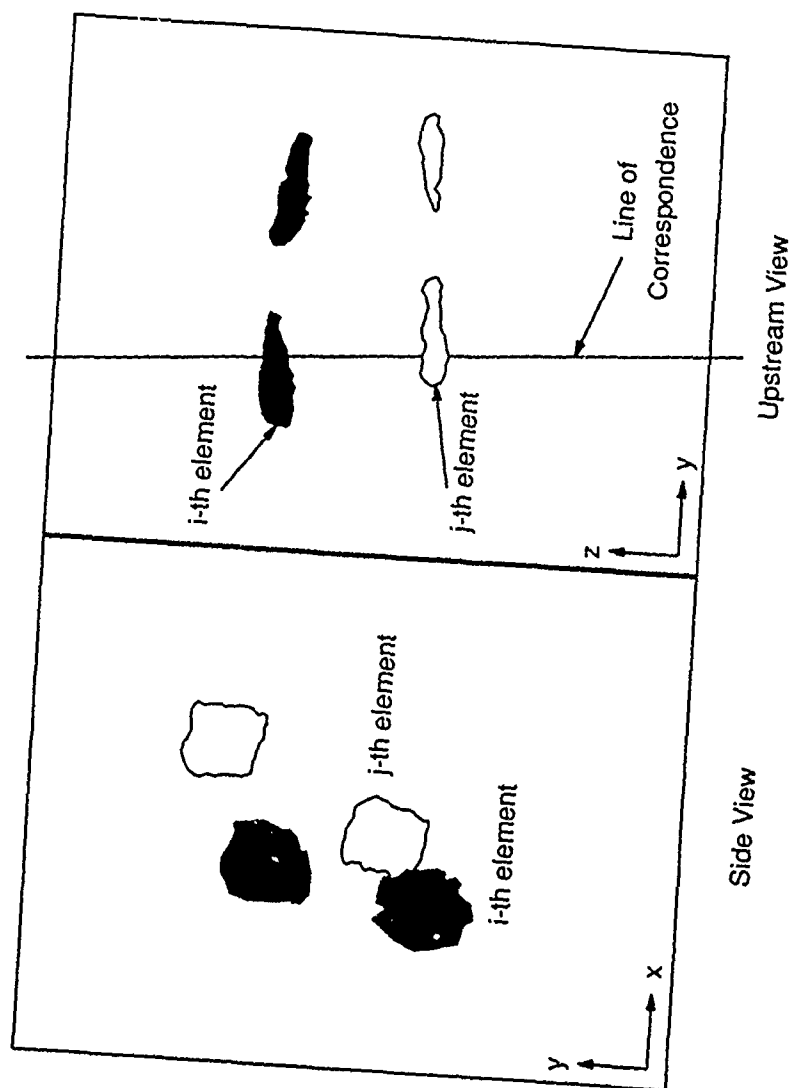


Figure 24. Bubble overlapping problem

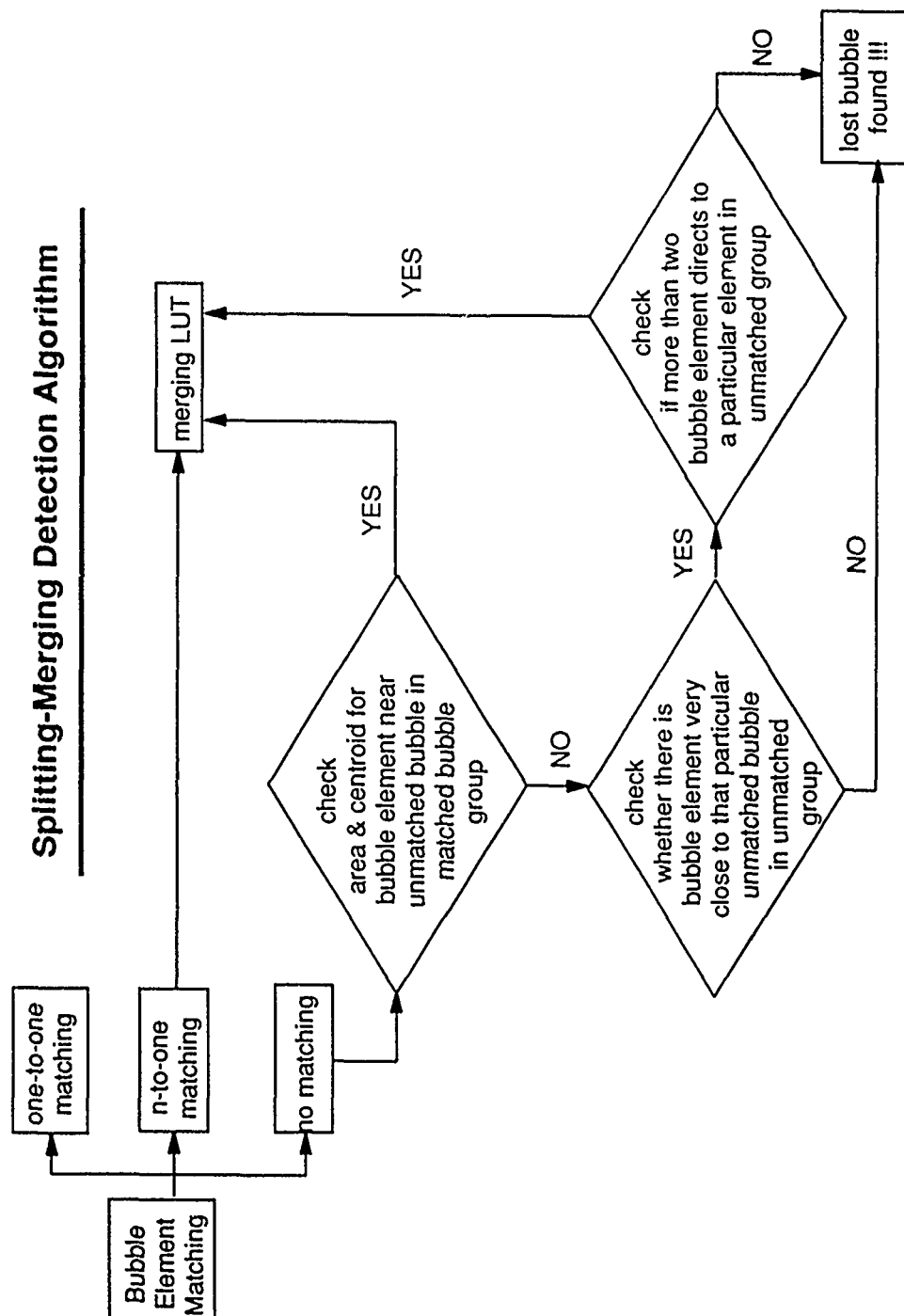


Figure 25. Algorithm for the detection of the split-merging bubbles

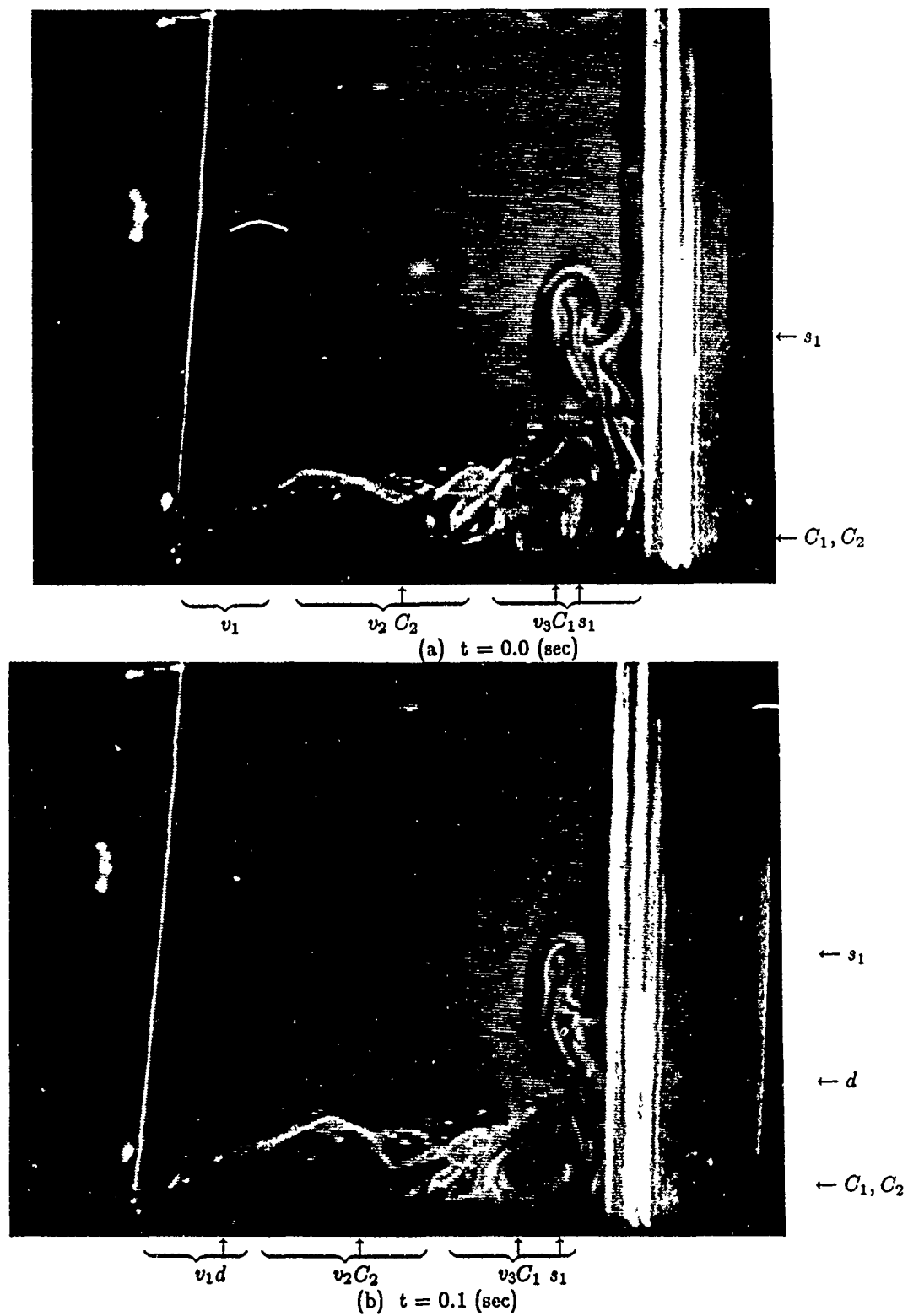
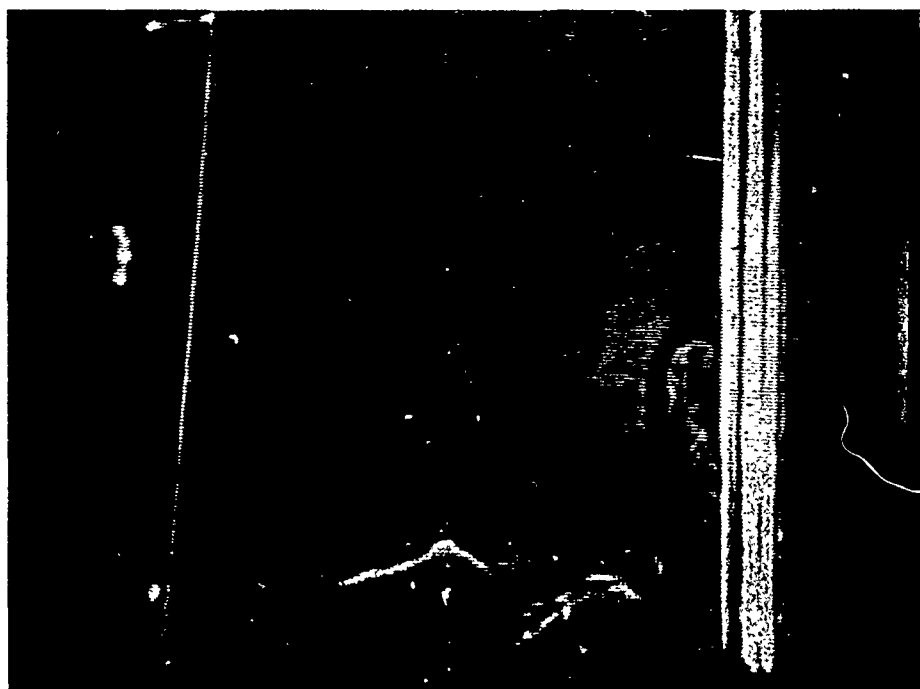


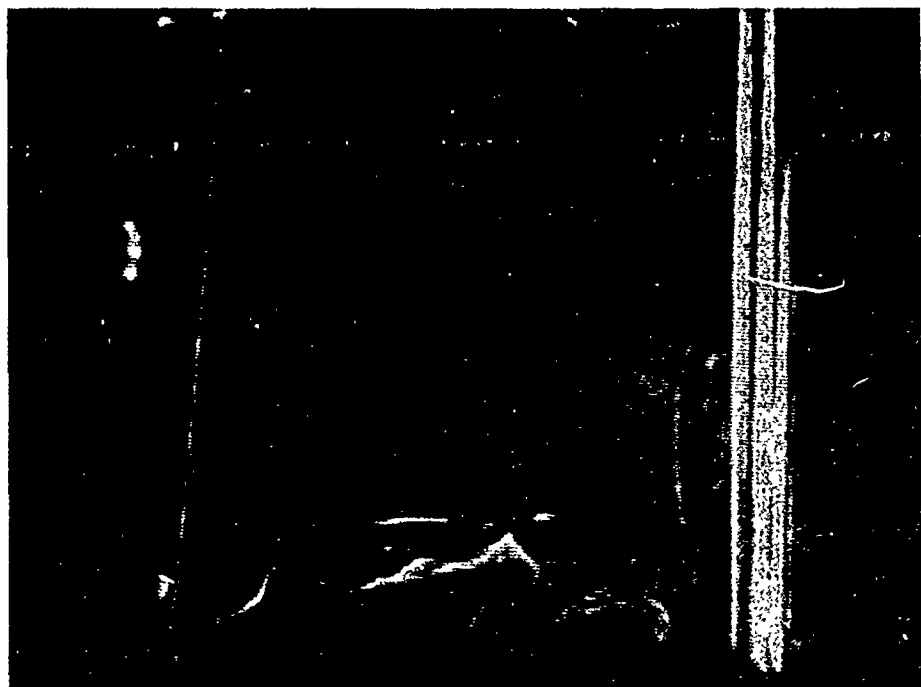
Figure 26. Sequence of the flow upstream of the nose of a wing-body junction : an inverted hydrogen bubble time-line.





$\underbrace{\quad}_{v_1}$ 
 $\underbrace{\quad}_{v_2 C_2}$ 
 $\underbrace{\quad}_{C_1 v_3}$ 
 $\underbrace{\quad}_{s_1}$

(c)  $t = 0.2$  (sec)



$\underbrace{\quad}_{v_1}$ 
 $\underbrace{\quad}_{d}$ 
 $\underbrace{\quad}_{v_2 C_2}$ 
 $\underbrace{\quad}_{C_1 v_3}$ 
 $\underbrace{\quad}_{s_1}$

(d)  $t = 0.3$  (sec)

Figure 26. Continued

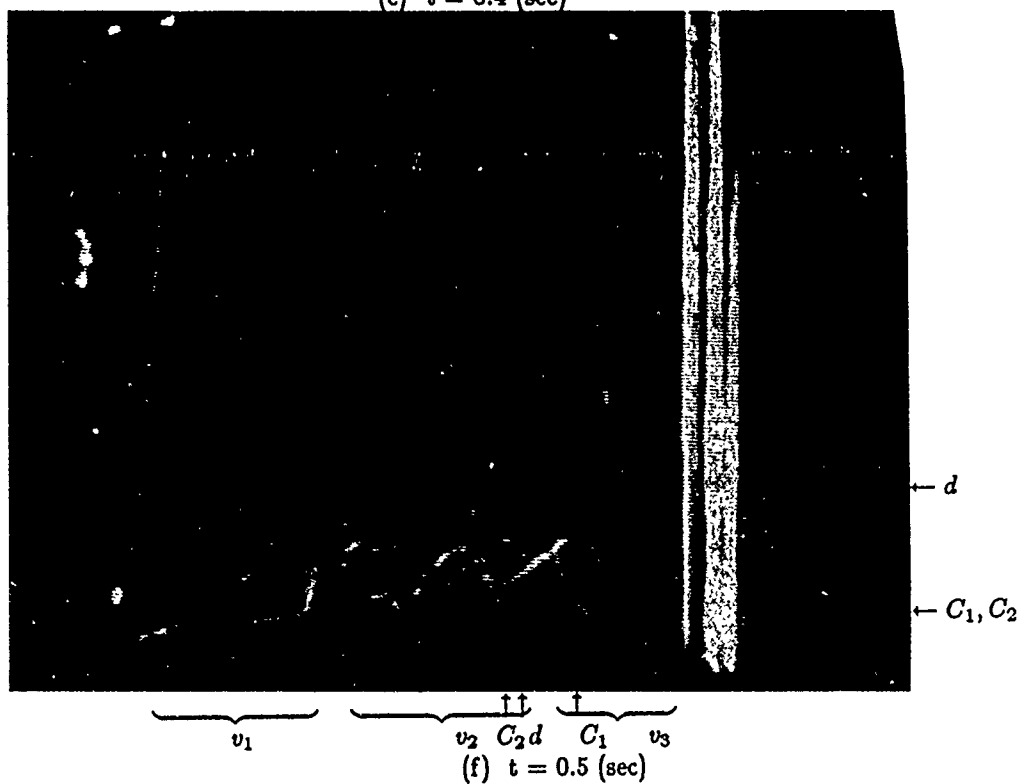
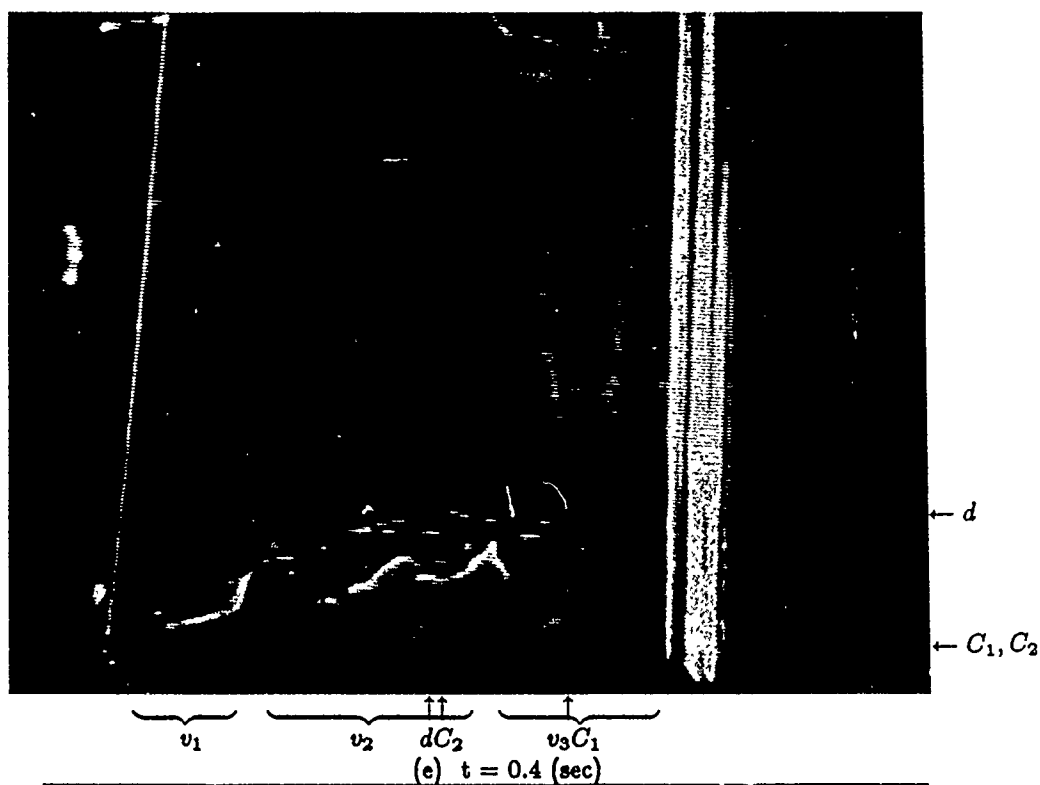


Figure 26. Continued

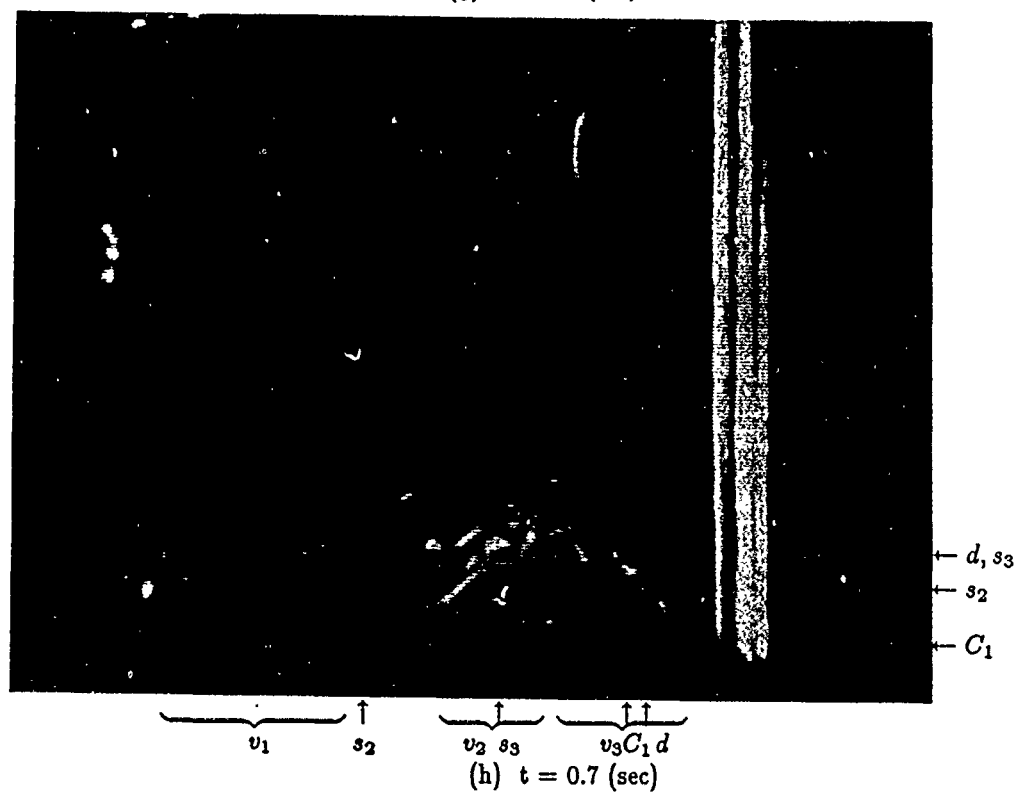
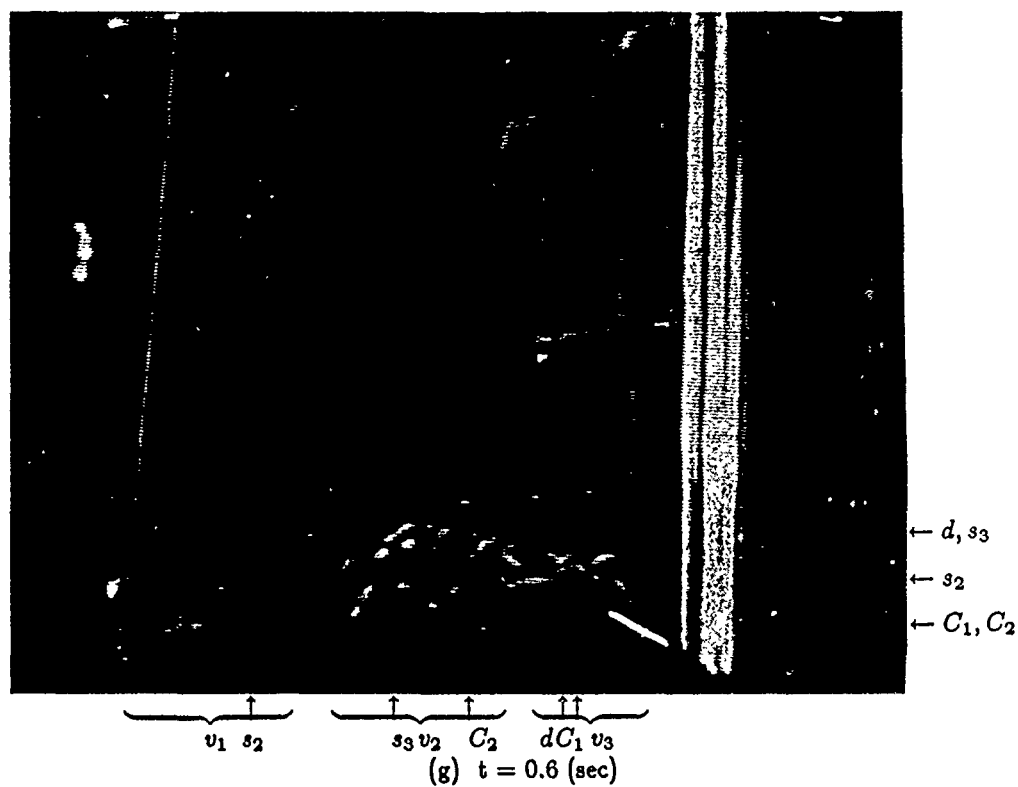


Figure 26. Continued

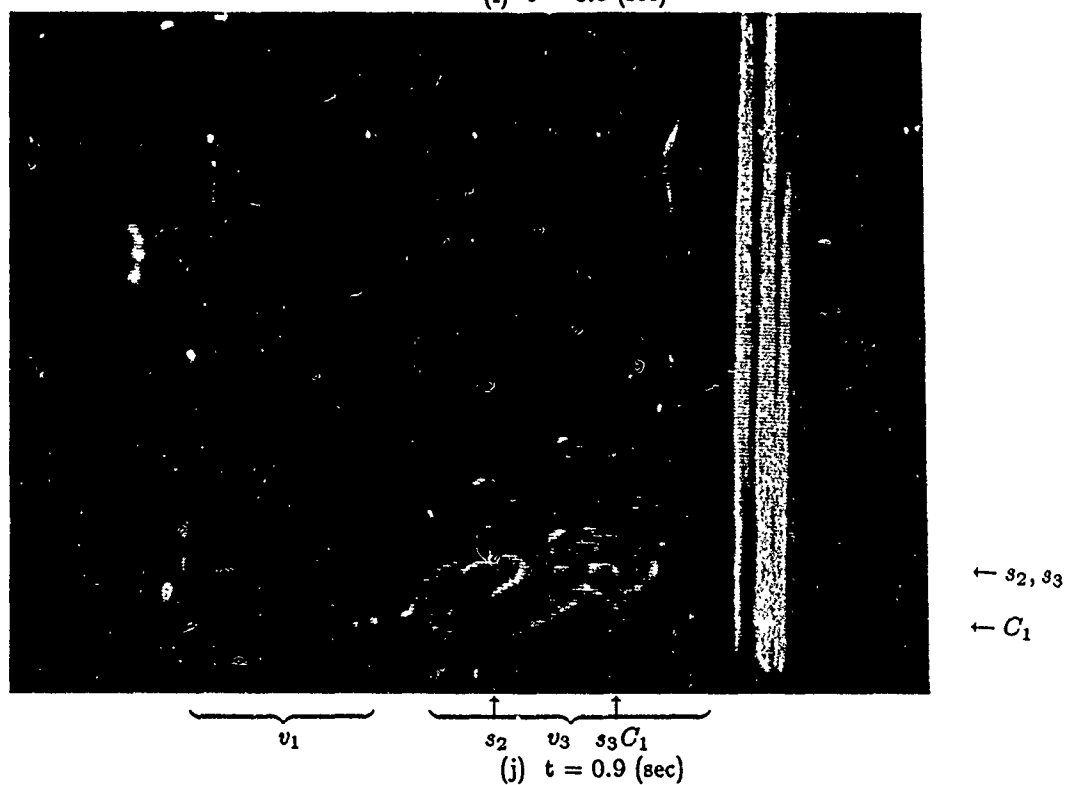
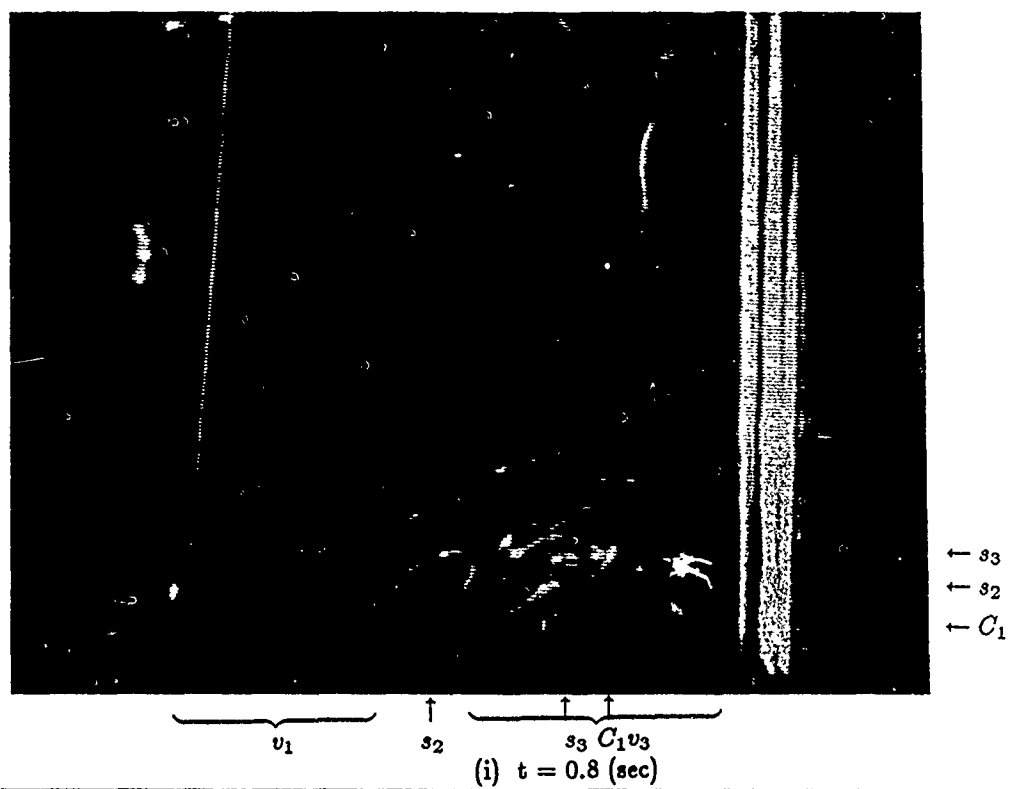
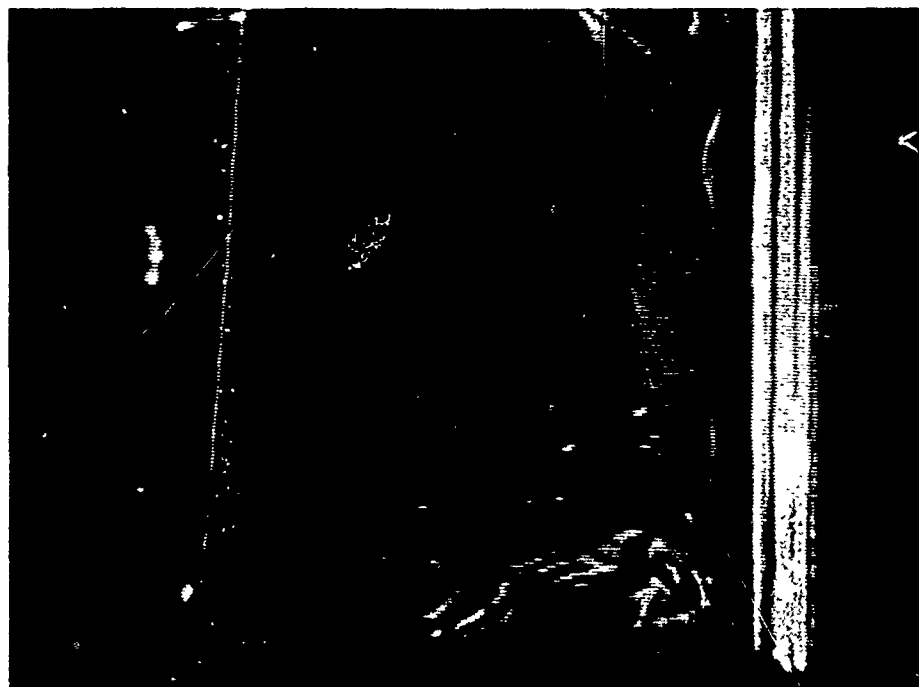


Figure 26. Continued



←  $C_1$

$v_1$   $v_3$   $C_1$

(k)  $t = 1.0$  (sec)



←  $C_1$

$v_1$   $v_3$   $C_1$

(l)  $t = 1.1$  (sec)

Figure 26. Continued

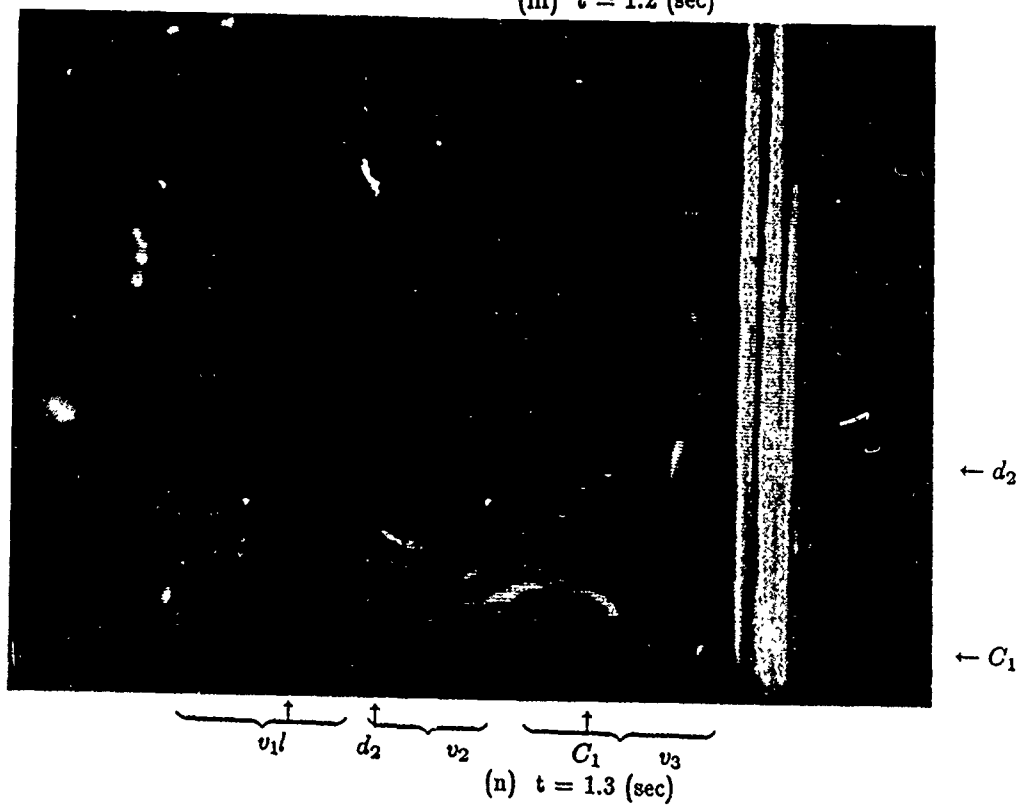
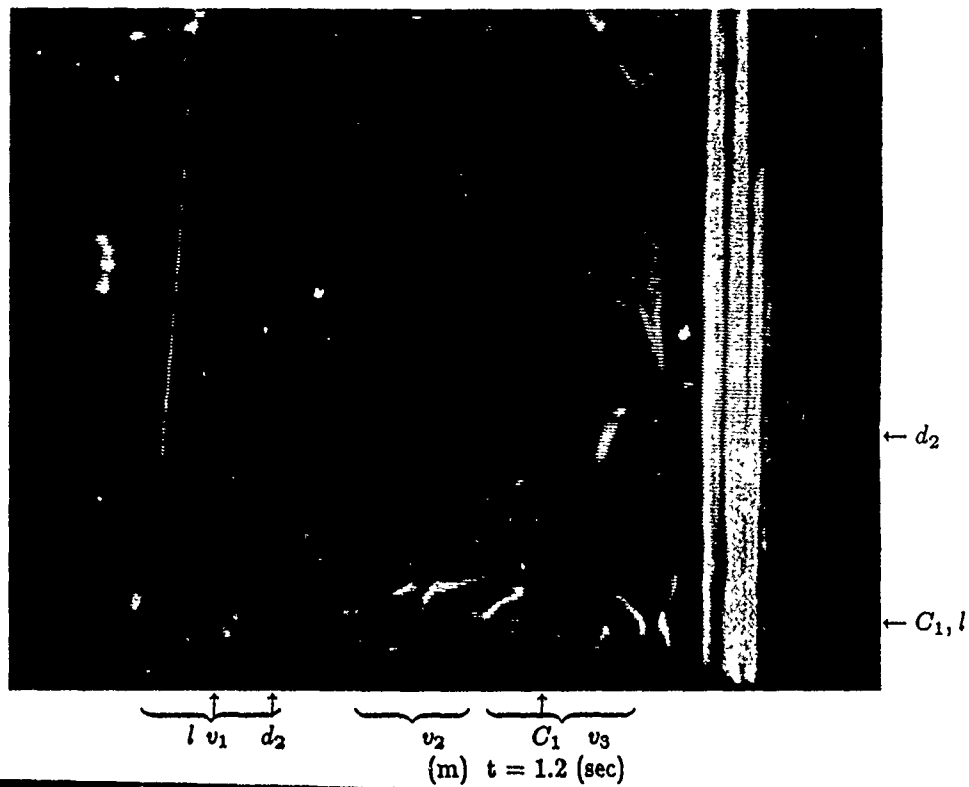
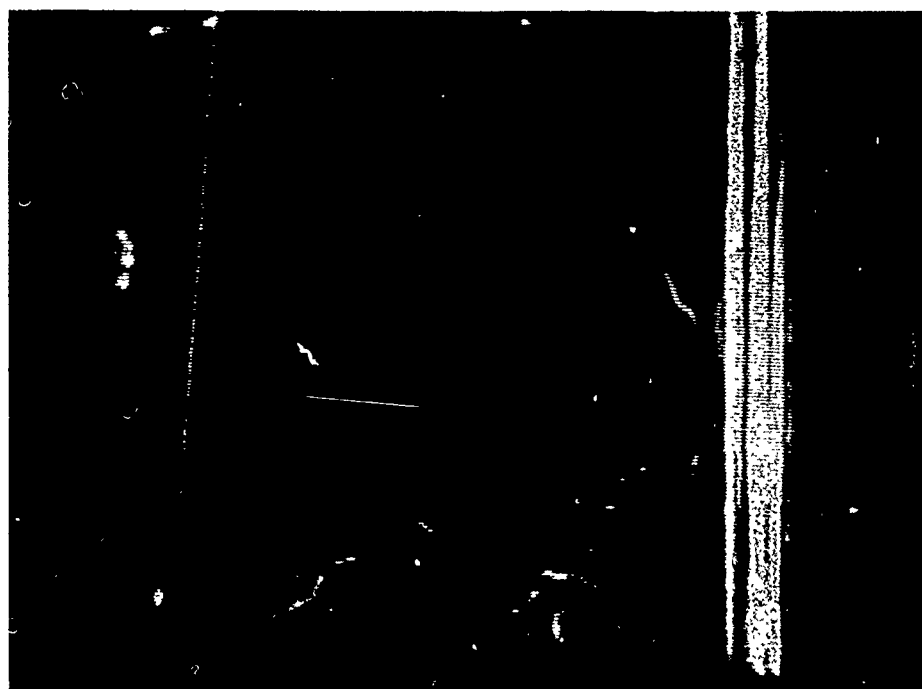
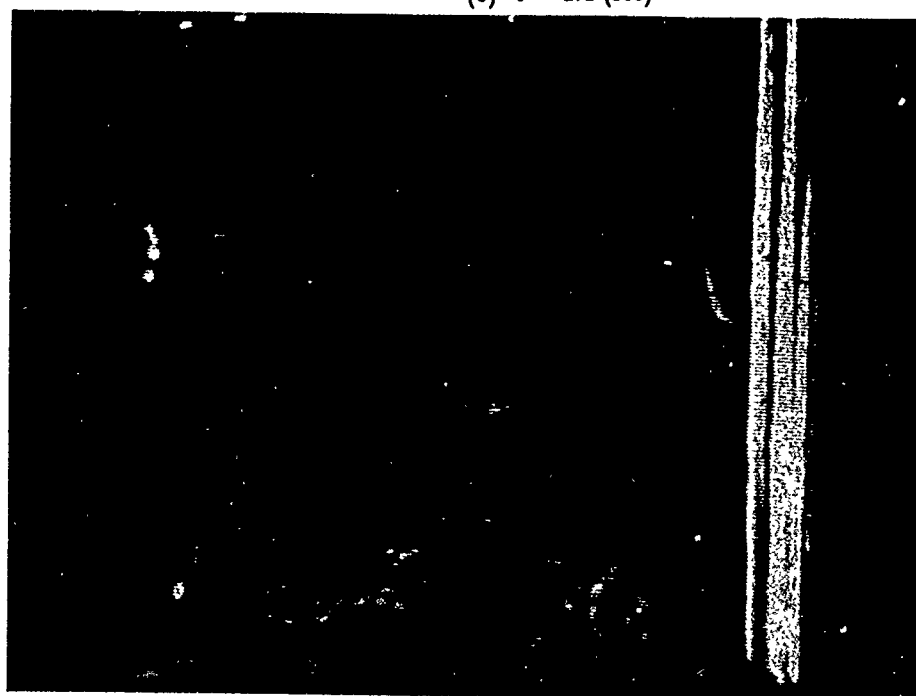


Figure 26. Continued

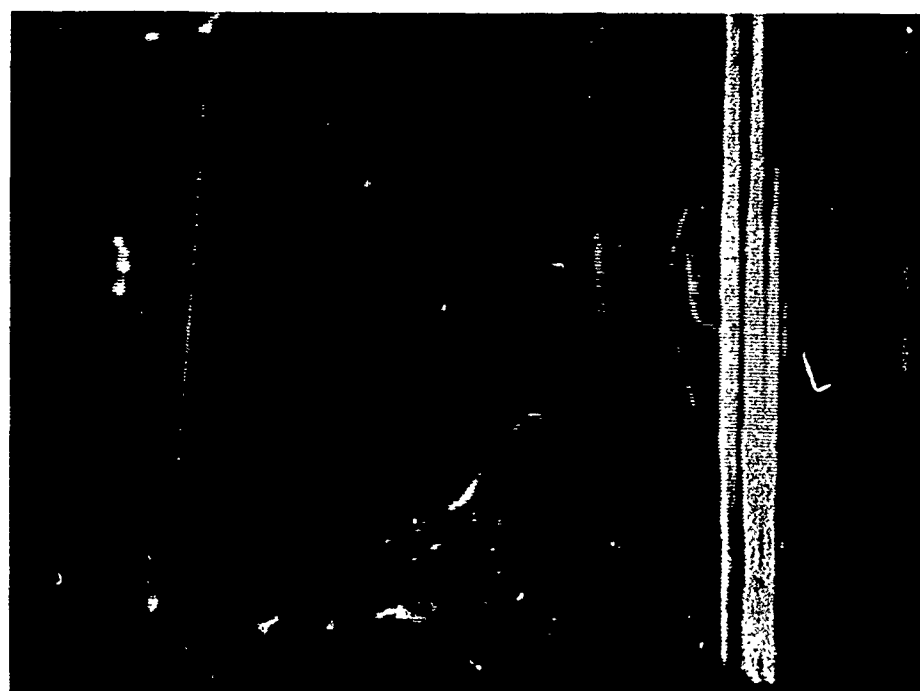


$\overbrace{l \ v_1} \quad \overbrace{s_4 \ v_2 \ d_2} \quad \overbrace{v_3 \ C_1}$   
 (o)  $t = 1.4 \text{ (sec)}$



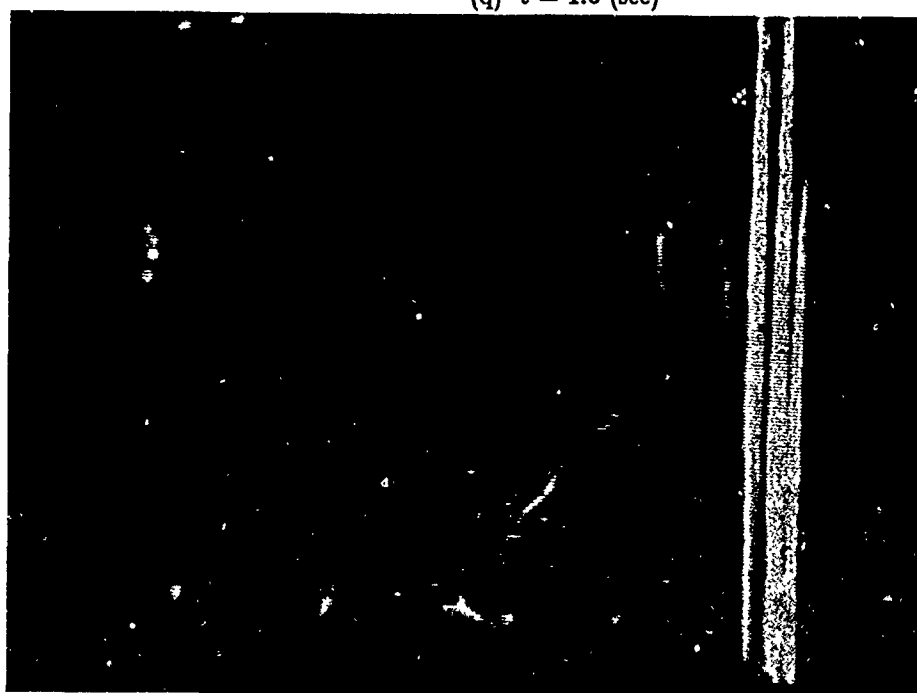
$\overbrace{v_1 \ l} \quad \overbrace{s_4 \ v_2 \ d_2} \quad \overbrace{C_1 \ v_3}$   
 (p)  $t = 1.5 \text{ (sec)}$

Figure 26. Continued



←  $d_2$   
←  $s_4$   
←  $C_1, l$

$\underbrace{\quad \uparrow}_{v_1 \quad l} \quad \underbrace{\quad \uparrow}_{v_2 \quad s_4} \quad \underbrace{\quad \uparrow}_{d_2} \quad \underbrace{\quad \uparrow}_{v_3 \quad C_1}$   
(q)  $t = 1.6 \text{ (sec)}$

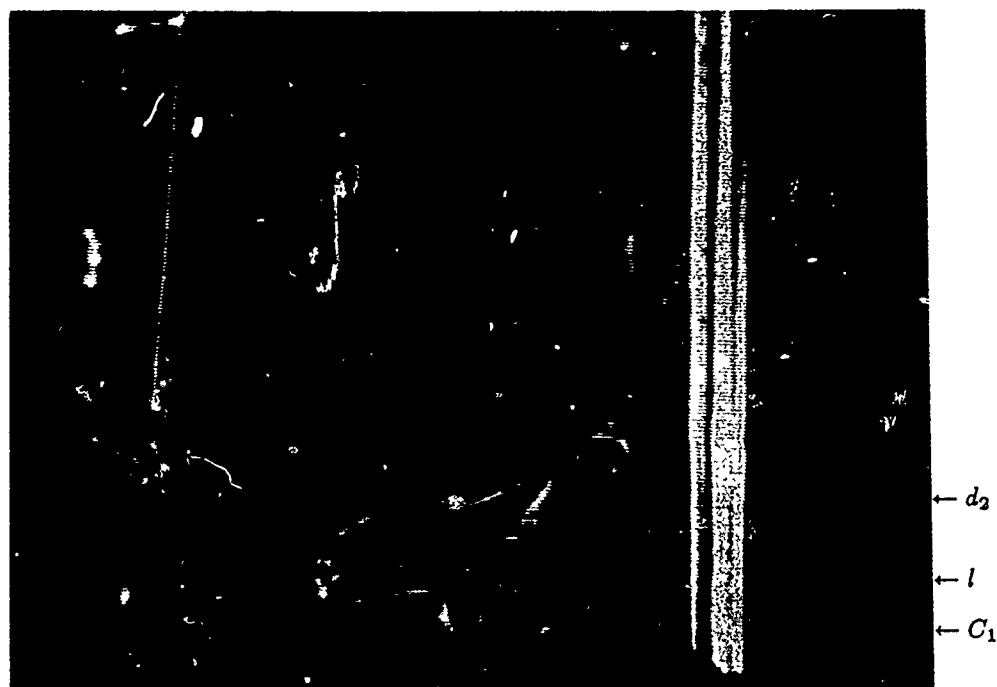


←  $d_2$   
←  $s_4$   
←  $l, C_1$

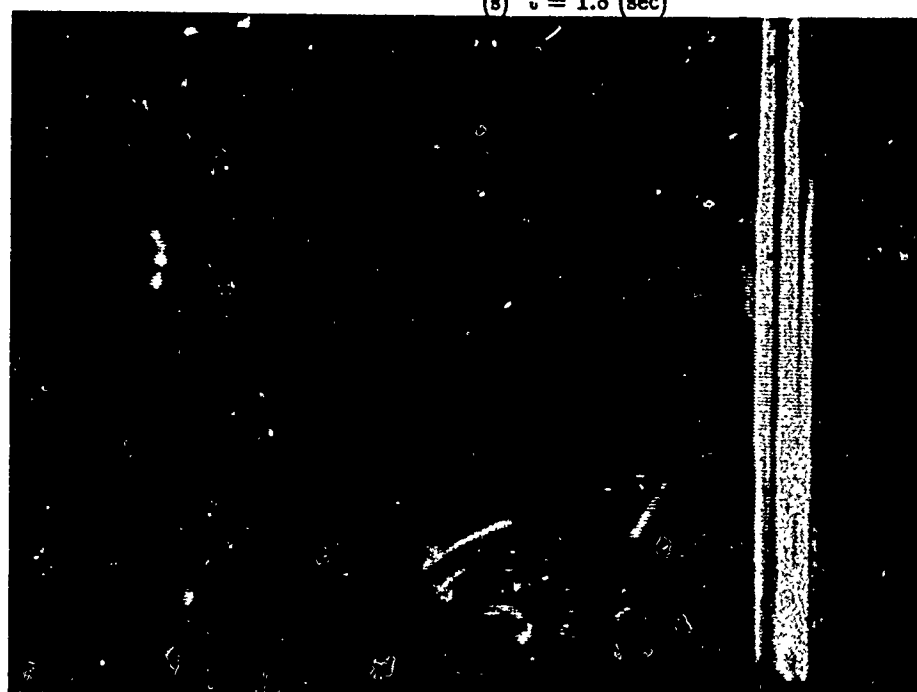
$\underbrace{\quad \uparrow}_{v_1 \quad l} \quad \underbrace{\quad \uparrow}_{v_2 \quad s_4} \quad \underbrace{\quad \uparrow \quad \uparrow}_{d_2 \quad C_1 \quad v_3}$   
(r)  $t = 1.7 \text{ (sec)}$

Figure 26. Continued





(s)  $t = 1.8$  (sec)



(t)  $t = 1.9$  (sec)

Figure 26. Continued

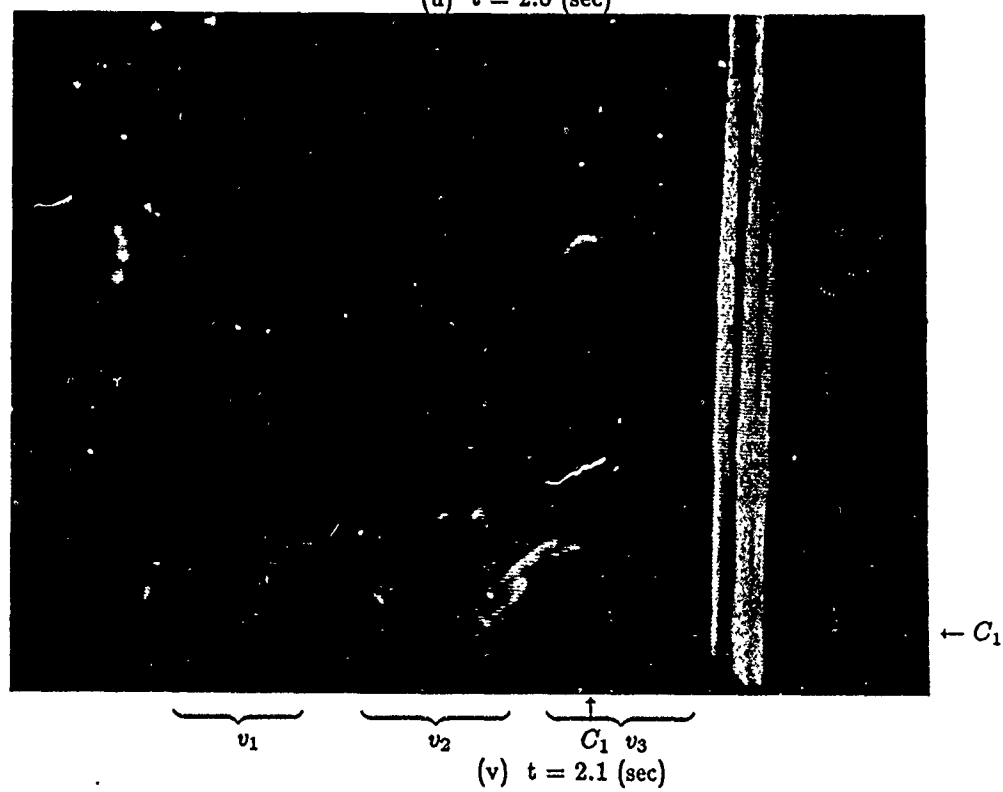
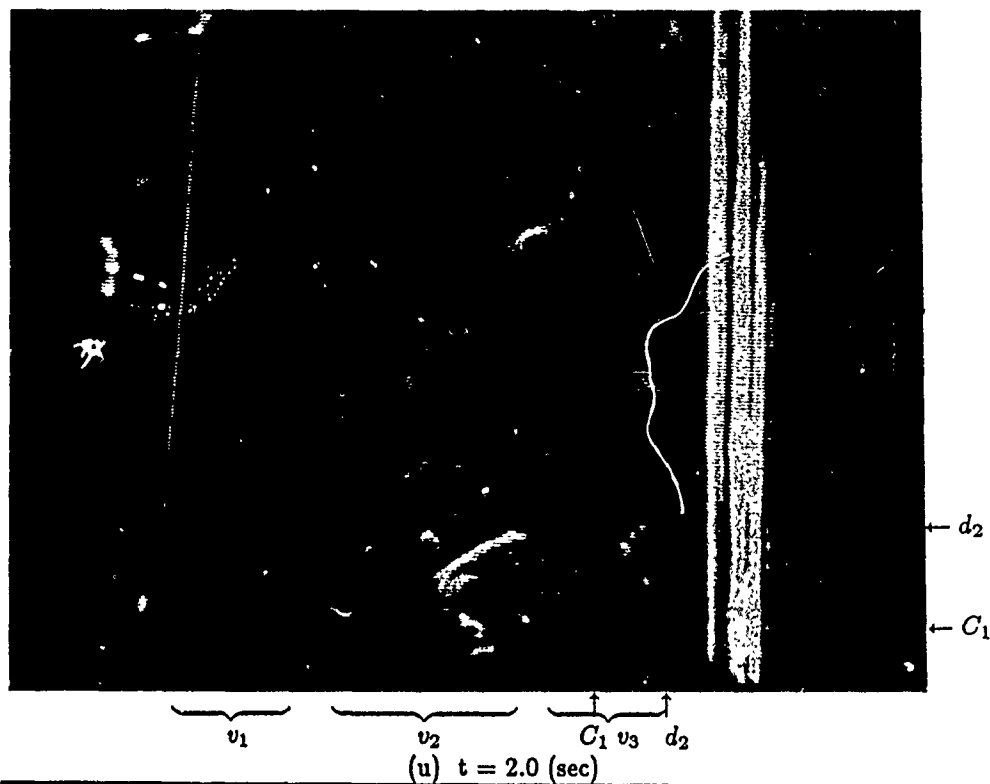
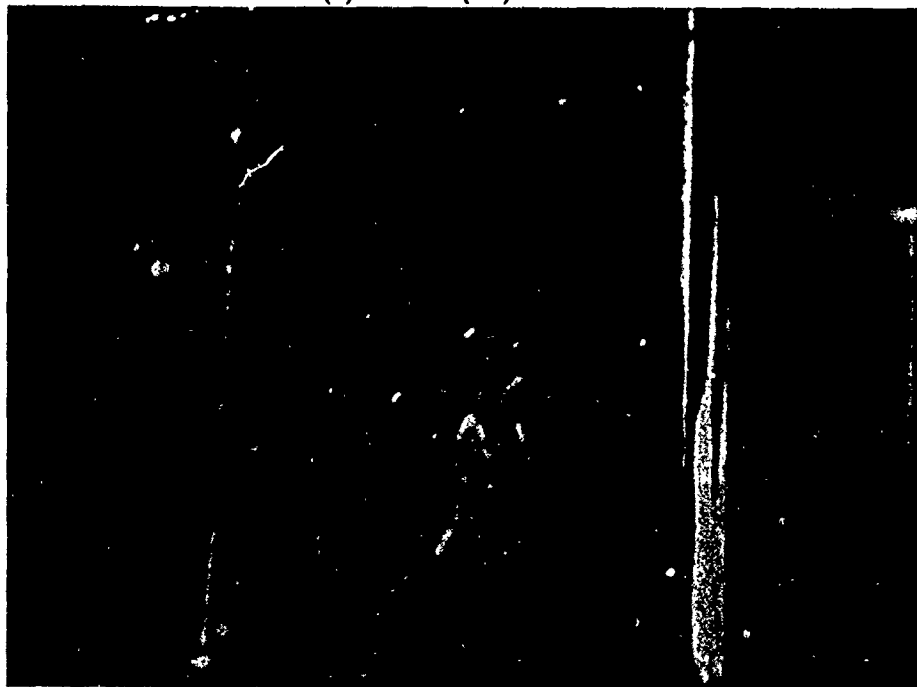


Figure 26. Concluded



$\underbrace{\quad S \quad}_S \quad \uparrow \quad T \quad \underbrace{\quad P \quad}_P$   
 (a)  $t = 0.0$  (sec)



$\underbrace{\quad S \quad}_S \quad \uparrow \quad T \quad \underbrace{\quad P \quad}_P$   
 (b)  $t = 0.1$  (sec)

Figure 27. Sequence of continuous bubble sheet pictures showing strong interaction of two vortices near the wall

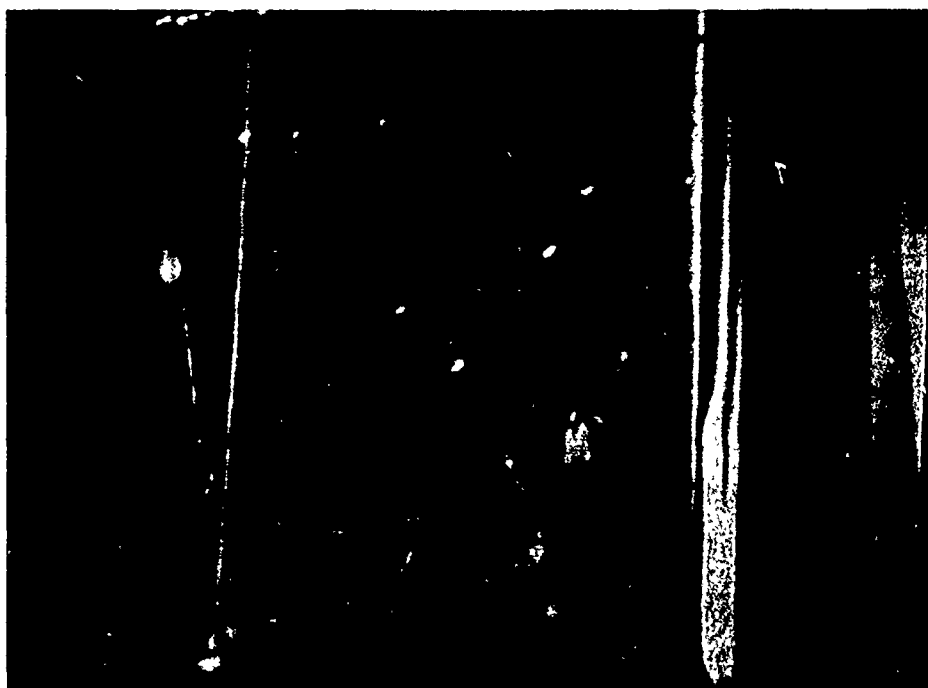


$\underbrace{\quad}_S \quad \uparrow \quad \underbrace{\quad}_P$   
 (c)  $t = 0.2 \text{ (sec)}$

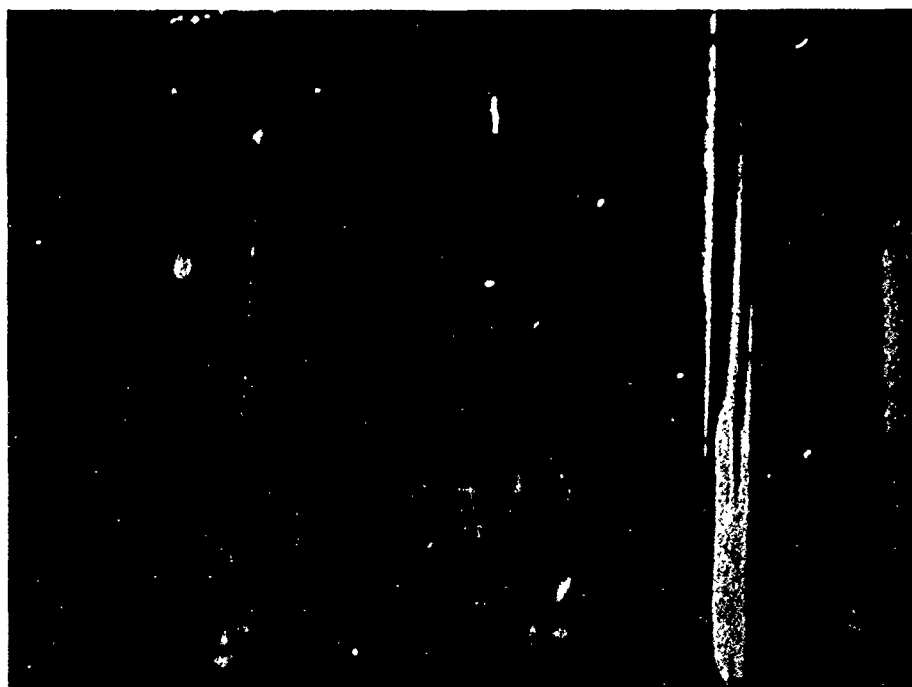


$\underbrace{\quad}_S \quad \uparrow \quad \underbrace{\quad}_P$   
 (d)  $t = 0.3 \text{ (sec)}$

Figure 27. Continued



$\underbrace{\quad S \quad} \quad \underbrace{\quad T \quad} \quad \underbrace{\quad P \quad}$   
 (e)  $t = 0.4 \text{ (sec)}$



$\underbrace{\quad S \quad} \quad \underbrace{\quad T \quad} \quad \underbrace{\quad P \quad}$   
 (f)  $t = 0.5 \text{ (sec)}$

Figure 27. Continued

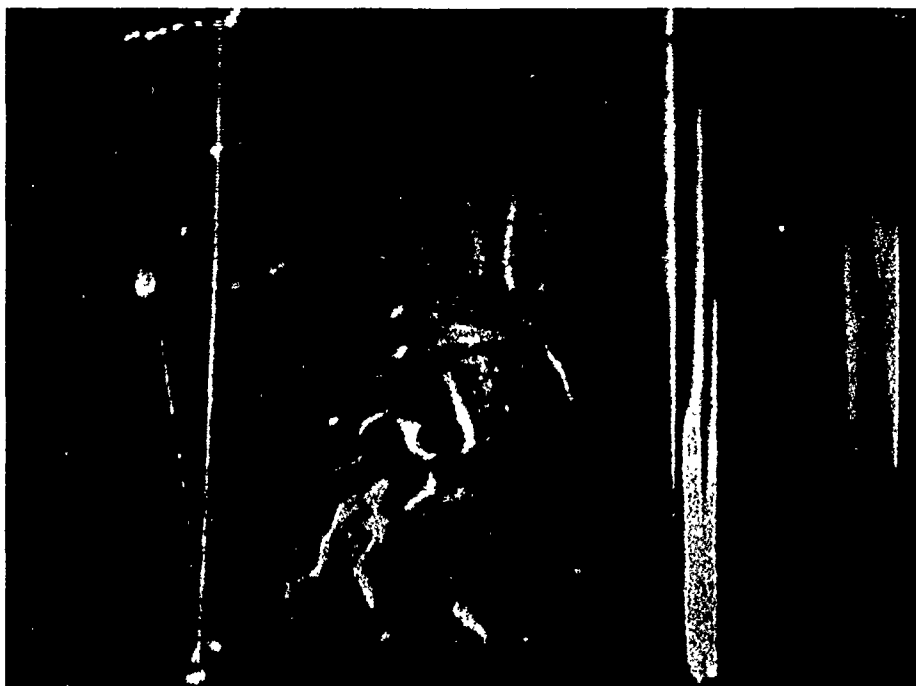


$\overbrace{S} \quad \overbrace{T} \quad \overbrace{P}$   
 (g)  $t = 0.6$  (sec)



$\overbrace{S} \quad \overbrace{T} \quad \overbrace{P}$   
 (h)  $t = 0.7$  (sec)

Figure 27. Continued



$\overbrace{S} \quad \overbrace{T} \quad \overbrace{P}$   
 (i)  $t = 0.8 \text{ (sec)}$



$\overbrace{S} \quad \overbrace{T} \quad \overbrace{P}$   
 (j)  $t = 0.9 \text{ (sec)}$

Figure 27. Continued

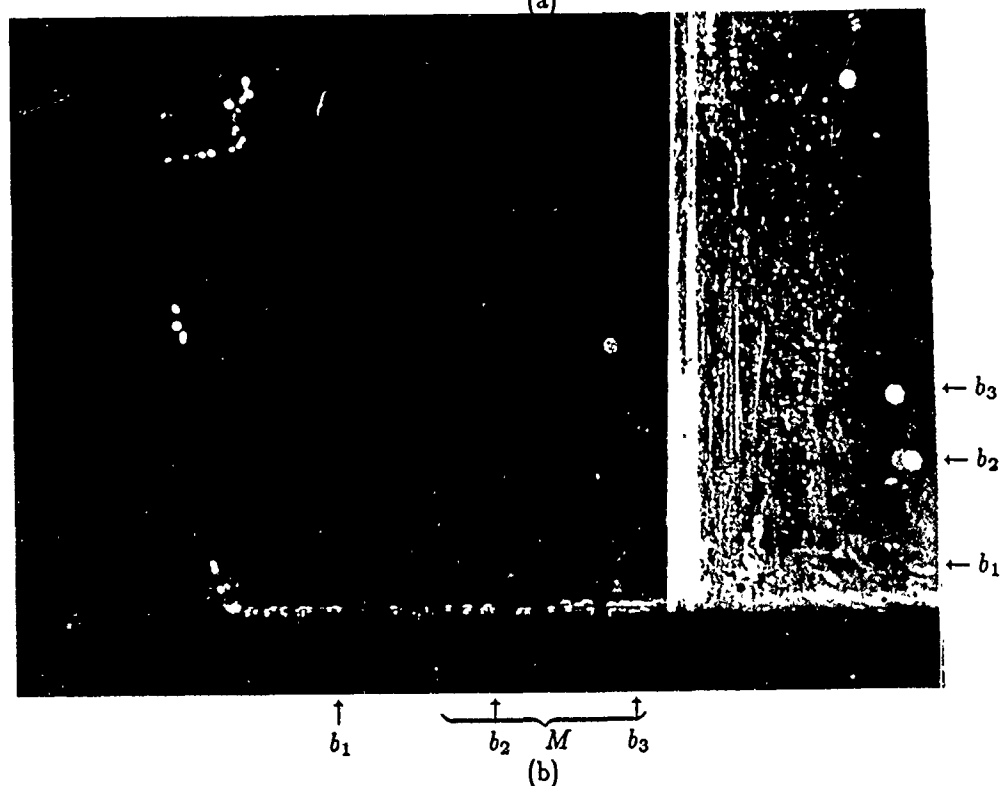
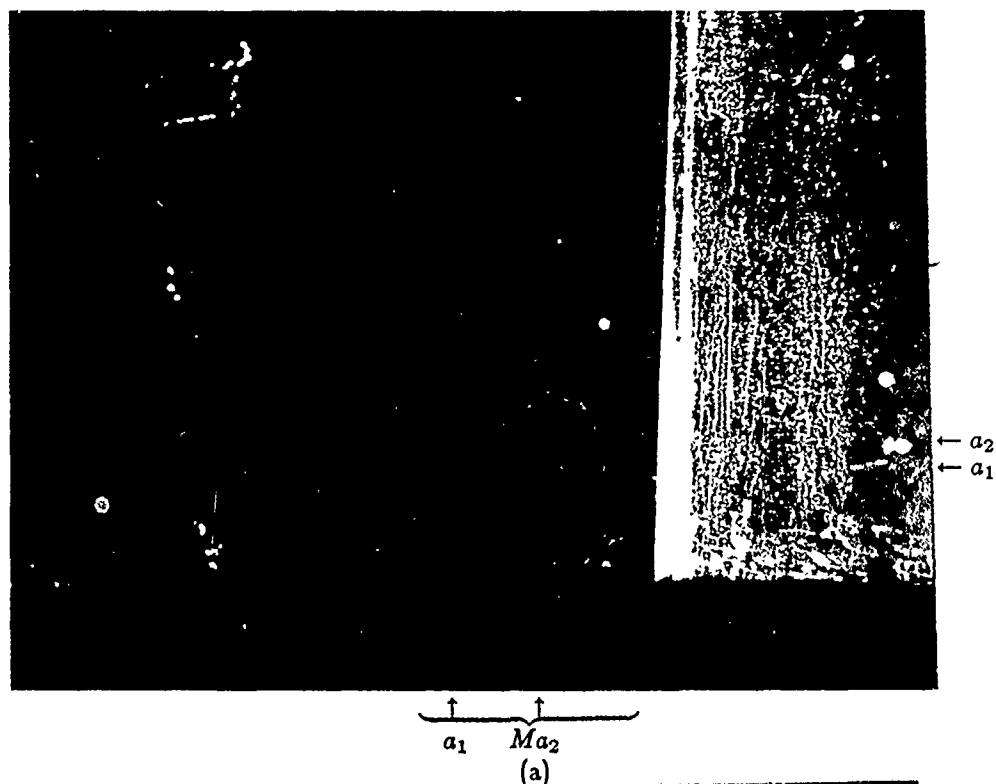
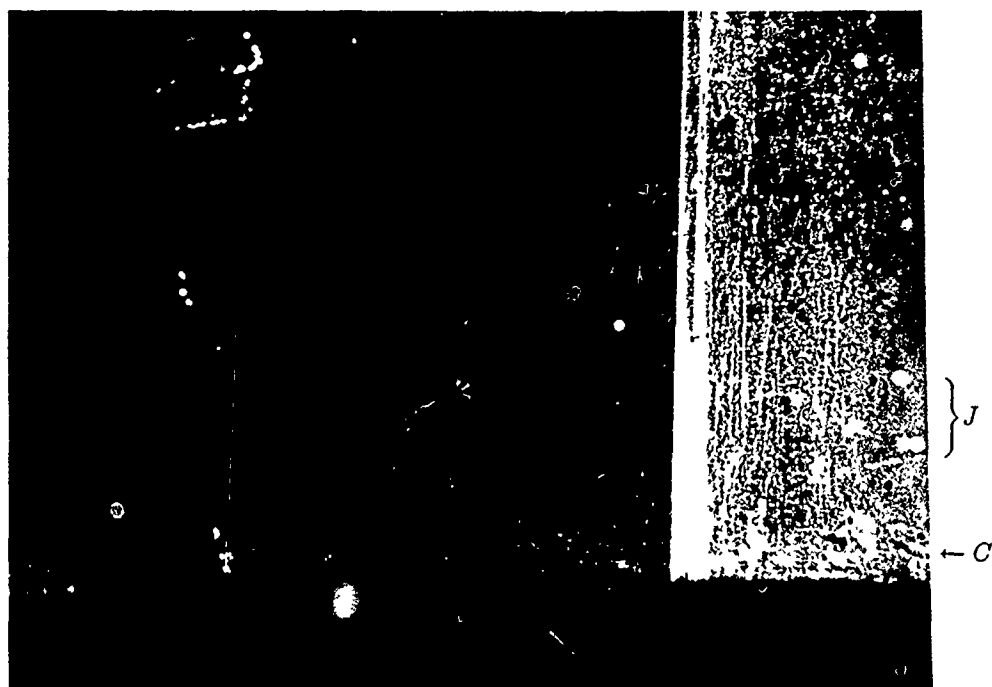
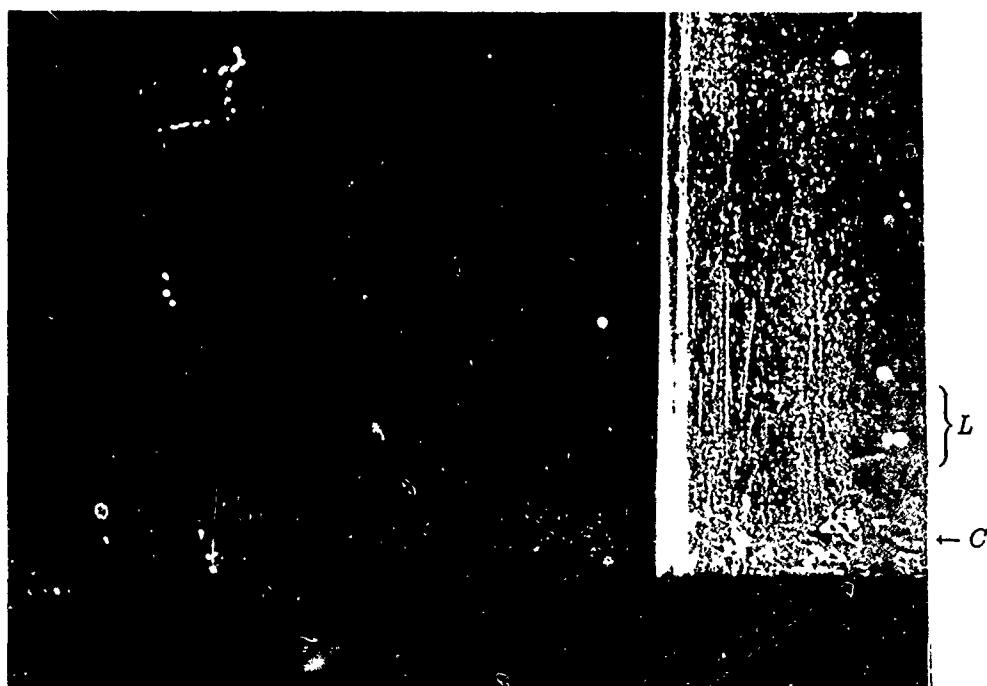


Figure 28. Some examples of the flow structures near the nose region of the wing-body junction : a conventional time-line technique.



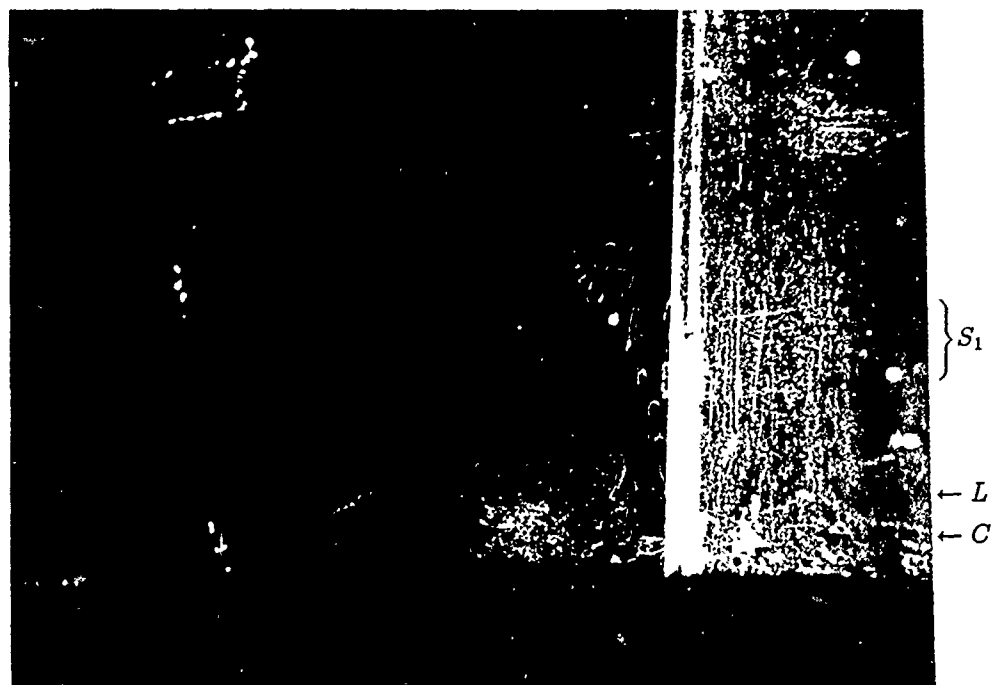


$\uparrow$   
 $J \overline{C}$   
 (c)

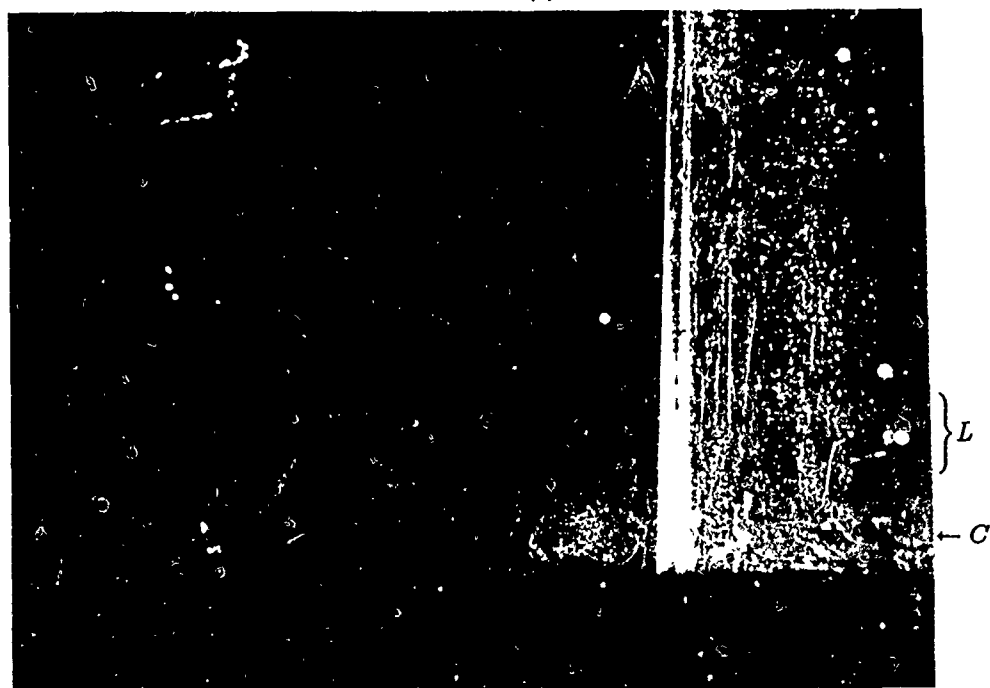


$\uparrow$   
 $L \overline{C}$   
 (d)

Figure 28. Continued

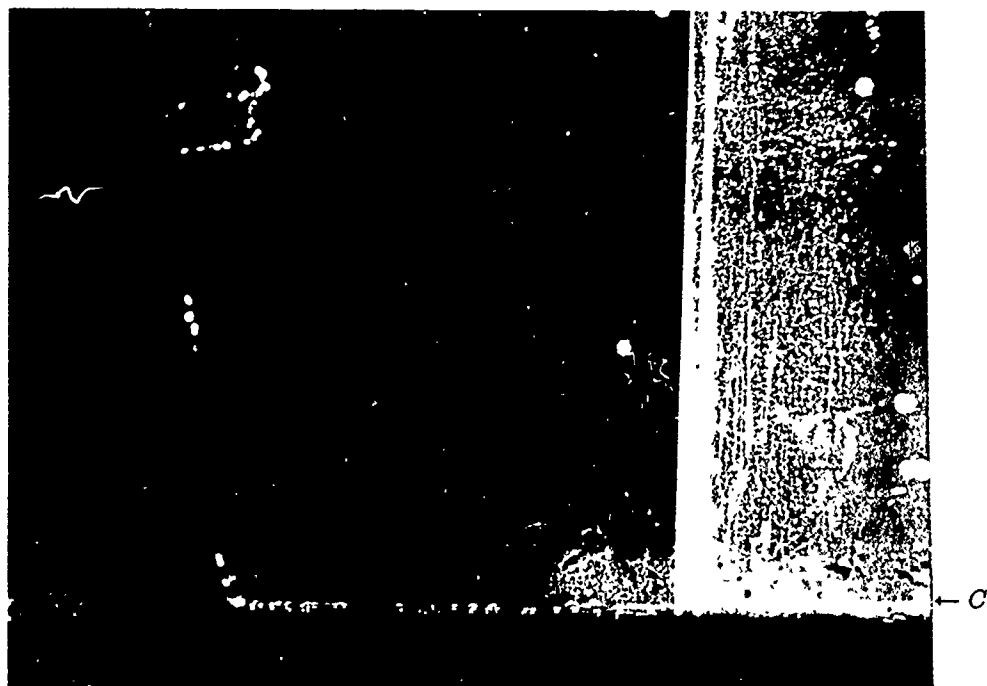


$\underbrace{\quad}_{L \quad S_1} \quad \uparrow$   
 $C$   
 (e)

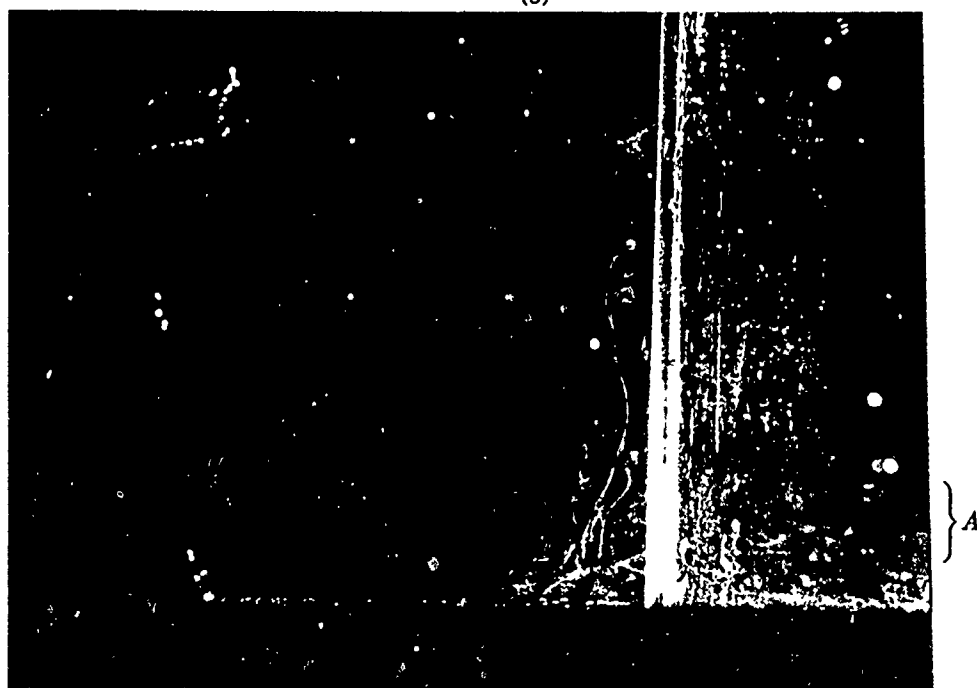


$\underbrace{\quad}_{L} \quad \uparrow \uparrow$   
 $C \quad e$   
 (f)

Figure 28. Continued

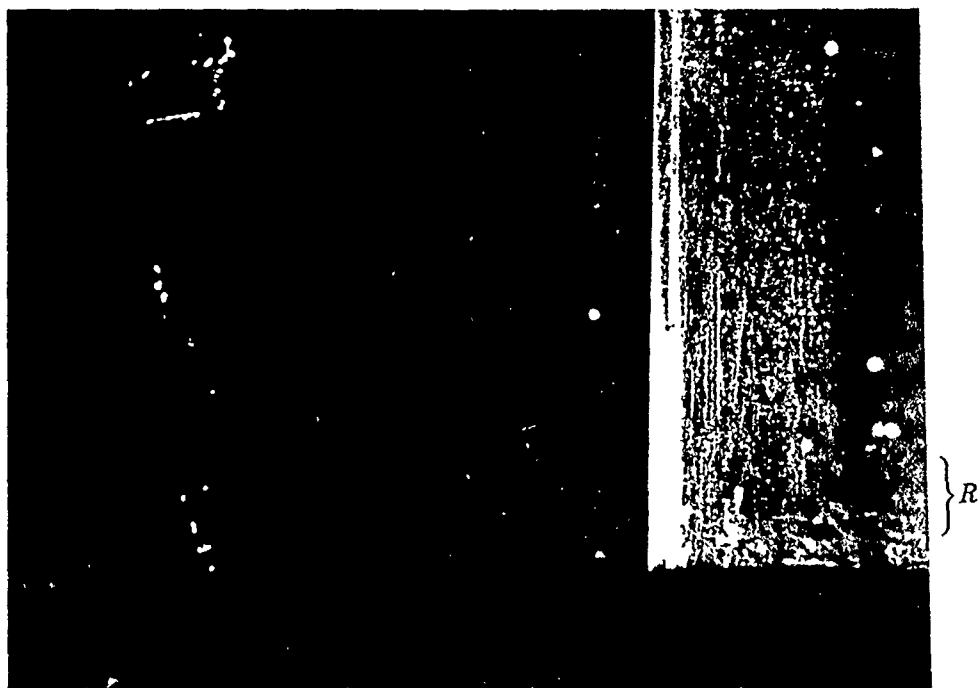


(g)  
↑  
C

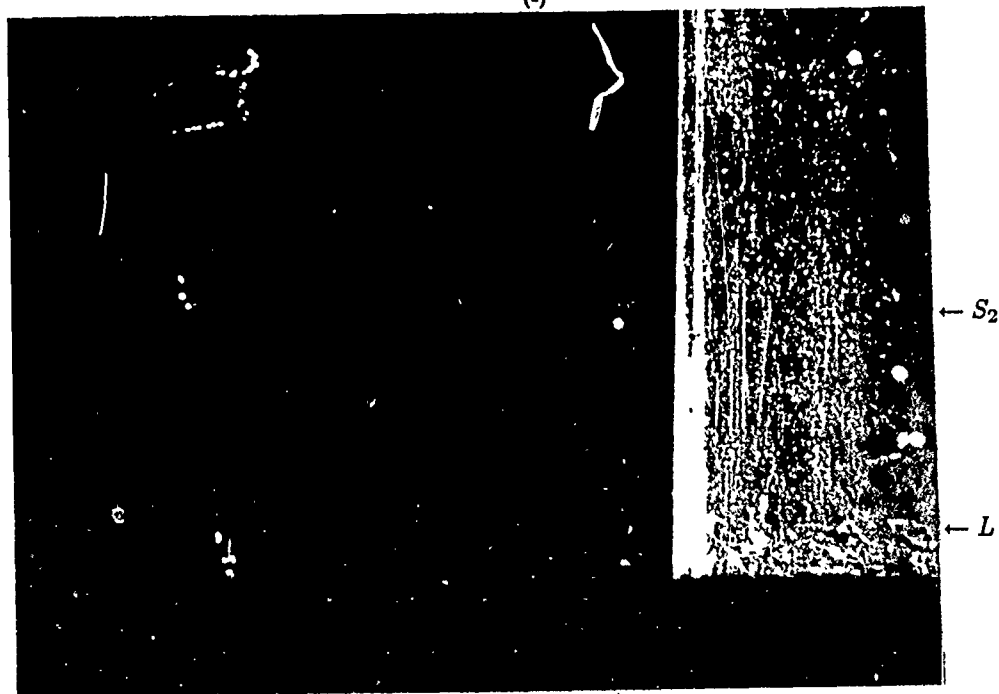


⏟  
A      ⏟  
S<sub>t</sub>  
(h)

Figure 28. Continued



(i)



$L$

$S_2$

(i)

Figure 28. Continued

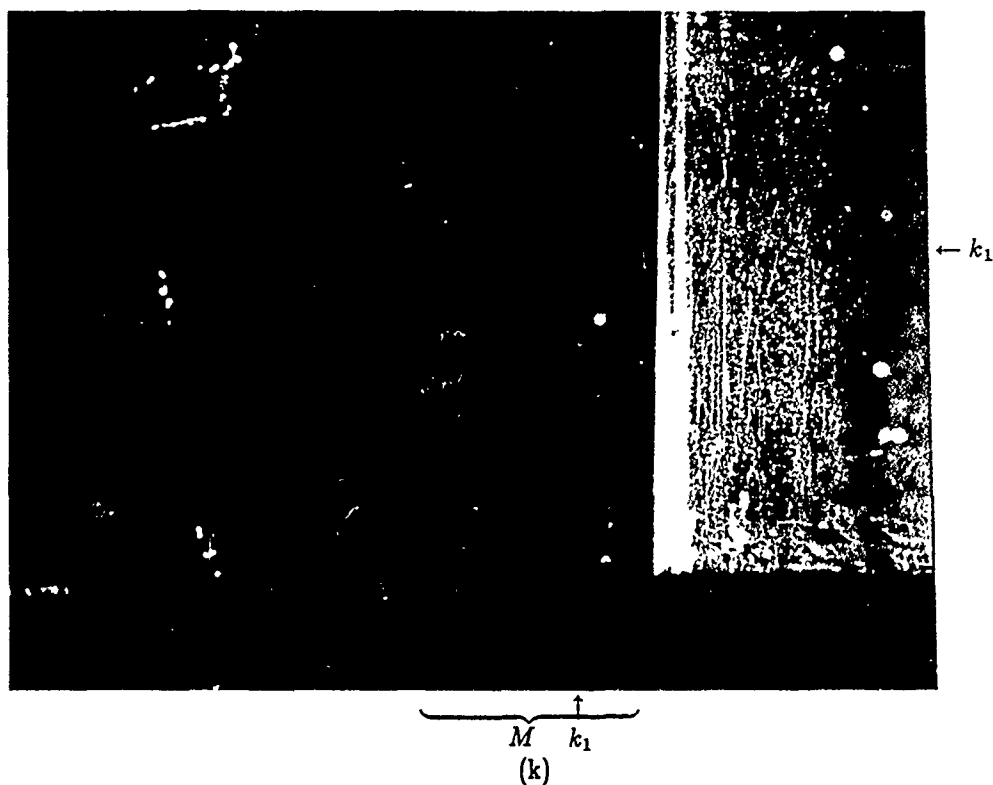


Figure 28. Concluded

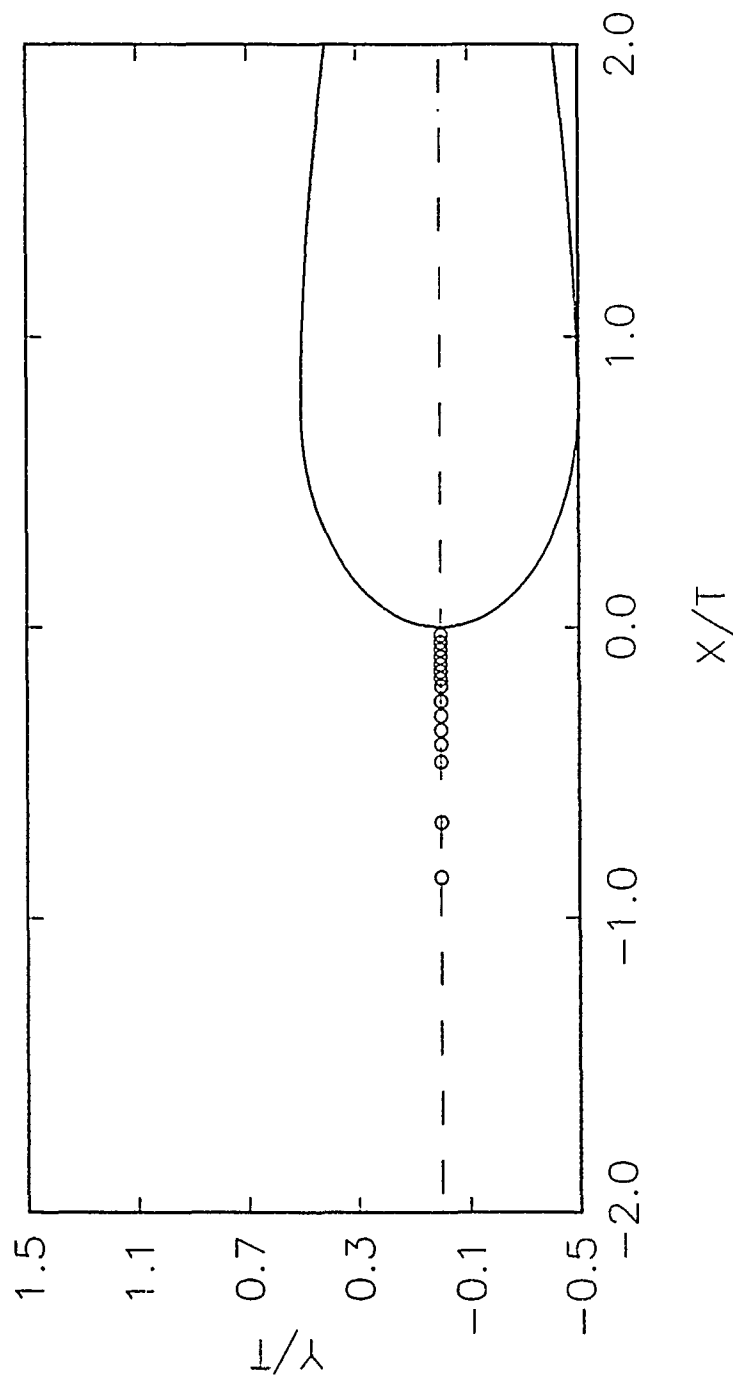


Figure 29. Measuring locations for LDV tests

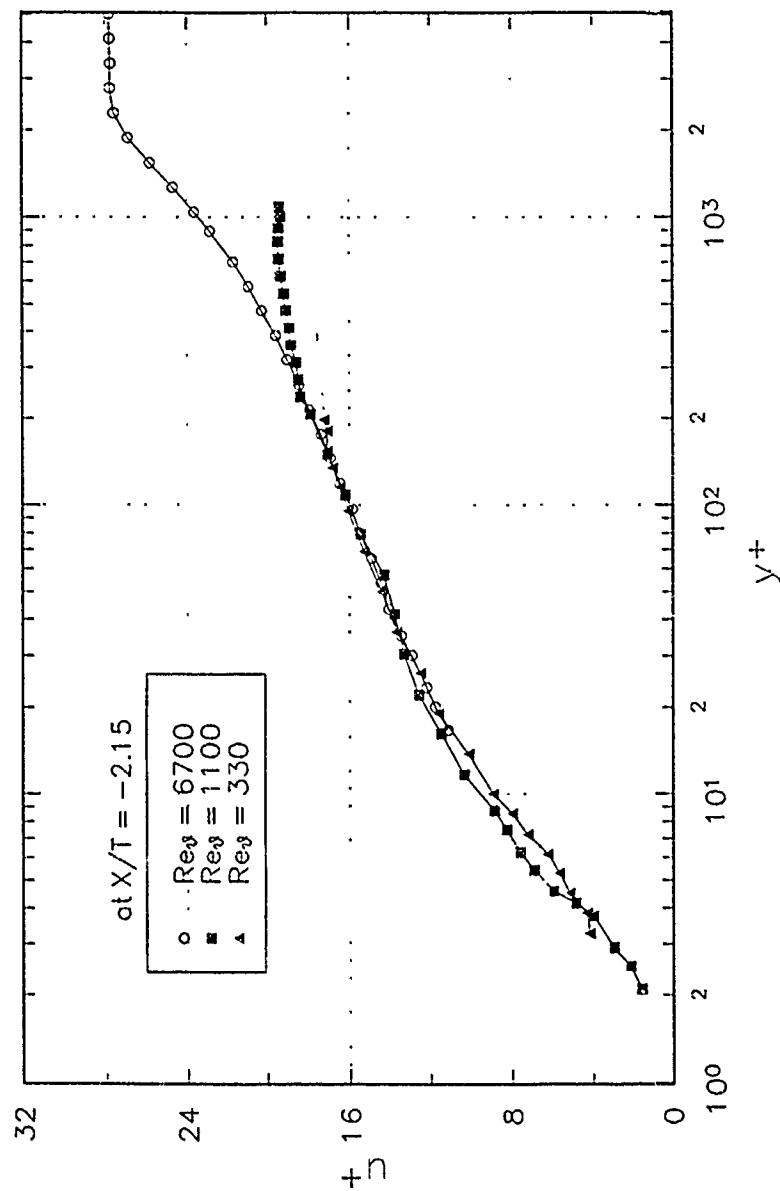
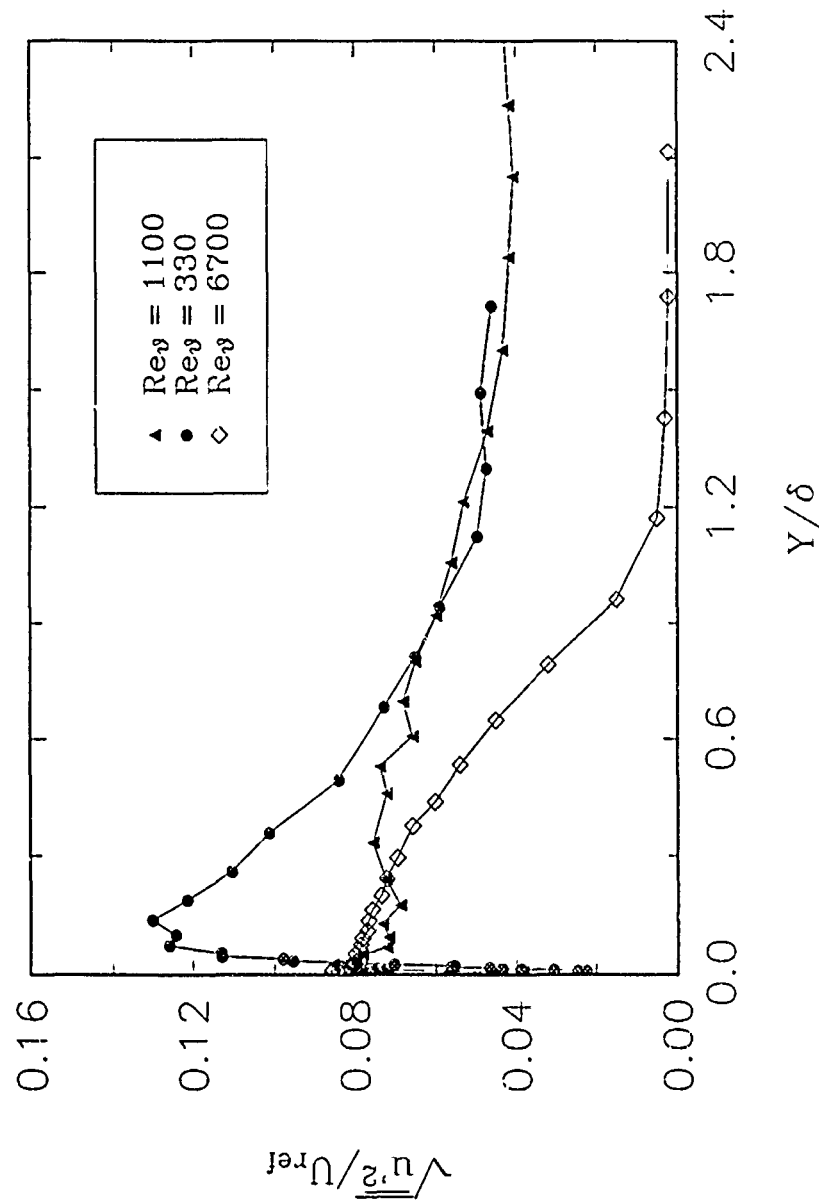
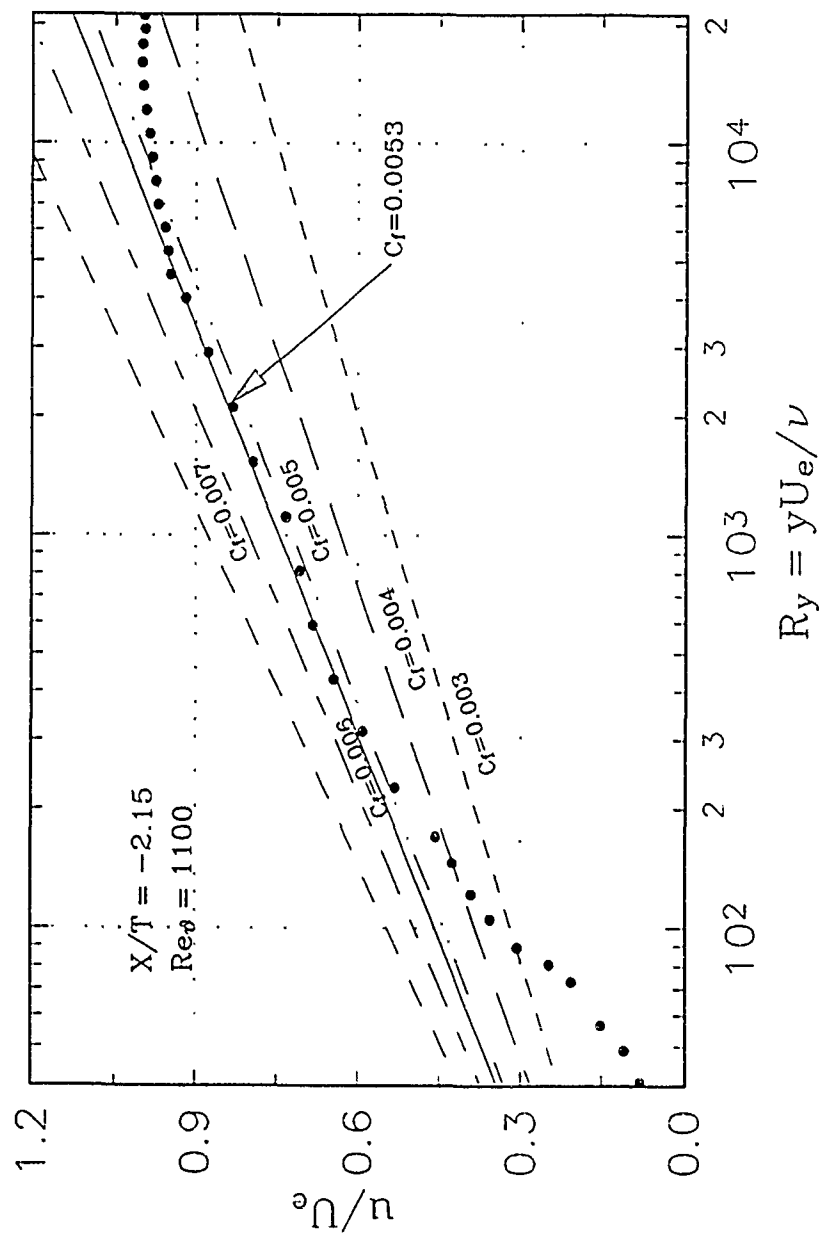


Figure 30. Turbulent normal stress distribution across the boundary layer at  $X/T = -2.15$  for  $Re_\theta = 330$ ,  $Re_\theta = 1100$  (LDV measurements) and  $Re_\theta = 6700$  (Hot-wire measurements by Devenport and Simpson (1990b))



**Figure 31.** Turbulent normal stress distribution across the boundary layer at  $X/T = -2.15$  for  $Re_\theta = 330, Re_\theta = 1100$  (LDV measurements) and  $Re_\theta = 6700$  (Hot wire measurements by Devenport)





**Figure 32.** Estimation of the local friction coefficient at  $X/T = -2.15$  using the "cross plot of log region" procedure for  $Re_\theta = 1100$

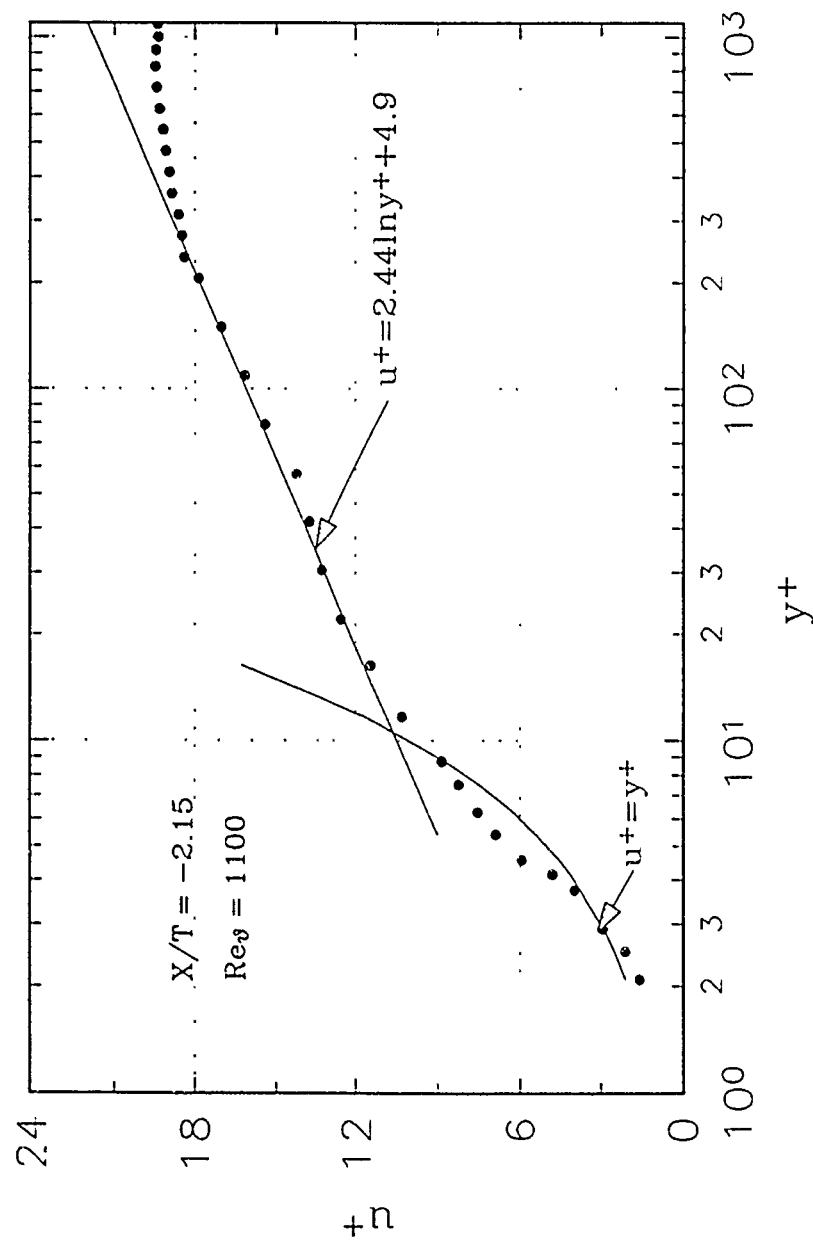


**Figure 33.** Law of the wall plot at  $X/T = -2.15$  for  $Re_\theta = 1100$ ;  $u_\tau$  is calculated using the "cross plot of log region" procedure assuming  $\frac{dP}{dx} = 0$

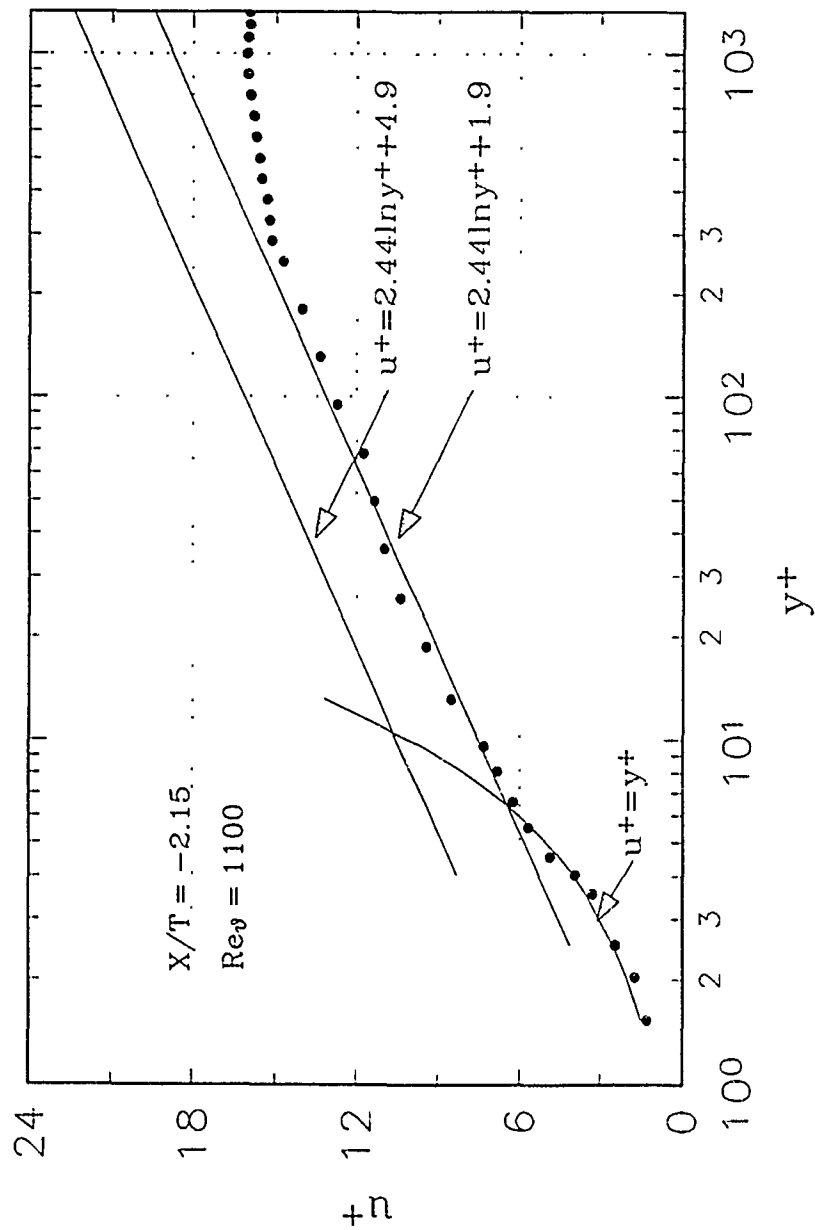


**Figure 34.** Law of the wall plot at  $X/T = -2.15$  for  $Re_\theta = 1100$ :  $u_r$  is calculated using the "wall profile plot" assuming  $\frac{dP}{dx} = 0$

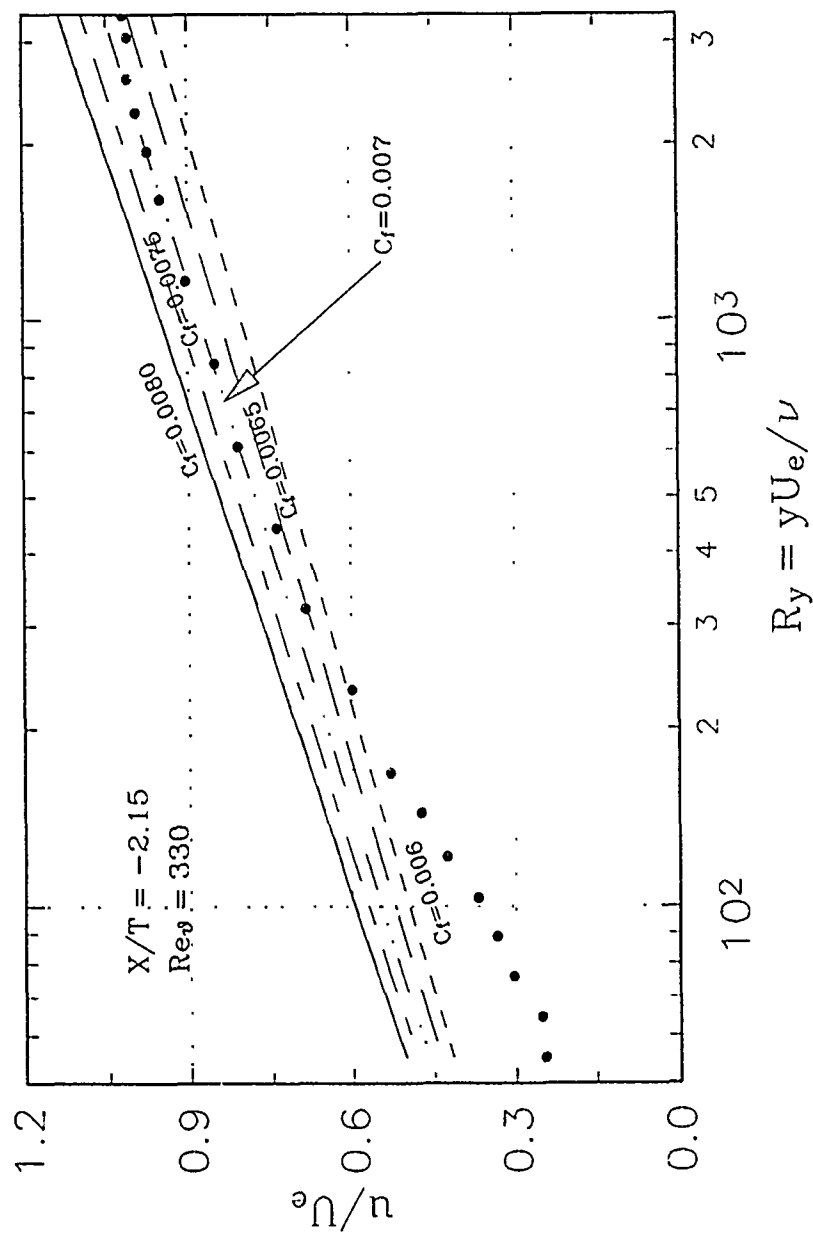
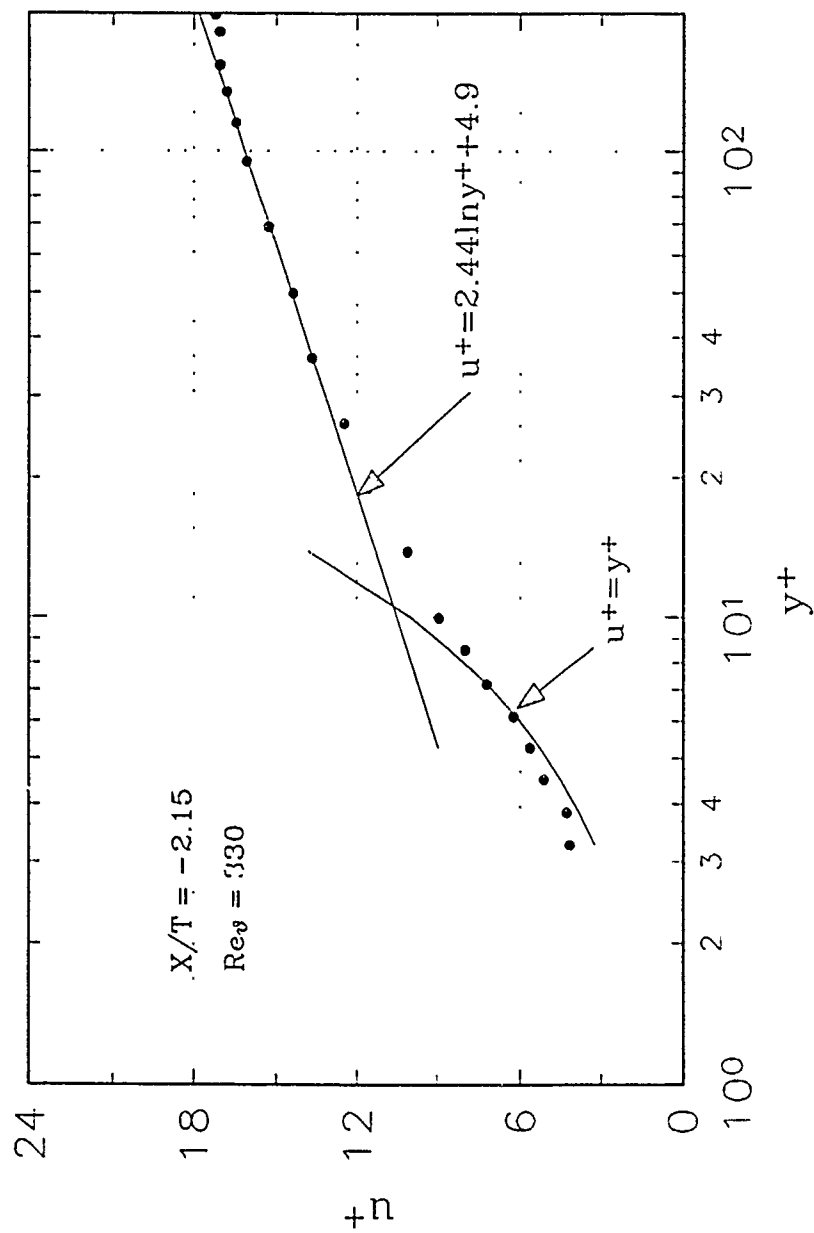


Figure 35. Estimation of local friction coefficient at  $X/T = -2.15$  using the "cross plot of log region" procedure for  $Re_\theta = 330$



**Figure 36.** Law of the wall plot at  $X/T = -2.15$  for  $Re_\theta = 330$ :  $u_\tau$  is calculated using the "cross plot of log region" procedure assuming  $\frac{dP}{dx} = 0$

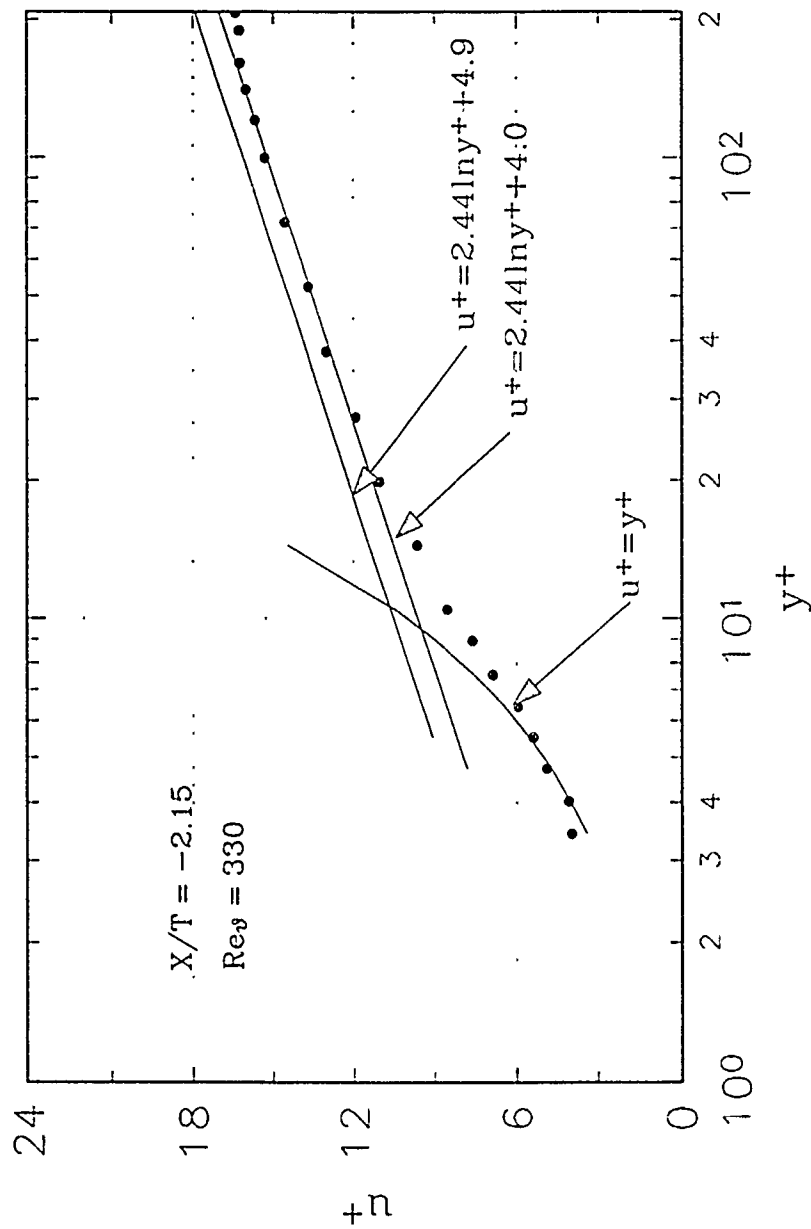
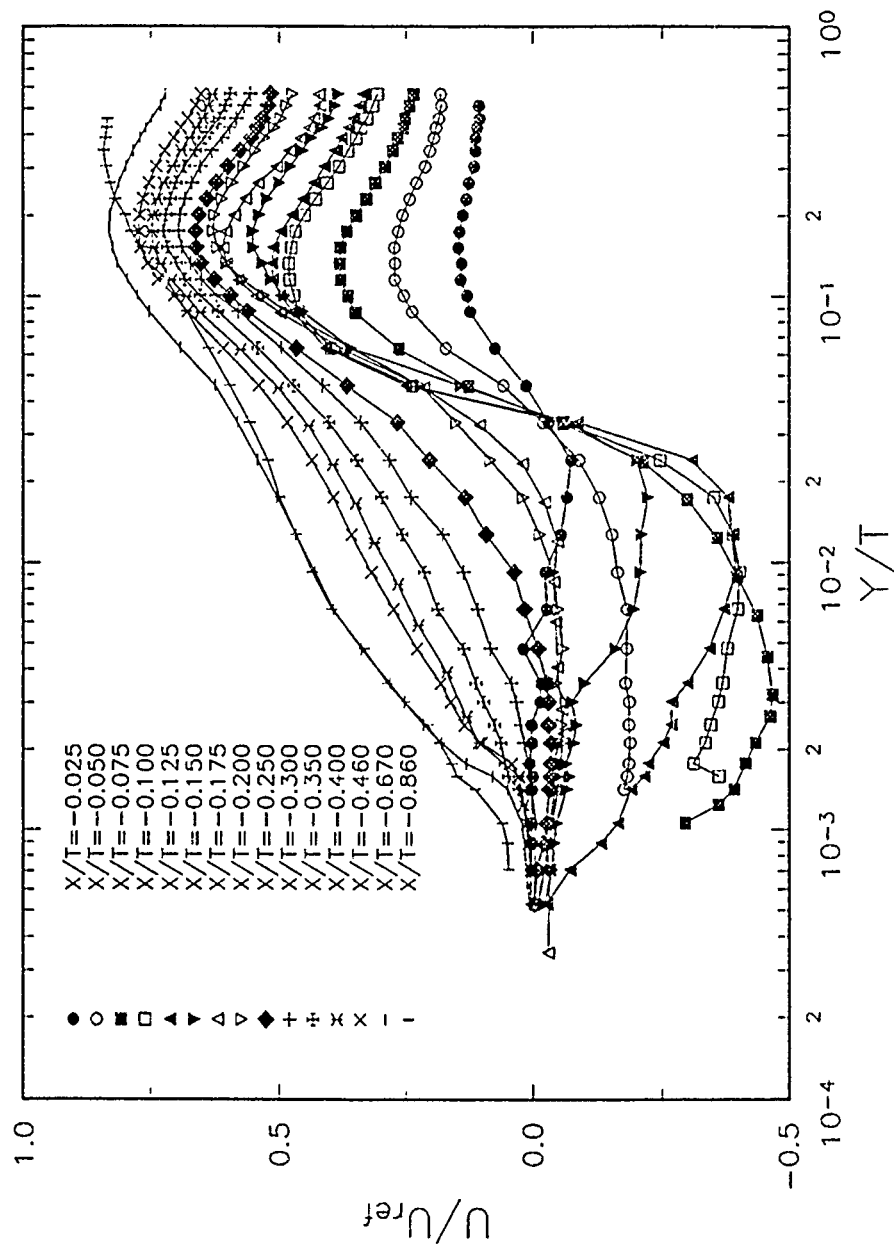


Figure 37. Law of the wall plot at  $X/T = -2.15$  for  $Re_\theta = 330$ :  $u_\tau$  is calculated using the "wall profile plot" assuming  $\frac{dP}{dx} = 0$



**Figure 38.** Mean velocity profiles using LDV measurements for  $Re_\theta = 1100$  at all measuring locations

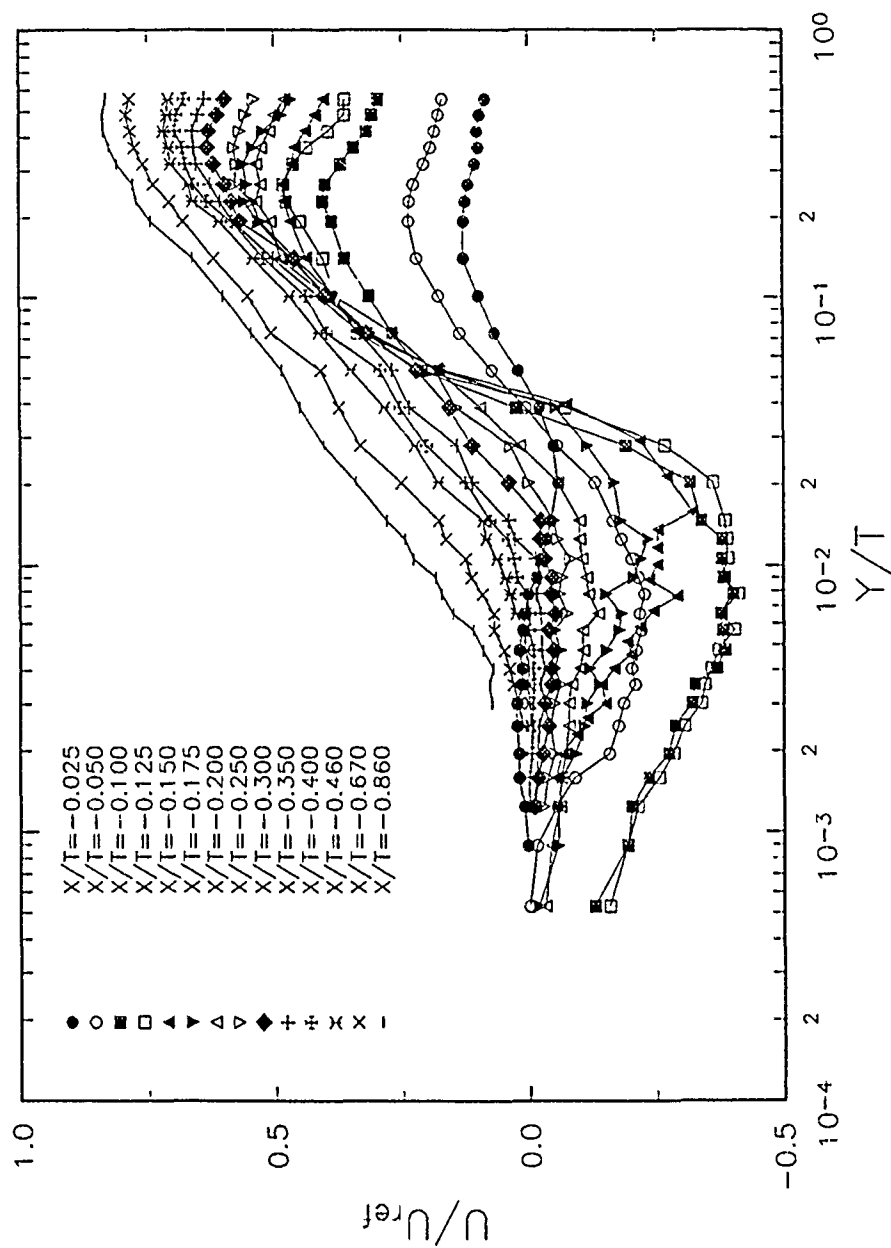
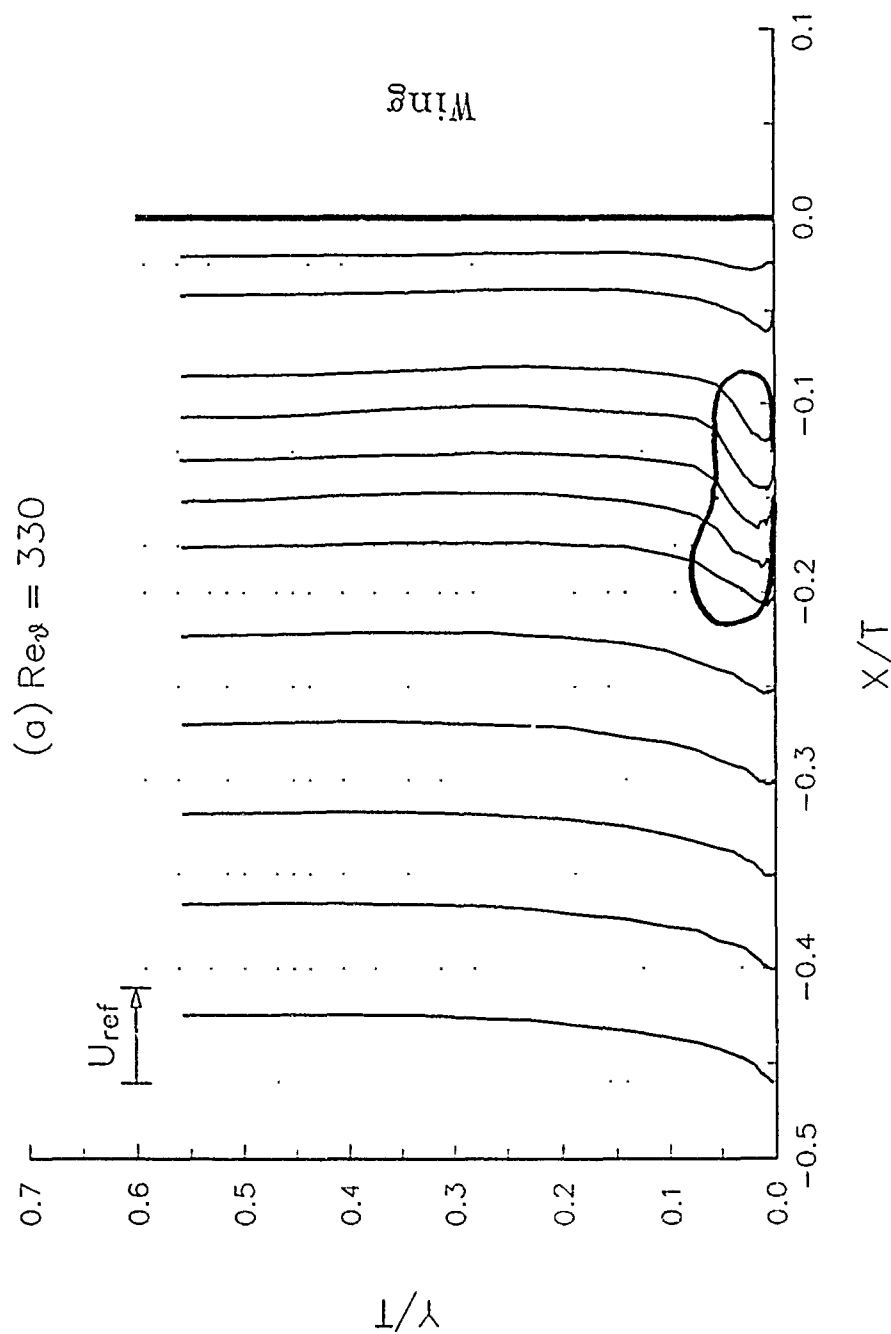


Figure 39. Mean velocity profiles using LDV measurements for  $Re_\theta = 330$  at all measuring locations





**Figure 40.** Mean boundary layer profiles constructed using only axial component velocity for (a)  $Re_\theta = 330$  and (b)  $Re_\theta = 1100$ ; Solid loop represents the bimodal zone

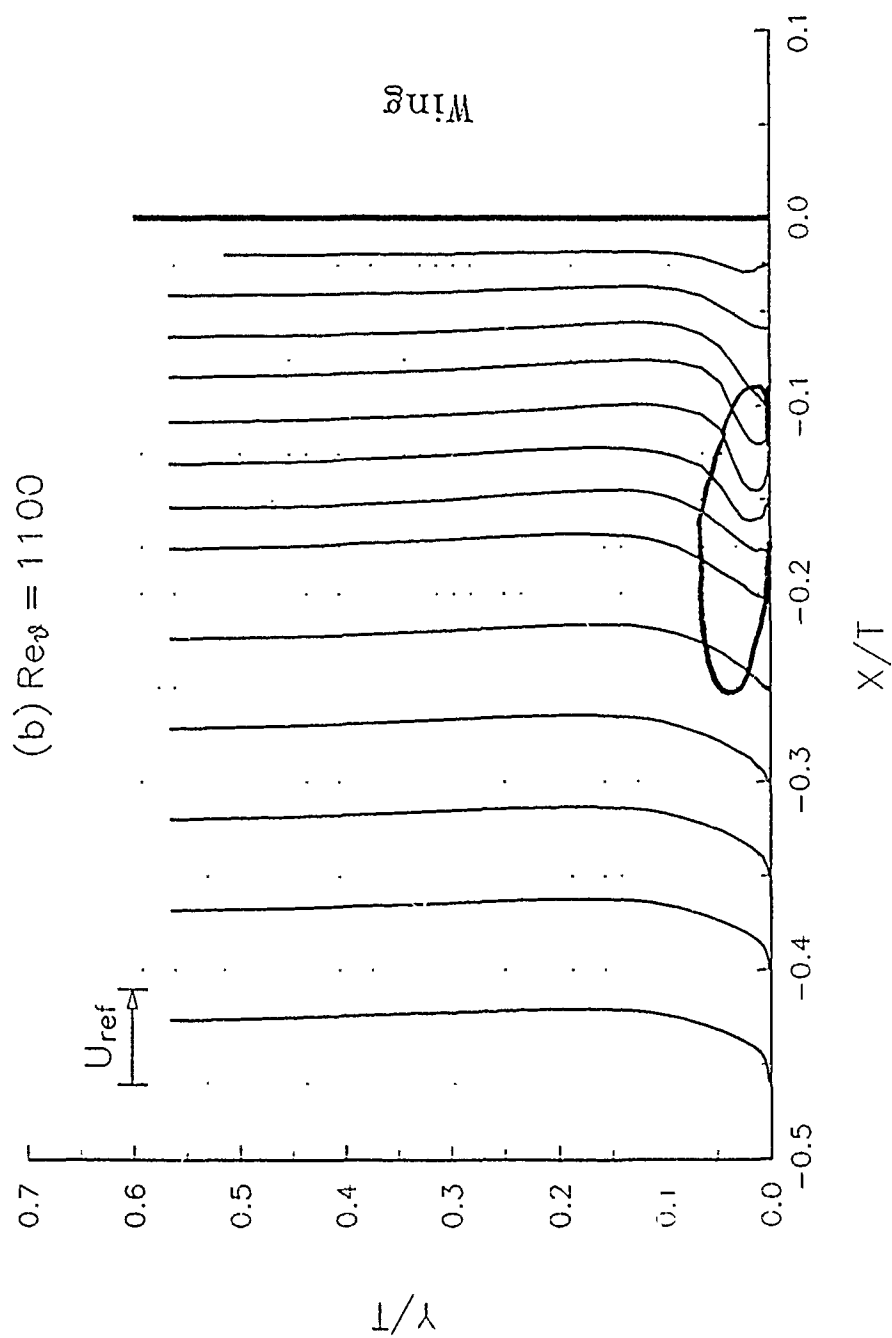
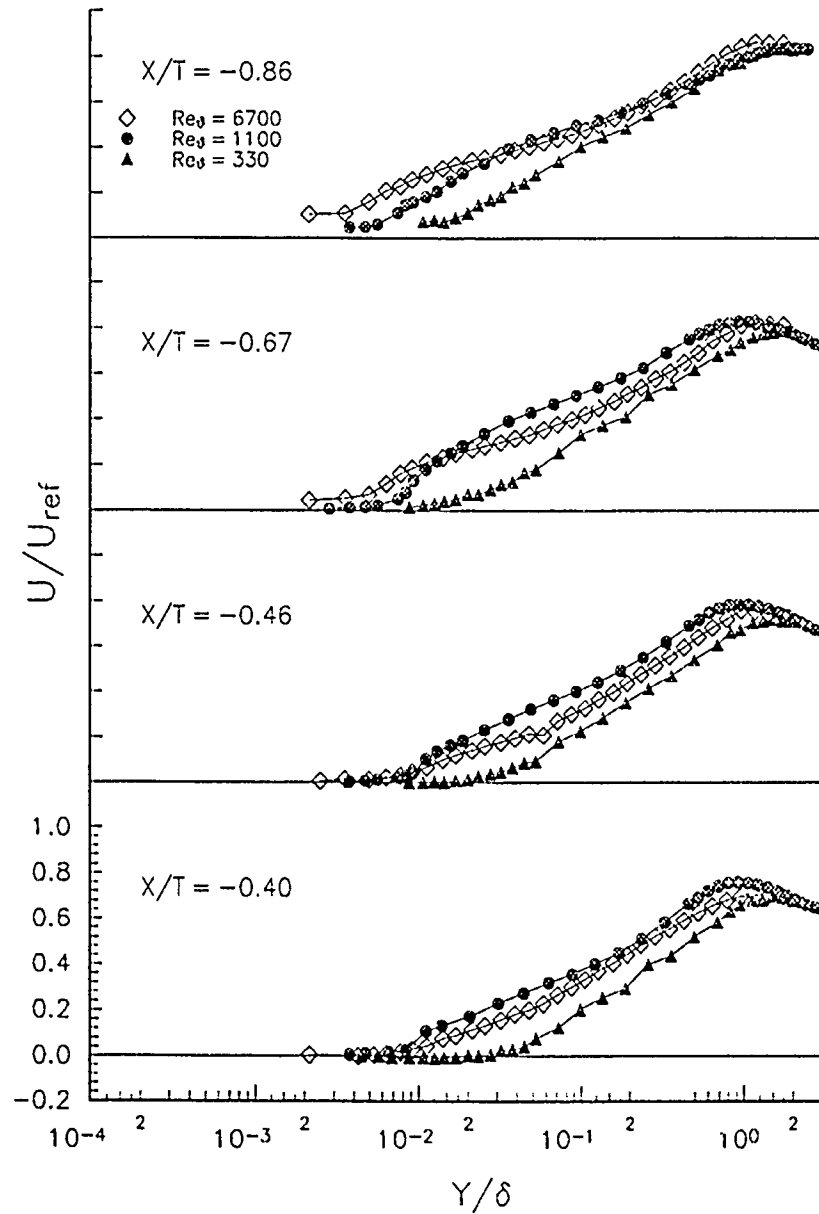


Figure 40. Concluded



**Figure 41.** Mean velocity profile comparison for three Reynolds numbers at each measurement location ( $Re_\theta = 330$  and  $Re_\theta = 1100$  — present data :  $Re_\theta = 6700$  — Devenport and Simpson (1990b))

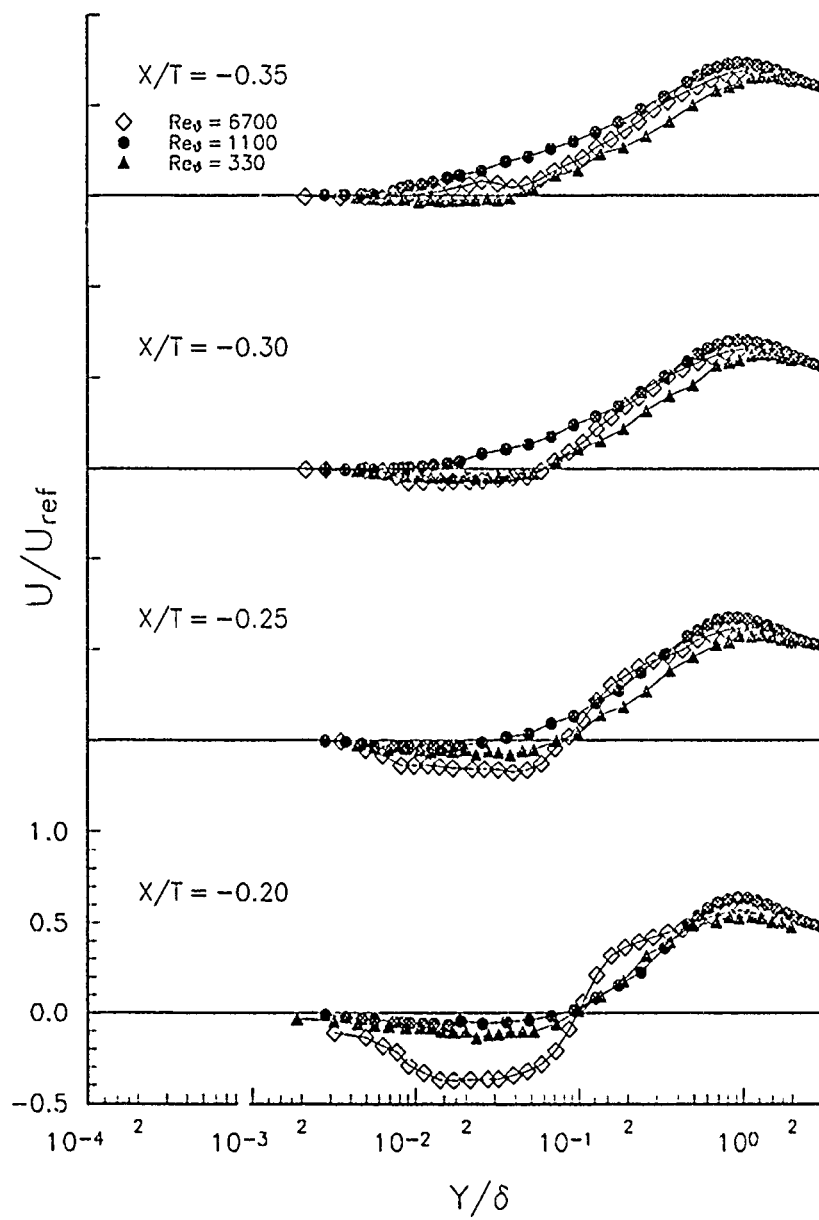


Figure 41. Continued

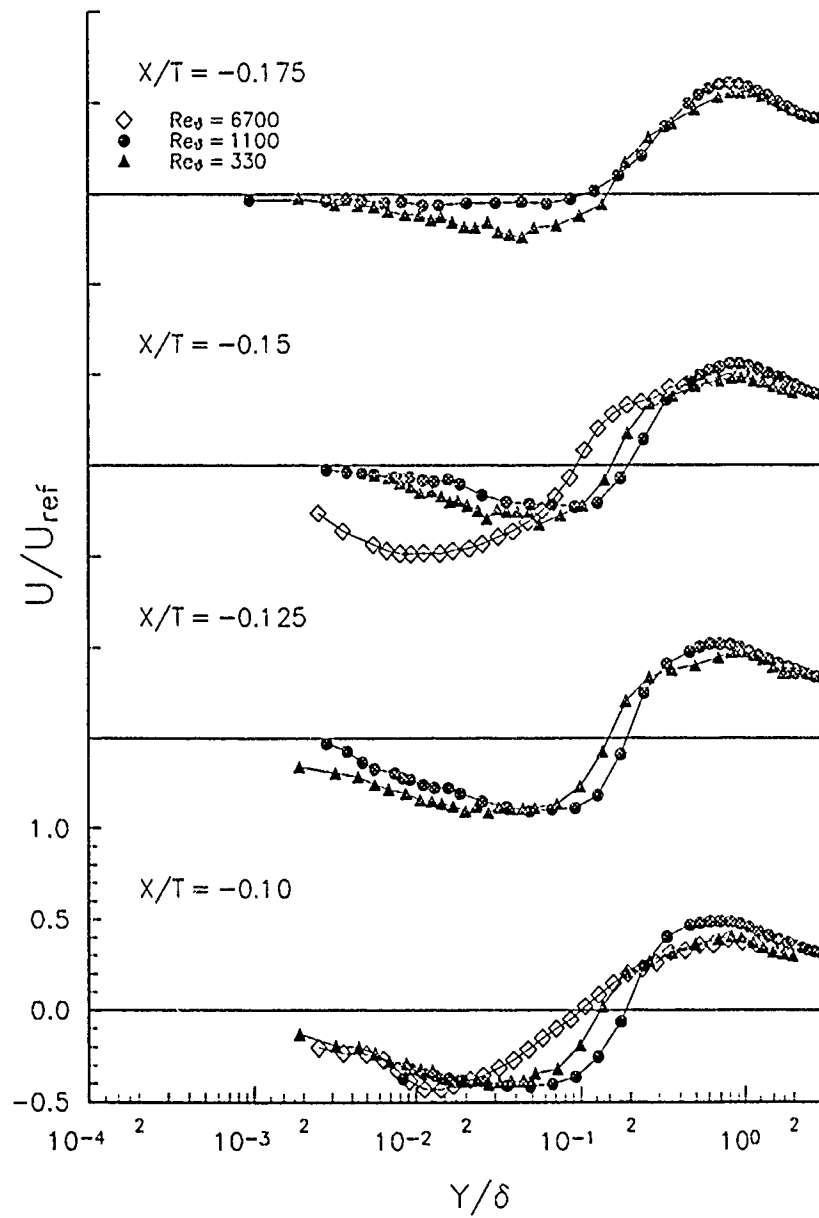


Figure 41. Continued

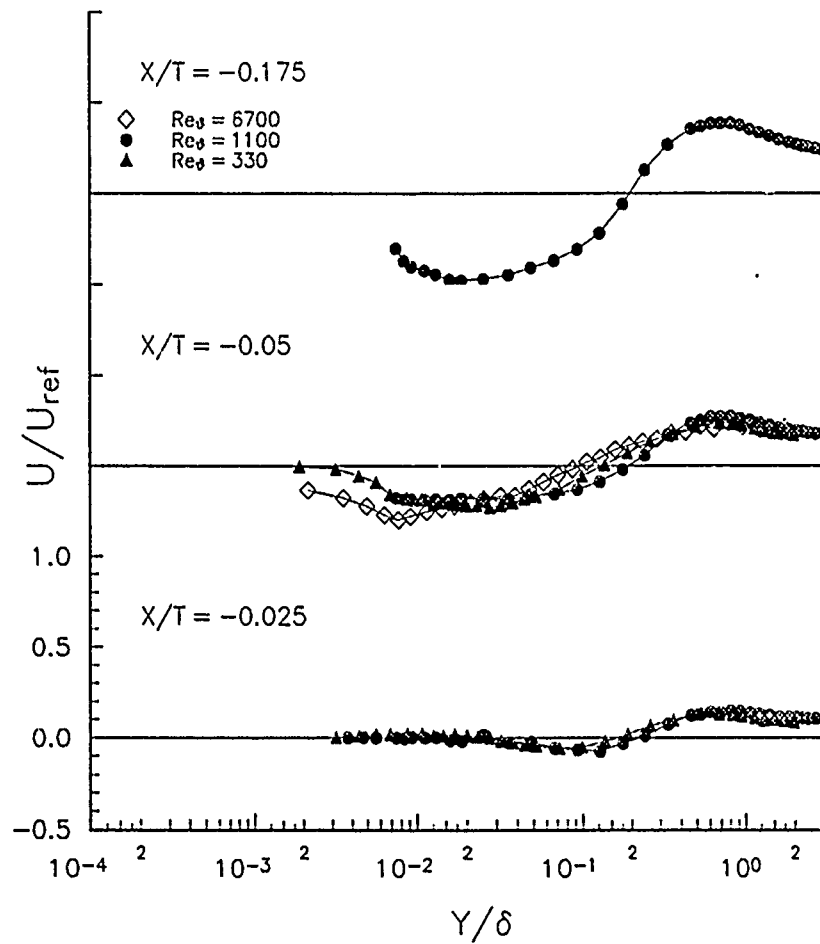
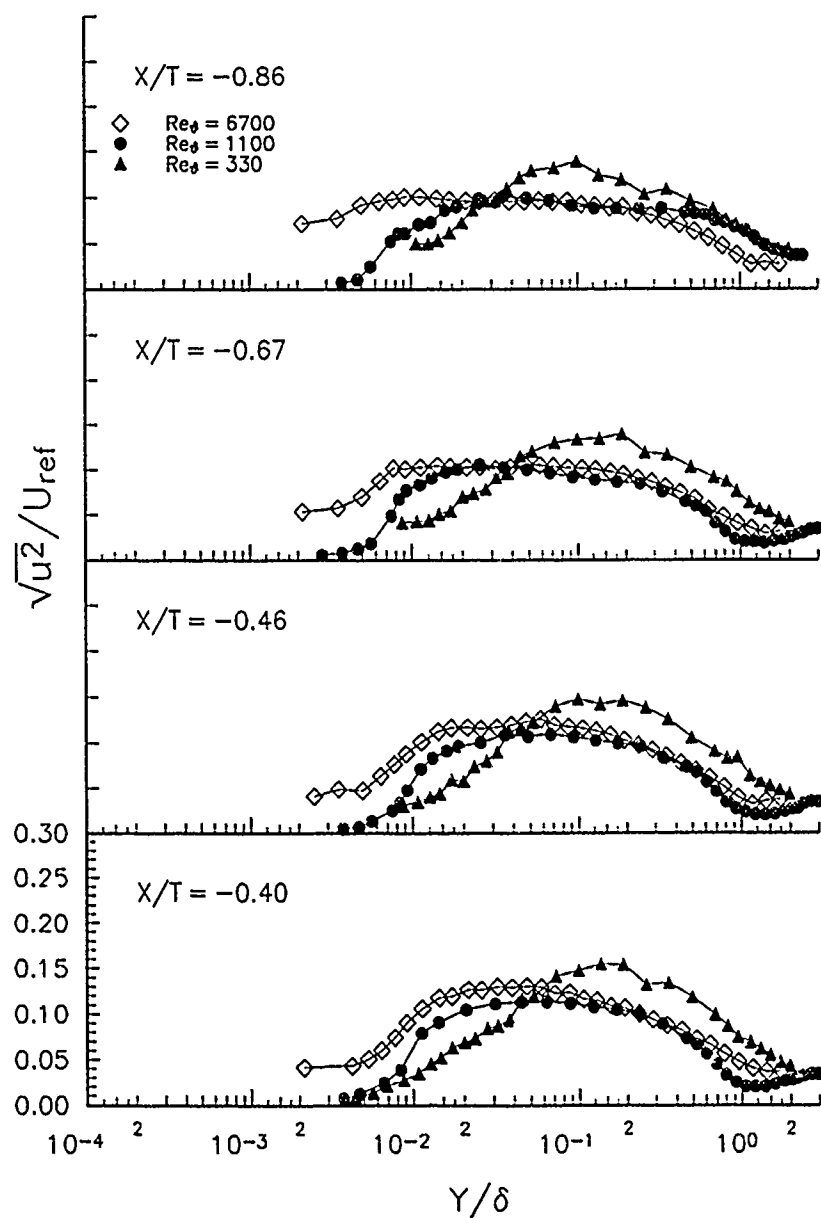


Figure 41. Concluded



**Figure 42.** U-component turbulent fluctuations for three Reynolds numbers at each measurement location ( $Re_\theta = 330$  and  $Re_\theta = 1100$  — present data :  $Re_\theta = 6700$  — Devenport and Simpson (1990b))

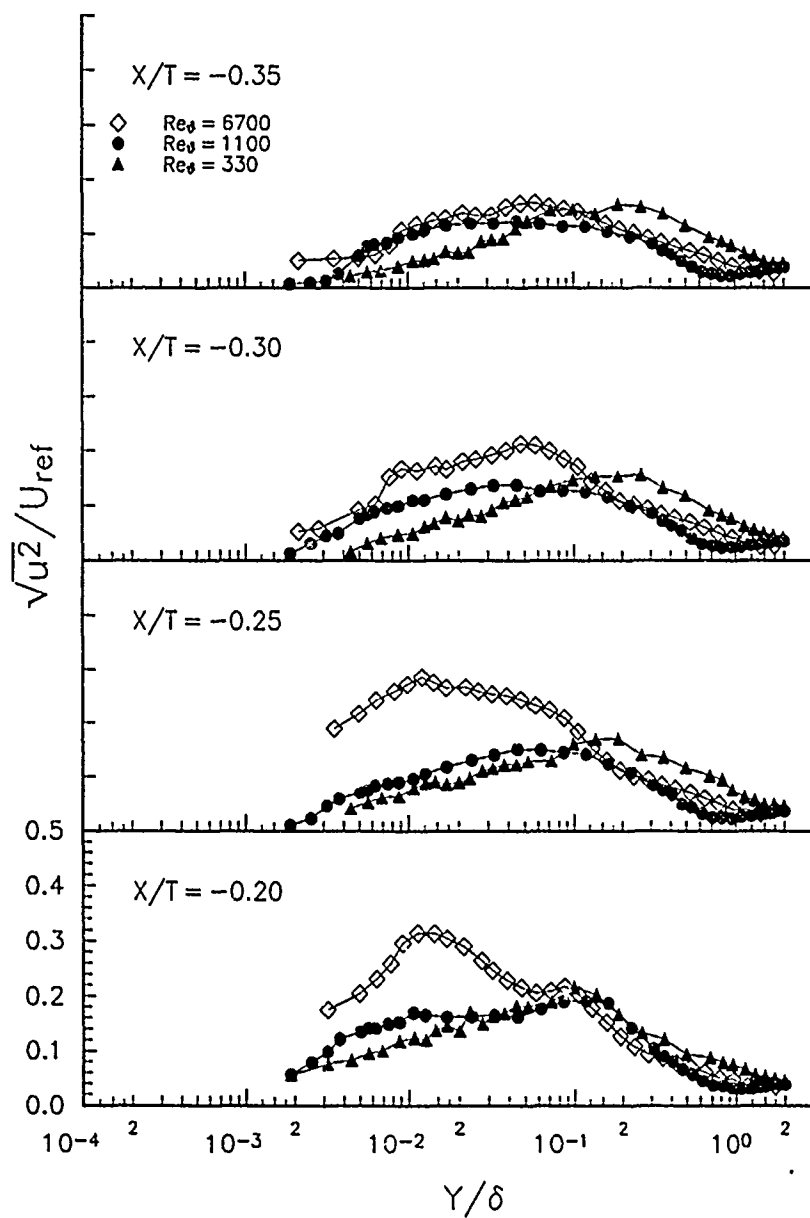


Figure 42. Continued



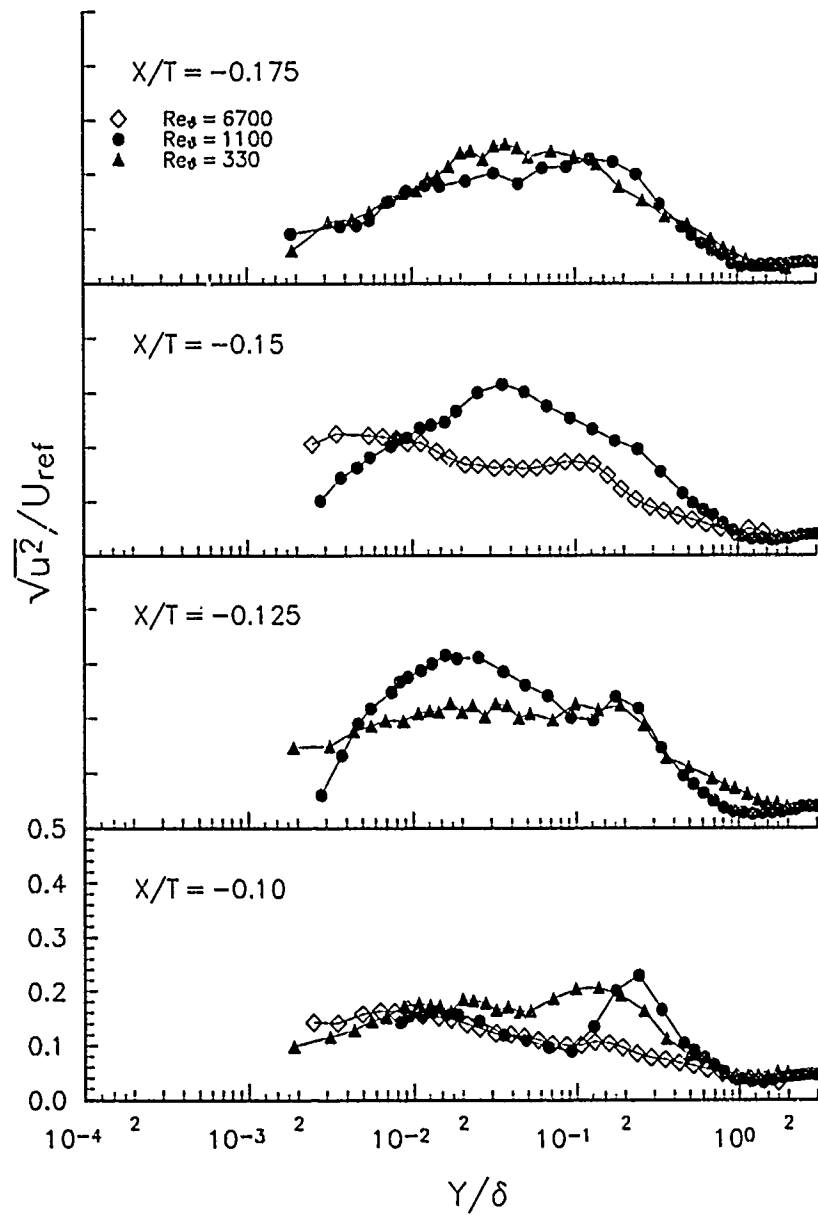


Figure 42. Continued

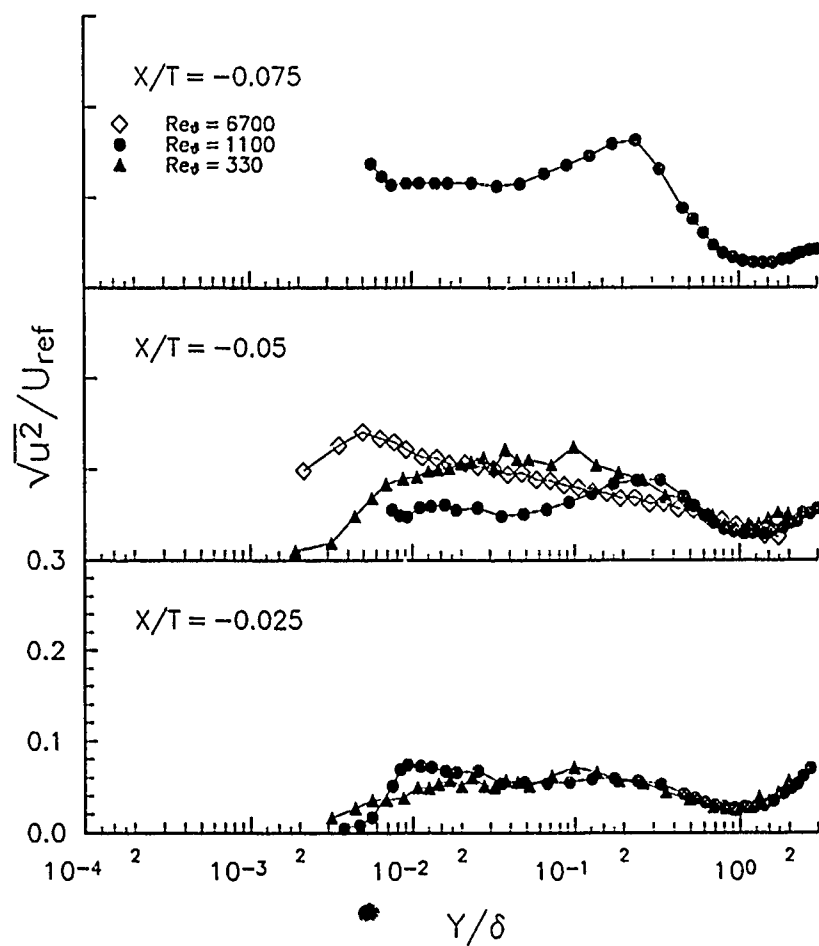


Figure 42. Concluded

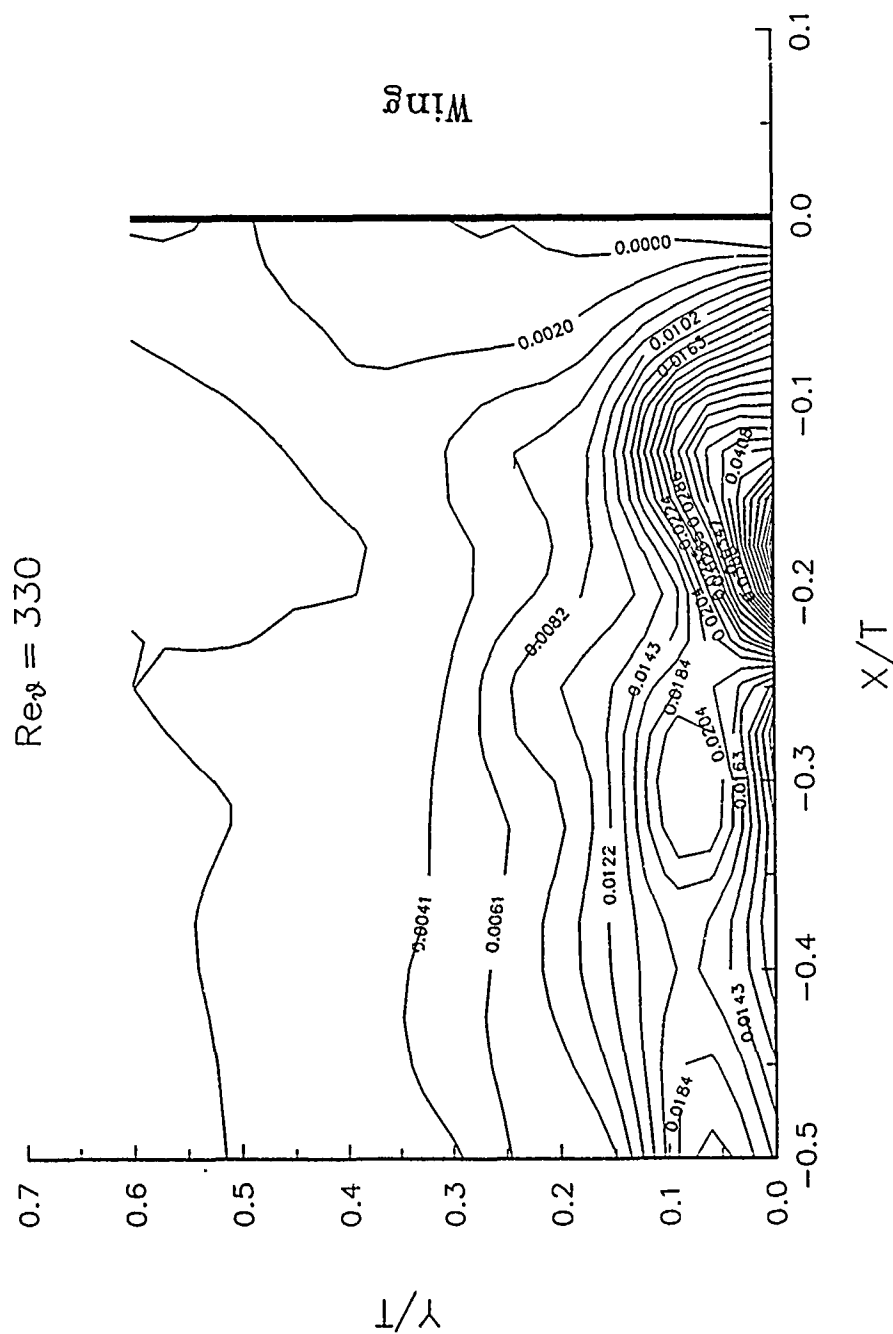


Figure 43.(a). Contour plot for the  $\overline{w^2}$  upstream of the nose of the wing-body junction for  $Re_\theta = 330$

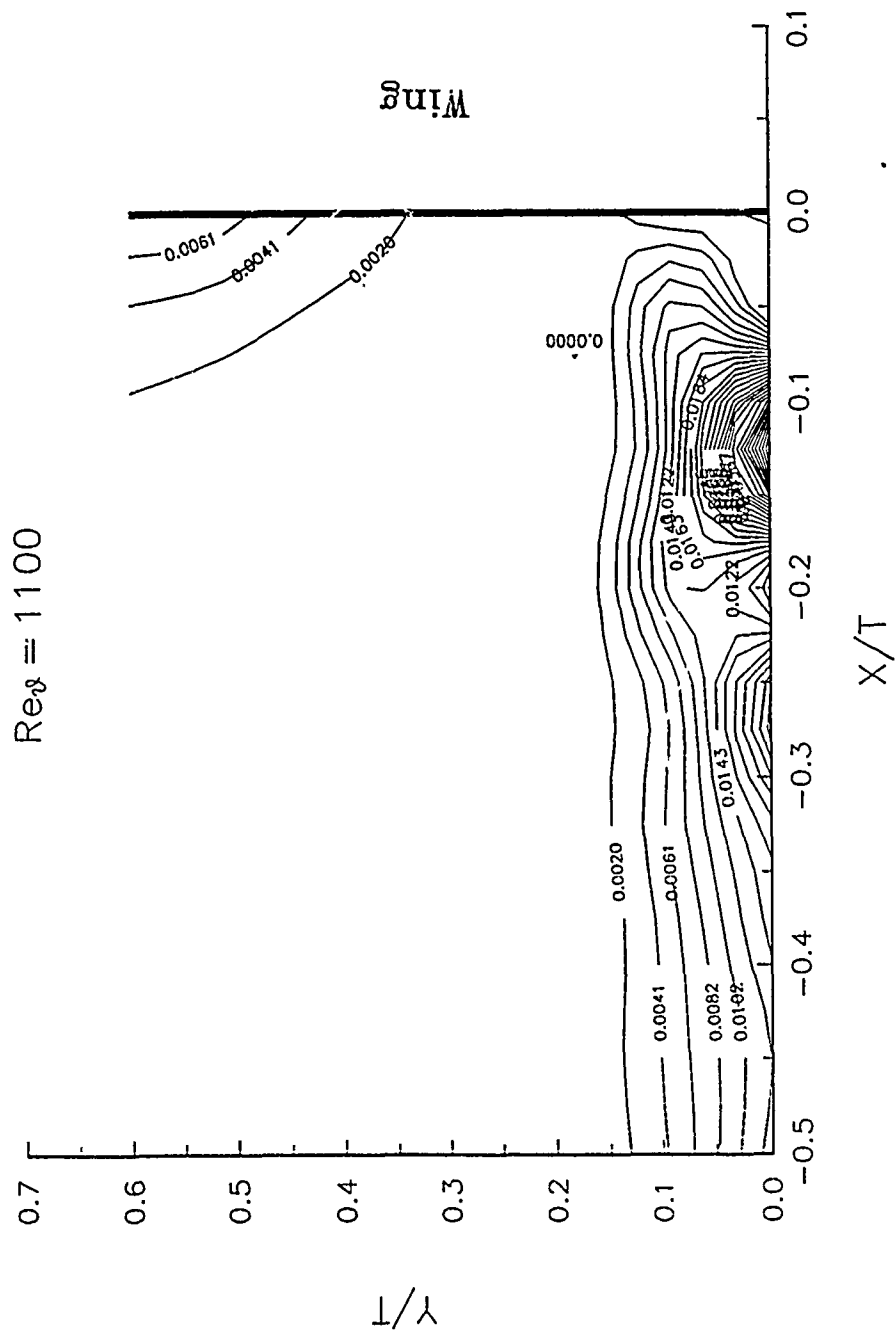
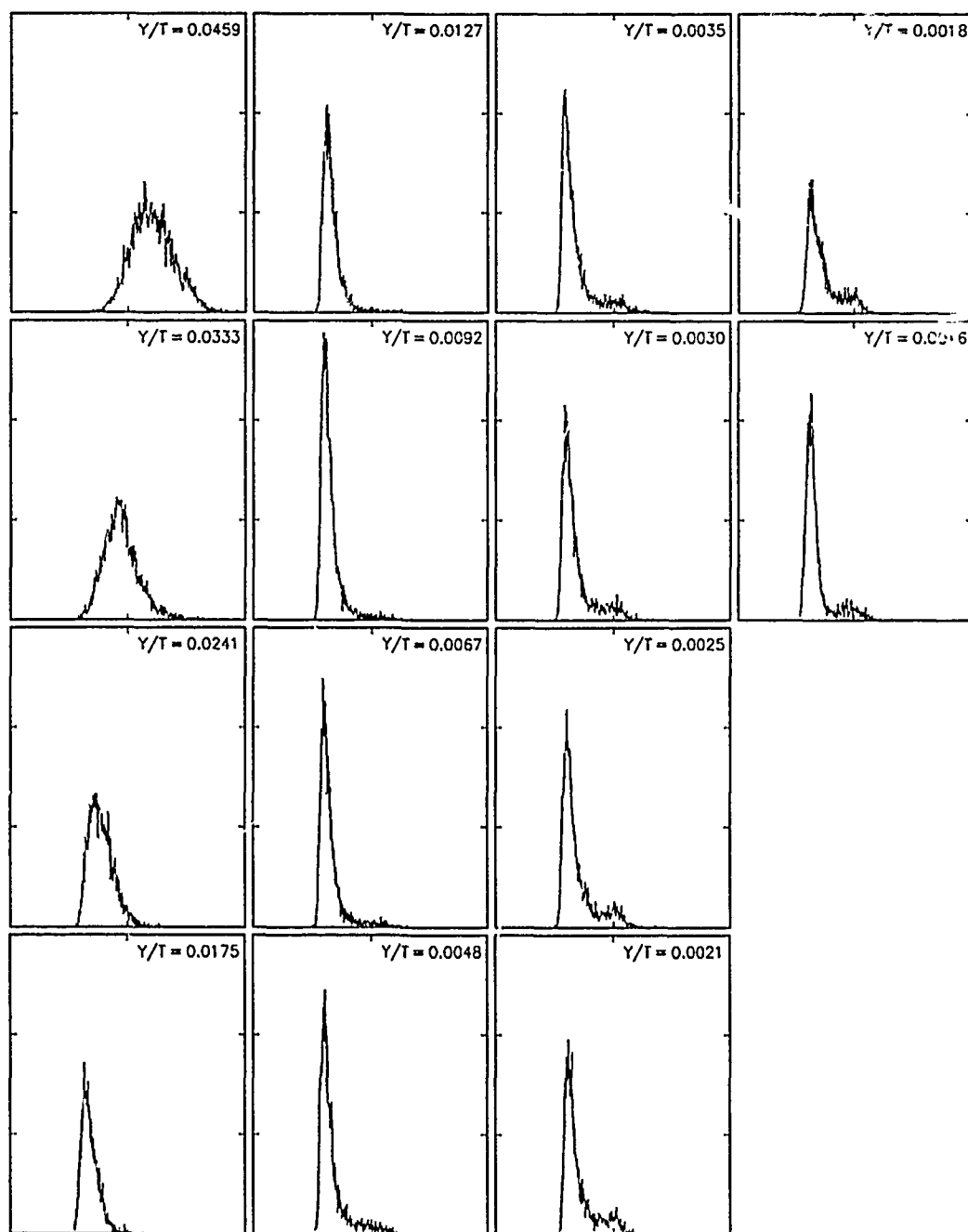
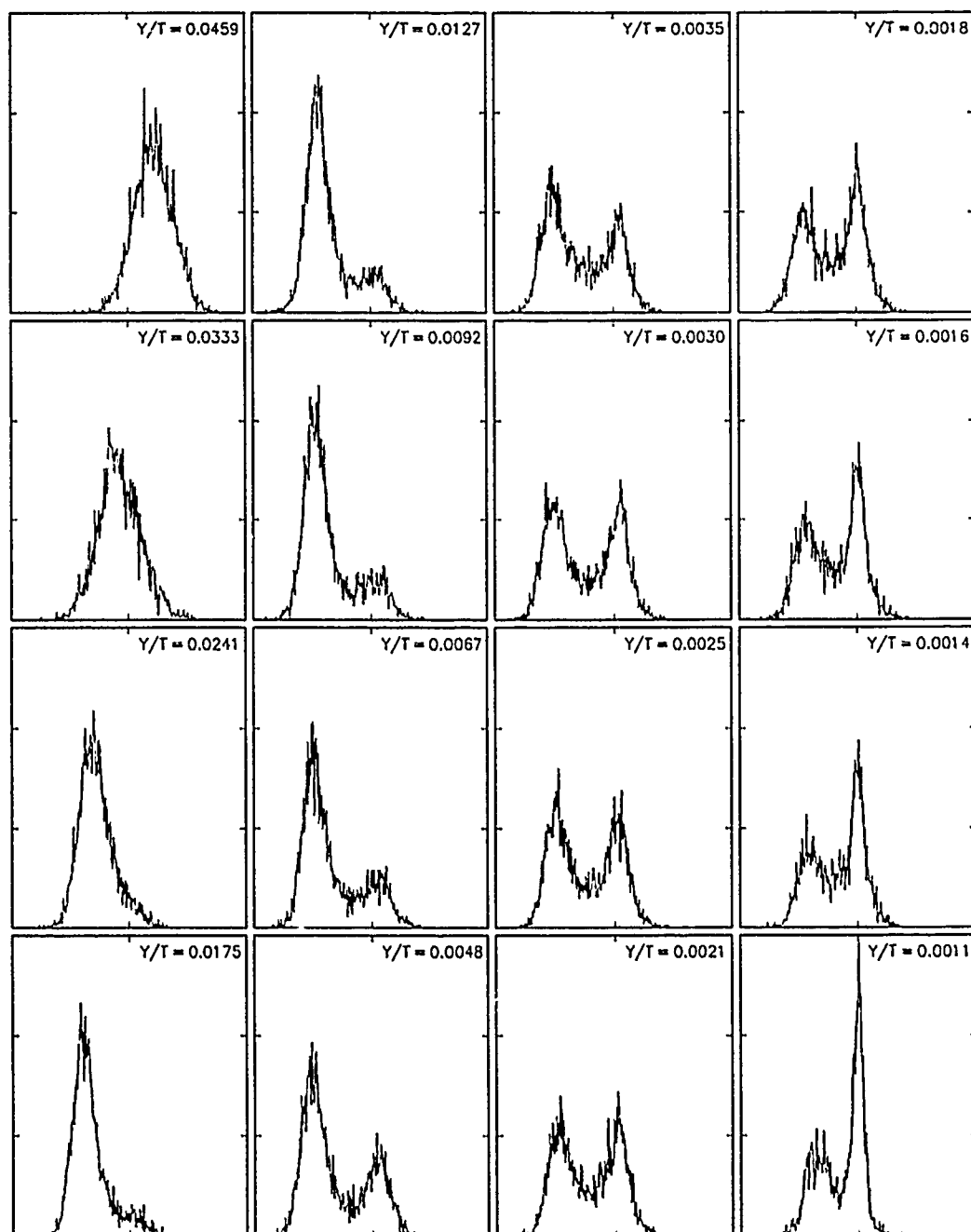


Figure 43.(b). Contour plot for the  $\overline{u'^2}$  upstream of the nose of the wing-body junction for  $Re_\theta = 1100$



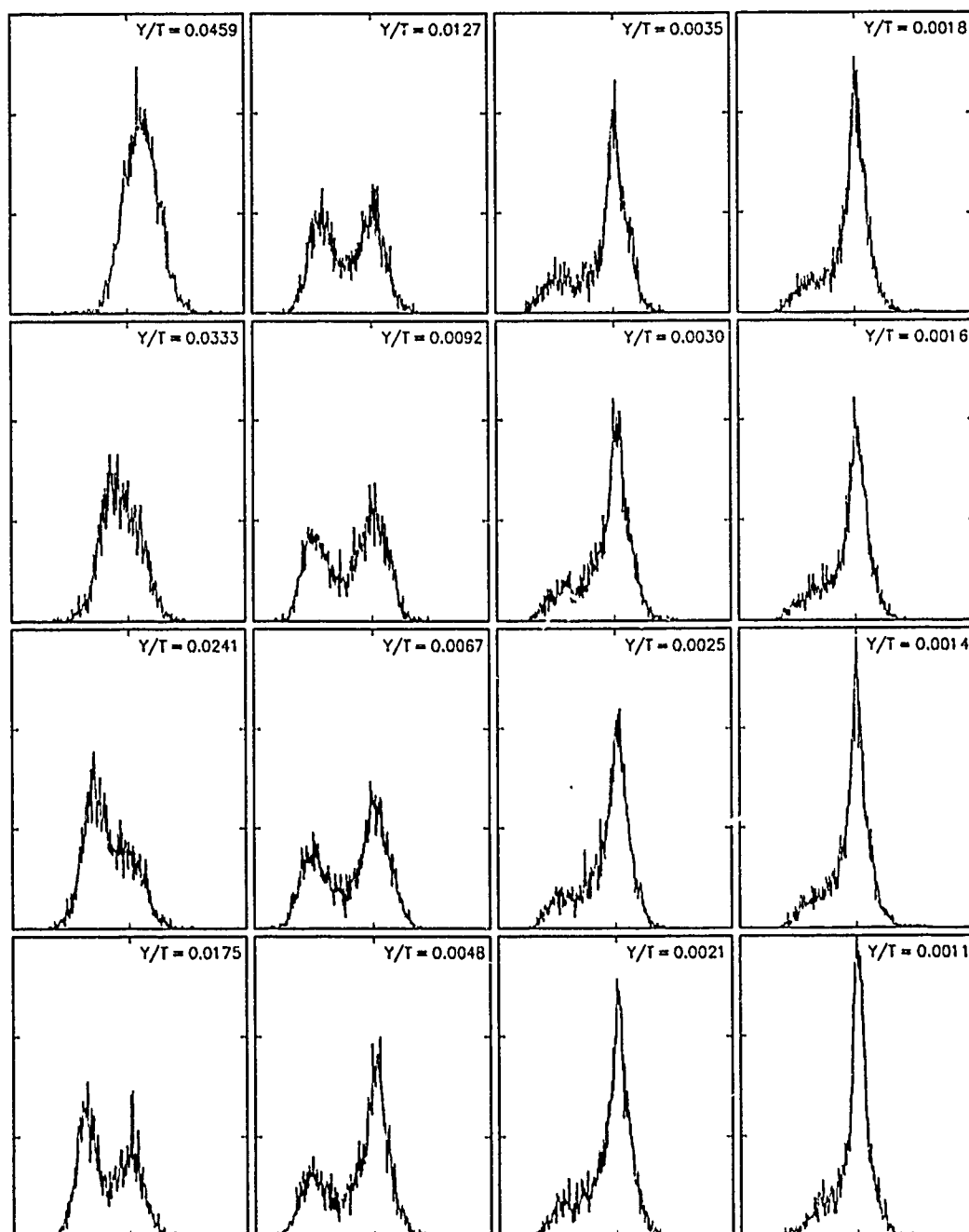
(a) for  $Re_\theta = 1100$  at  $X/T = -0.10$

Figure 44. Velocity histograms across the boundary layer



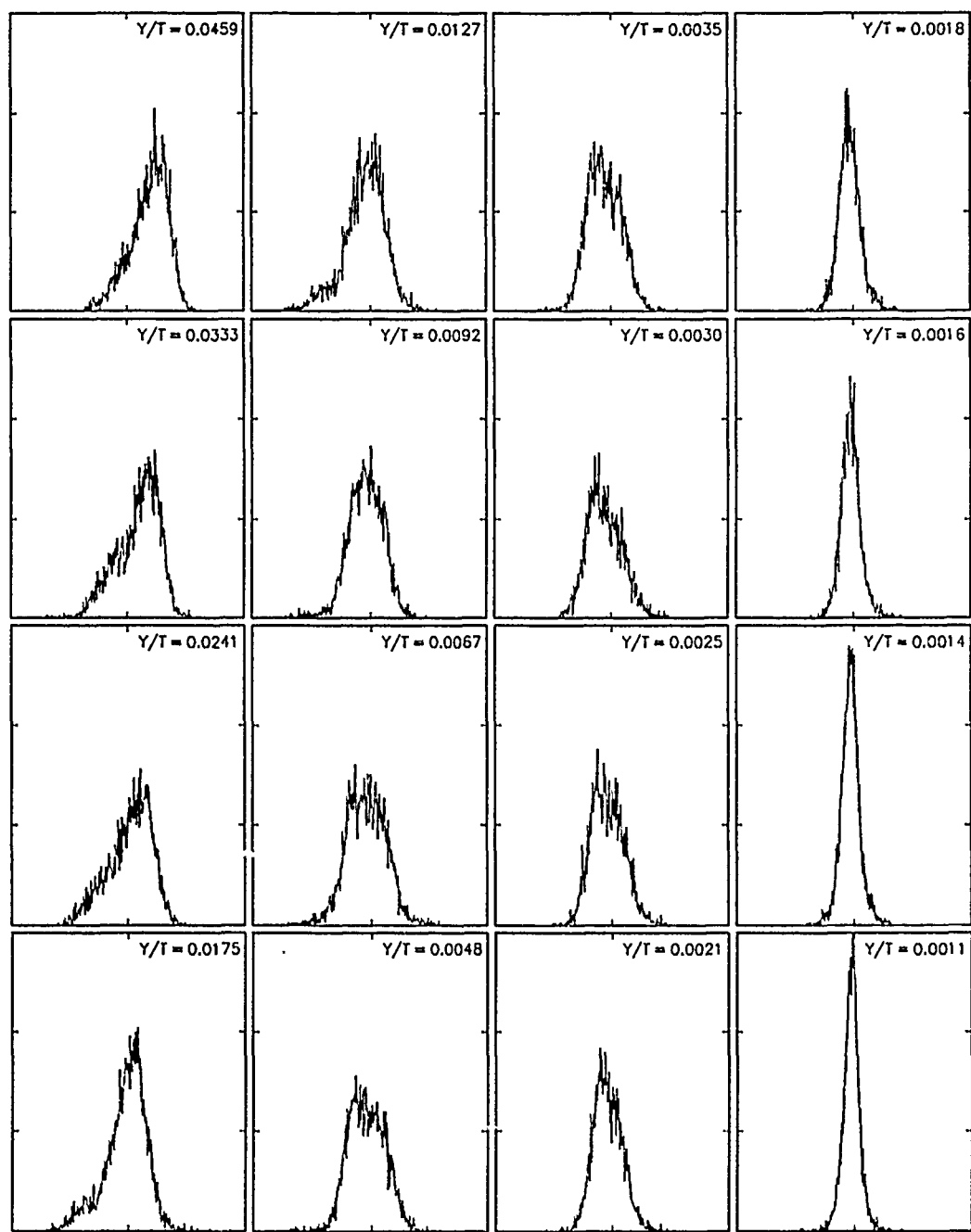
(b) for  $Re_\theta = 1100$  at  $X/T = -0.125$

Figure 44. Continued



(c) for  $Re_\theta = 1100$  at  $X/T = -0.150$

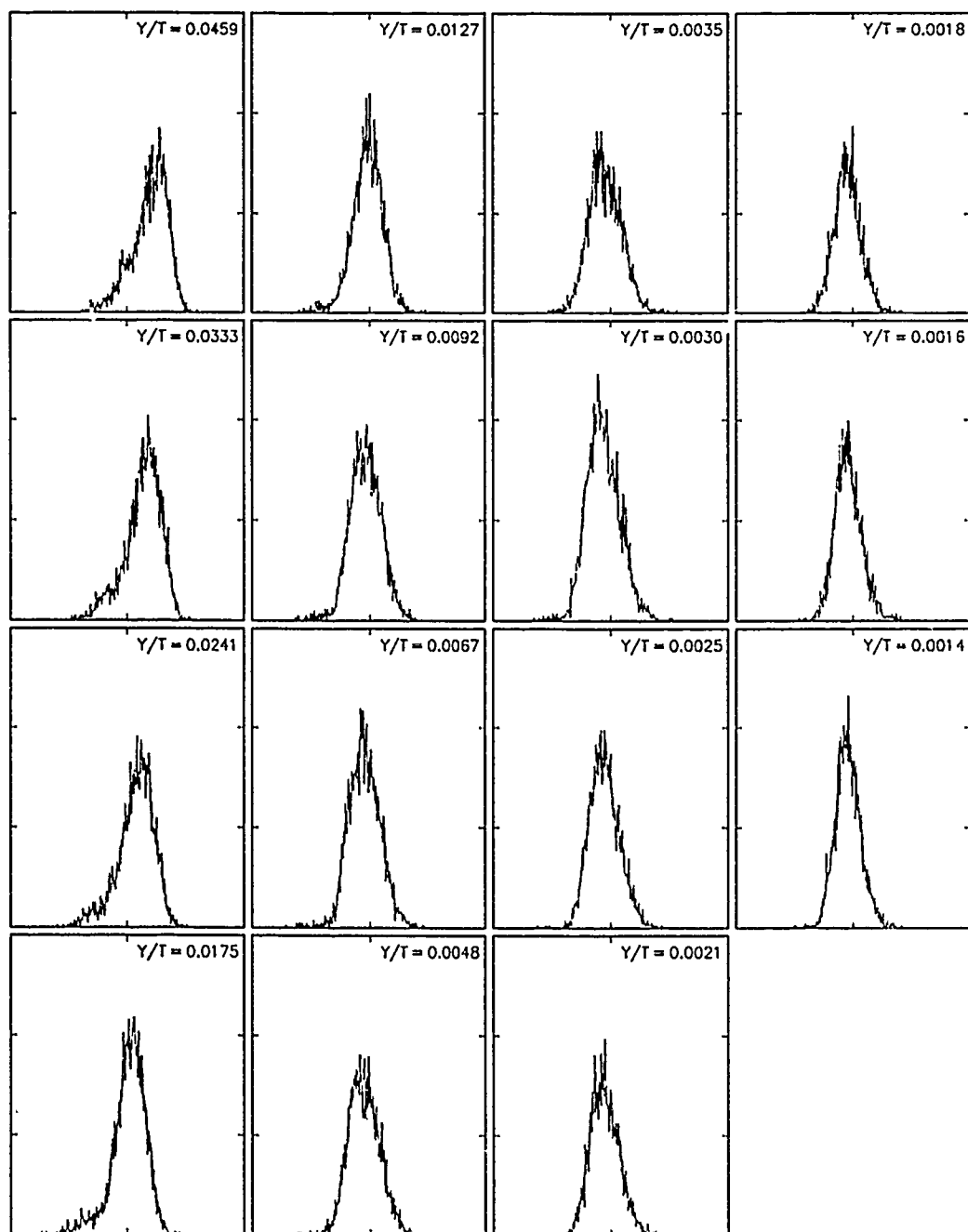
Figure 44. Continued



(d) for  $Re_\theta = 1100$  at  $X/T = -0.175$

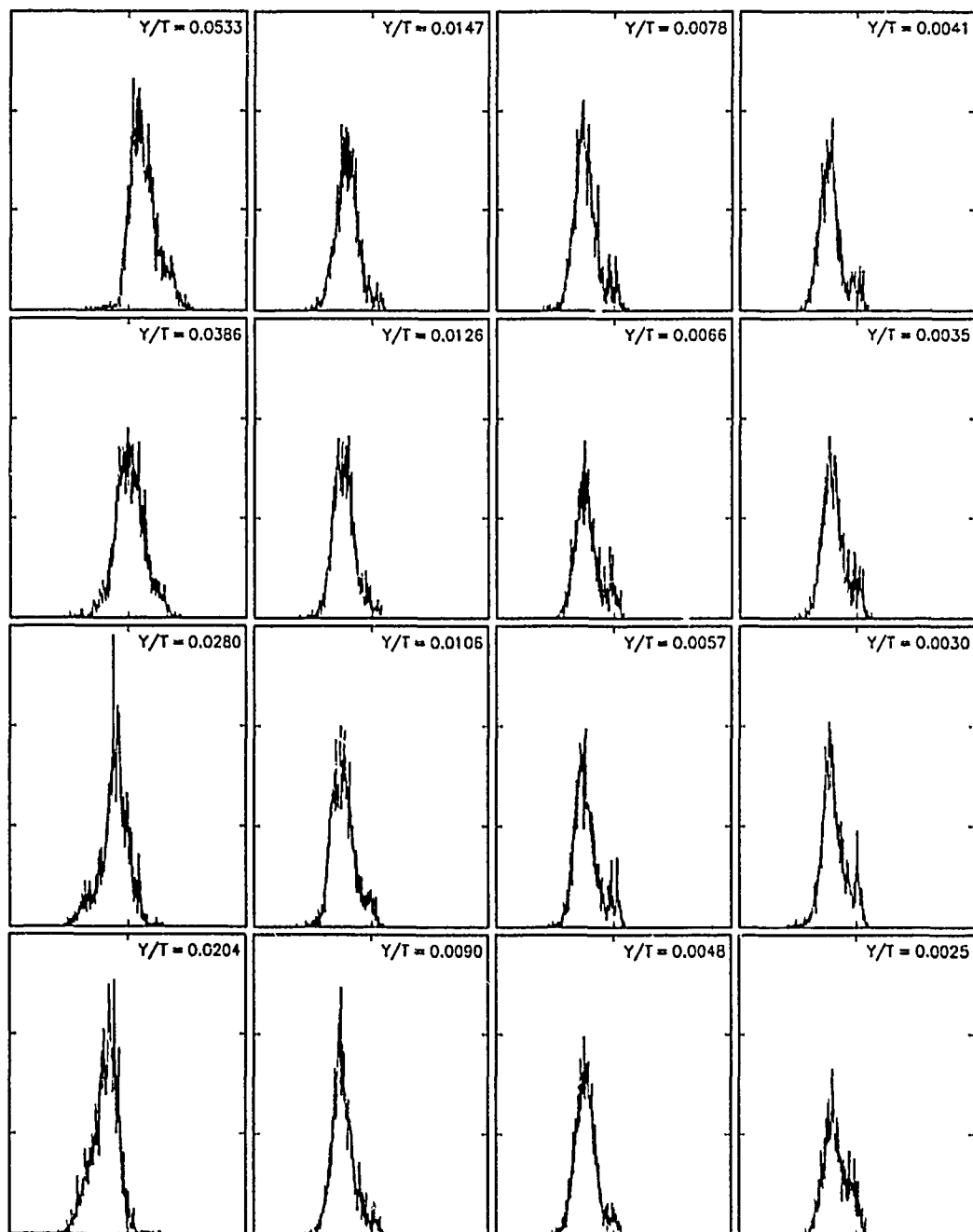
Figure 44. Continued





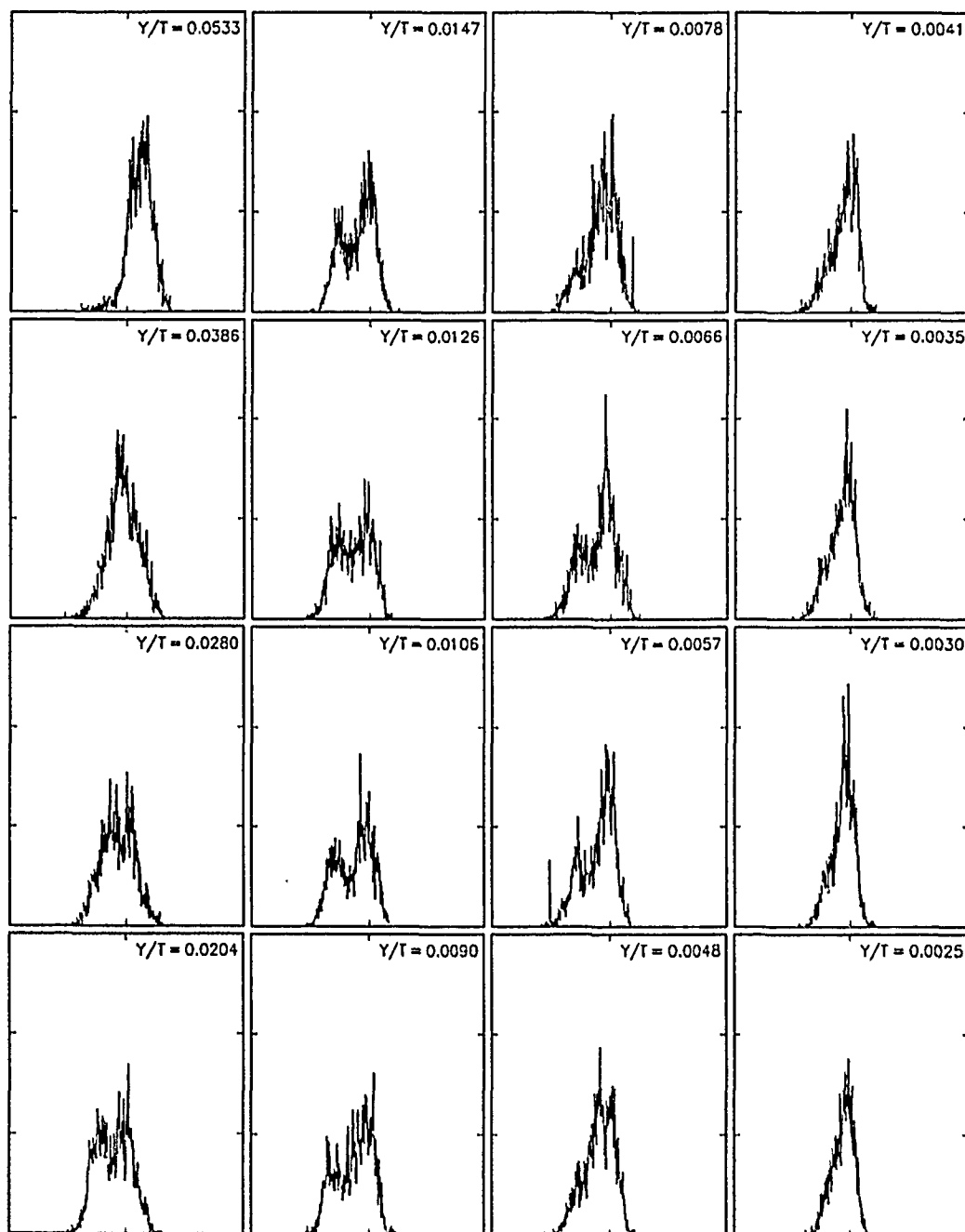
(e) for  $Re_\theta = 1100$  at  $X/T = -0.20$

Figure 44. Continued



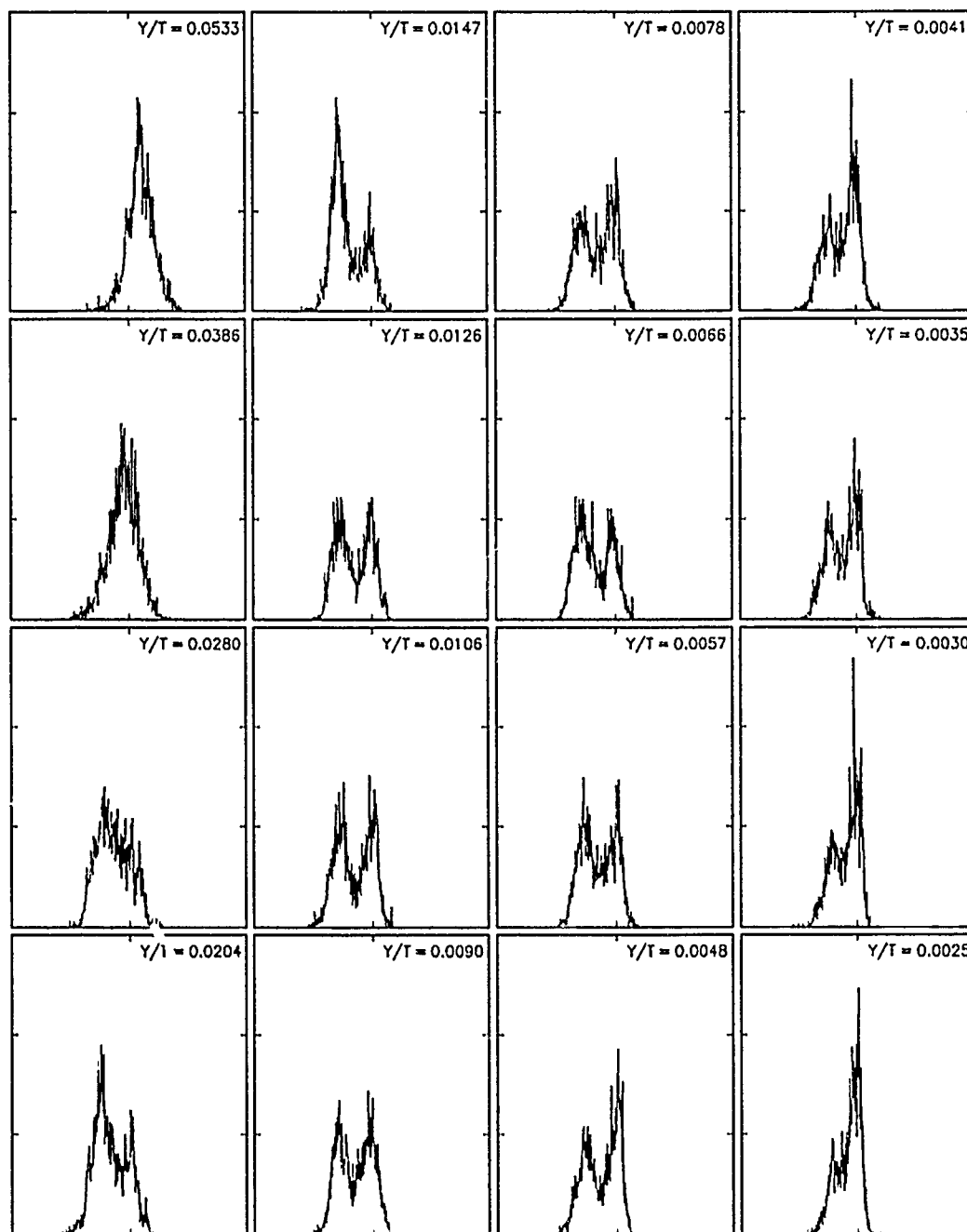
(f) for  $Re_\theta = 330$  at  $X/T = -0.10$

Figure 44. Continued



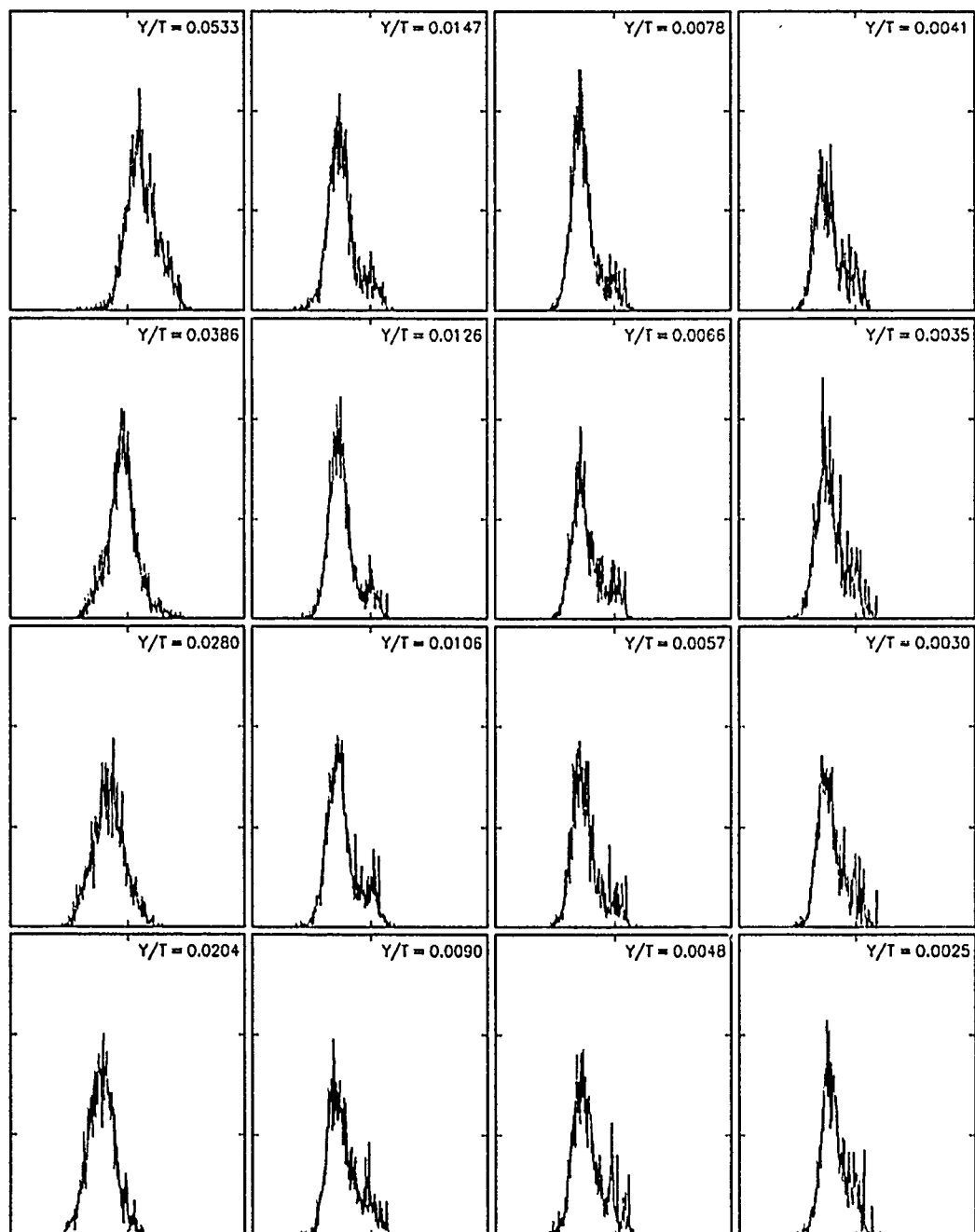
(g) for  $Re_\theta = 330$  at  $X/T = -0.125$

Figure 44. Continued



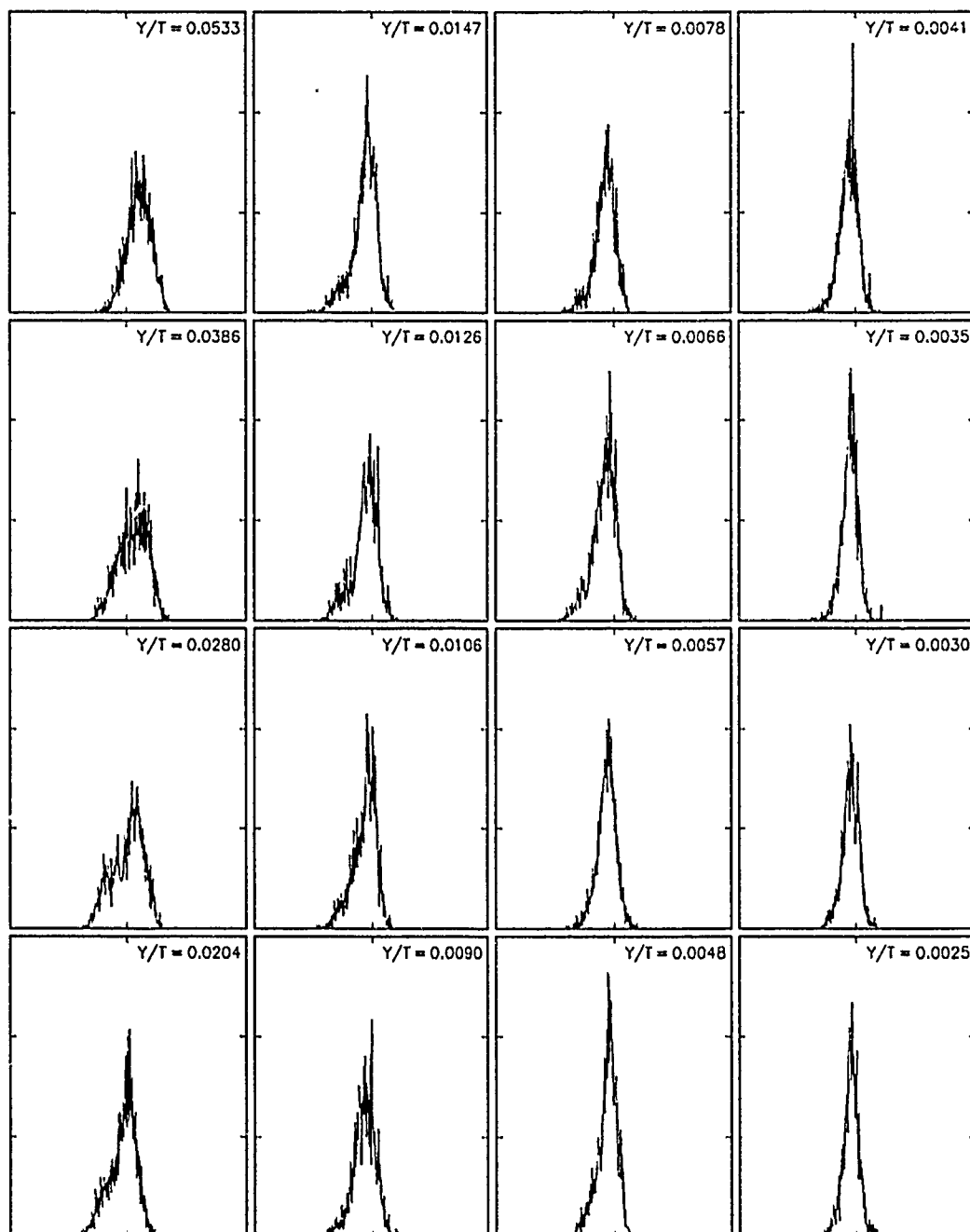
(h) for  $Re_\theta = 330$  at  $X/T = -0.150$

Figure 44. Continued



(i) for  $Re_\theta = 330$  at  $X/T = -0.175$

Figure 44. Continued



(j) for  $Re_\theta = 330$  at  $X/T = -0.20$

Figure 44. Concluded

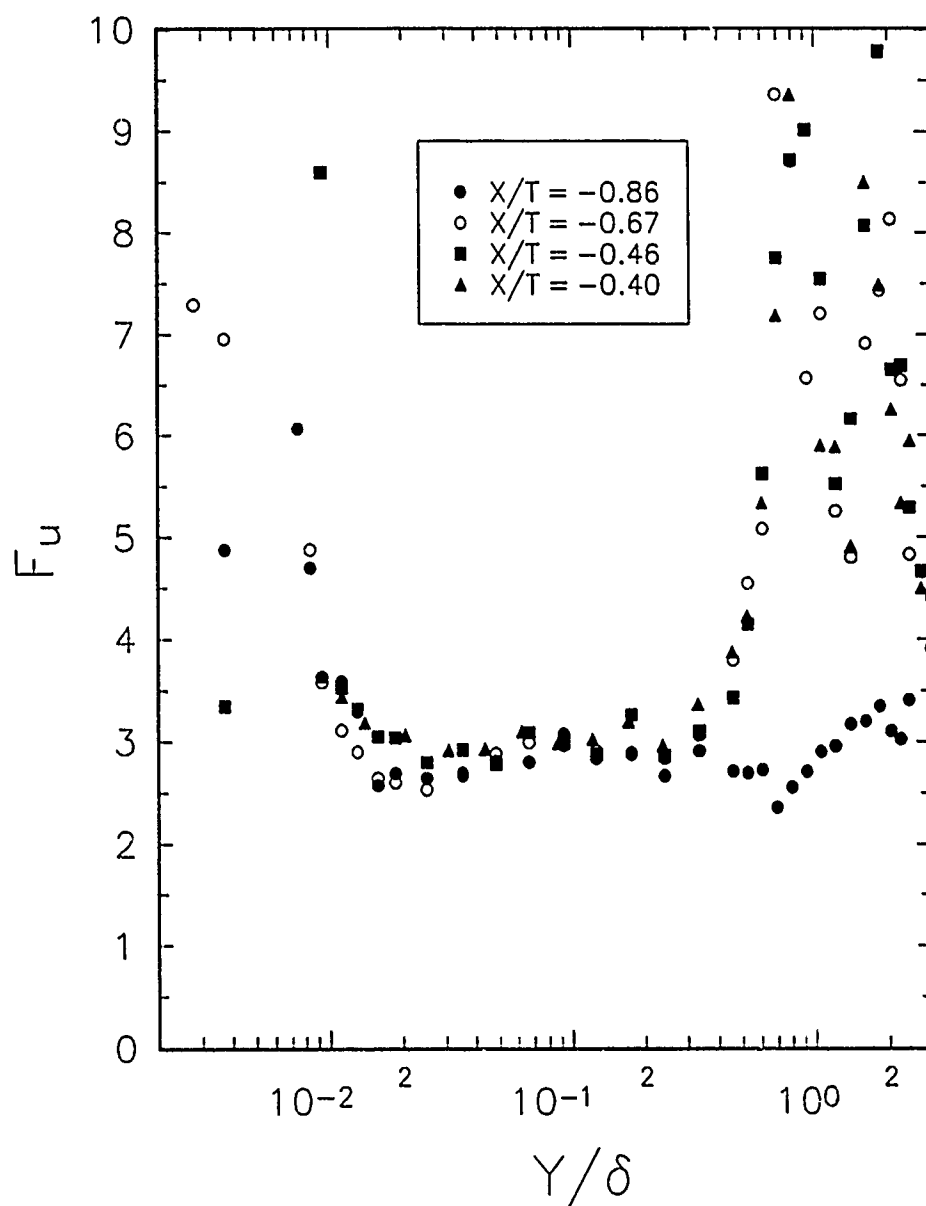


Figure 45. Flatness factor plots across the shear layer for  $Re_\theta = 1100$

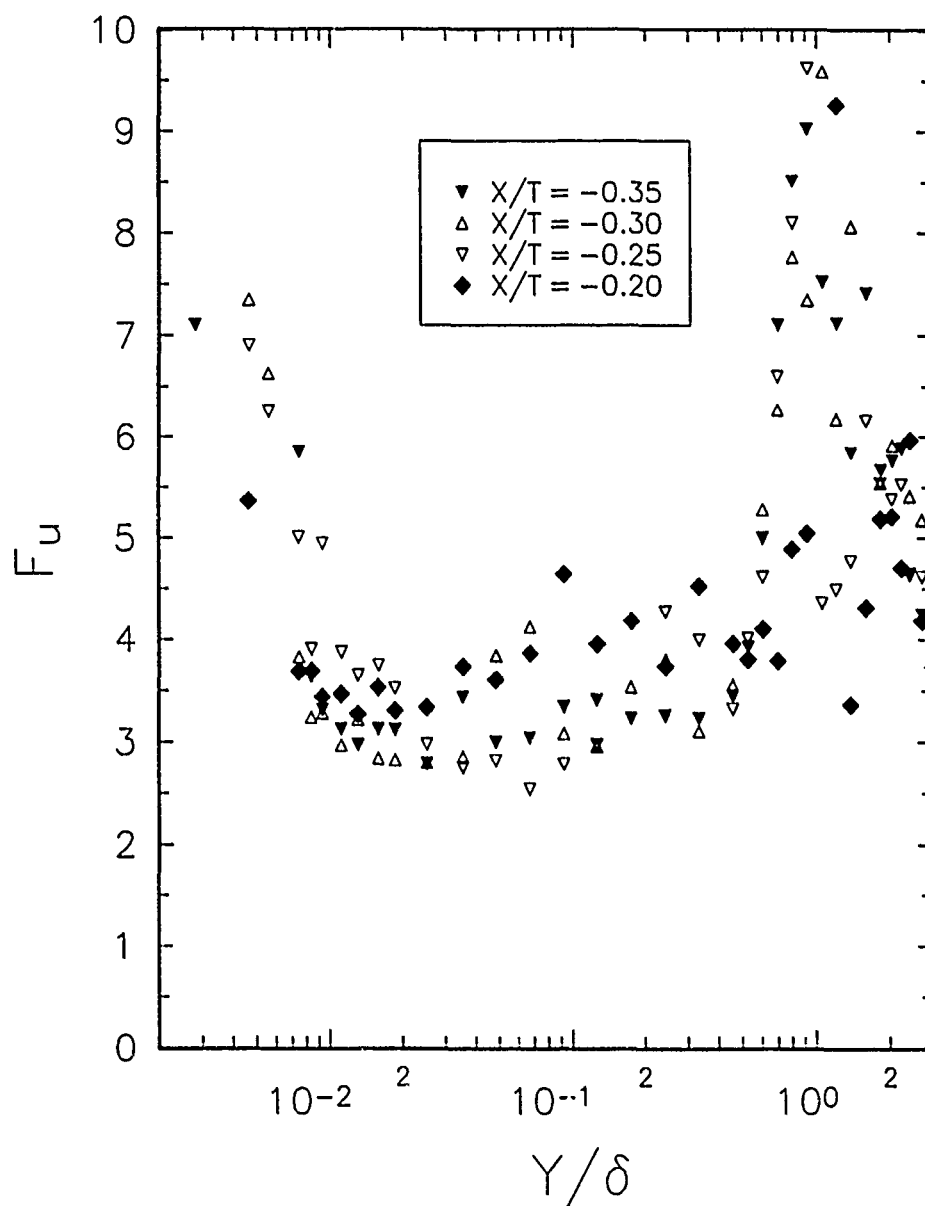


Figure 45. Continued



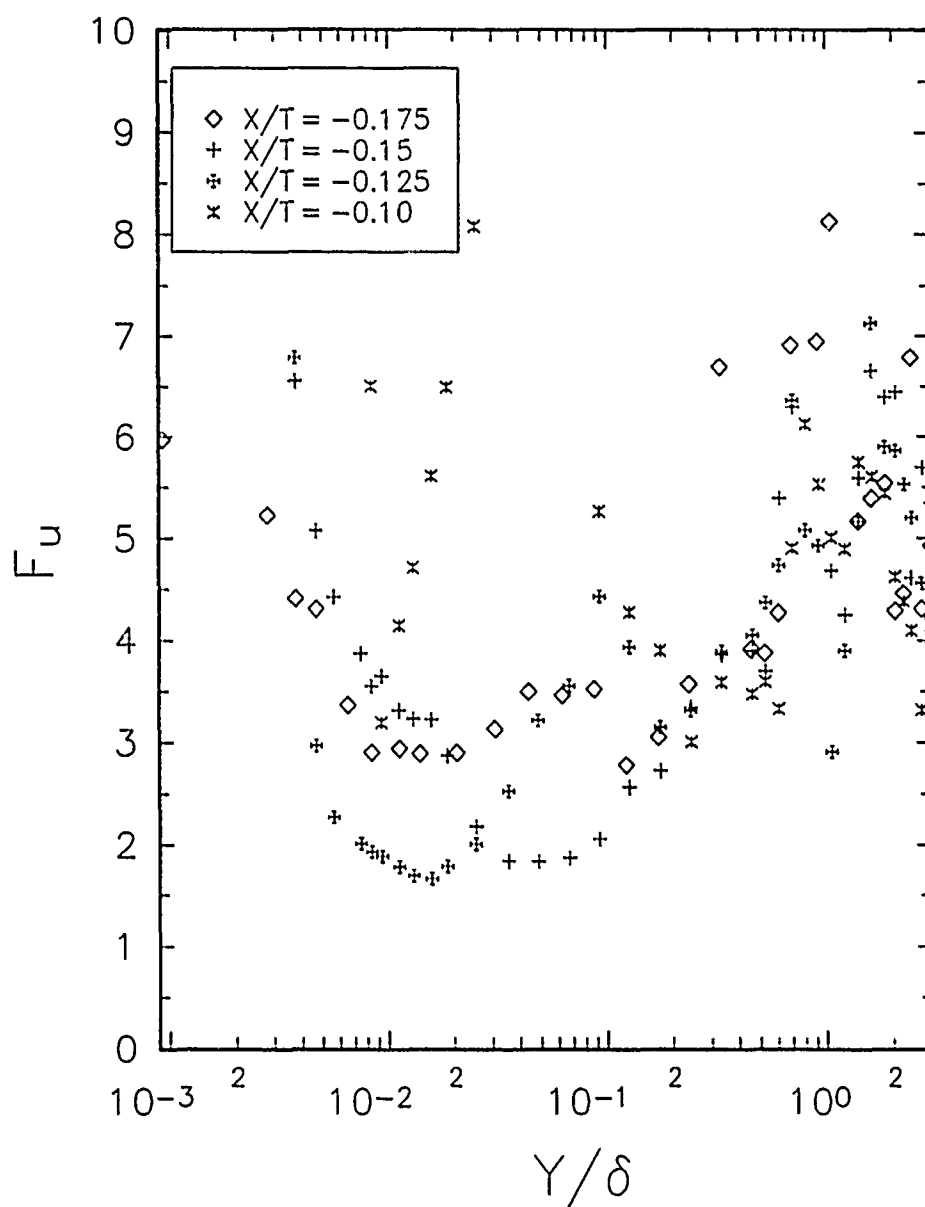


Figure 45. Continued

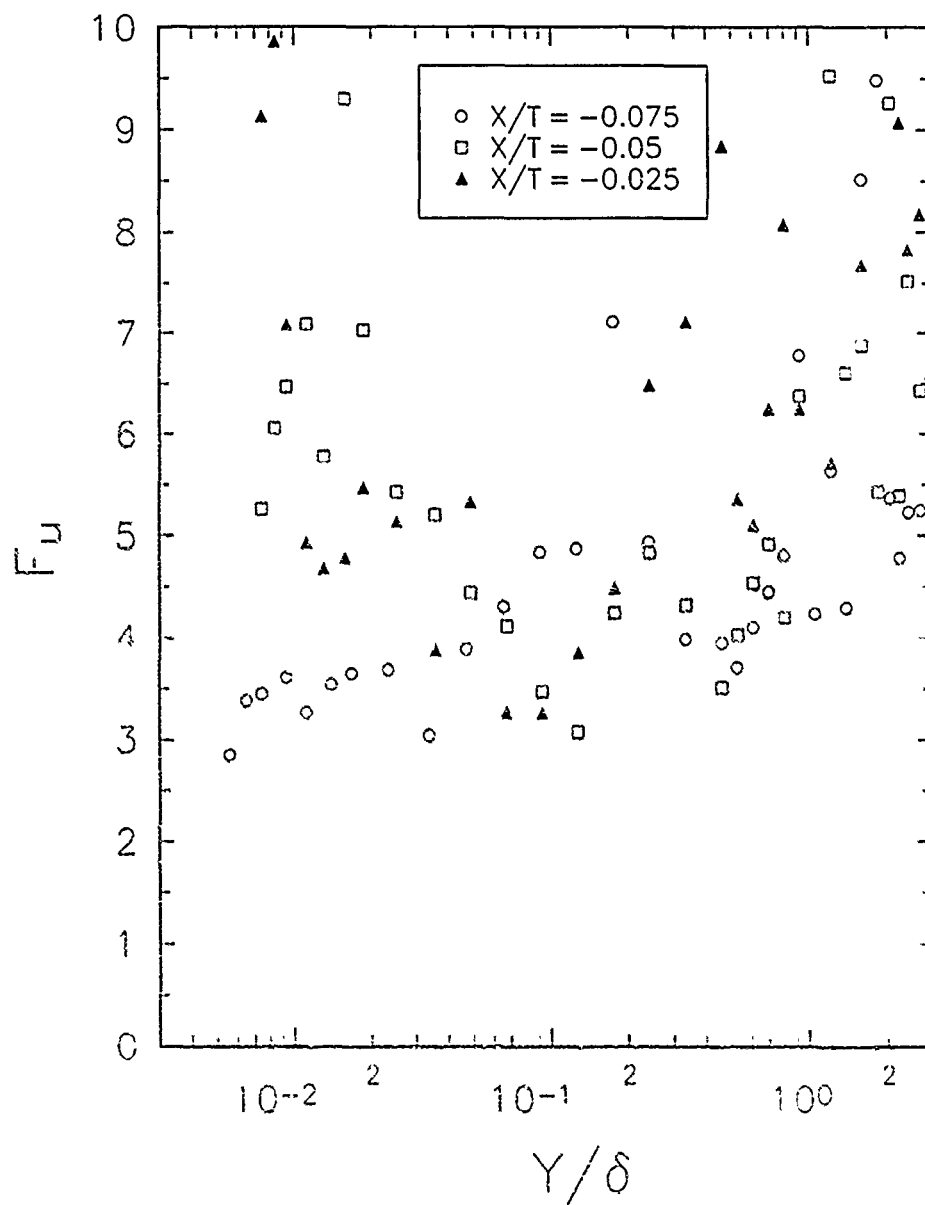
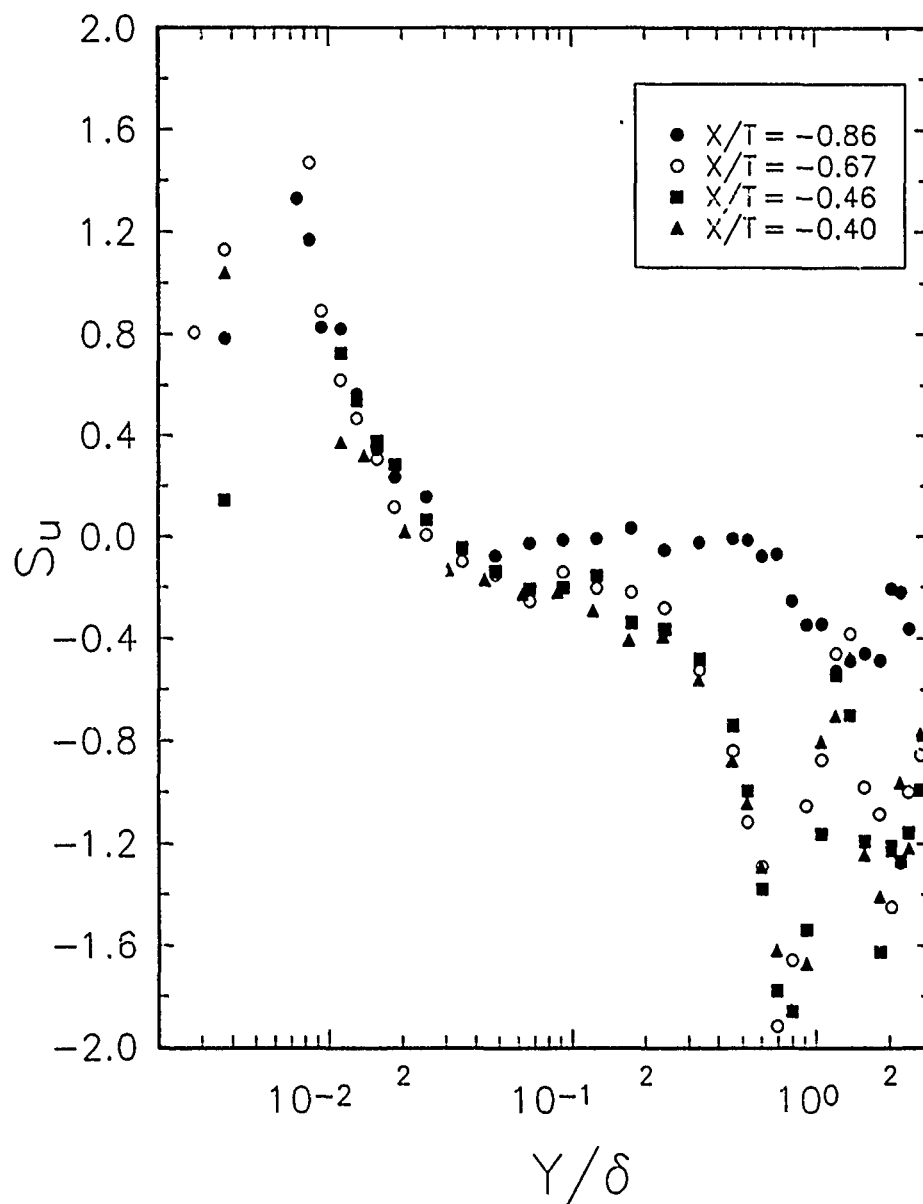


Figure 45. Concluded



**Figure 46.** Skewness factor plots across the shear layer for  $Re_\theta = 1100$

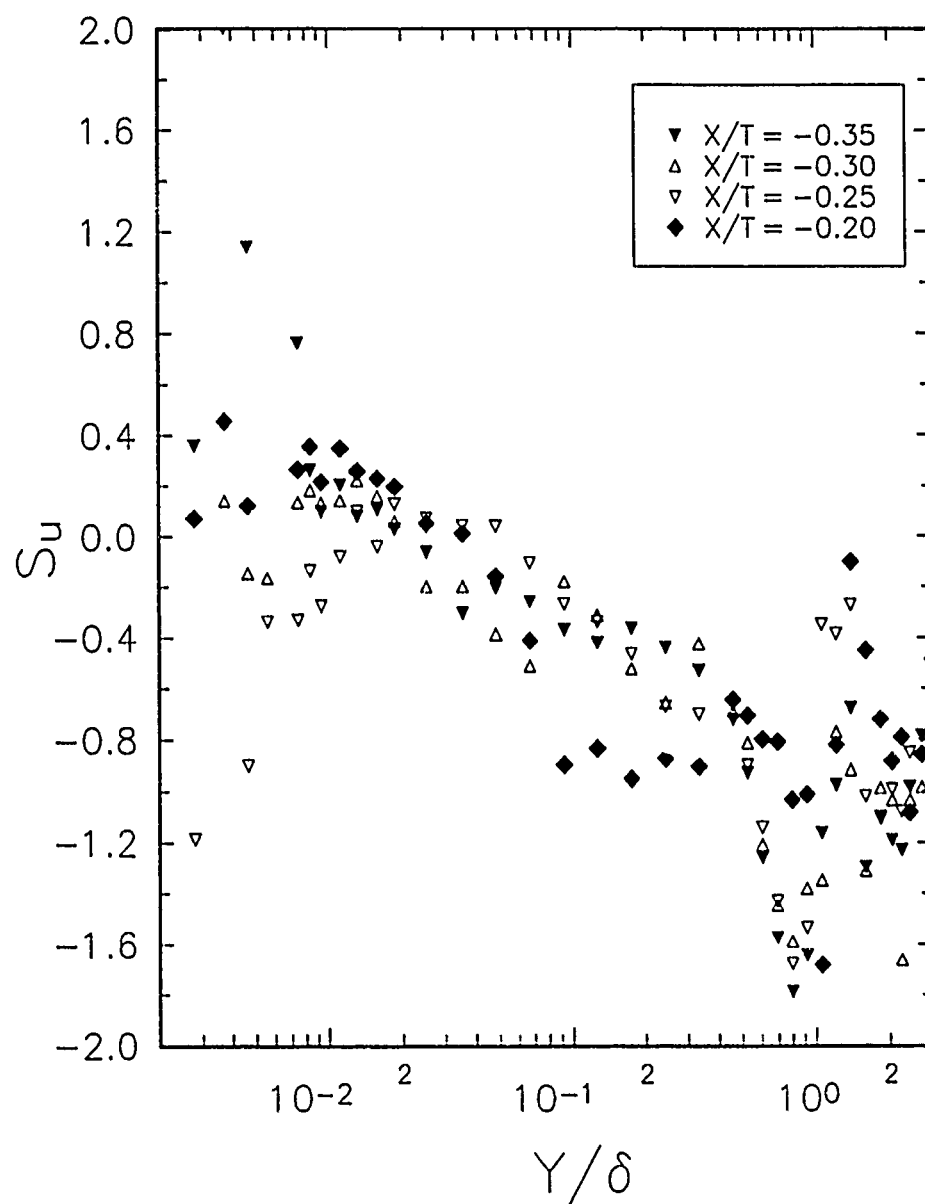


Figure 46. Continued

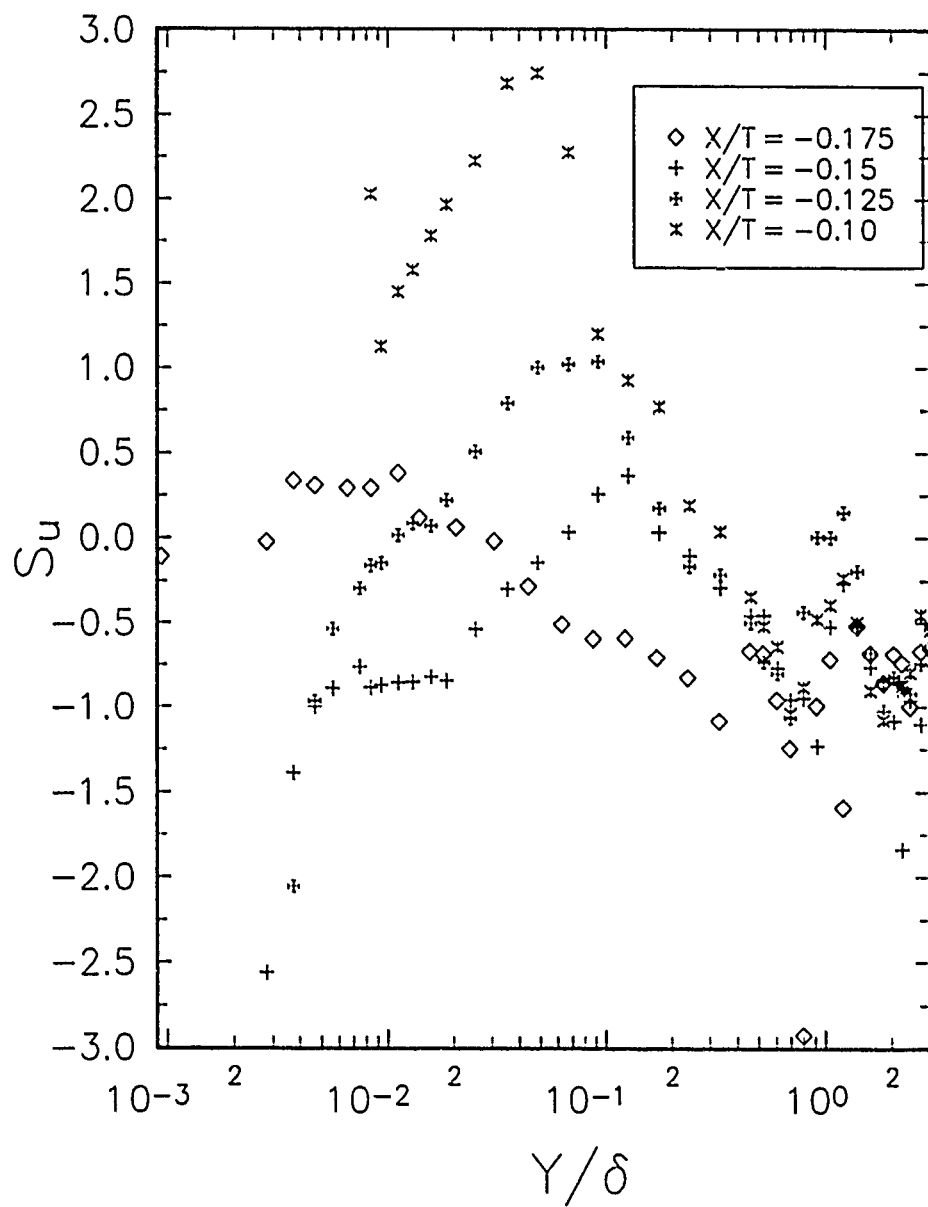


Figure 46. Continued

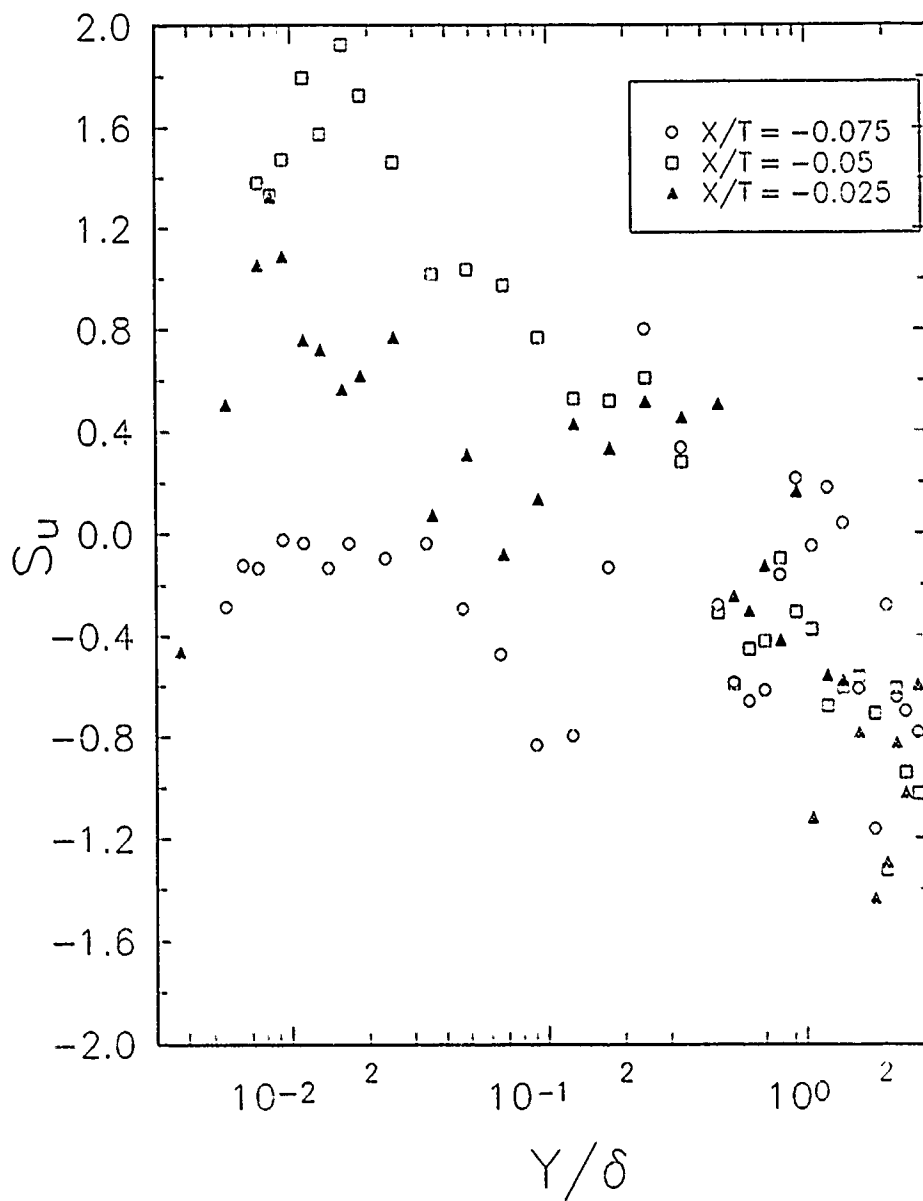


Figure 46. Concluded

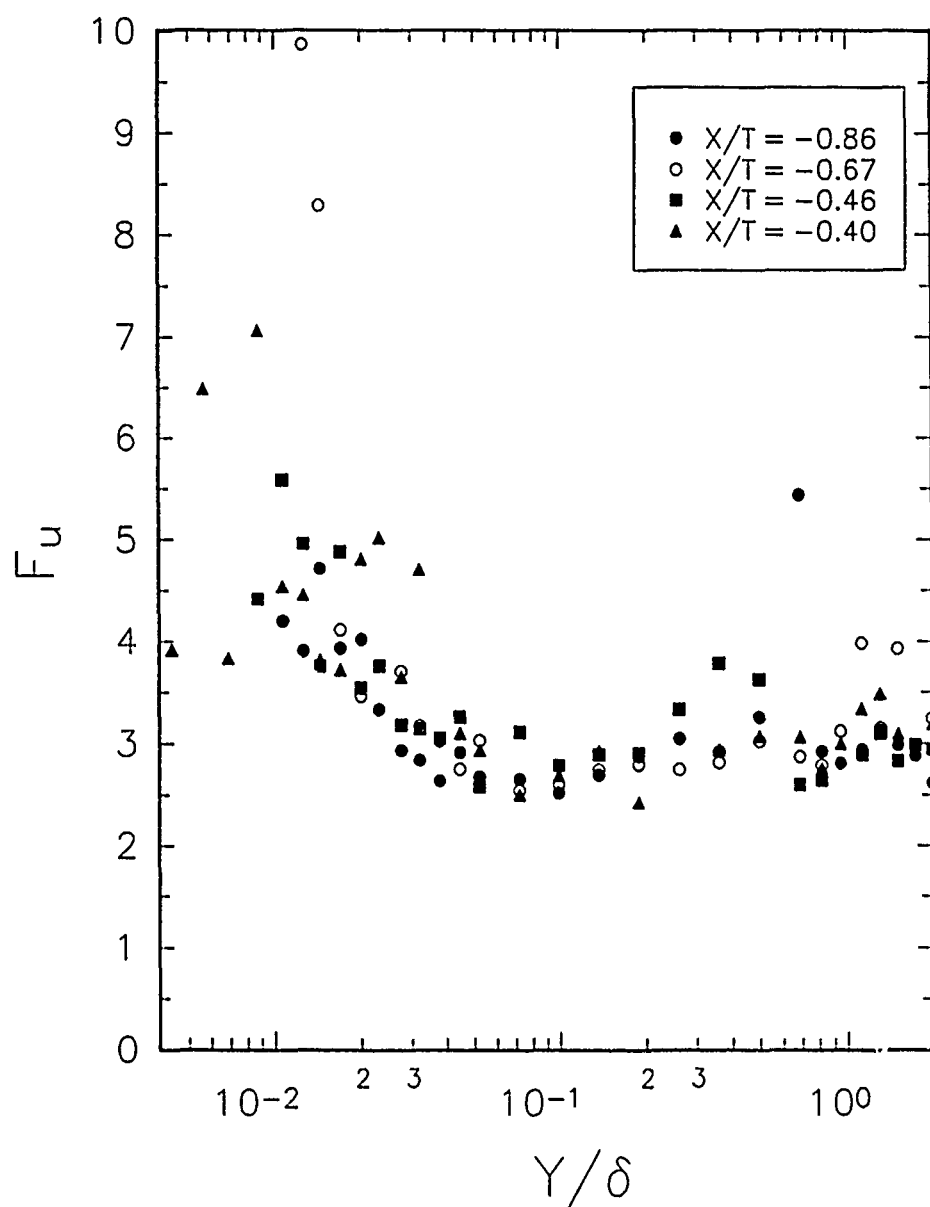


Figure 47. Flatness factor plots across the shear layer for  $Re_\theta = 330$

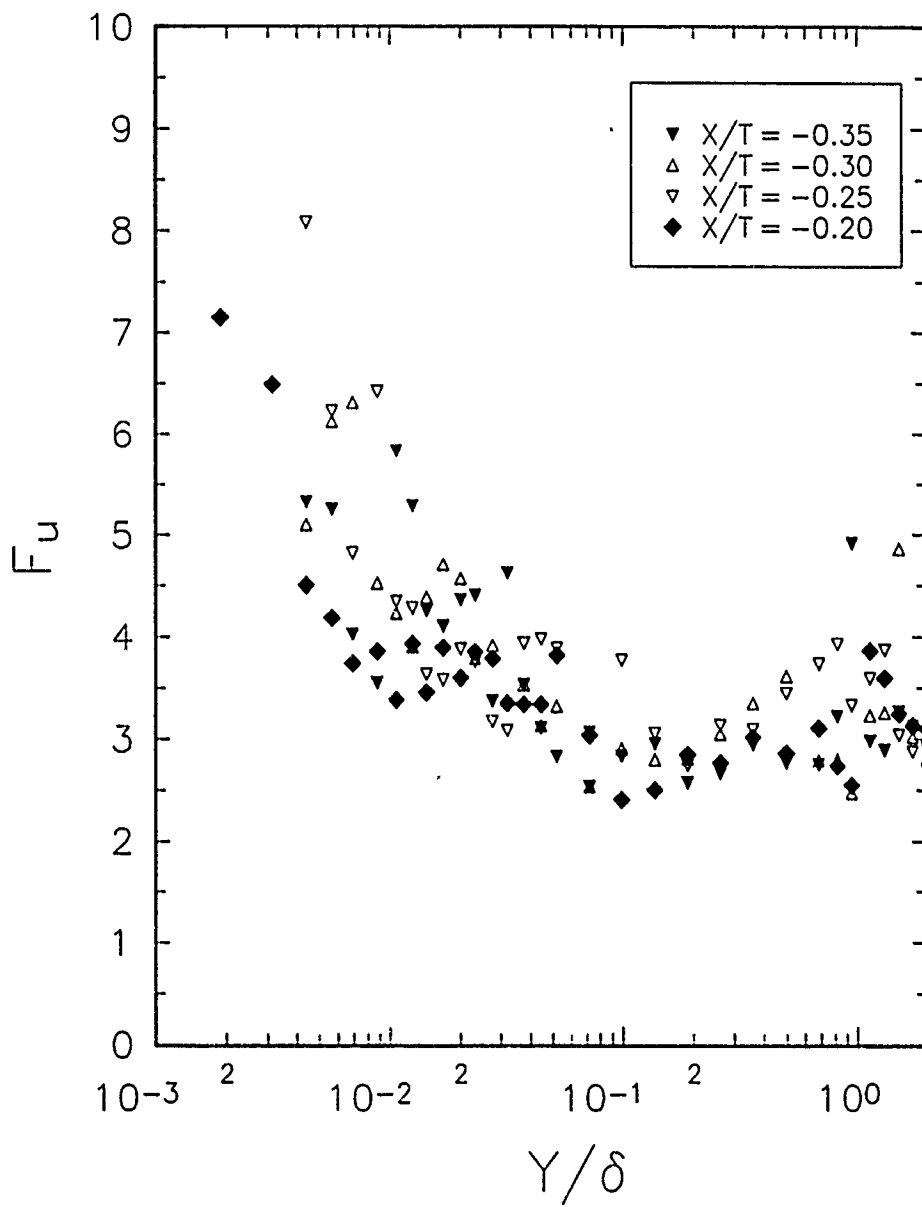


Figure 47. Continued



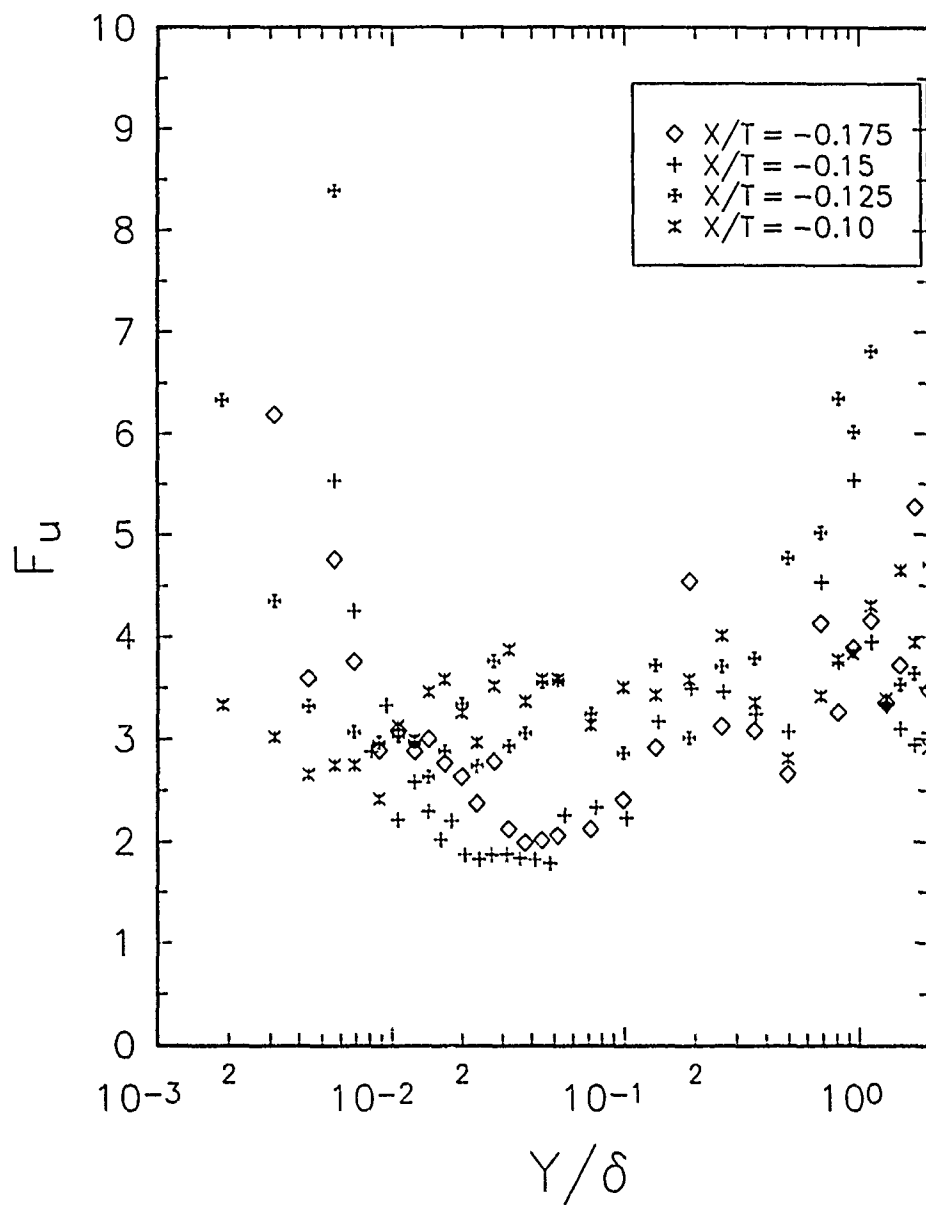


Figure 47. Continued

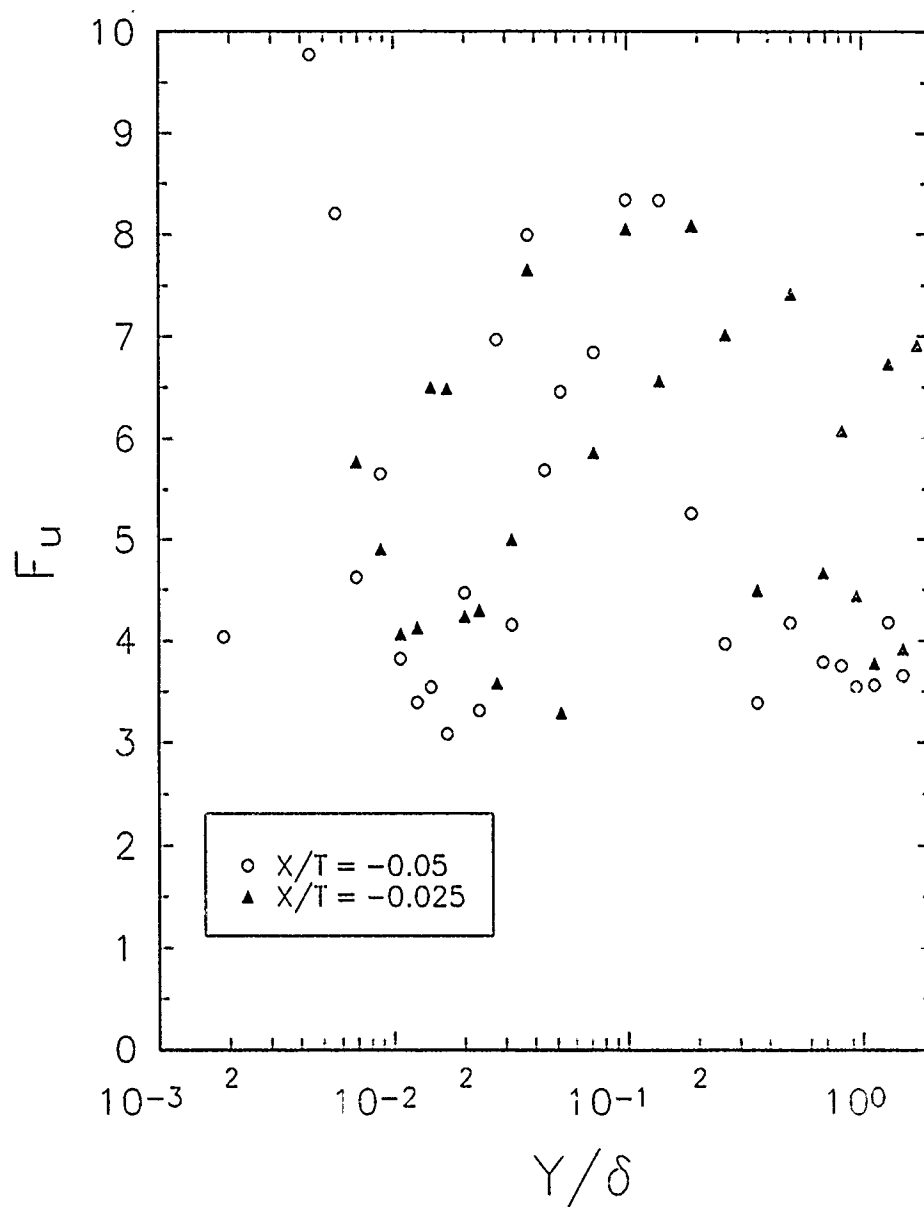


Figure 47. Concluded

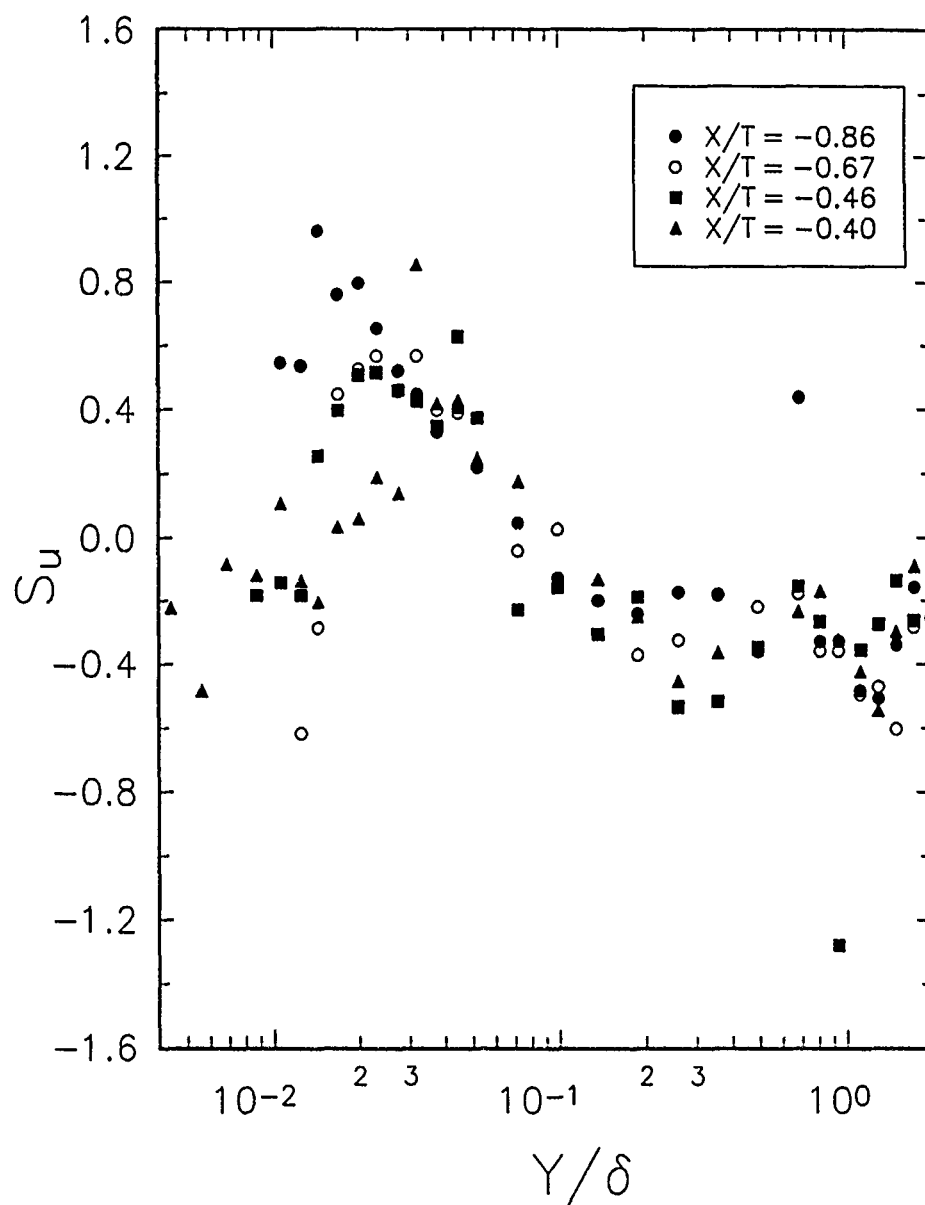


Figure 48. Skewness factor plots across the shear layer for  $Re_\theta = 330$

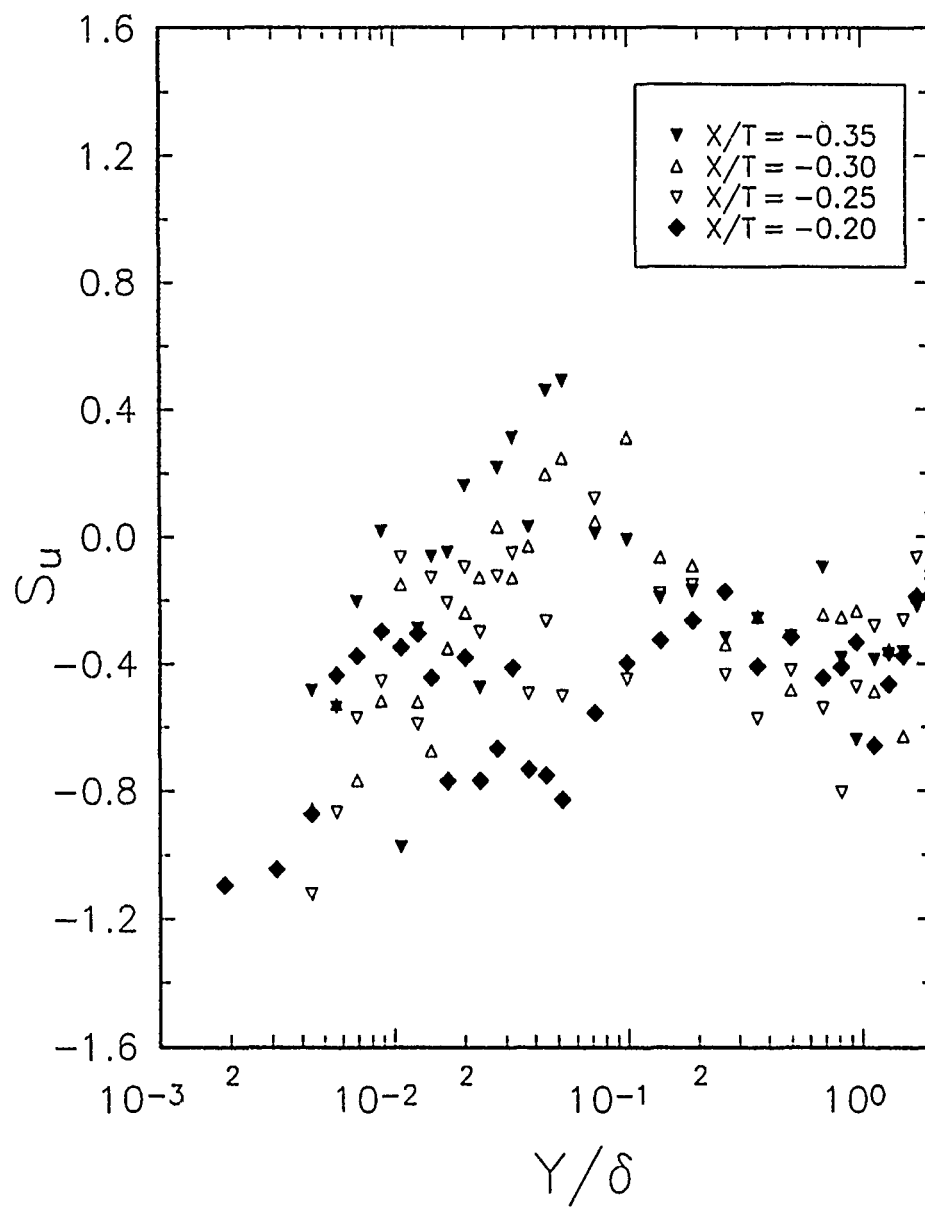


Figure 48. Continued

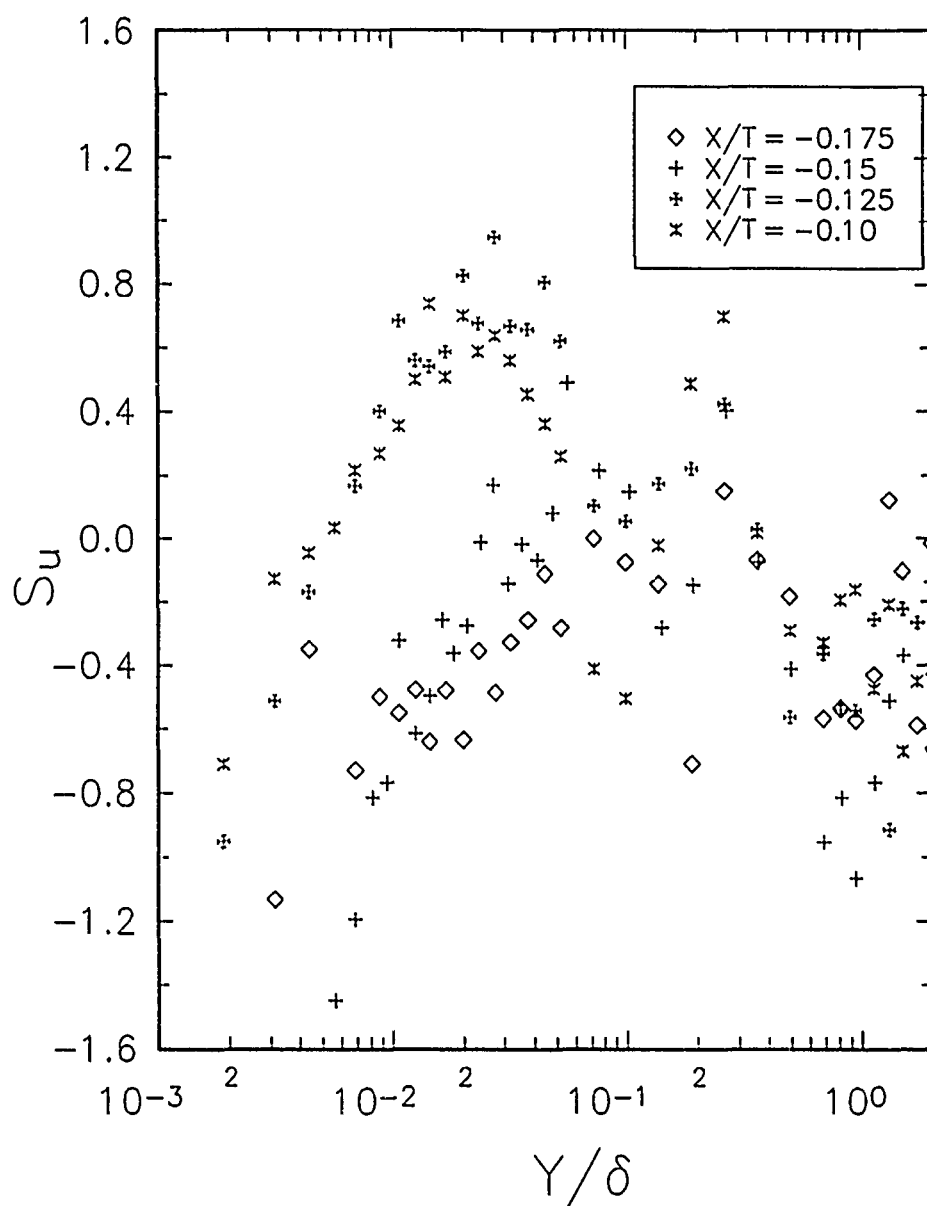


Figure 48. Continued

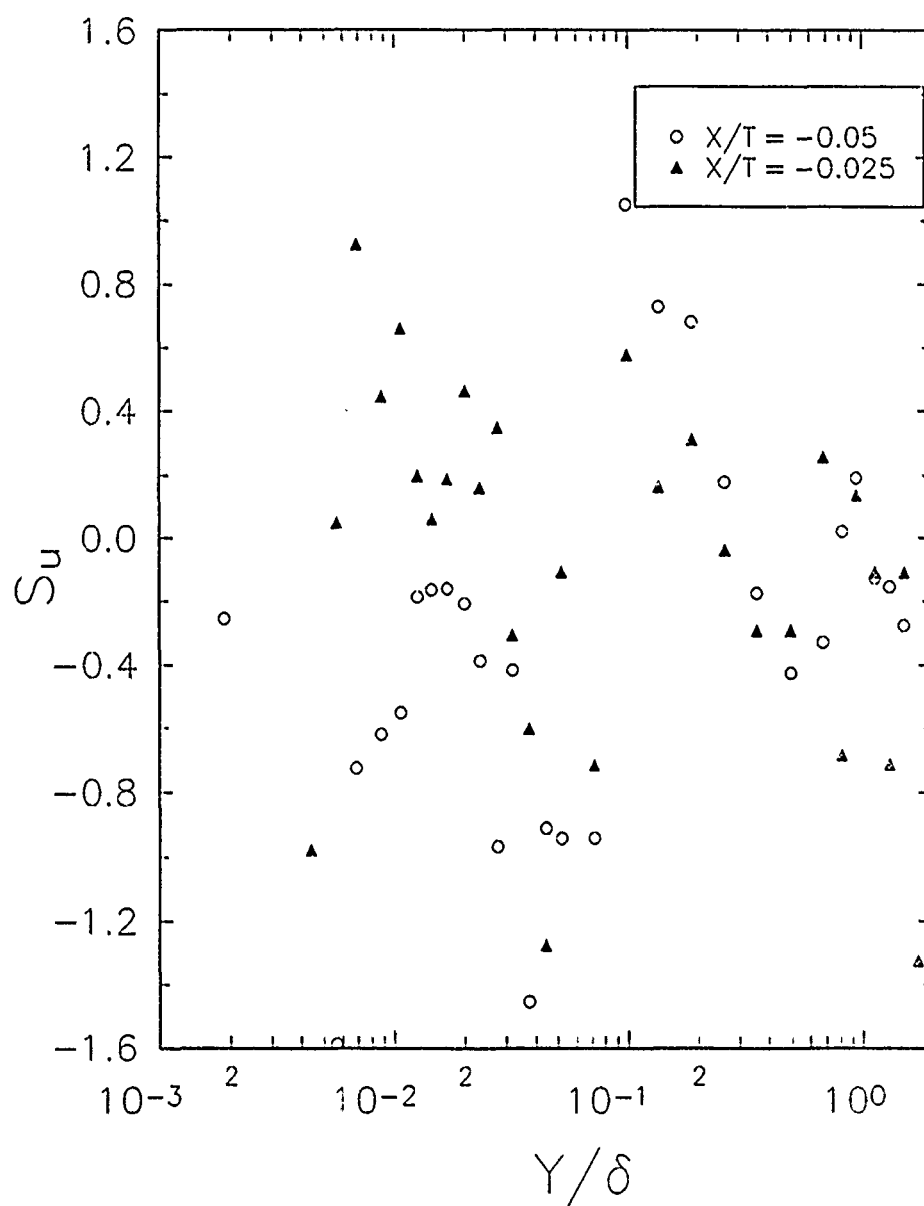
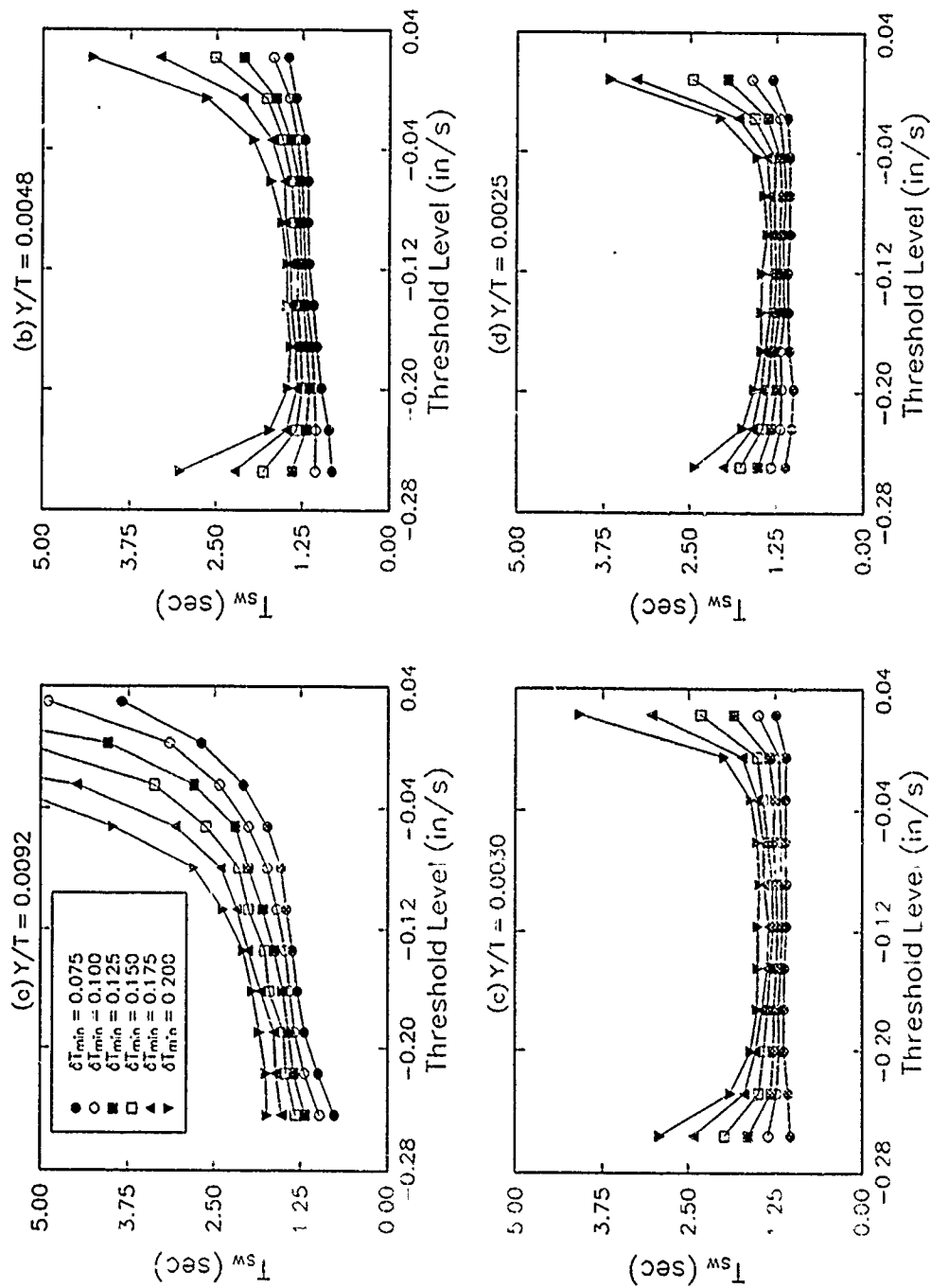


Figure 48. Concluded



**Figure 49.** Some results obtained from a single threshold switching frequency analysis (SFA) with  $\delta T_{min}$

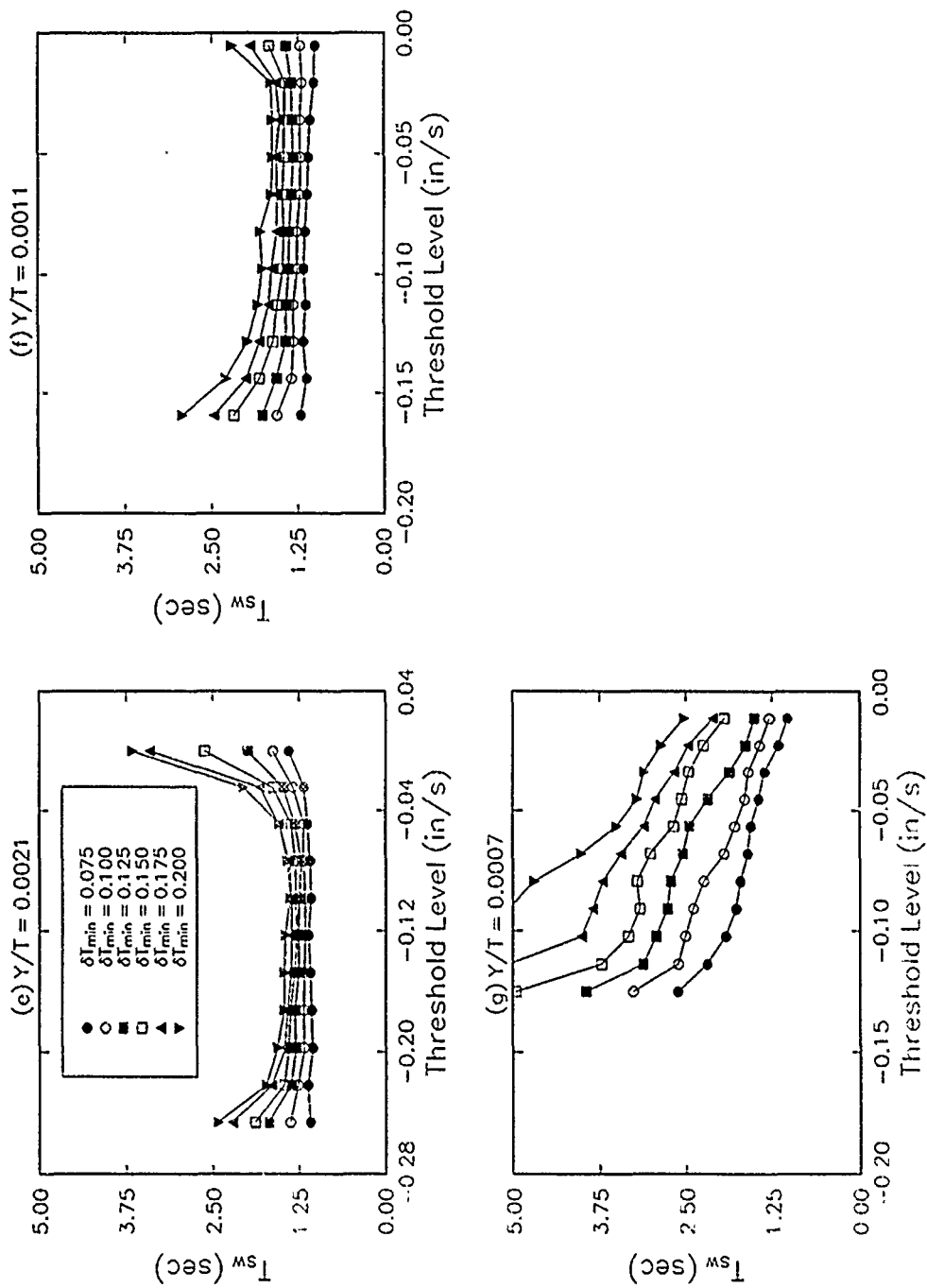


Figure 49. Concluded



## FIR Low Pass Filter Design

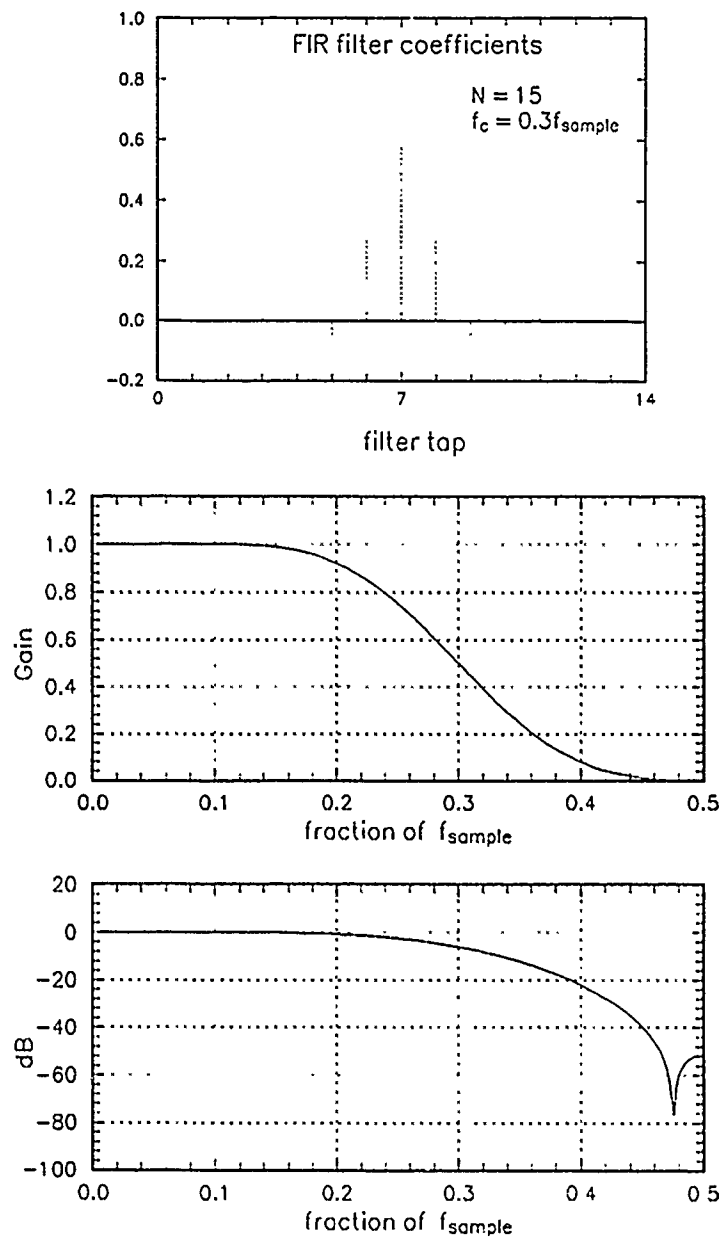


Figure 50. FIR low pass filter design

## FIR Low Pass Filter Design

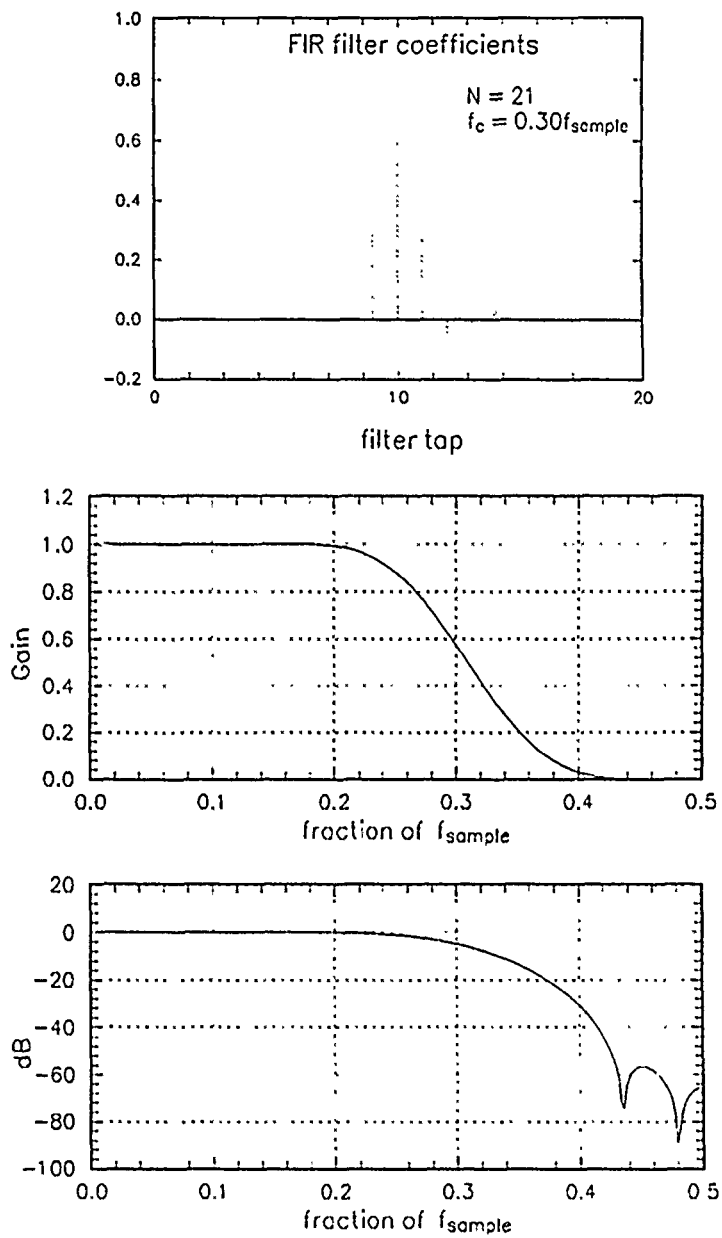


Figure 50. Continued

## FIR Low Pass Filter Design

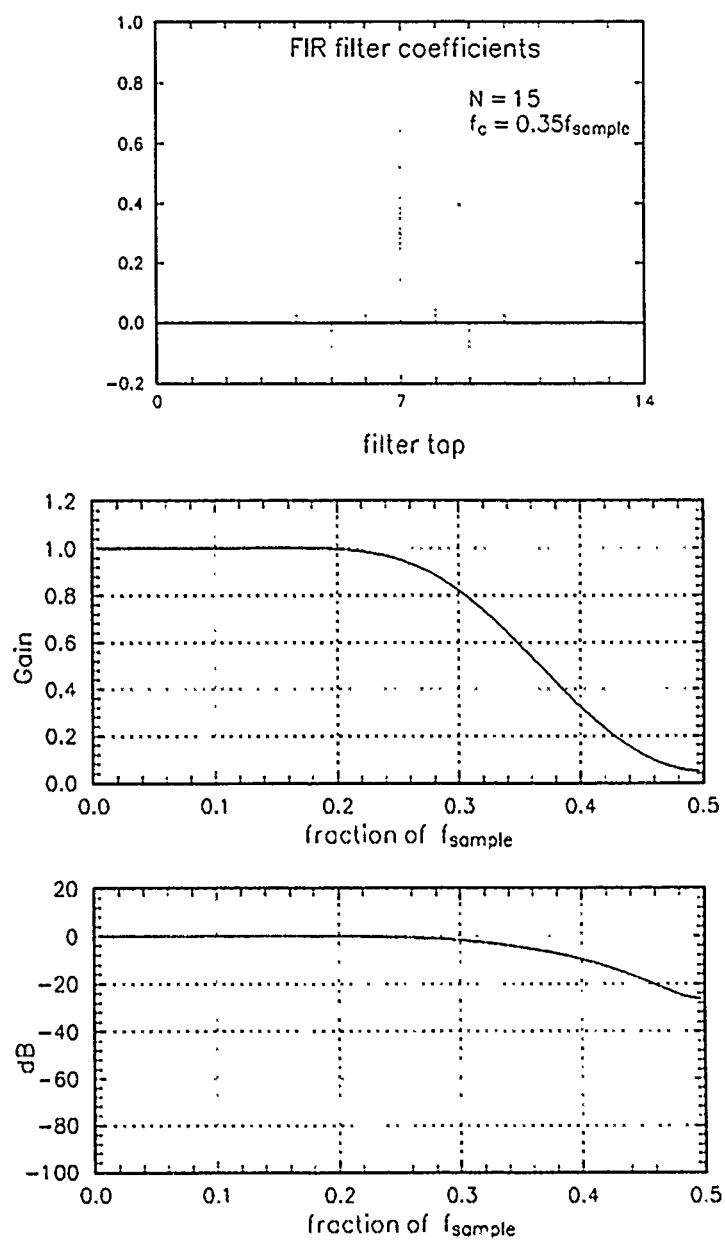


Figure 50. Continued

## FIR Low Pass Filter Design

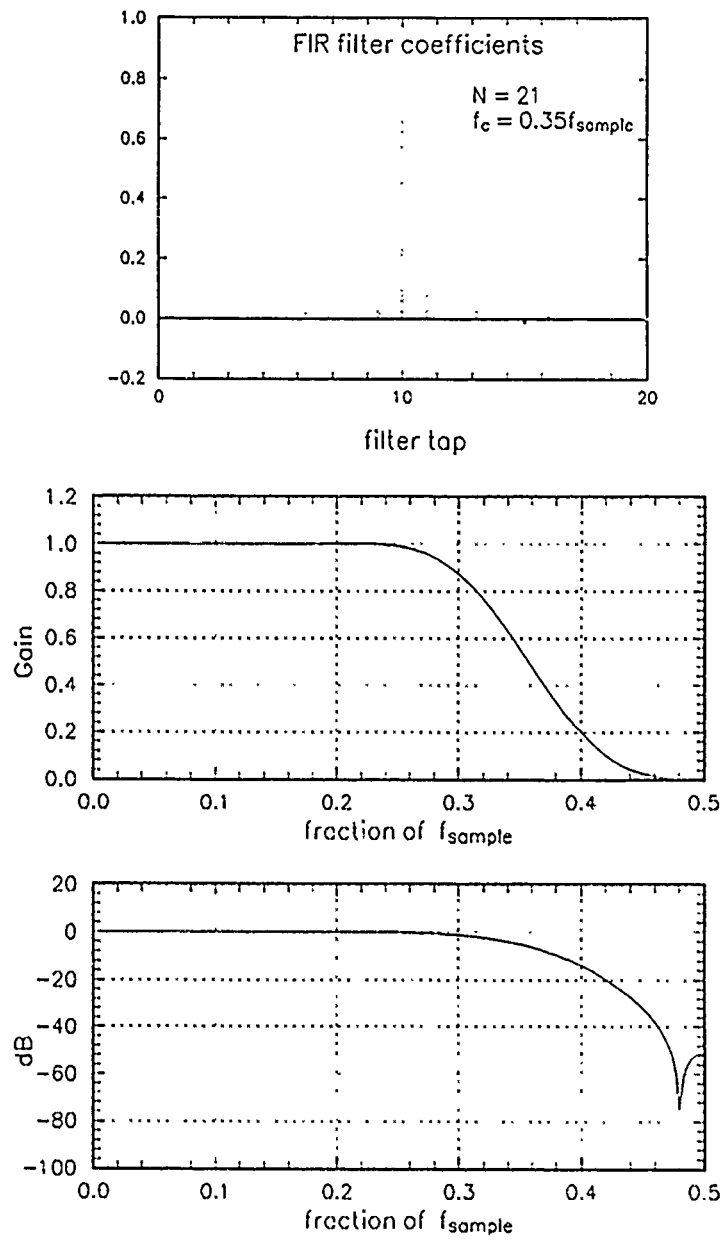
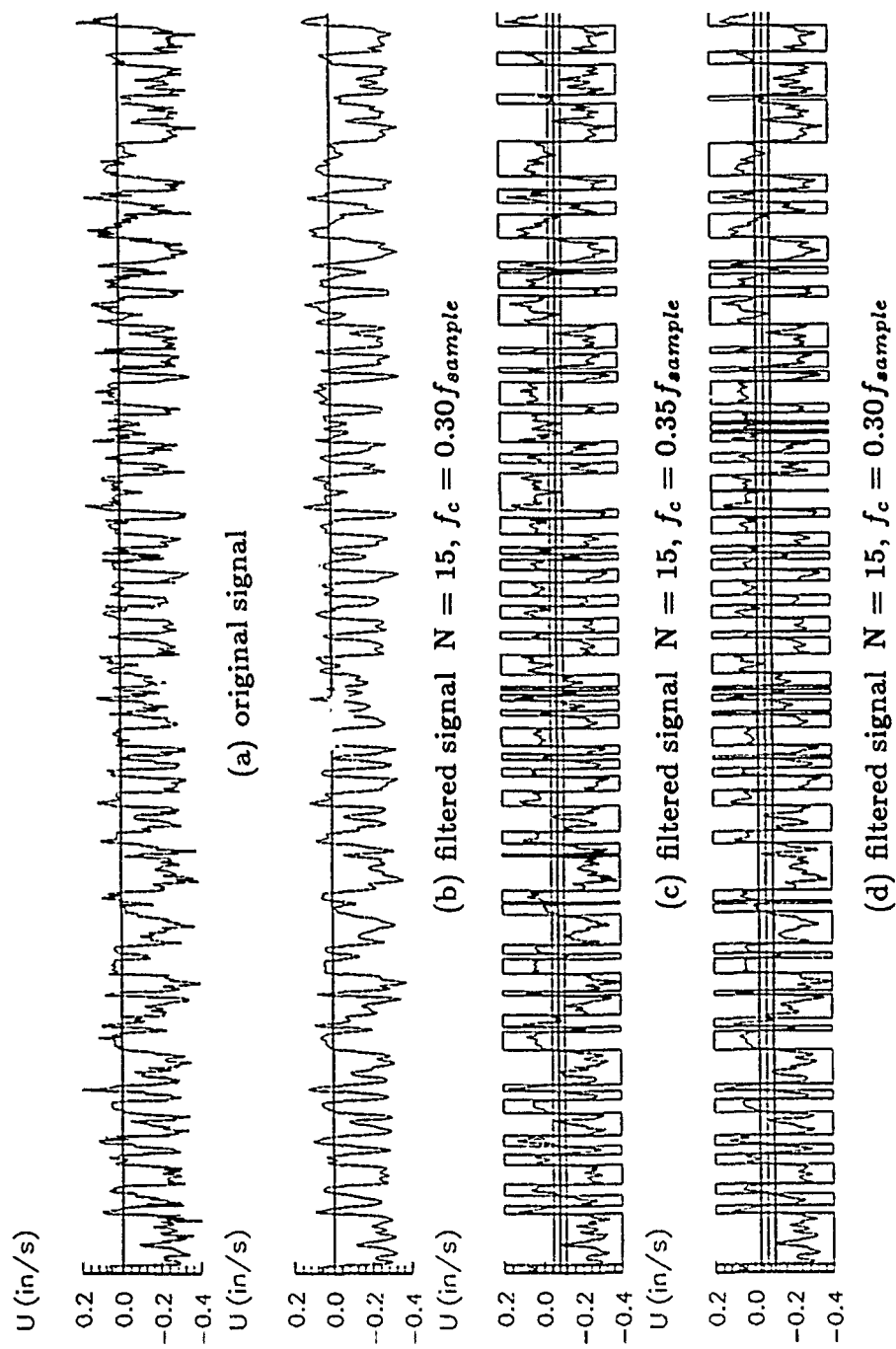


Figure 50. Concluded



**Figure 51.** Comparison of all the filters designed to detect the mode switching in time Series of LDV signal

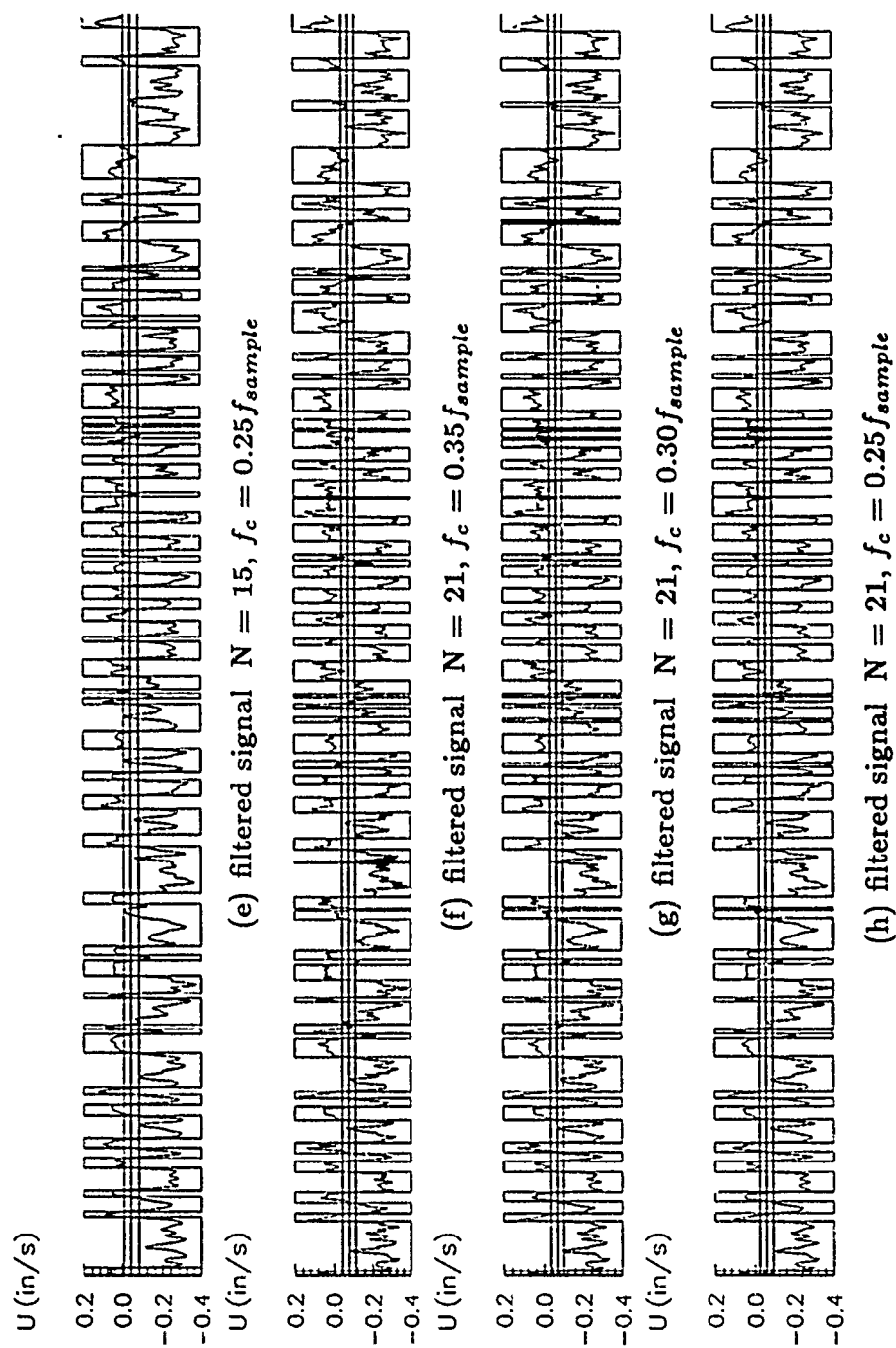
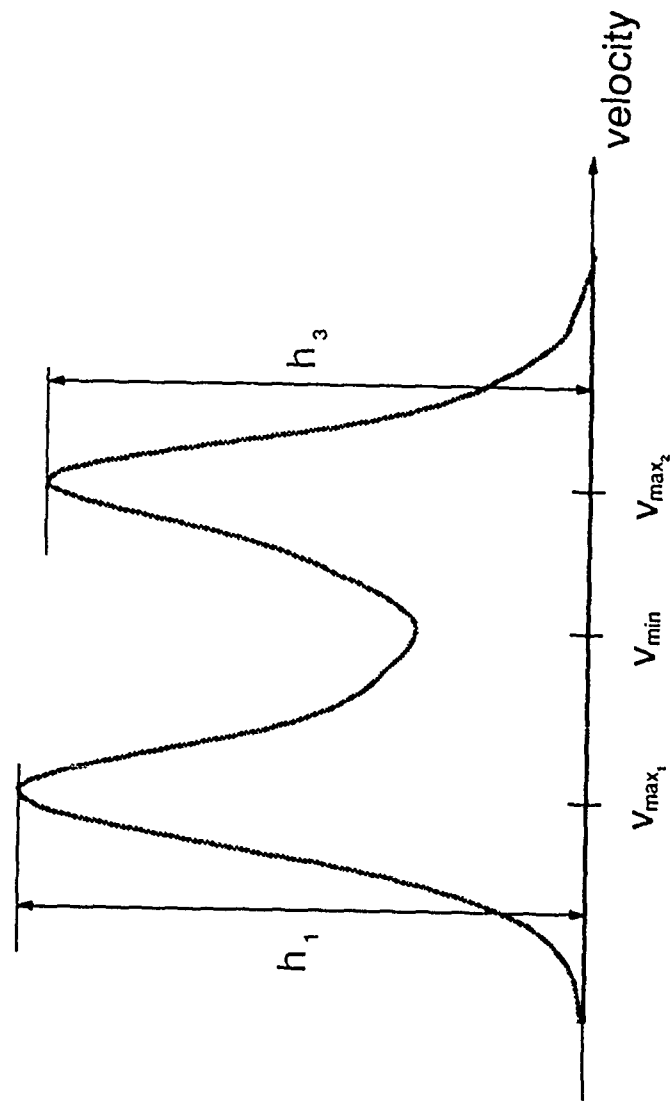


Figure 51. Concluded



**Figure 52.** A schematic diagram showing the parameters used in three threshold level SFA

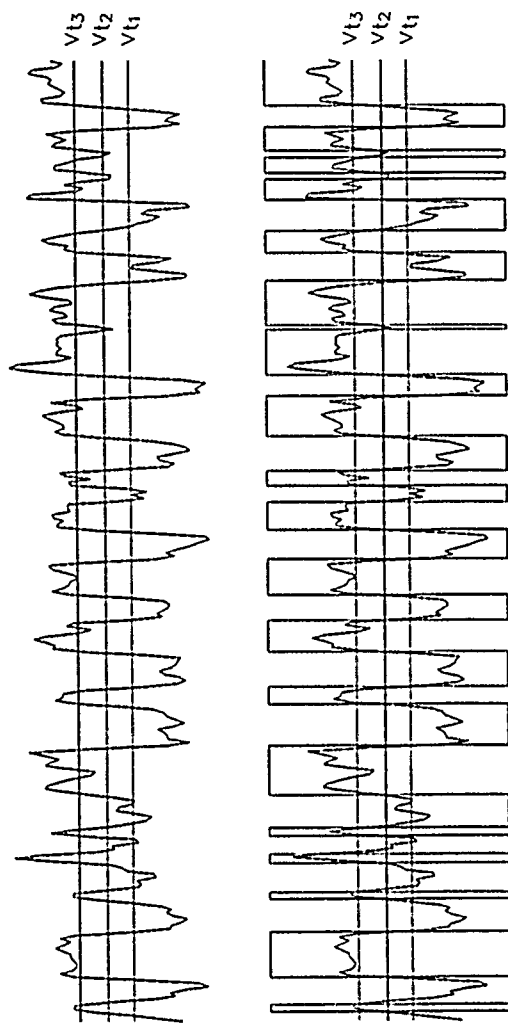
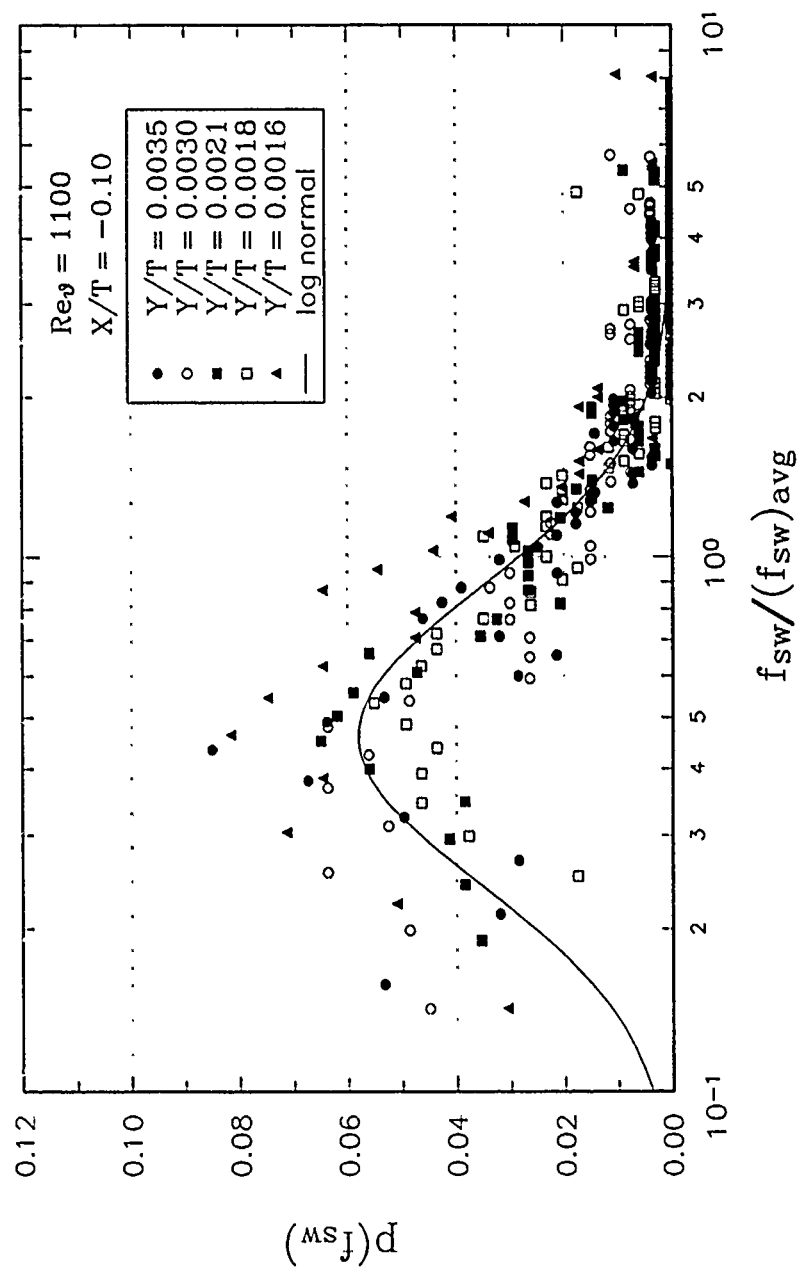


Figure 53. Typical example of triggered LDV signals using three threshold values





**Figure 54.** Probability density function of the normalized switching frequency  $(f_{sw})$  across the bimodal zone

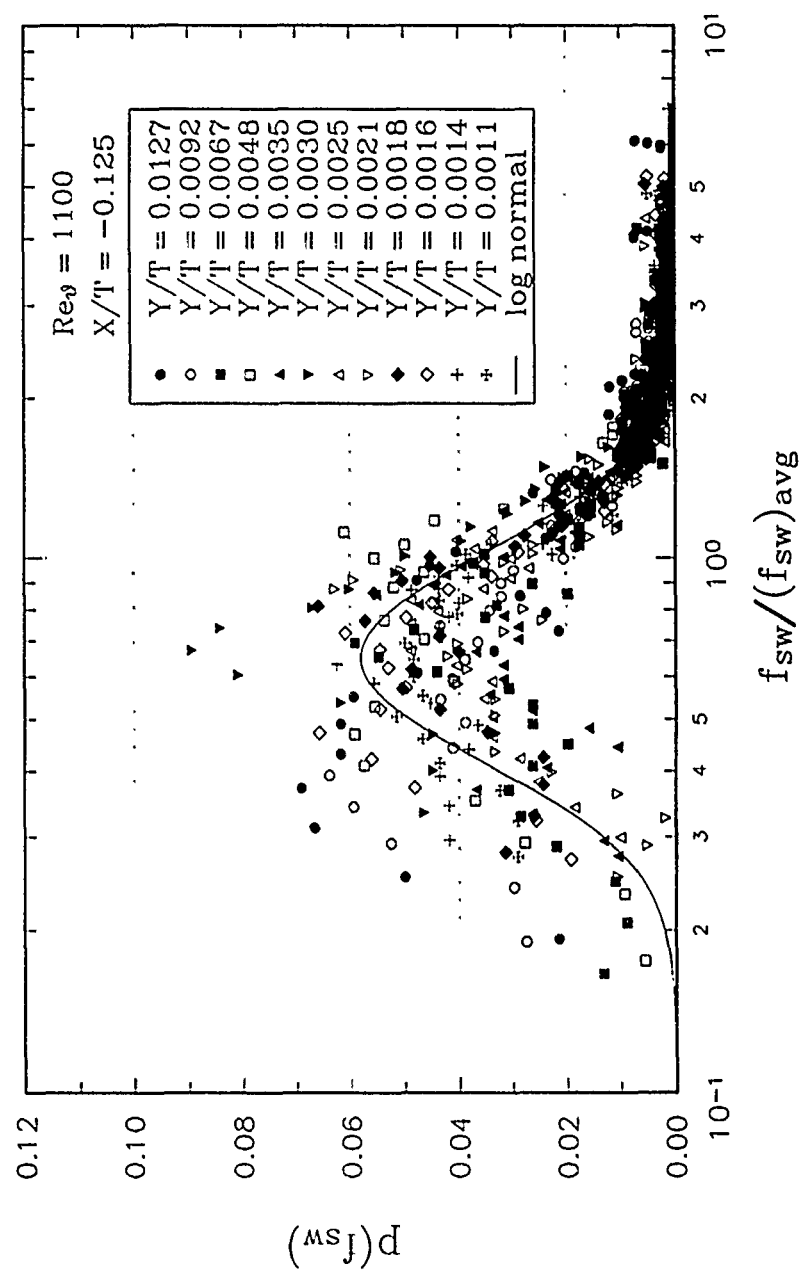


Figure 54. Continued

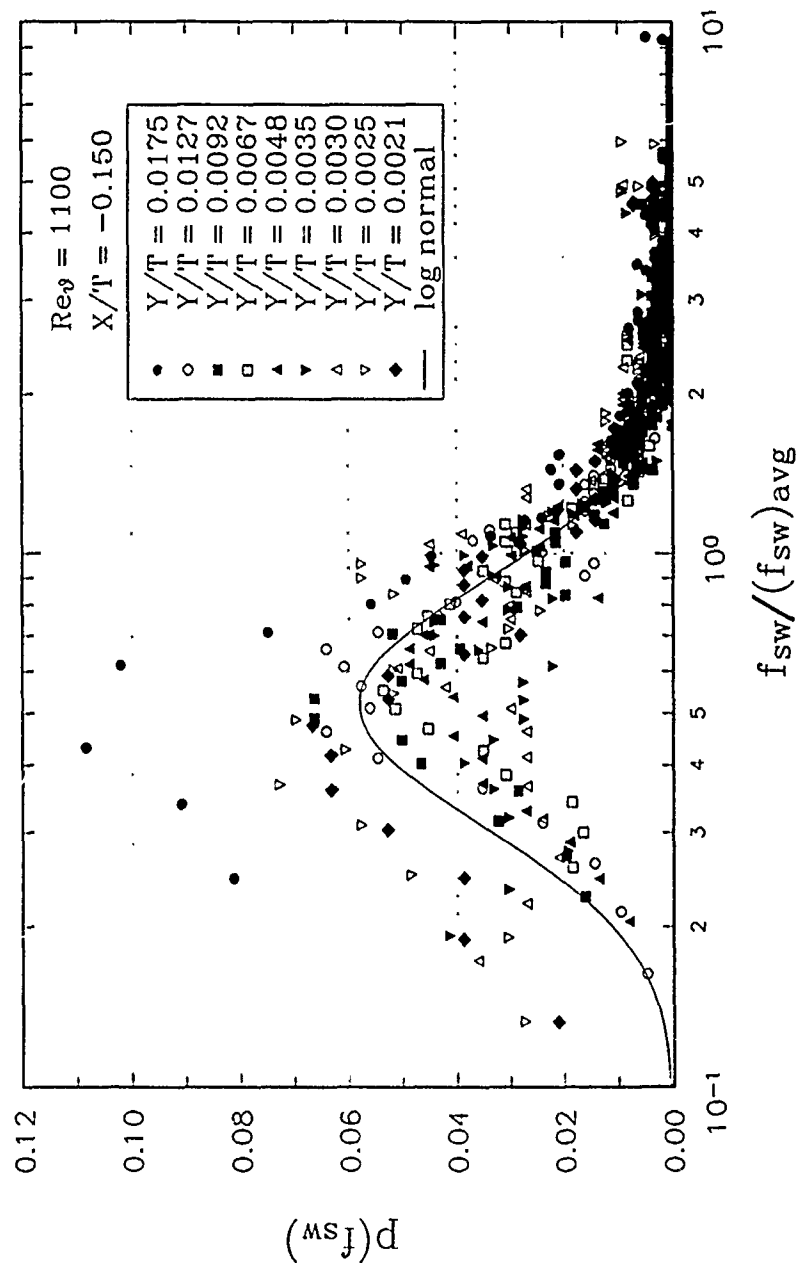


Figure 54. Concluded

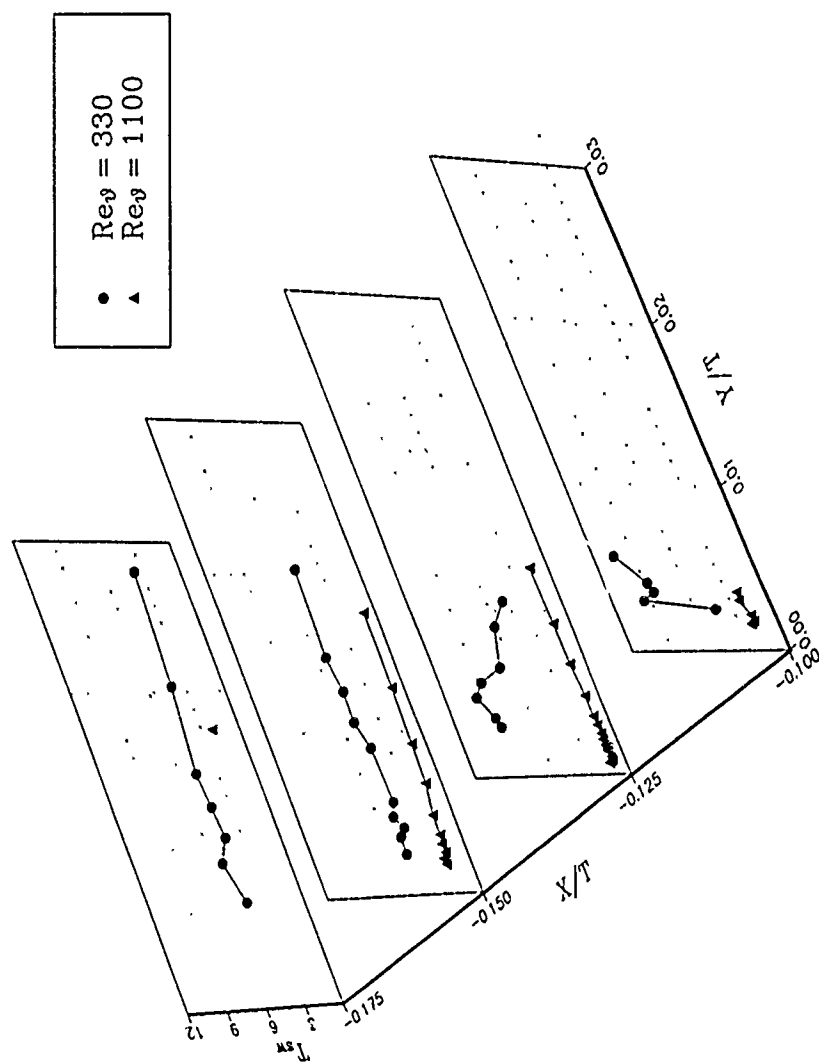


Figure 55. Variations of the average switching time ( $T_{sw}$ ) in the bimodal zone for each flow condition

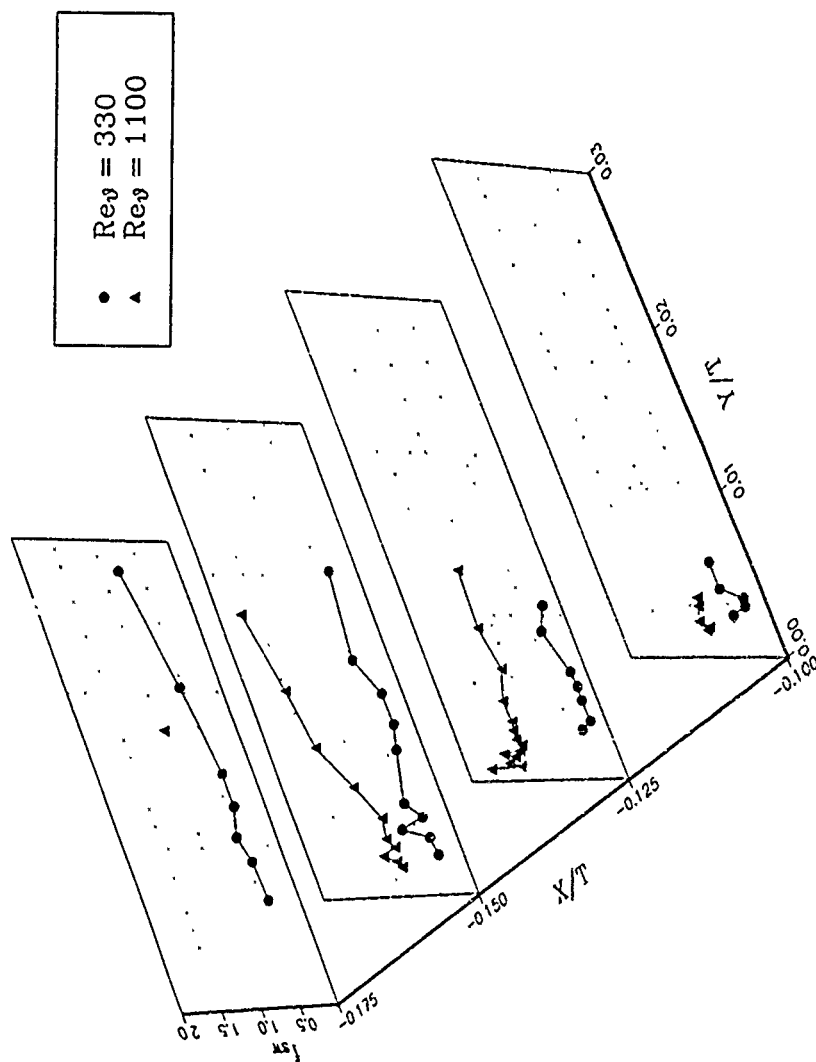


Figure 56. Variations of the average switching frequency ( $f_{sw}$ ) in the bimodal zone for each flow condition

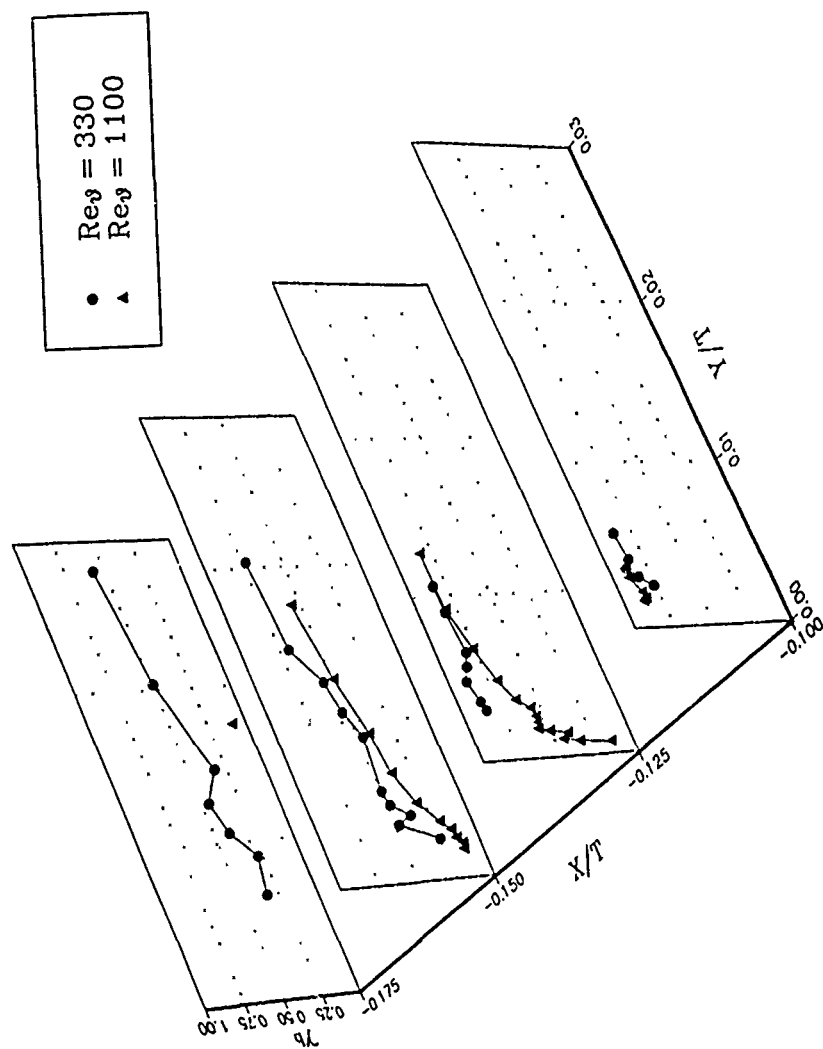


Figure 57. Fraction of a backflow mode ( $\gamma_b$ ) in the bimodal zone for each flow condition

(a)  $Re_\theta = 330$

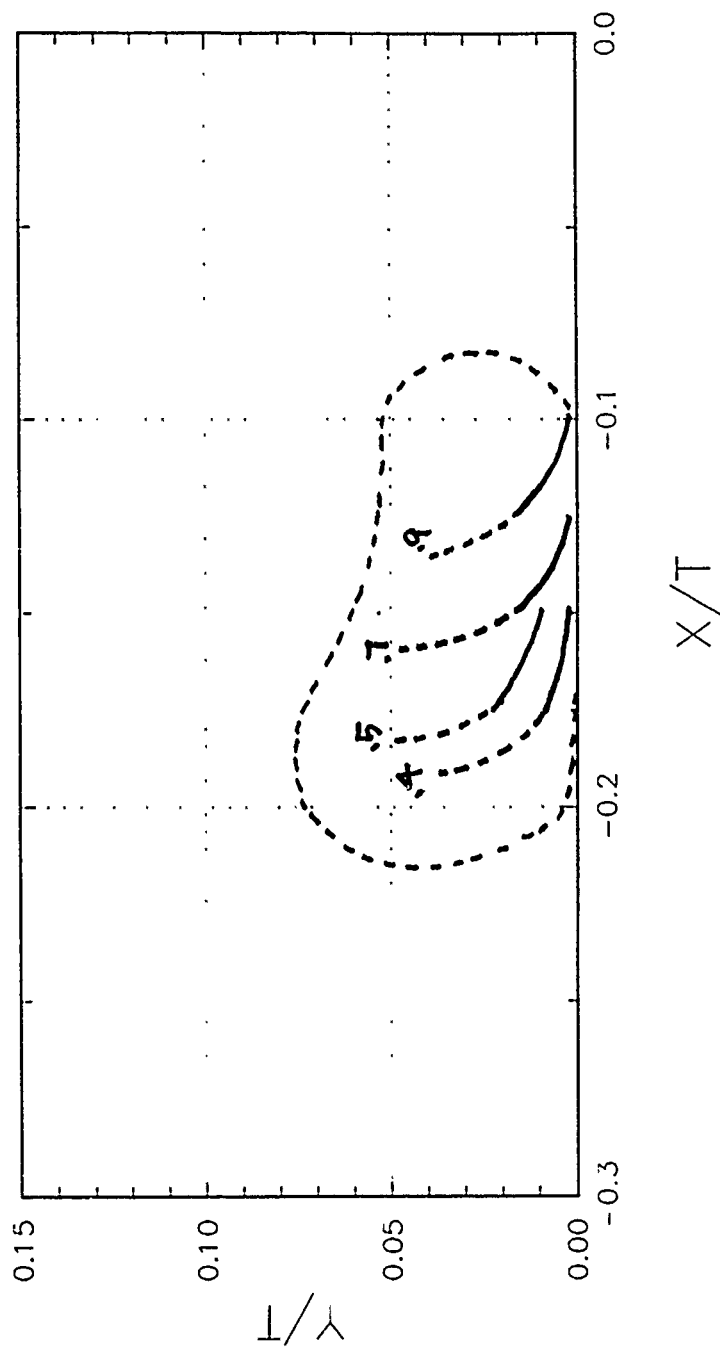


Figure 58. Contour plots of the estimated fraction of backflow mode ( $\gamma_b$ ) in the bimodal zone for each flow condition

(b)  $Re_\theta = 1100$

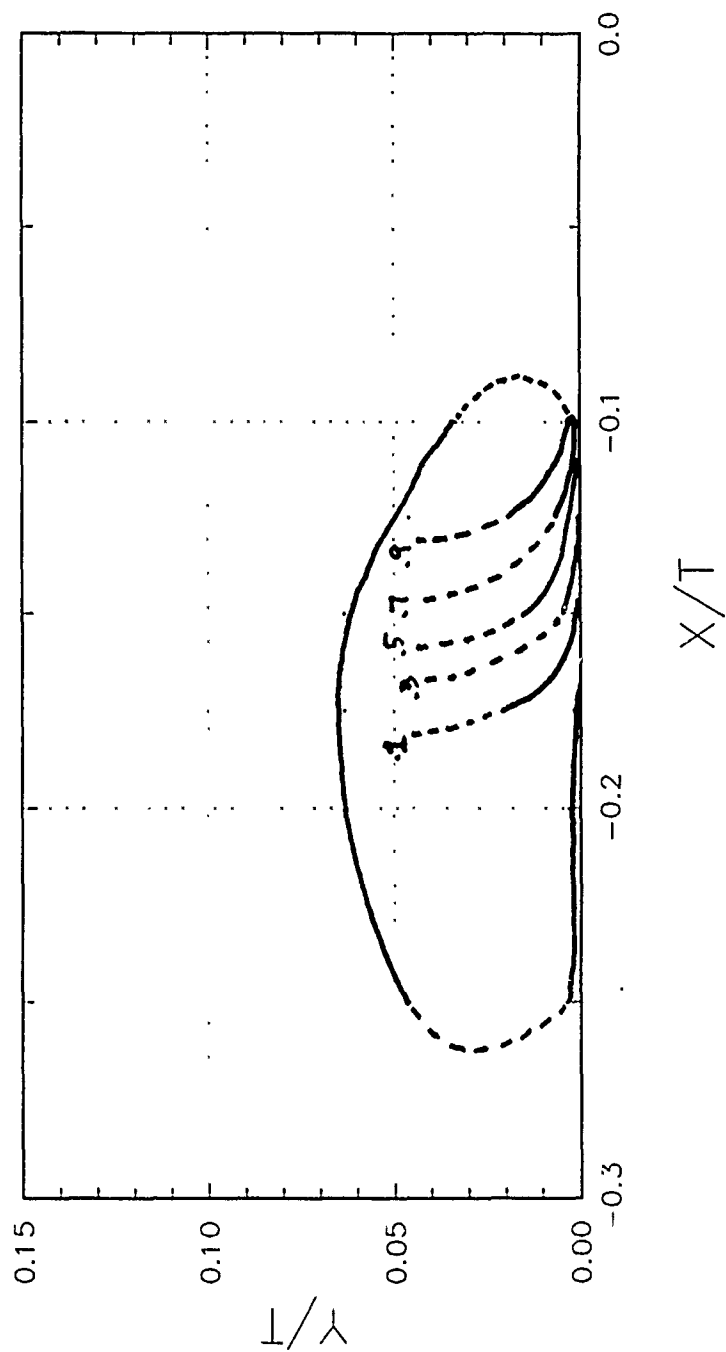
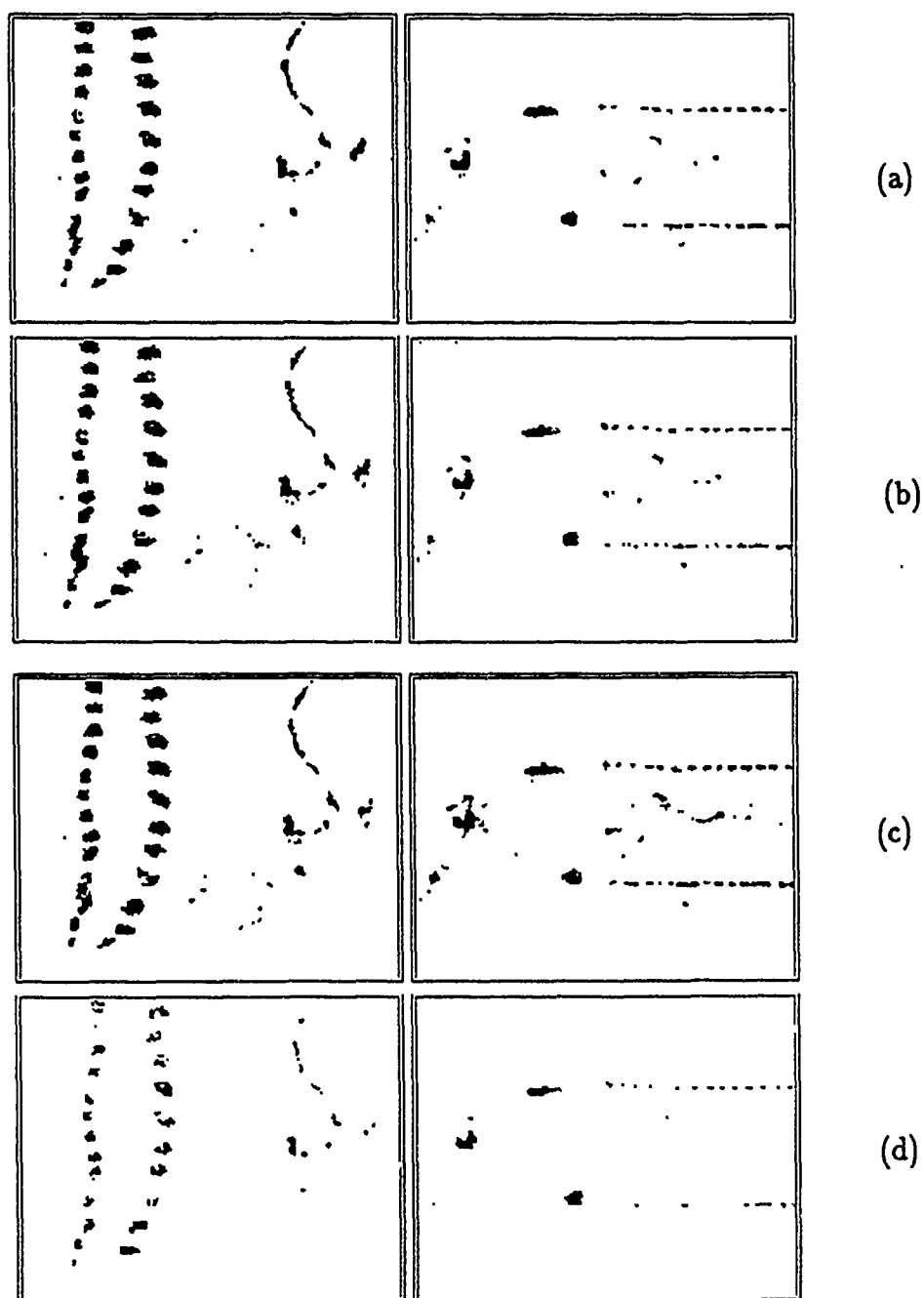
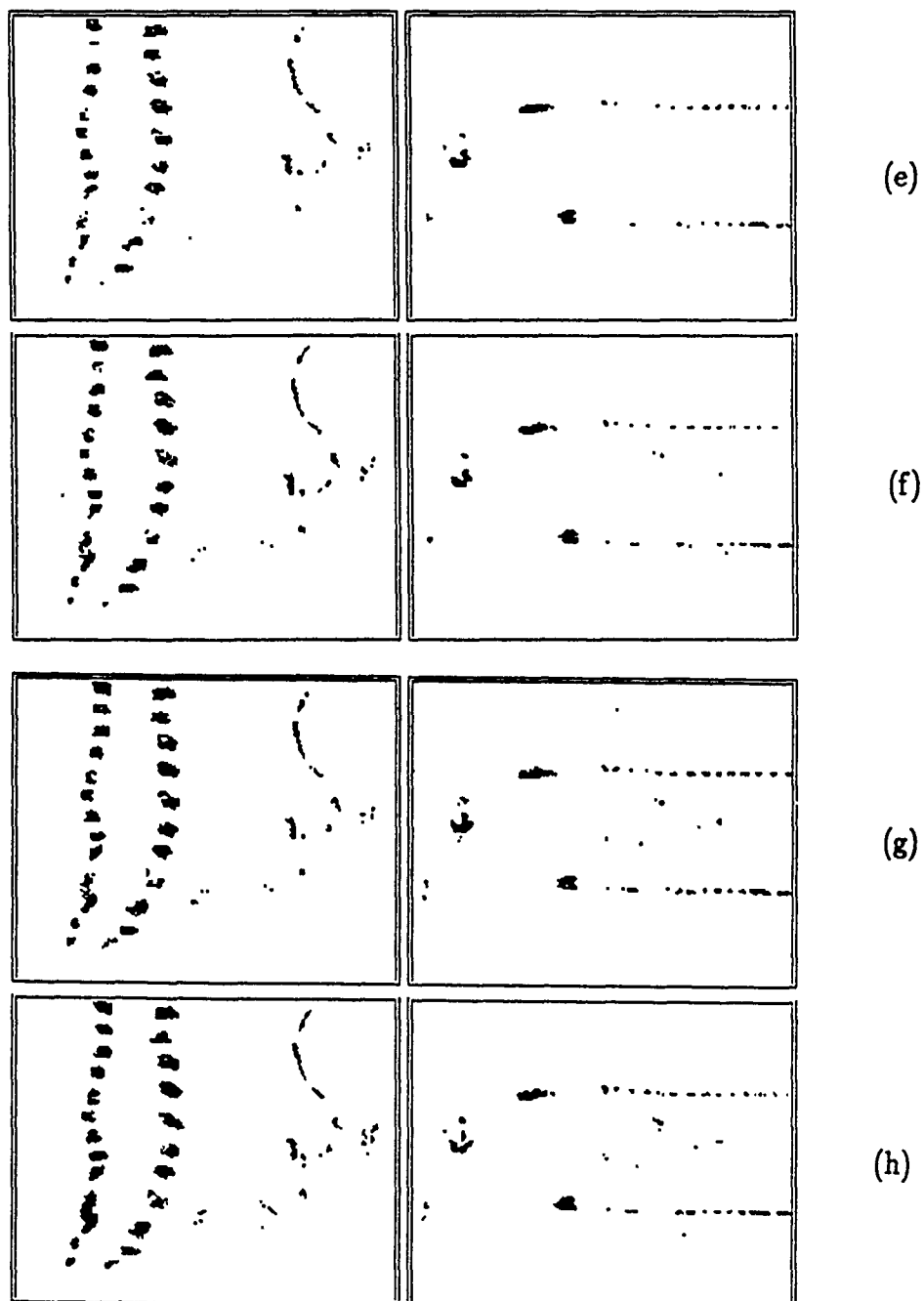


Figure 58. Concluded





**Figure 59.** Sequence of the bilevel images after local averaging technique and thresholding : (a)  $t = t_o$ , (b)  $t = t_o + 0.008(sec)$ , (c)  $t = t_o + 0.016(sec)$ , and (d)  $t = t_o + 0.024(sec)$



**Figure 59.** Continued : (e)  $t = t_o + 0.032(sec)$ , (f)  $t = t_o + 0.040(sec)$ , (g)  $t = t_o + 0.048(sec)$ , and (h)  $t = t_o + 0.056(sec)$

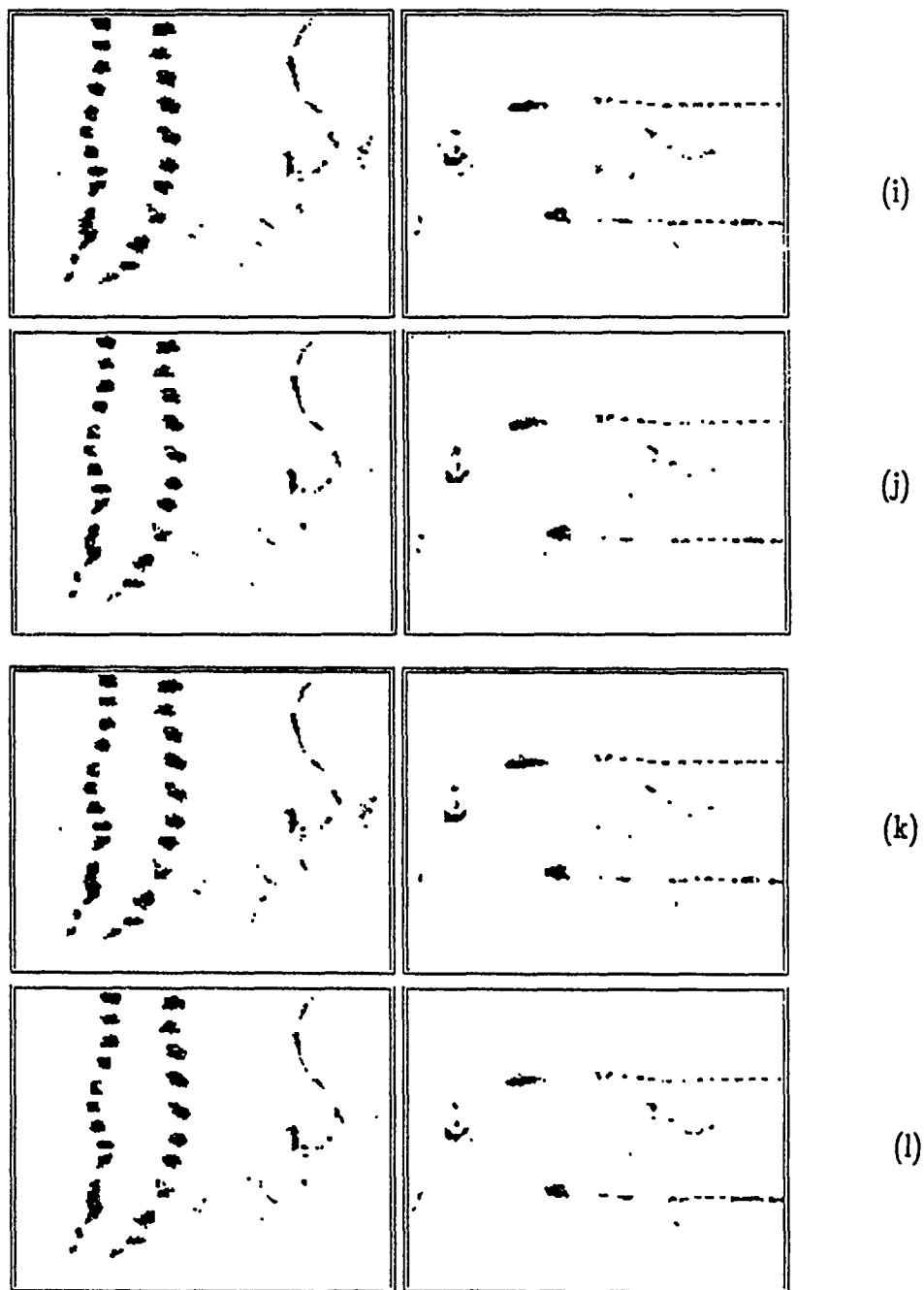
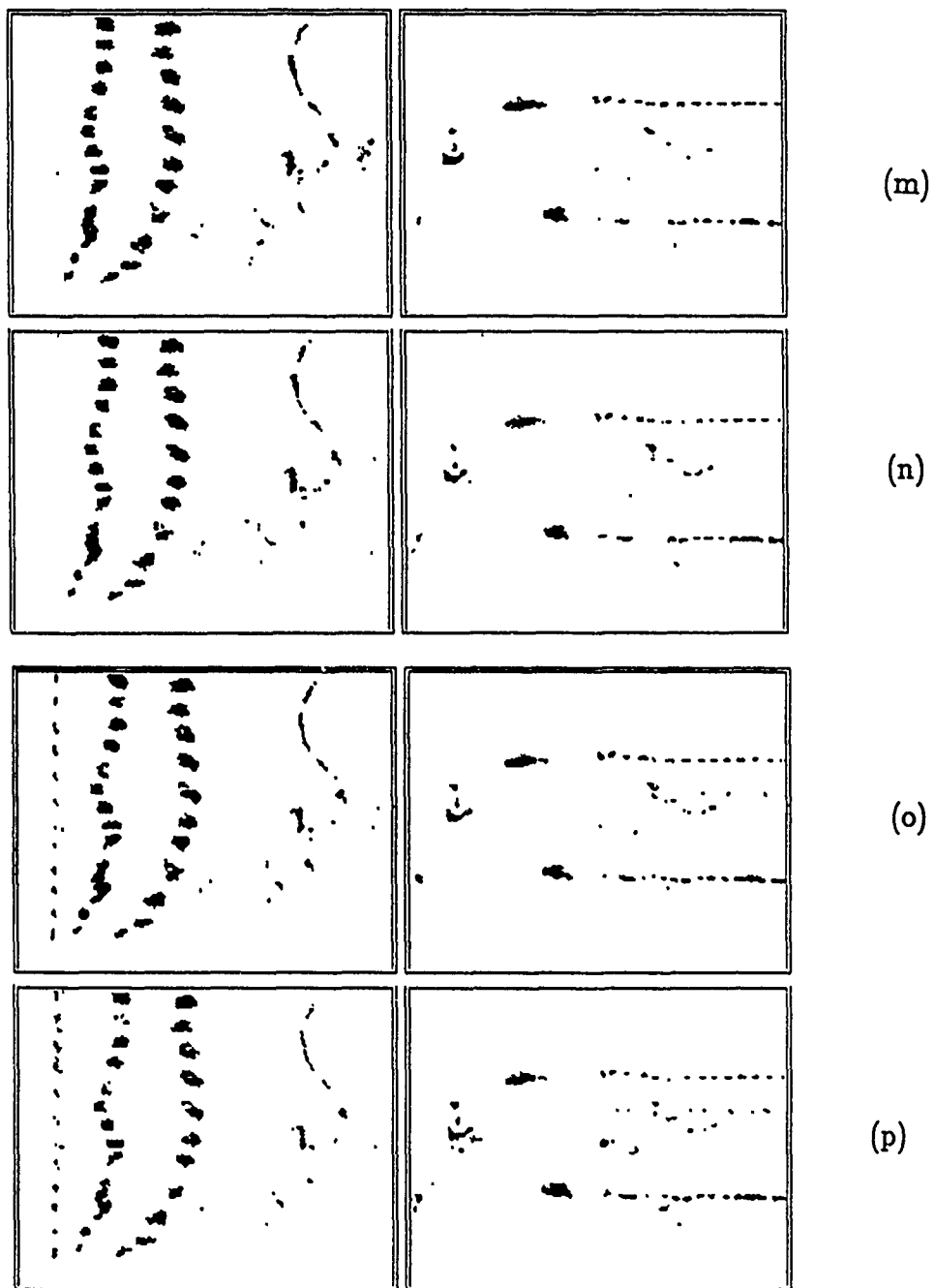
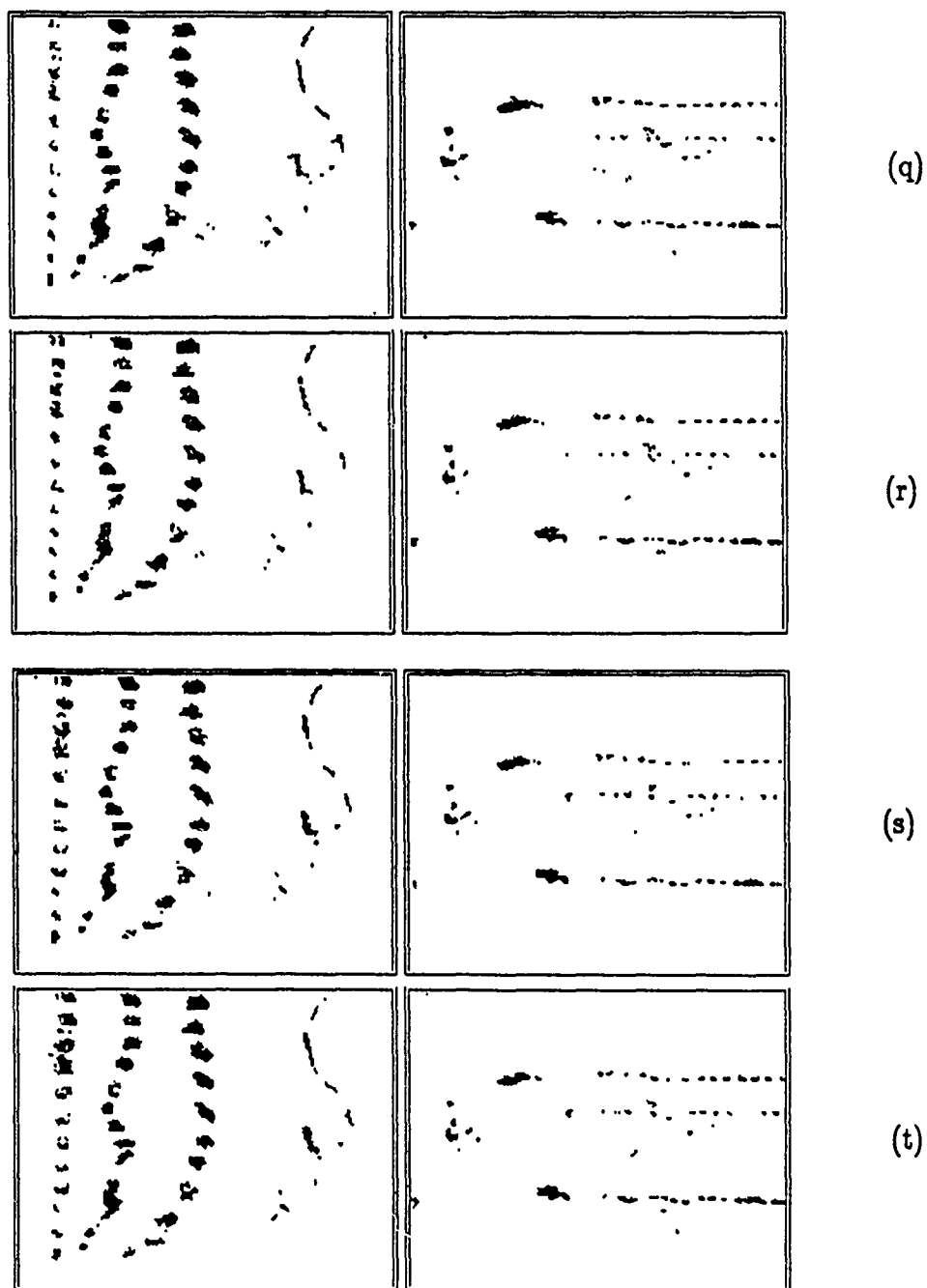


Figure 59. Continued : (i)  $t = t_o + 0.064(sec)$ , (j)  $t = t_o + 0.072(sec)$ , (k)  $t = t_o + 0.080(sec)$ , and (l)  $t = t_o + 0.088(sec)$



**Figure 59.** Continued : (m)  $t = t_o + 0.096(sec)$ , (n)  $t = t_o + 0.104(sec)$ , (o)  $t = t_o + 0.112(sec)$ , and (p)  $t = t_o + 0.120(sec)$



**Figure 59.** Continued : (q)  $t = t_o + 0.128(sec)$ , (r)  $t = t_o + 0.136(sec)$ , (s)  $t = t_o + 0.144(sec)$ , and (t)  $t = t_o + 0.152(sec)$

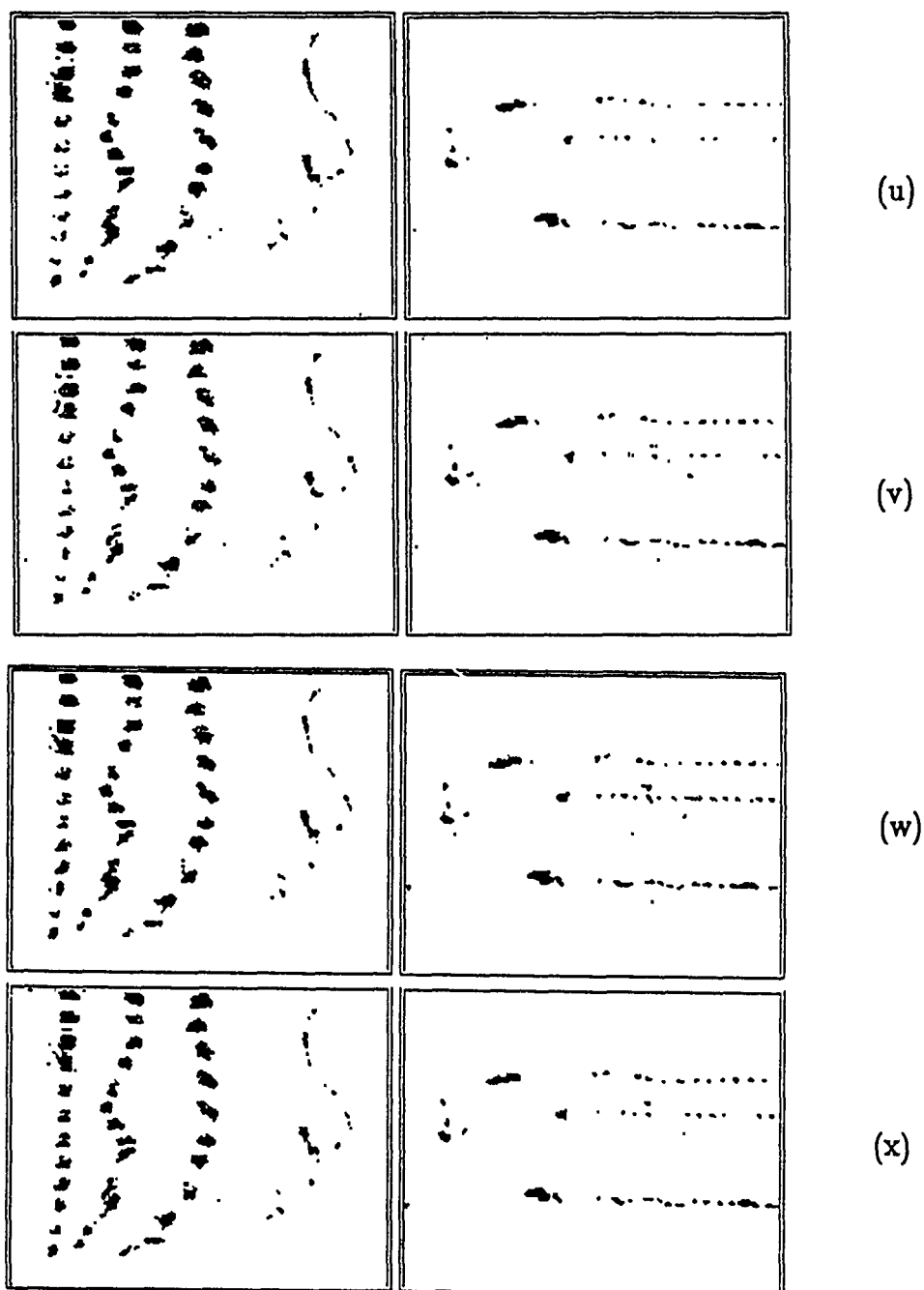


**Figure 59.** Concluded : (u)  $t = t_o + 0.160(sec)$ , (v)  $t = t_o + 0.168(sec)$ , (w)  $t = t_o + 0.176(sec)$ , and (x)  $t = t_o + 0.184(sec)$

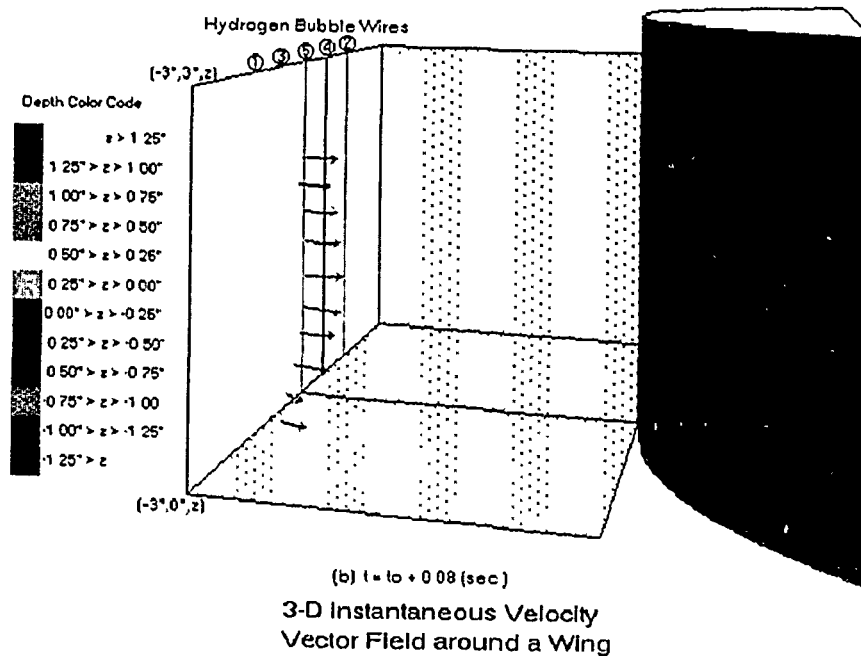
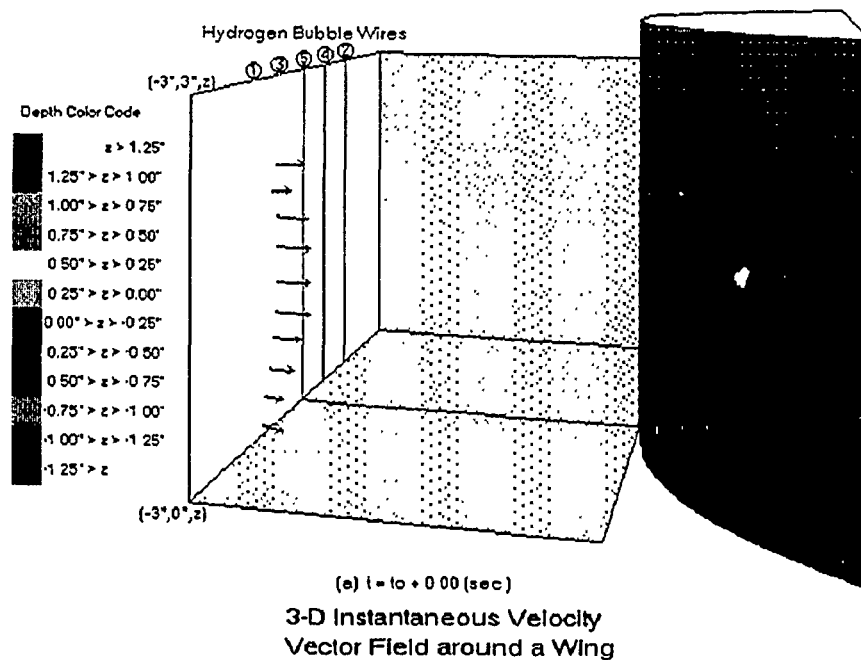


**Figure 60.** Sequence of instantaneous three-dimensional velocity vector field in the nose region of the wing-body junction (measured by PIDV)

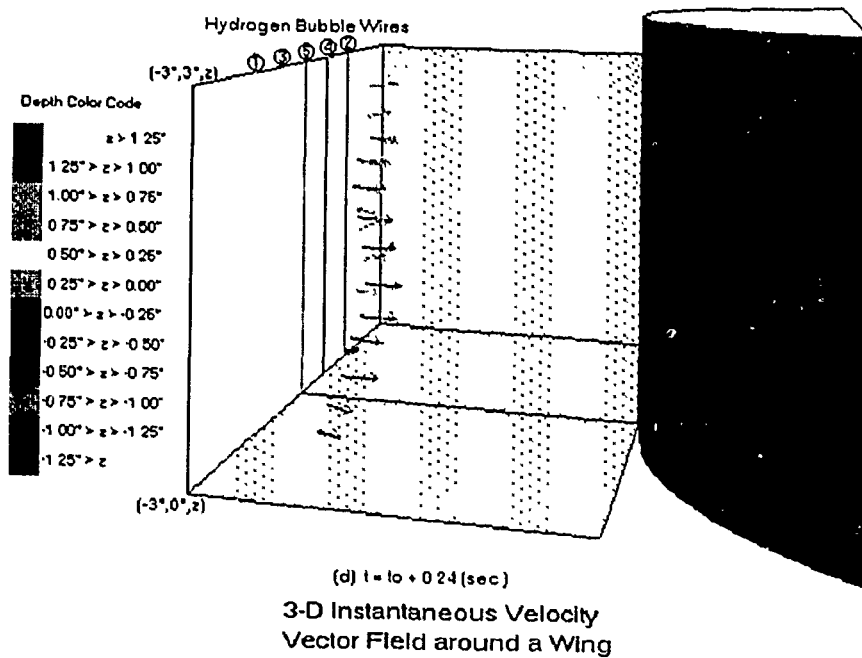
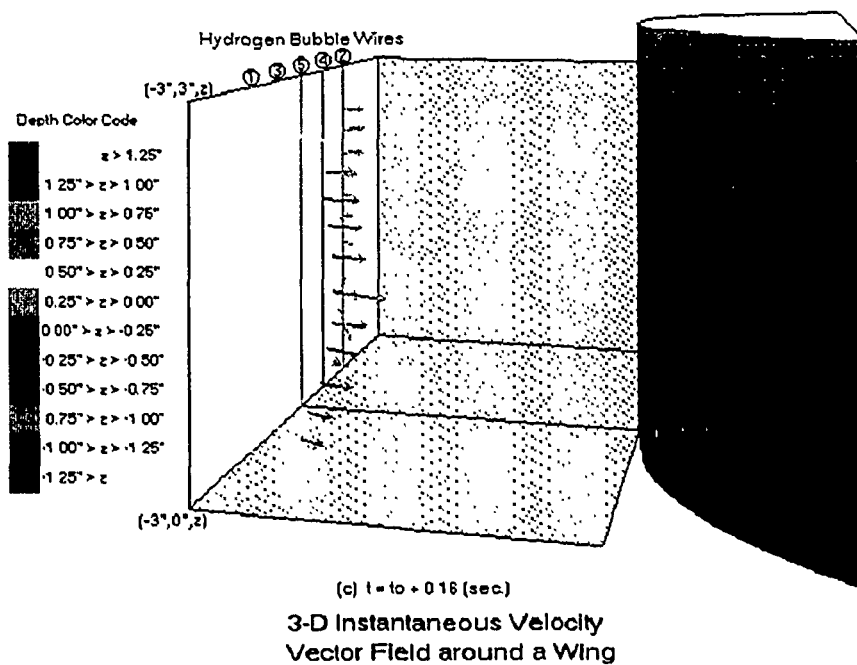
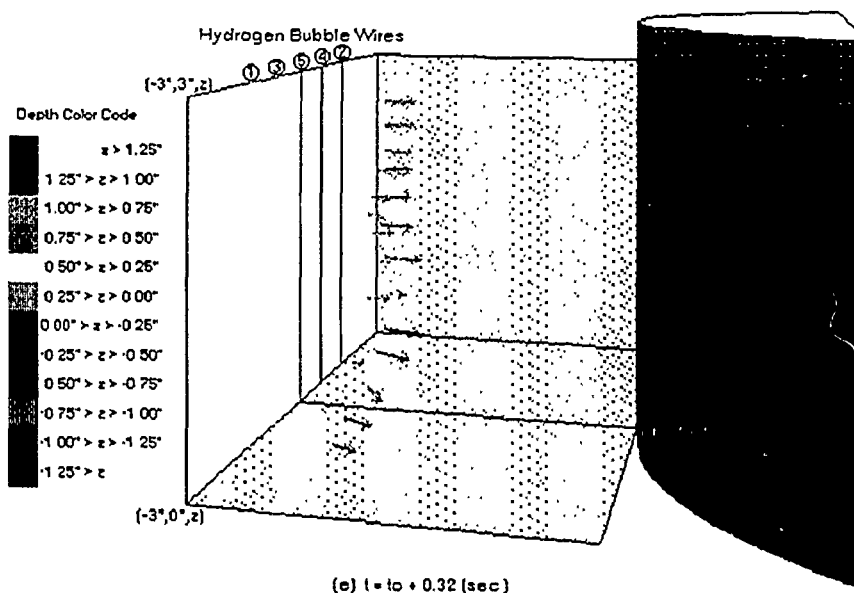
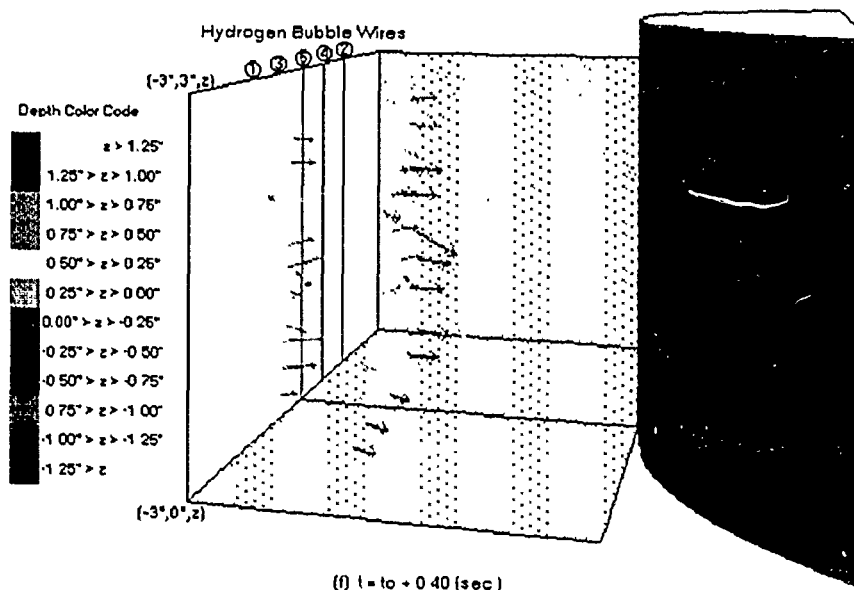


Figure 60. Continued





3-D Instantaneous Velocity  
Vector Field around a Wing



3-D Instantaneous Velocity  
Vector Field around a Wing

Figure 60. Continued

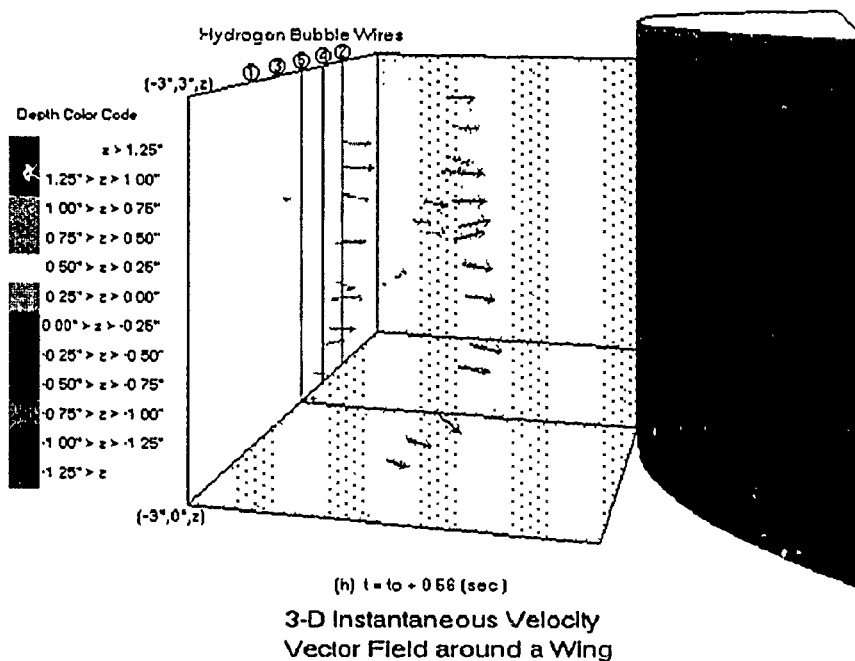
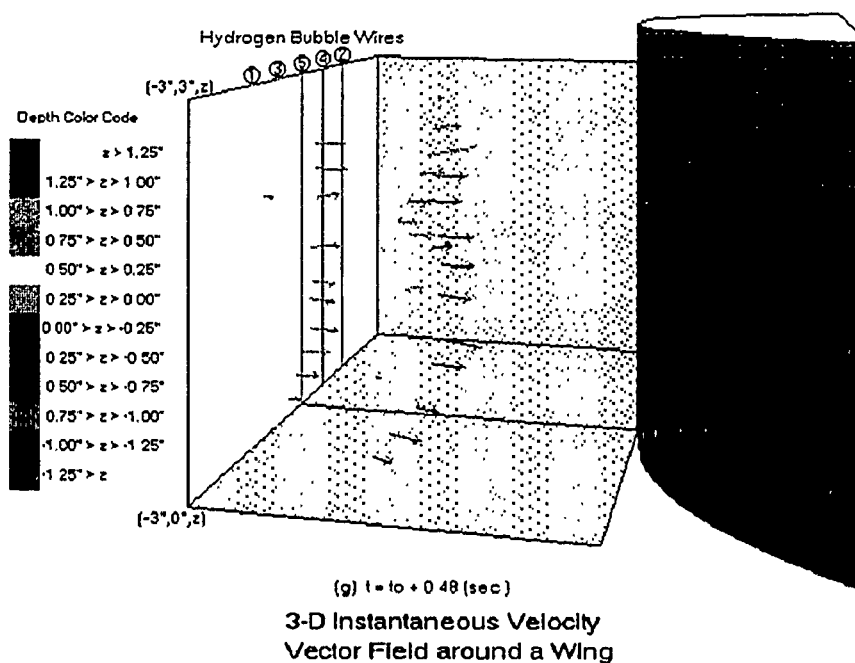


**Figure 60. Continued**

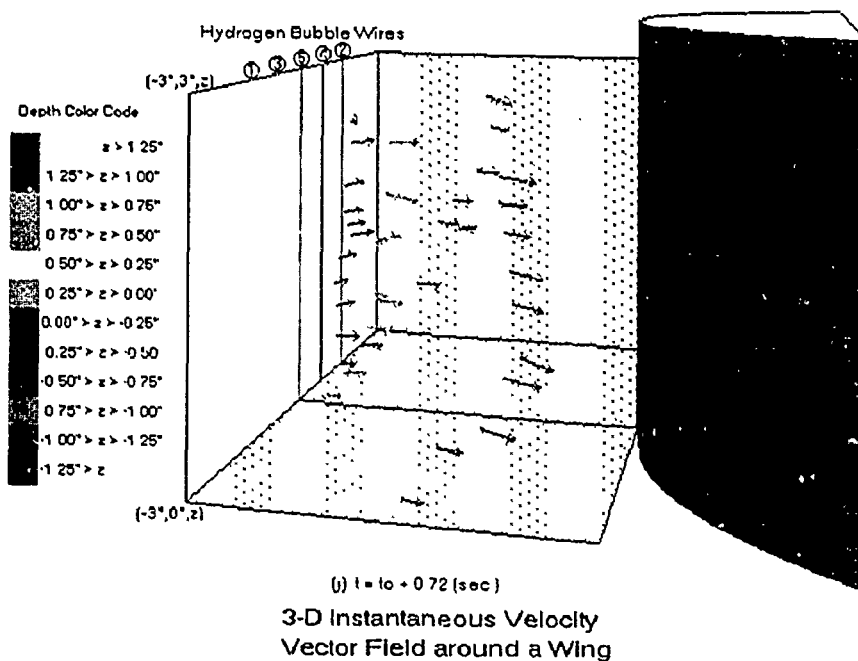
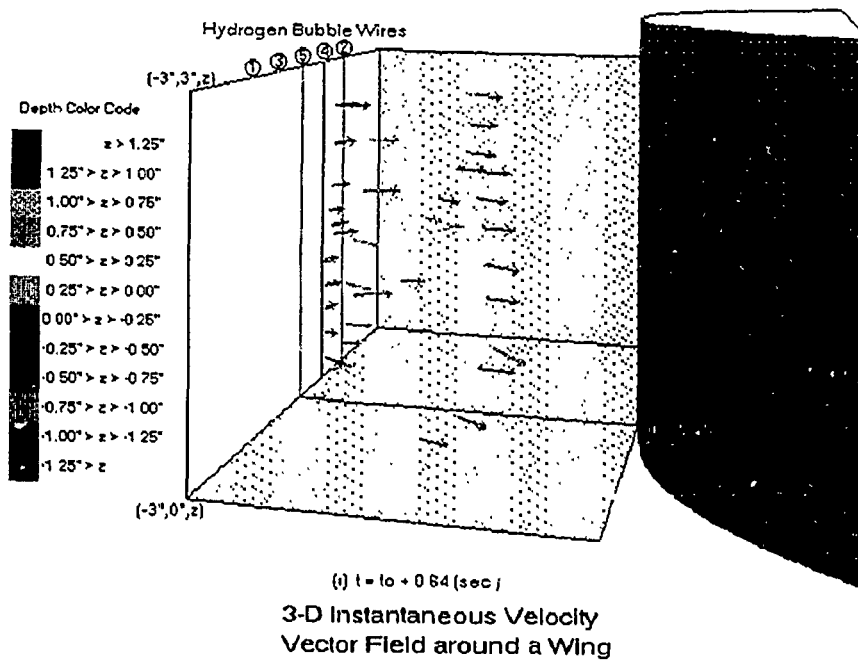


Figure 60. Continued

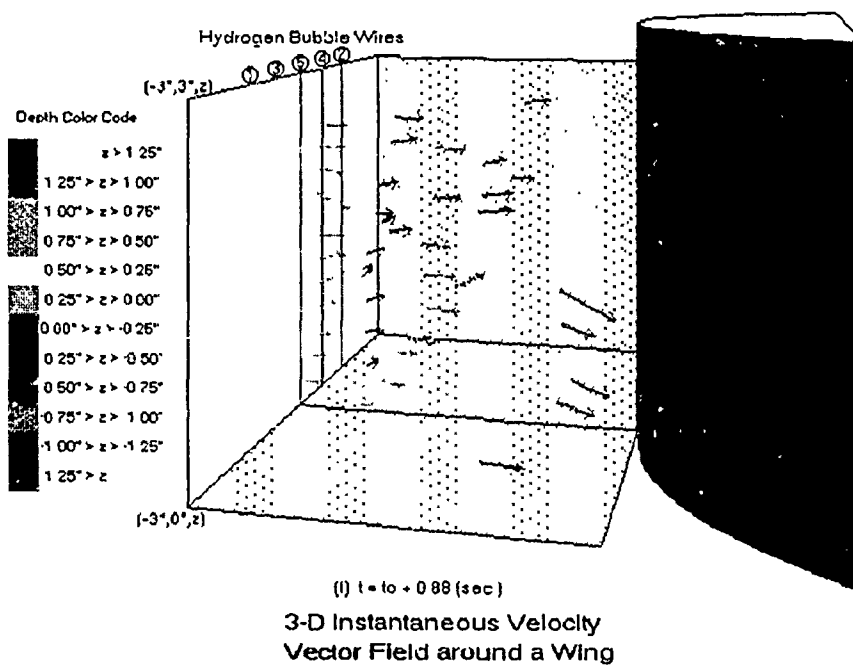
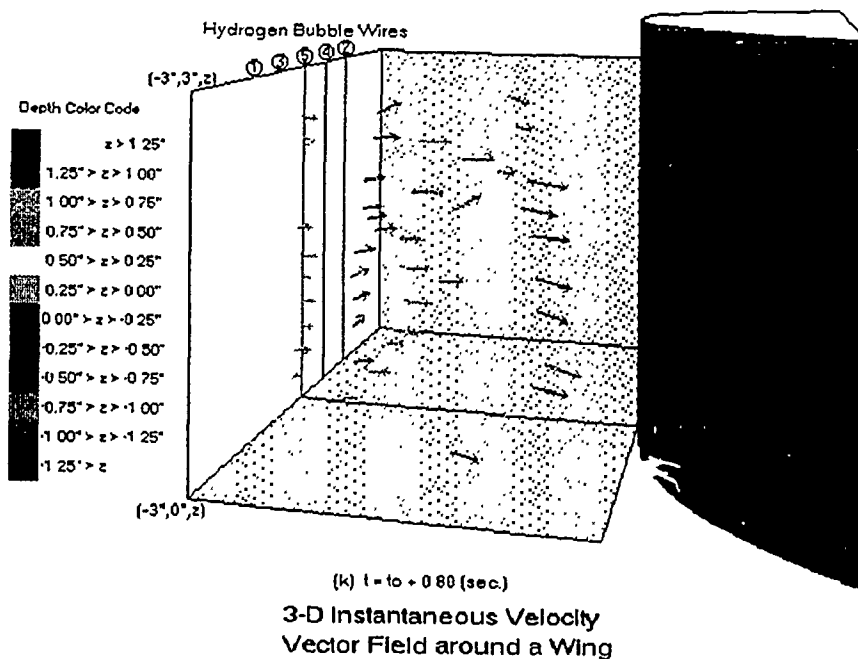
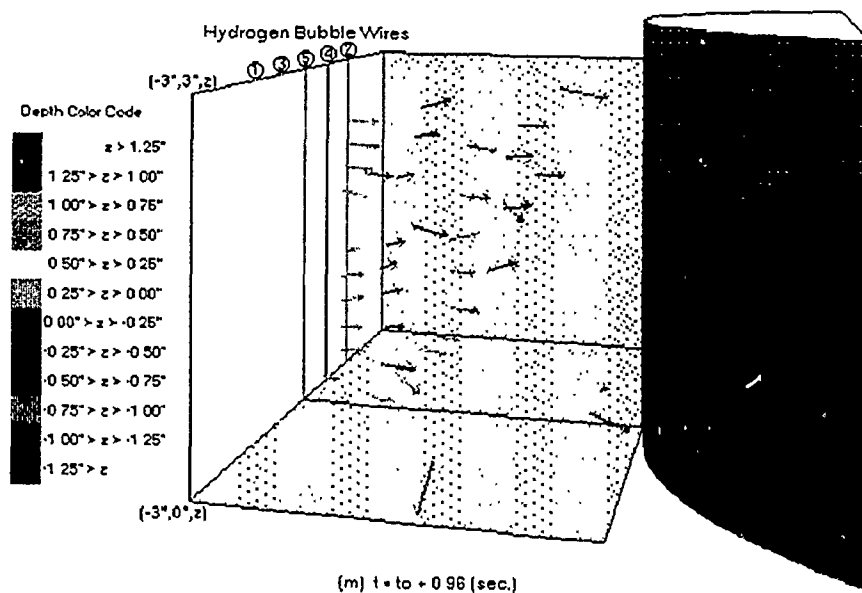
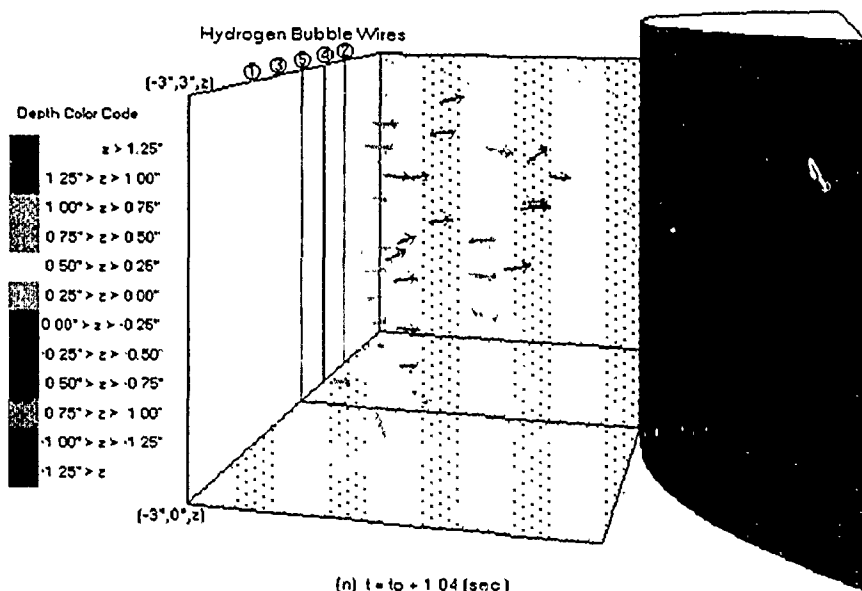


Figure 60. Continued

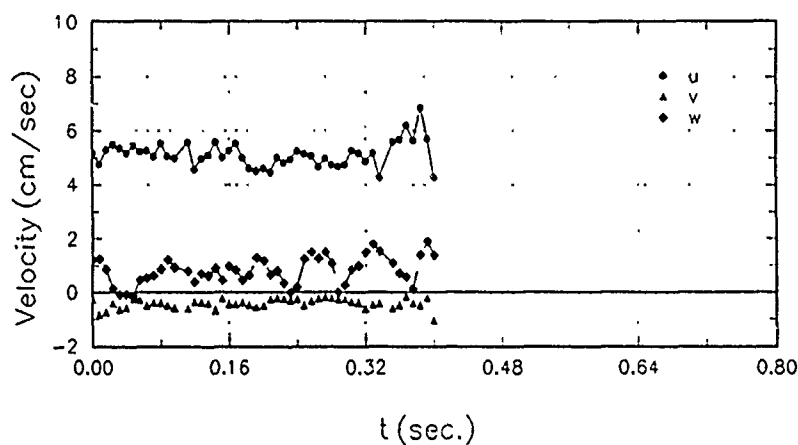
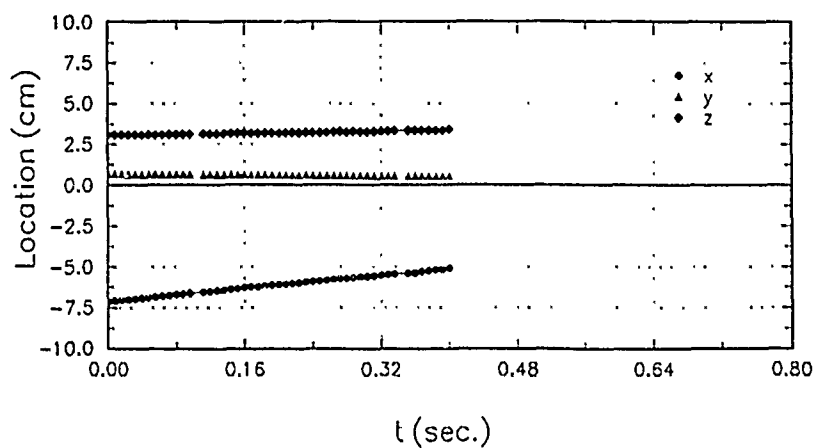


3-D Instantaneous Velocity  
Vector Field around a Wing



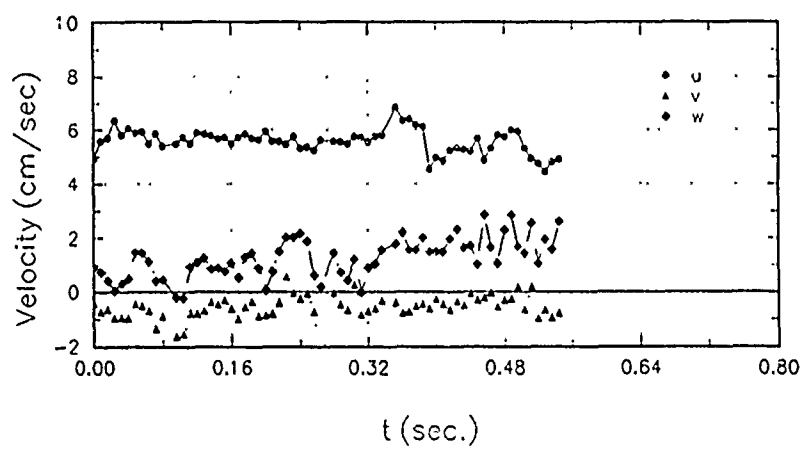
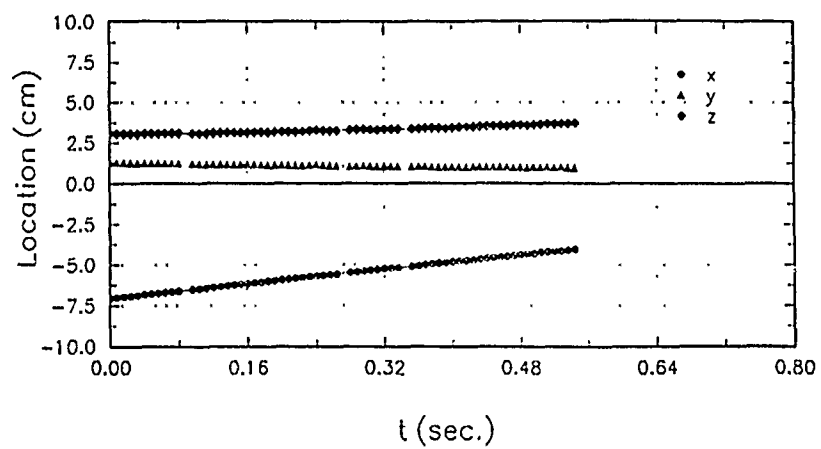
3-D Instantaneous Velocity  
Vector Field around a Wing

Figure 60. Concluded



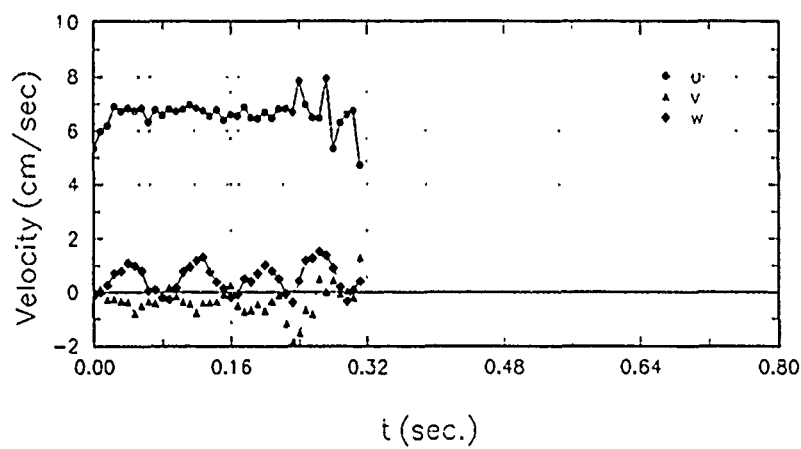
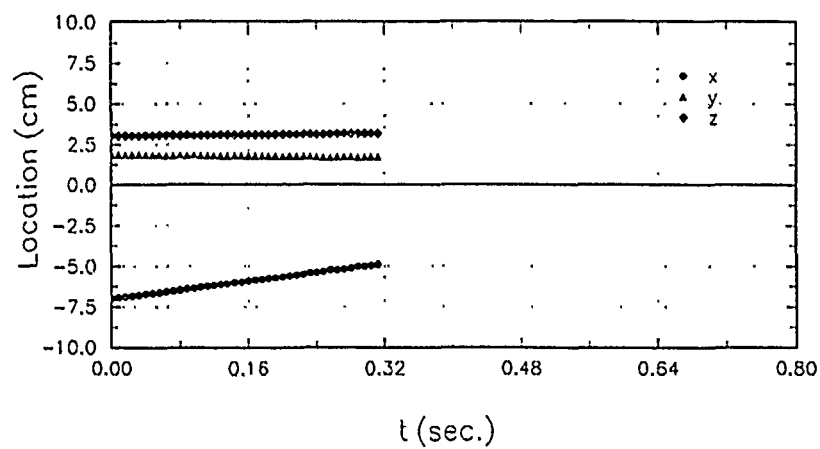
(a) 0-th bubble element

**Figure 61.** Three-dimensional instantaneous velocity components and locations of the individual bubble elements generated from the hydrogen bubble wire ; the results obtained by tracing the hydrogen bubble patches generated at the first wire are provided from the bottommost element to the top.



(b) 1-st bubble element

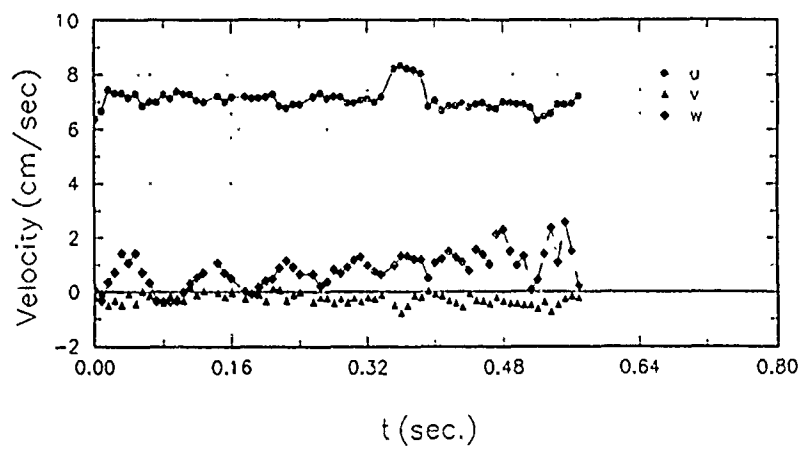
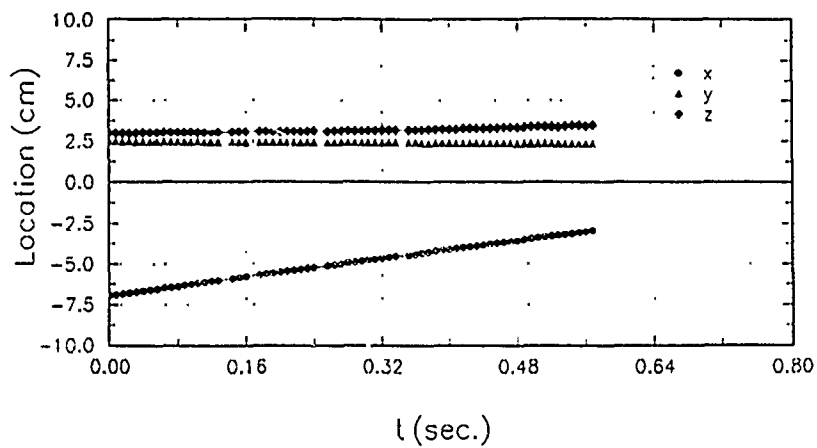
Figure 61. Continued



(c) 2-nd bubble element

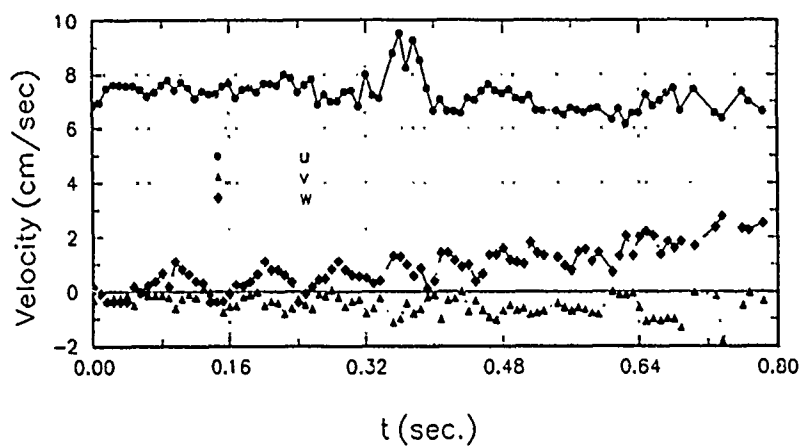
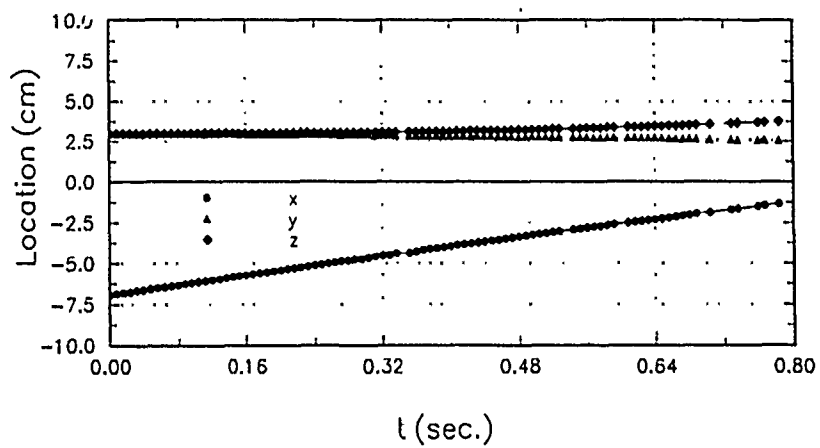
Figure 61. Continued





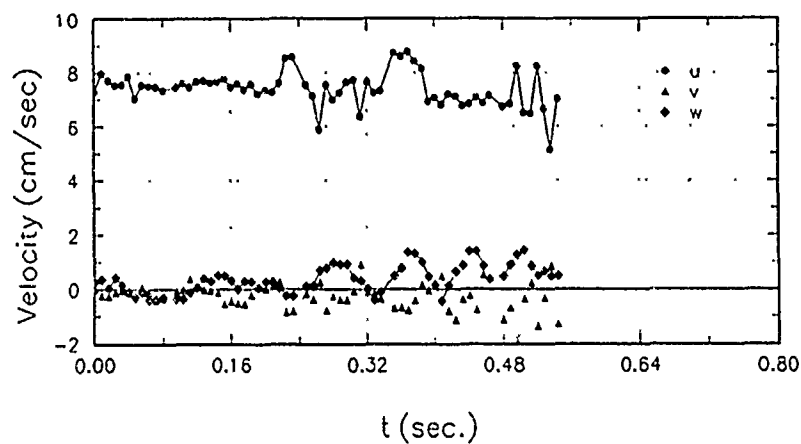
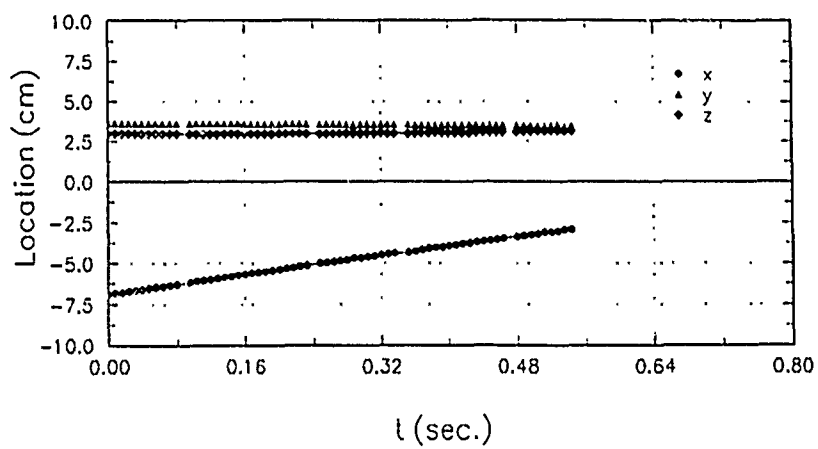
(d) 3-rd bubble element

Figure 61. Continued



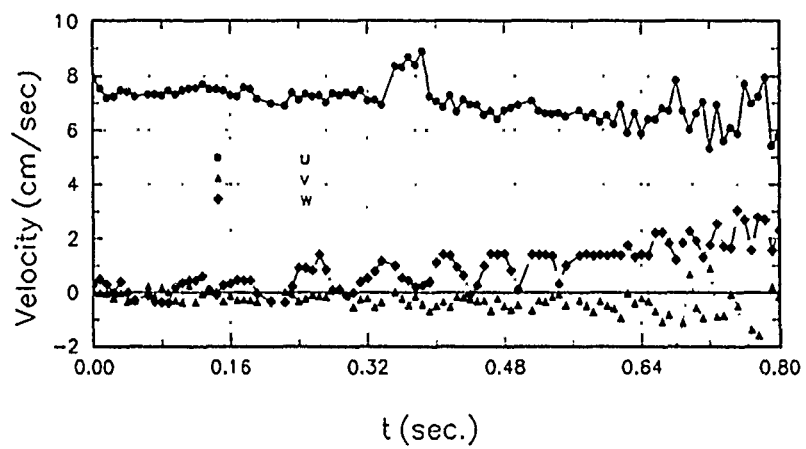
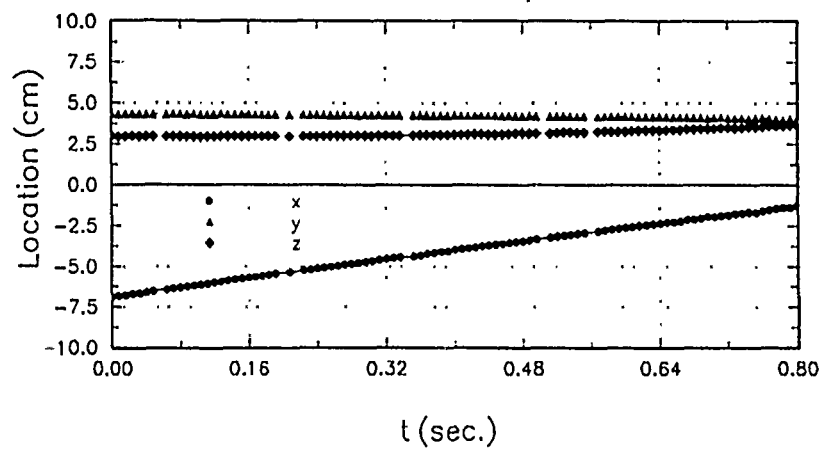
(e) 4-th bubble element

Figure 61. Continued



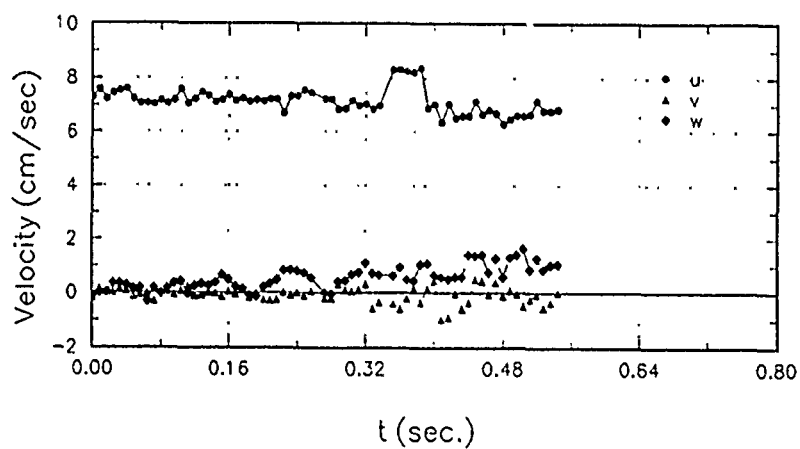
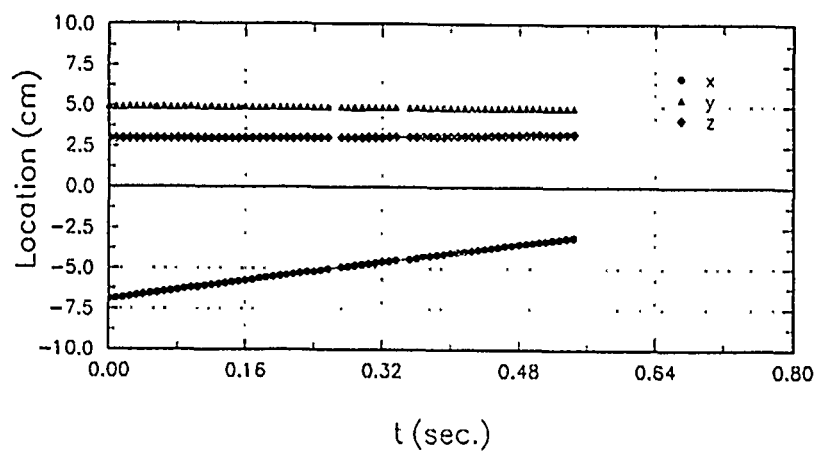
(f) 5-th bubble element

Figure 61. Continued



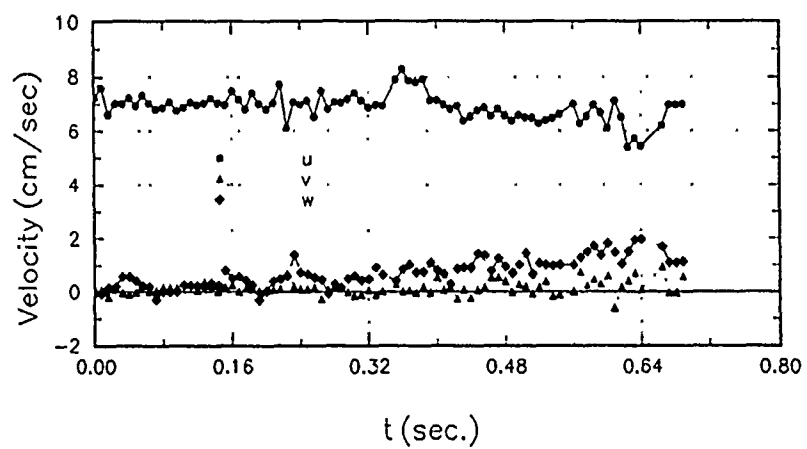
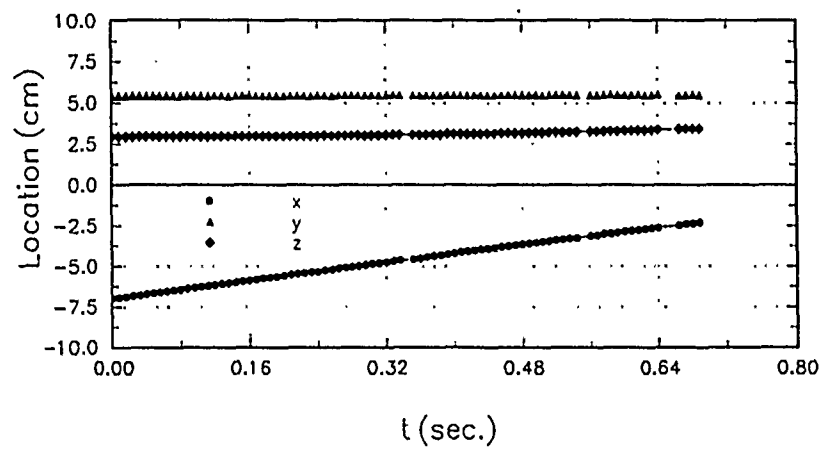
(g) 6-th bubble element

Figure 61. Continued



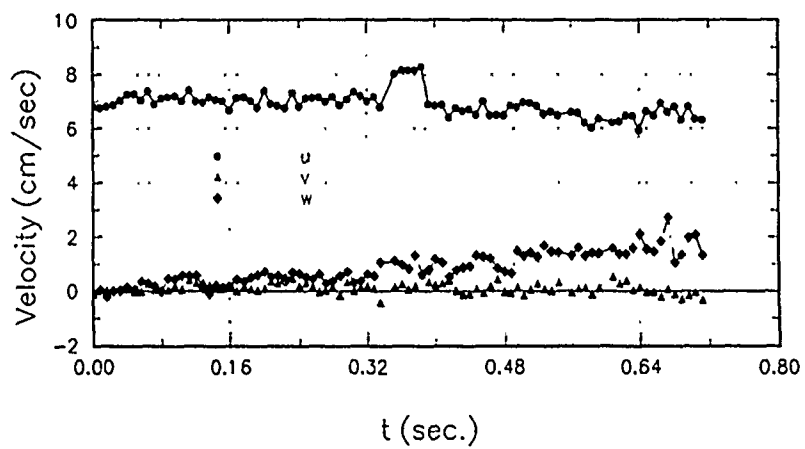
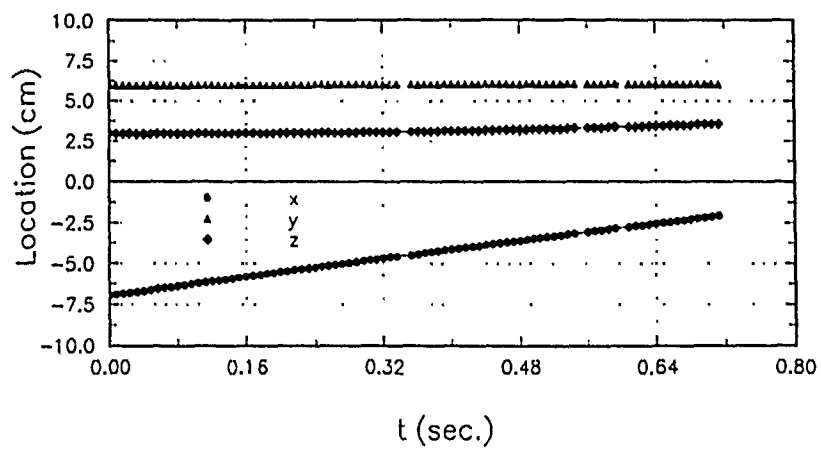
(h) 7-th bubble element

Figure 61. Continued



(i) 8-th bubble element

Figure 61. Continued



(j) 9-th bubble element

Figure 61. Concluded

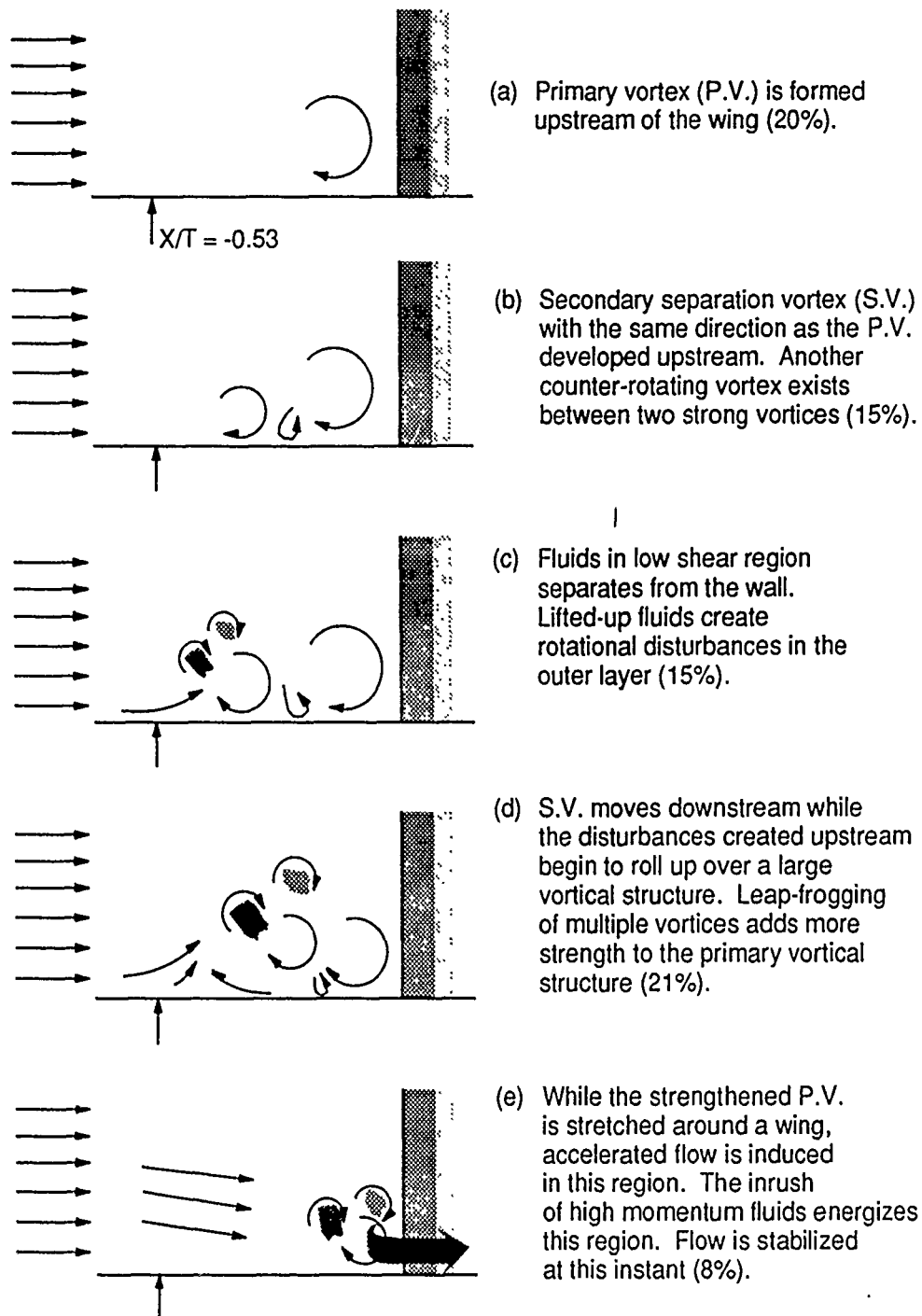
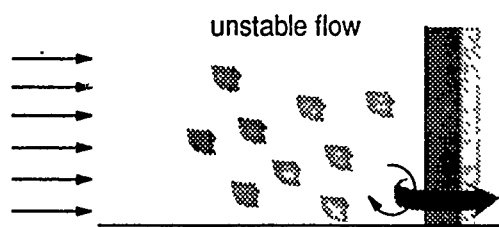
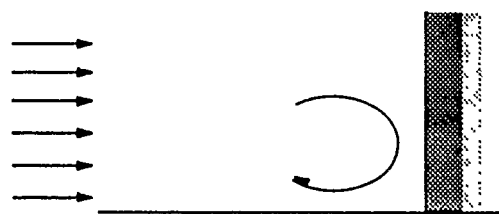


Figure 62. Descriptive model for the sequence of flow events in the nose region of a wing-body junction. The percentage in the parenthesis represents the approximate time proportion of the event.





(f) After a while, flow in this region becomes very unstable (7%).



(g) Some time later, a weak large vortical structure is formed again upstream of the wing. A cycle of (a) to (g) is repeated building up time-dependent characteristics of a junction flow (14%).

Figure 62. Concluded

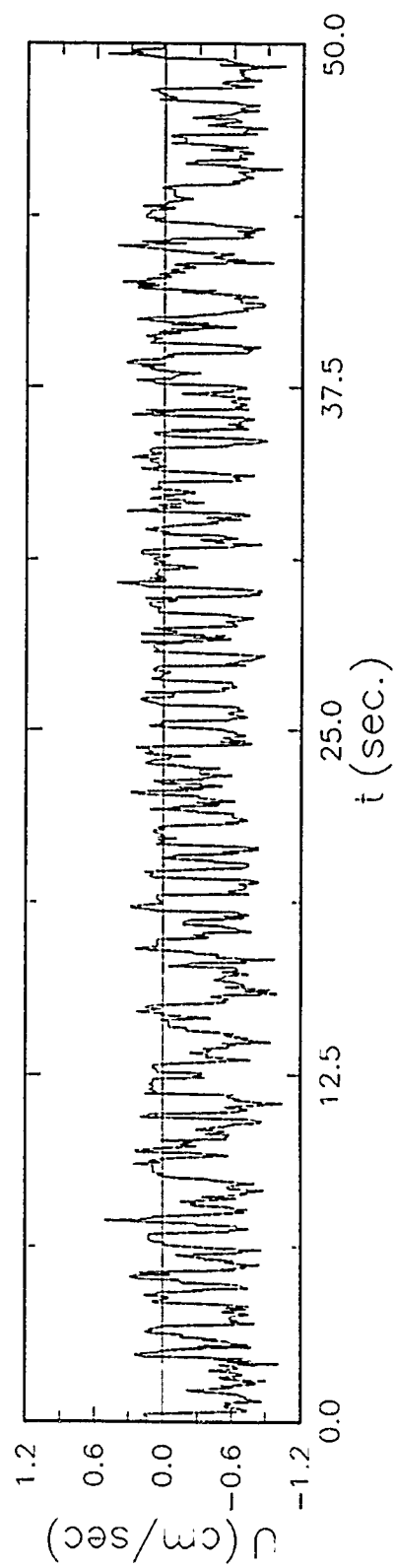


**Figure 63.** Typical LDV signal in the backflow region (measured at  $X/T = -0.125$  and  $Y/T = 0.0025$ )

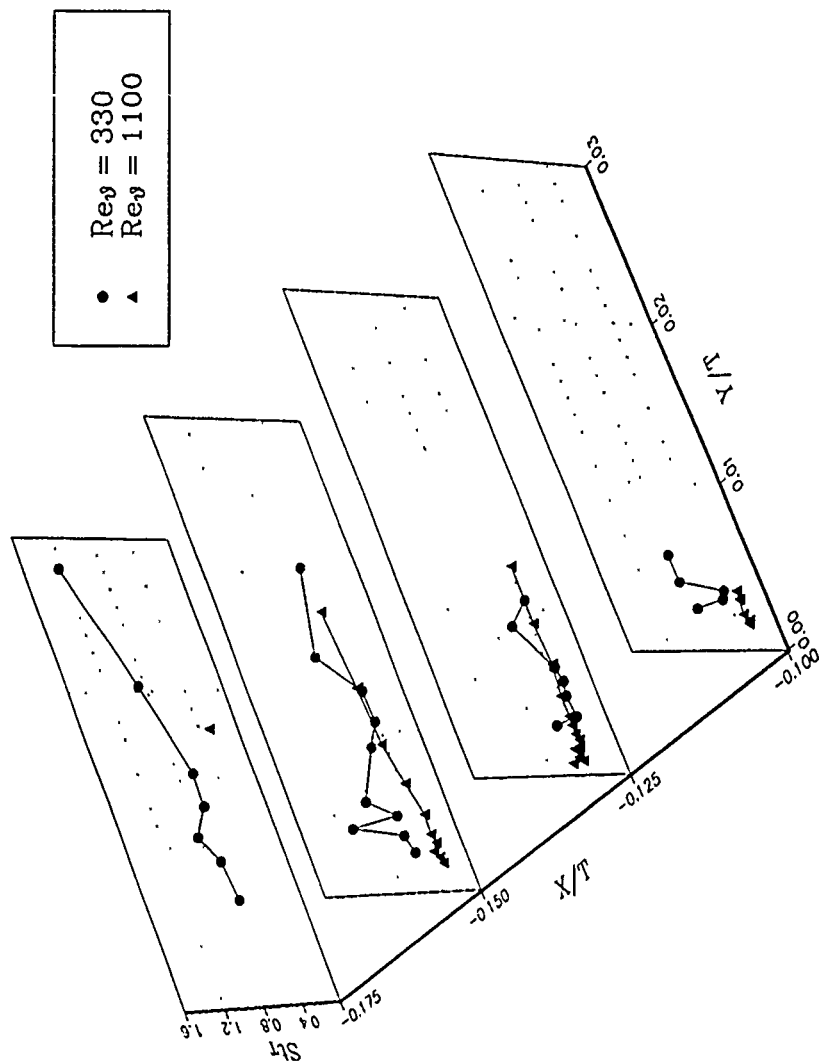


**Figure 64.** Variations of Strouhal numbers ( $St_T$ ) in the bimodal zone for each flow condition

## APPENDICES

## APPENDIX A. UNCERTAINTY ANALYSIS

Suppose that  $x, y, \dots, z$  are measured with uncertainties  $\delta x, \delta y, \dots, \delta z$ , and the measured values used to compute the function  $q(x, y, \dots, z)$ . If the uncertainties in  $x, y, \dots, z$  are independent and random, then the uncertainty in  $q$  is

$$\delta q = \sqrt{\left(\frac{\partial q}{\partial x} \delta x\right)^2 + \left(\frac{\partial q}{\partial y} \delta y\right)^2 + \dots + \left(\frac{\partial q}{\partial z} \delta z\right)^2} \quad (A.1)$$

In any case, it is never larger than the ordinary sum

$$\delta q \leq \left| \frac{\delta q}{\delta x} \right| \delta x + \left| \frac{\delta q}{\delta y} \right| \delta y + \dots + \left| \frac{\delta q}{\delta z} \right| \delta z \quad (A.2)$$

In case of the random errors, we can repeat our measurements in order to achieve reliability of the experiments, and the measured data set now can be analyzed statistically.

For the random variable  $x$  with  $N$  independent measurements  $(x_1, x_2, \dots, x_N)$ , the best estimate would be the average.

$$x_{best} = \bar{x} \quad (A.3)$$

$$\begin{aligned} \text{where } \bar{x} &= \frac{x_1 + x_2 + \dots + x_N}{N} \\ &= \frac{\sum_{i=1}^N x_i}{N}. \end{aligned} \quad (A.4)$$

The standard deviation ( $\sigma_x$ ) of the measurement  $x_1, x_2, \dots, x_N$  is an estimate of the average uncertainty of that measurement, and defined by

$$\sigma_x = \sqrt{\frac{1}{N-1} \sum_{i=1}^N (x_i - \bar{x})^2} \quad (A.5)$$

Actual uncertainty in random variable  $x$  with  $N$  measurements, however, is using another quantity, which is the standard deviation of the mean that is defined by

$$\sigma_{\bar{x}} = \frac{\sigma_x}{\sqrt{N}} \quad (A.6)$$

Thus, the value of the random variable  $x$  can be expressed as

$$(\text{value of } x) = \bar{x} \pm \sigma_{\bar{x}} \quad (A.7)$$

Here, the value of  $x$  expressed in Equation (A.7) has the confidence level of 68%, which means that only 68% of any subsequent measurements of  $x$  are expected to fall in the range  $\bar{x} \pm \sigma_{\bar{x}}$ . If the final value is written by

$$(\text{value of } x) = \bar{x} \pm 2\sigma_{\bar{x}} \quad (A.8)$$

or

$$(\text{value of } x) = \bar{x} \pm 3\sigma_{\bar{x}}, \quad (A.9)$$

the confidence level of each value would be 95% and 99%.

The present study used confidence level of 68% to compute the uncertainties of the individual measured variables, and then Equation (A.1) was applied to obtain the combined uncertainties of the target quantity  $q$ .

## APPENDIX B. Q - R ALGORITHM

Suppose we are given an overdetermined linear equation of the form

$$A\underline{x} = \underline{b} \quad (B.1)$$

where  $\underline{b}$  is  $m \times 1$ ,  $\underline{x}$  is  $n \times 1$ , and  $A$  is an  $m \times n$  matrix of rank  $m$ .

Q - R method is based on the decomposition of the  $m \times n$  matrix  $A$  into

$$A = QR \quad (B.2)$$

where  $Q$  is  $m \times m$  and satisfies

$$Q^T Q = D \quad (B.3)$$

$D$  is the diagonal matrix with non-zero diagonal elements.  $R$  is upper triangular  $n \times n$  matrix with diagonal entries  $r_{kk} = 1$ . (Notice, therefore,  $R^{-1}$  exists.) Given Equation (B.1) and Equation (B.2), we may reformulate the least-squares solution as

$$R^T Q^T (\underline{b} - A\underline{x}) = 0. \quad (B.4)$$

Since

$$Q^T A = Q^T Q R = D R \quad (B.5)$$

the preceding equation may be rewritten as

$$R^T (Q^T \underline{b} - D R \underline{x}) = 0. \quad (B.6)$$

Thus, we arrive at

$$D R \underline{x} = Q^T \underline{b}$$

or

$$R \underline{x} = D^{-1} Q^T \underline{b}. \quad (B.7)$$

Thus, if this equation were formulated, we could solve for  $\underline{x}$  via back substitution.

## APPENDIX C. $m_i$ ' COEFFICIENTS

The coefficients  $m_i$ 's in Equation (5.15) can be derived by arithmetically expanding Equation (5.14) as follows,

$$\begin{aligned}
 m_1 &= a_{131}D + a_{132}J + a_{133}P + a_{134}V \\
 m_2 &= -a_{111}B - a_{112}H - a_{113}N - a_{114}T \\
 m_3 &= a_{131}E + a_{132}K + a_{133}Q + a_{134}W \\
 m_4 &= -a_{111}A - a_{112}G - a_{113}M - a_{114}S \\
 m_5 &= a_{131}F + a_{132}L + a_{133}R + a_{134}X \\
 m_6 &= -a_{111}D - a_{112}J - a_{113}P - a_{114}V \\
 m_7 &= -a_{111}C - a_{112}I - a_{113}O - a_{114}U \\
 m_8 &= -a_{111}E - a_{112}K - a_{113}Q - a_{114}W \\
 m_9 &= -a_{111}F - a_{112}L - a_{113}R - a_{114}X.
 \end{aligned}$$

Here, the coefficients ( $m_1, \dots, m_9$ ) are derived for the coefficients of the line of correspondence in the upstream view image plane for a point in the side view image plane. The constants A thru X are functions of camera calibration coefficients and expressed in the following pages.



$$\begin{aligned}
A &= a_{132}(a_{223}a_{234} - a_{224}a_{233}) + a_{133}(a_{232}a_{224} - a_{222}a_{234}) + a_{134}(a_{233}a_{222} - a_{232}a_{223}) \\
B &= a_{132}(a_{214}a_{233} - a_{213}a_{234}) + a_{133}(a_{212}a_{234} - a_{214}a_{232}) + a_{134}(a_{213}a_{232} - a_{212}a_{233}) \\
C &= a_{132}(a_{213}a_{224} - a_{214}a_{223}) + a_{133}(a_{214}a_{222} - a_{212}a_{224}) + a_{134}(a_{212}a_{223} - a_{213}a_{222}) \\
D &= a_{122}(a_{224}a_{233} - a_{223}a_{234}) + a_{123}(a_{222}a_{234} - a_{224}a_{232}) + a_{124}(a_{223}a_{232} - a_{222}a_{233}) \\
E &= a_{122}(a_{213}a_{234} - a_{214}a_{233}) + a_{123}(a_{214}a_{232} - a_{212}a_{234}) + a_{124}(a_{212}a_{233} - a_{213}a_{232}) \\
F &= a_{122}(a_{214}a_{223} - a_{213}a_{224}) + a_{123}(a_{212}a_{224} - a_{214}a_{222}) + a_{124}(a_{213}a_{222} - a_{212}a_{223}) \\
G &= a_{131}(a_{224}a_{233} - a_{223}a_{234}) + a_{133}(a_{221}a_{234} - a_{224}a_{231}) + a_{134}(a_{223}a_{231} - a_{221}a_{233}) \\
H &= a_{131}(a_{213}a_{234} - a_{214}a_{233}) + a_{133}(a_{214}a_{231} - a_{211}a_{234}) + a_{134}(a_{211}a_{233} - a_{213}a_{231}) \\
I &= a_{131}(a_{214}a_{223} - a_{213}a_{224}) + a_{133}(a_{211}a_{224} - a_{214}a_{221}) + a_{134}(a_{213}a_{221} - a_{211}a_{223}) \\
J &= a_{121}(a_{223}a_{234} - a_{224}a_{233}) + a_{123}(a_{224}a_{231} - a_{221}a_{234}) + a_{124}(a_{221}a_{233} - a_{223}a_{231}) \\
K &= a_{121}(a_{214}a_{233} - a_{213}a_{234}) + a_{123}(a_{211}a_{234} - a_{214}a_{231}) + a_{124}(a_{213}a_{231} - a_{211}a_{233}) \\
L &= a_{121}(a_{213}a_{224} - a_{214}a_{223}) + a_{123}(a_{214}a_{221} - a_{211}a_{224}) + a_{124}(a_{211}a_{223} - a_{221}a_{213})
\end{aligned}$$

$$\begin{aligned}
M &= a_{131}(a_{222}a_{234} - a_{224}a_{232}) + a_{132}(a_{231}a_{224} - a_{221}a_{234}) - a_{134}(a_{231}a_{222} - a_{232}a_{221}) \\
N &= a_{131}(a_{214}a_{232} - a_{212}a_{234}) + a_{132}(a_{211}a_{234} - a_{214}a_{231}) - a_{134}(a_{211}a_{232} - a_{212}a_{231}) \\
O &= a_{131}(a_{212}a_{224} - a_{214}a_{222}) + a_{132}(a_{214}a_{221} - a_{211}a_{224}) - a_{134}(a_{212}a_{221} - a_{211}a_{222}) \\
P &= a_{121}(a_{224}a_{232} - a_{222}a_{234}) + a_{122}(a_{221}a_{234} - a_{224}a_{231}) - a_{124}(a_{221}a_{232} - a_{222}a_{231}) \\
Q &= a_{121}(a_{212}a_{234} - a_{214}a_{232}) + a_{122}(a_{214}a_{231} - a_{211}a_{234}) - a_{124}(a_{212}a_{231} - a_{211}a_{232}) \\
R &= a_{121}(a_{214}a_{222} - a_{212}a_{224}) + a_{122}(a_{211}a_{224} - a_{214}a_{221}) - a_{124}(a_{211}a_{222} - a_{212}a_{221}) \\
S &= -a_{131}(a_{222}a_{233} - a_{223}a_{232}) + a_{132}(a_{221}a_{233} - a_{223}a_{231}) + a_{133}(a_{222}a_{231} - a_{221}a_{232}) \\
T &= -a_{131}(a_{213}a_{232} - a_{212}a_{233}) + a_{132}(a_{213}a_{231} - a_{211}a_{233}) + a_{133}(a_{211}a_{232} - a_{212}a_{231}) \\
U &= -a_{131}(a_{212}a_{223} - a_{213}a_{222}) + a_{132}(a_{211}a_{223} - a_{213}a_{221}) + a_{133}(a_{212}a_{221} - a_{211}a_{222}) \\
V &= -a_{121}(a_{223}a_{232} - a_{222}a_{233}) + a_{122}(a_{223}a_{231} - a_{221}a_{233}) + a_{123}(a_{221}a_{232} - a_{222}a_{231}) \\
W &= -a_{121}(a_{212}a_{233} - a_{213}a_{232}) + a_{122}(a_{211}a_{233} - a_{213}a_{231}) + a_{123}(a_{212}a_{231} - a_{211}a_{232}) \\
X &= -a_{121}(a_{213}a_{222} - a_{212}a_{223}) + a_{122}(a_{213}a_{221} - a_{211}a_{223}) + a_{123}(a_{211}a_{222} - a_{221}a_{212})
\end{aligned}$$